Synthesis and Surface Chemistry of Phase-Stable Caesium Lead Halide Perovskite Colloidal Nanocrystals

Chujie Wang
Bachelor of Engineering (honours)

A thesis submitted for the degree of Doctor of Philosophy at
Monash University in 2020
Department of Materials Science and Engineering

Copyright notice

© Chujie Wang (*2020*).

I certify that I have made all reasonable efforts to secure copyright permissions for third-party content included in this thesis and have not knowingly added copyright content to my work without the owner's permission.

Abstract

All inorganic $CsPbX_3$ ($X=Cl^-$, Br^-, I^-) perovskite nanocrystals (PNCs) possess near-unity photoluminescence quantum yield (PLQY), narrow PL peak full width half maximum (FWHM) within 50 nm, and fully tuneable emission across the entire visible spectrum. As a result of these superb properties, these materials have emerged as promising candidates for a variety of optoelectronic applications, such as LED, solar cells, lasers and photodetectors. Yet, the understandings towards the synthesis of this material class is still limited. Therefore, the aim of this thesis is to further investigate the synthesis of $CsPbX_3$ NCs with an overarching goal to developing phase stable $CsPbX_3$ PNCs that can be assembled and used within practical applications.

Chapter 1 introduces the research scope and reviews the current research in the PNC field, which includes: the birth of $CsPbX_3$ PNCs; their optoelectronic and physical properties; the different synthesis methods developed; studies on the nucleation and growth dynamics and the surface chemistry; post-synthetic treatments; and finally the research gaps remaining. Chapter 2 provides an overview of the detailed synthesis and experimental procedures and analysis methods used in this thesis. Chapter 3 presents research on the phase transformation mechanism of $CsPbI_3$ PNCs and introduces a novel synthetic method that enables stabilizes cubic-phased $CsPbI_3$ PNCs. This synthesis protocol is also expanded to all the $CsPbX_3$. In Chapter 4, the surface chemistry of the $CsPbX_3$ NCs is explored and a facile purification procedure is developed to obtain high quality and high purity $CsPbX_3$ NCs inks. Chapter 5 introduces an innovative synthetic protocol to achieve the self-assembly of $CsPbX_3$ super-crystals with modified optical and colloidal properties. Finally, Chapter 6 summarises the thesis and provides a perspective of current challenges and future works.

Declaration

This thesis is an original work of my research and contains no material which has been accepted for the award of any other degree or diploma at any university or equivalent institution and that, to the best of my knowledge and belief, this thesis contains no material previously published or written by another person, except where due reference is made in the text of the thesis.

Signature: Chujie Wang

Print Name: Chujie Wang

Date: ……15/01/2020…….

Publications during enrolment

[1] **C. Wang**, A. S. R. Chesman, J. J. Jasieniak, Stabilizing the cubic perovskite phase of CsPbI 3 nanocrystals by using an alkyl phosphinic acid. *Chem. Commun.* **2017**, *53*, 232.

[2] **C. Wang**, A. S. R. Chesman, W. Yin, L. Frazer, A. M. Funston, J. J. Jasieniak, Facile purification of CsPbX3 (X =Cl^-, Br^-,I^-) perovskite nanocrystals, *J. Chem. Phys.* **2019**, *151*, 121105.

[3] C. K. Ng, **C. Wang**, J. J. Jasieniak, Synthetic Evolution of Colloidal Metal Halide Perovskite Nanocrystals, *Langmuir* **2019**, *35*, 11609.

[4] Z. Dai, Q. Ou, **C. Wang**, G. Si, B. Shabbir, C. Zheng, Z. Wang, Y. Zhang, Y. Huang, Y. Dong, J. J. Jasieniak, B. Su, Q. Bao, Capillary-bridge mediated assembly of aligned perovskite quantum dots for high-performance photodetectors, *J. Mater. Chem. C* **2019**, *7*, 5954.

[5] J. Liu, B. Shabbir, **C. Wang**, T. Wan, Q. Ou, P. Yu, A. Tadich, X. Jiao, D. Chu, D. Qi, D. Li, R. Kan, Y. Huang, Y. Dong, J. Jasieniak, Y. Zhang, Q. Bao, Flexible, Printable Soft‐X‐Ray Detectors Based on All‐Inorganic Perovskite Quantum Dots, *Adv. Mater.* **2019**, *31*, 1901644.

[6] J. Zheng, C. Luo, B. Shabbir, **C. Wang**, W. Mao, Y. Zhang, Y. Huang, Y. Dong, J. J. Jasieniak, C. Pan, Q. Bao, Flexible photodetectors based on reticulated SWNT/perovskite quantum dot heterostructures with ultrahigh durability, *Nanoscale* **2019**, *11*, 8020.

Thesis including published works declaration

I hereby declare that this thesis contains no material which has been accepted for the award of any other degree or diploma at any university or equivalent institution and that, to the best of my knowledge and belief, this thesis contains no material previously published or written by another person, except where due reference is made in the text of the thesis.

This thesis includes 2 original papers published in peer reviewed. The core theme of the thesis is synthesising phase stable $CsPbI_3$ PNCs and developing high purity and quality PNCs dispersion. The ideas, development and writing up of all the papers in the thesis were the principal responsibility of myself, the student, working within the Materials Science Engineering, Monash University under the supervision of Professor Jacek Jasieniak.

The inclusion of co-authors reflects the fact that the work came from active collaboration between researchers and acknowledges input into team-based research.

In the case of **Chapter 3** and **4** my contribution to the work involved the following:

Thesis Chapter	Publication Title	Status (published, in press, accepted or returned for revision, submitted)	Nature and % of student contribution	Co-author name(s) Nature and % of Co-author's contribution*	Co-author(s), Monash student Y/N*
3	Stabilizing the cubic perovskite phase of $CsPbI_3$ nanocrystals by using an alkyl phosphinic acid	Published	70%. Concept and collecting data and writing draft.	(1). Anthony S. R. Chesman, collect NMR data, input into manuscript 15%. (2). Jacek J. Jasieniak, input into manuscript 15%.	No No
4	Facile purification of $CsPbX_3$ (X = Cl−, Br−, I−) perovskite nanocrystals	Published	65%. Concept and collecting data and writing draft.	(1). Anthony S. R. Chesman, collect NMR data, input into manuscript 10%. (2). Wenping Yin, analysis the TRPL data, input into manuscript 5%. (3). Laszlo Frazer, collect the TRPL data, input into manuscript 5%. (4). Alison M. Funston, input into manuscript 5%. (5). Jacek J. Jasieniak, input into manuscript 10%.	No Yes Yes No No

I have renumbered sections of submitted or published papers in order to generate a consistent presentation within the thesis.

Student signature: Chujie Wang **Date: 15/01/2020**

The undersigned hereby certify that the above declaration correctly reflects the nature and extent of the student's and co-authors' contributions to this work. In instances where I am not the responsible author I have consulted with the responsible author to agree on the respective contributions of the authors.

Main Supervisor signature: **Date: 15/01/2020**

Acknowledgements

I have experienced four fantastic years doing research and living in Monash University. Here, I would like to express my sincere gratitude to many people who helped me throughout my PhD.

First of all, I would like give my heartful appreciation to my supervisor, Prof. Jacek J. Jasieniak for his guidance and support. He has taught me plenty of beneficial skills throughout my PhD, which includes setting up explicit research plans, efficiently conducting experiments, drawing clear and simple figures, writing precise and concise articles and so on. His inspiration encouraged me on continuously improving my work, and his foresight always pointed out the right direction. Meanwhile, he has not only passed on his knowledge, but also his enthusiasm and passion towards science and life to me. I am so fortunate to have him as my mentor.

Then I would like to thank my second supervisor Dr. Anthony S. R. Chesman for helping me with experiments, teaching me research skills and providing all sorts of support. Thanks to all my co-workers in Jacek's research group and in the Renewable Energy Lab for their cooperation and enlightening throughout my works. I will always remember the time we worked together. Also, thanks to the staff in Monash Centre of Electron Microscopy, Monash X-ray Platform and Monash Nuclear Magnetic Resonance facility for providing training in the equipment and teaching data analysis methods.

Finally, I am grateful to my family and friends. Thanks to my parents, Fengying Chu and Baisheng Wang who have given me enormous love for my entire life. Every time I felt depressed, my mother's kind encouragement always raised me up again. Every time when I felt overwhelmed by the difficulties in research or life, the "keep calm and patient" spirit taught by my father always let me find the way through. Also, thanks to my beloved partner Yuqi. It is so joyful to share my opinions in research questions, current affairs, movies, games, and even Fermi Paradox to you. These four years of PhD accompanied by you are as short as a blink. My life with you is always so wonderful.

Abbreviations

CSIRO	Commonwealth scientific and industrial research organization
DLS	Dynamic light scattering
DMF	Dimethylformamide
DMSO	Dimethyl sulfoxide
DOA	Dodecylamine
DOSY	Diffusion-ordered spectroscopy
DPA	Diisooctylphosphinic acid
DTA	2-decyltetradecaonic acid
EDX	Energy dispersive x-ray
ERETIC	Electronic reference to access in vivo concentrations
FA	Formamidinium
FTIR	Fourier-transform Infrared Spectroscopy
FWHM	Full width half maximum
HBr	Hydrobromic acid
HCl	Hydrochloric acid
HDA	Hexadecylamine
HI	Hot injection
HI	Hydroiodic acid
HLA	2-hexyldecanoic acid
HX	Hydrohalic acid
ICP-MS	Inductively coupled plasma mass spectrometry
IPA	Isopropanol
LED	Light emitting diode

LI	Low temperature injection
MA	Methylammonium
MCEM	Monash centre of electron microscopy
MXP	Monash X-ray platform
NC	Nanocrystal
NCU	Nanocube
NIR	Near infrared
NMR	Nuclear magnetic resonance
NPL	Nanoplatelet
NR	Nanorod
NS	Nanosheet
NW	Nanowire
OA	Oleic acid
OCDA	Octadecylamine
OCT	Octylamine
ODE	Octadecene
OLA	Oleylamine
PL	Photoluminescence
PLQY	Photoluminescence quantum yield
PMMA	Poly methyl methacrylate
PNCs	Perovskite nanocrystals
ppm	Part per million
PTFE	Polytetrafluoroethylene
QD	Quantum dot

SADP	Selected area diffraction pattern
SC	Super-crystal
STEM	Scanning transmission electron microscopy
TCSPC	Time-correlated single photon counting
TEM	Transmission electron microscopy
TMPPA	Bis(2,4,4-trimethylpentyl) phosphinic acid
TOP	Trioctylphosphine
TOPO	Trioctylphosphine oxide
TRPL	Time resovled photoluminescence
VDW	Van Der Waals force
XRD	X-ray diffraction

Table of contents

Abbreviations x

Chapter 1. Introduction to $CsPbX_3$ Perovskite Nanocrystals 1

1.1 Synopsis 1

1.2 Perovskites 2

1.2.1 Metal Halide Perovskite 2

1.2.2 Inorganic Metal Halide Perovskite 3

1.2.3 Optical Properties of $CsPbX_3$ 5

1.3 Synthesis of $CsPbX_3$ PNCs 7

1.3.1 Hot-Injection 8

1.3.2 Low-Temperature Injection 16

1.3.3 Non-Injection 18

1.4 Nucleation & Growth of PNCs 19

1.4.1 Nucleation 20

1.4.2 Growth 22

1.5 Ligand Interactions with PNCs 25

1.6 Post-Synthetic Treatments 26

1.6.1 Purification 27

1.6.2 Anion Exchange 28

1.6.3 Cation Exchange 29

1.6.4 Post-synthetic Self-assembly of PNCs 31

1.7 Thesis Overview 33

References 34

Chapter 2. Experimental Methods 43
2.1 Synopsis 43
2.2 Materials 44
2.3 Synthesis of Materials 45
2.3.1 Synthesis of Cs Precursor 45
2.3.2 Synthesis of $CsPbX_3$ NCs 45
2.3.3 Preparation of Mixed Halide $CsPbX_3$ PNCs Dispersion 46
2.3.4 Synthesis of Branched Carboxylic Acid 47
2.3.5 Synthesis of Hexadecylammonium Iodide (RNH_3I). 47
2.3.6 Preparation of RNH_3I solution. 48
2.3.7 Preparation of PbX_2 solution 48
2.3.8 Synthesis of $CsPbX_3$ Super-Crystals 48
2.4 Purification of $CsPbX_3$ PNCs 49
2.4.1 Washing without any additives 49
2.4.2 Washing with ligand additives 50
2.4.3 Washing with RNH_3I 50
2.4.4 Washing with RNH_3I solution 50
2.4.5 Washing with PbI_2 solution 51
2.4.6 Washing of the Super-crystals 51
2.5 Preparation of SC-PMMA composite 51
2.6 Characterization 52
2.6.1 UV-vis Spectroscopy 52
2.6.2 Photoluminescence (PL) 53

2.6.3 X-ray Diffraction (XRD) 54

2.6.4 Transmission Electron Microscopy (TEM) 54

2.6.5 Time-Resolved Photoluminescence (TRPL) 56

2.6.6 Nuclear Magnetic Resonance Spectroscopy (NMR) 56

2.6.7 Inductively Coupled Plasma Mass Spectrometry (ICP-MS) 56

2.6.8 Dynamic Light Scattering (DLS) 57

2.7 Data processing 57

2.7.1 Photoluminescence Quantum Yield (PLQY) Measurement 57

2.7.2 Determination of [NC] for $CsPbX_3$ PNCs 58

2.7.3 Determination of Extinction Coefficient 59

2.7.4 Determination of [Surface ions] 59

2.7.5 Estimation of Diffusion Coefficient 60

2.7.6 Ligand density Calculation 61

References 62

Chapter 3. Synthesis of $CsPbX_3$ PNCs 63

3.1 Declaration 63

3.2 Introduction 63

3.3 Phase Transformation of $CsPbI_3$ 64

3.3.1 XRD 65

3.3.2 Ex-situ TEM 67

3.3.3 In-situ Heating TEM 68

3.4 Synthesis of Cubic Phase-stable $CsPbI_3$ 70

3.4.1 Ligand Selection & Synthesis 70

3.4.2 Optical and Structural Characterisation 72

3.4.3 NCs Size Evolution during Purification 74

3.4.4 Surface Chemistry of $CsPbI_3$-TMPPA 76

3.4.5 TMPPA-Suppressed Coarsening of the $CsPbI_3$ PNCs 83

3.4.6 Stabilization of the α-$CsPbI_3$ with Branching Ligands 87

3.5 Generalized Synthesis of $CsPbX_3$ PNCs 90

3.6 Conclusions 92

References 93

Chapter 4. Surface Chemistry and Purification of $CsPbI_3$ PNCs 95

4.1 Synopsis 95

4.2 Introduction 97

4.2.1 Synthesis of $CsPbI_3$ 98

4.2.2 Anti-solvent Selection 98

4.2.3 Challenges of multiple Washing cycles 98

4.3 Purification Protocol using Additive 99

4.3.1 Optical Characterizations 99

4.3.2 TEM Characterization 100

4.3.3 Purification of $CsPbX_3$ PNCs 100

4.4 Quantitative Surface Chemistry Determination 101

4.4.1 Surface Chemistry Balance 101

4.4.2 TRPL measurement 101

4.4.3 NMR measurement 102

References 102

Supplementary Figures and information 103
$CsPbI_3$ Crude solution Stability 103
Anti-Solvent Treatments 104
PLQY of NC solutions featuring different Additives 105
NMR Tracking of ODE content 105
EDX of $CsPbI_3$ NCs 106
TEM of $CsPbI_3$ multiple Washing Steps 106
XRD Patterns of $CsPbI_3$ after multiple Washing cycles 107
Absorption, PL and TEM of $CsPbI_3$ NCs Washed 1 and 10 times 108
Comparison of Washing Effectiveness for $CsPbX_3$ 108
Washing of the conventional $CsPbX_3$-OA 109
ICP-MS 109
Determination of [NC] and [Surface States] 109
TRPL Analysis 112
NMR Results 113
Surface Ligand density 116
References 118
Chapter 5. $CsPbX_3$ PNC Super-crystals 119
5.1 Introduction 119
5.2 Synthesis of $CsPbX_3$ SCs 121
5.2.1 Reaction Chemistry 121
5.2.2 SCs Characterizations 123

5.2.3 Effect of Stoichiometry 126

5.2.4 Reaction Yield 128

5.3 Surface Interactions 129

5.3.1 NMR Characterization 129

5.3.2 Role of Ligands Interaction 130

5.3.3 Self- assembly of HDA-NCs 133

5.4 Hydrophobic Interaction 135

5.4.1 Assembling of Heterogeneous Structures 135

5.4.2 Role of Saturated Amine Ligand Chain Length 137

5.4.3 Breaking and Reassembling of the SCs 139

5.4.4 Solvent Polarity 140

5.5 Optical Characterizations 142

5.6 Conclusion 143

Reference 144

Chapter 6. Conclusion and Perspective 147

6.1 Conclusions 147

6.2 Perspectives 149

6.3 Ending remarks 153

References 153

Appendix 154

Table of Figures

Figure 1-1. Unit cell of ABX_3 perovskite with (a) cubic, (b) γ-orthorhombic, (c) δ-orthorhombic phases. (d) A range of perovskite materials with different A, B, X elements or molecules, demonstrating their compositional versatility and optoelectronic tenability. 3

Figure 1-2. (a) The different phase structures of the $CsPbI_3$ during the phase transformation.[23] (b) Simulated Gibbs free energy for the δ- $CsPbI_3$ and the γ-$CsPbI_3$ as a function of the surface area per molar of the $CsPbI_3$.[24] 5

Figure 1-3. (a) Colloidal dispersions of all-inorganic $CsPbX_3$ perovskite nanocrystals under UV light (λ = 365 nm), (b) their tuneable PL emission depending on halide composition, (c) their full UV-Vis absorption and PL spectra, (d) their Time-Resolved PL spectra, (e) the transmission electron microscopy (TEM) image for the $CsPbBr_3$ PNCs,[1](f), (g) The Absorption and PL spectra for the Mn doped $CsPbCl_3$ PNCs synthesised at 150- 210 °C.[34] 7

Figure 1-4. HI synthesised $CsPbB_3$ PNCs at reaction temperature of (a) 150 °C, (b) 130 °C, (c) 90 °C. [44] scale bar: 50 nm. 10

Figure 1-5. HI synthesised $CsPbB_3$ PNCs at reaction time of (a) 5 s, (b) 10 mins, (c) 30 mins, (d) 40 mins, (e) 90 mins, (f) 180 mins. [46] scale bar: 100 nm. 10

Figure 1-6. (a) Absorption and PL spectra of $FA_{0.1}Cs_{0.9}PbI_3$ and $FAPbI_3$ PNCs freshly synthesized and 6 months later. Insets show photographs of their respective solutions under sunlight and λ = 365 nm UV light.[56] (b) XRD and (c) PL characterization of Lanthanide doped $CsPbCl_3$ PNCs.[59] 14

Figure 1-7. (a) XRD and (b) UV-Vis absorption spectra of $CsSnX_3$ (X = Cl, Br, I or mixed $Cl_{0.5}Br_{0.5}$, $Br_{0.5}I_{0.5}$) PNCs, (c) TEM of $CsSnI_3$ PNCs,[61] (d) UV-Vis absorption and PL spectra of $Cs_3Bi_2I_9$ PNCs showing dual emission peaks and (e) Corresponding TEM of hexagonal shape $Cs_3Bi_2I_9$ PNCs with size of ~18 nm. 16

Figure 1-8. (a), (b) UV-Vis Absorption and PL spectra for the $CsPbX_3$ PNCs synthesized from the LI method, (c) TEM and HRTEM images for the $CsPbBr_3$ prepared via the LI method,[68] (d) $CsPbX_3$

with different morphologies synthesized via the LI method using acid and amine ligand with different chain lengths. [70] 18

Figure 1-9. (a) Classical LaMer nucleation model of nanoparticles consisting three stages: (i) monomer accumulation, (ii) nucleation after reaching a critical monomer supersaturation and (iii) growth of the nuclei through nuclei attachment. (b) The surface, bulk and total free energies as a function of cluster radius, where the critical radius, r_c is the minimum stable radius. 20

Figure 1-10. (a) Evolution of $CsPbI_3$ absorption spectra at reaction times between 0.4 to 2.4 seconds, (b) Evolution of PNC sizes at different reaction times with various reaction temperatures,[48]TEM images showing the black dots for PNCs prepared from (c) LI synthesis, [70](d) HI synthesis, [90](e) non-injection synthesis.[75] 22

Figure 1-11. TEM images for (a-d) $CsPbI_3$ PNCs synthesized with different times, (e) The evolution of the corresponding PL spectra and the size distribution of the PNCs, [94] TEM images for $CsPbBr_3$ PNCs that has been (f) Original, (g) added with 20 vol % ethanol and underwent oriented growth into nanowires, (h) further grew into the nanorods and nanoplates. [90]..... 24

Figure 1-12. Post-synthesis anion exchange for $CsPbX_3$ PNCs; (a) schematic illustration of the anion exchange process, (b) XRD spectra and (c) UV-Vis absorption and PL spectra for the PNCs after exchange, TEM images of (d) $CsPb(Br_{1.5}Cl_{1.5})$ and (e) $CsPb(Br_{1.5}I_{1.5})$,[120](f),(g) TEM images of $CsPbX_3$ PNCs exchange transitions and their associated solutions under UV-light.[121]..... 29

Figure 1-13. $CsPbBr_3$ PNCs dispersion under UV light after the cation exchange with increasing additions of (a) $SnBr_2$, (b) $CdBr_2$, (c) $ZnBr_2$, UV-Vis absorption and PL emission spectra of $CsPbBr_3$ dispersions with (d) Sn^{2+}, (e) Cd^{2+} and Zn^{2+} additions.[123] 31

Figure 1-14. (a) TEM images, (b), (c) PL and TRPL spectra for the $CsPbBr_3$ super-lattice,[125] The self-assembled super-lattice structures for the $CsPbBr_3$ (d) Nanoplatelets,[128] (e) Nanorods,[129] (f) Nanosheet,[130] scale bar 500nm. 32

Figure 2-1. Schlenk line used in typical Cs-precursor and $CsPbX_3$ synthesis. 45

Figure 2-2. Schematic illustration for the hot injection synthesis. 46

Figure 2-3. Schematic illustration for the washing process. 49

Figure 2-4. Photo of the Allegra^{TM} X-22R Centrifuge. 50

Figure 2-5. Photo of the SC-PMMA composite material. The white, yellow and brown disks consist of the $CsPbCl_3$, $CsPbBr_3$ and $CsPbI_3$ SCs-PMMA composites, respectively. 52

Figure 2-6. Photo of the Perkin Elmer Lambda 950 UV-Vis-NIR spectrometer. 53

Figure 2-7. Photo of the Horiba Fluoromax-4 spectrofluorometer. 53

Figure 2-8. Photo of the Bruker D8 Advance diffractometer. 54

Figure 2-9. Photos of the (a) FEI Tecnai G2 T20, (b) FEI Tecnai G2 F20, (c) JOEL 2100F Transmission Electron Microscope. 55

Figure 2-10. Schematic illustration for the calculation of Cs atoms per PNC. 58

Figure 3-1. The schematic illustration of the (a) α-cubic and (b) δ- orthorhombic phases of the $CsPbI_3$. 63

Figure 3-2. Photos under room light and UV-lamp for the $CsPbI_3$-OA crude solution that is (a) As-synthesised, (b) Stored in ambient condition for 3 days. 65

Figure 3-3. XRD patterns of the $CsPbI_3$ nanocrystals deposited as films and measured (a) at room temperature over 3 consecutive days and (b) following in-situ heating at 150°C for 10 minutes. 66

Figure 3-4. TEM images of $CsPbI_3$ NCs capped with OA and OLA ligands that are (a) as-synthesised, cubic phased and (b) after their orthorhombic phase transition following 3 days post-synthesis. Insets show high resolution TEM images of the NCs. 67

Figure 3-5. TEM images for $CsPbI_3$ NCs that have been (a) Just put under the electron beam and (b) Experienced severe electron beam damage after 10 seconds. 68

Figure 3-6. (a)- (e) In-situ TEM images and (f)-(j) the corresponding SADP for the $CsPbI_3$ NCs during the in-situ heating experiment and different stages of the α to δ phase. transformation. These

images were taken of different areas on a single TEM grid to minimise any beam damage effects. The white and red label indicated the crystal planes of the α and δ phases, respectively. 69

Figure 3-7. Chemical structure of oleic acid (OA) and bis-(2,2,4-trimethylpentyl) phosphinic acid (TMPPA). 71

Figure 3-8. photos of (a) Cs- OA and Cs- TMPPA precursors at room temperature, (b) $CsPbI_3$ -TMPPA crude solution that has been stored for 20 days under ambient condition. 72

Figure 3-9. UV-Vis absorption and PL spectra for (a), (b) $CsPbI_3$-OA and(c), (d) $CsPbI_3$-TMPPA. Photos on side of (b, d): Solutions of the respective PNCs under UV light at different times following synthesis. 73

Figure 3-10. (a) XRD patterns of $CsPbI_3$-TMPPA stored in ambient condition for 30 days. Standard cubic phase is shown in red (bottom), orthorhombic phase in blue (top). (*) unidentified peaks. (b) In-situ heating TEM at 150 °C for the α-$CsPbI_3$-TMPPA at the beginning and after 4 hours. 74

Figure 3-11. TEM images and size distributions of (a) $CsPbI_3$-TMPPA, 1:3 solvent/anti-solvent (v/v), 8000 rpm, (b) $CsPbI_3$-TMPPA, 1:3 solvent/anti-solvent (v/v), 10000 rpm, (c) $CsPbI_3$-TMPPA, 2:1 solvent/anti-solvent (v/v), 10000 rpm, (d) $CsPbI_3$-OA, 1:3 solvent/anti-solvent (v/v), 10000 rpm. . 75

Figure 3-12. ^{31}P NMR spectrum of neat TMPPA. Asterisks (*) denote organophosphorus impurities. Annotated diffusion coefficients as measured by DOSY given in μm^2 / s. 77

Figure 3-13. ^{31}P NMR spectrum of a concentrated solution of $CsPbI_3$-TMPPA NCs (washed once). Asterisks (*) denote organophosphorus impurities. Annotated diffusion coefficients as measured by DOSY given in μm^2 / s. 78

Figure 3-14. ^{31}P NMR spectrum of TMPPA with an excess of OLA present in solution. Asterisks (*) denote organophosphorus impurities. Annotated diffusion coefficients as measured by DOSY given in μm^2 / s. 78

Figure 3-15. ^{31}P NMR spectrum of a PbI_2-TMPPA/OLA solution. Asterisks (*) denote organophosphorus impurities. Annotated diffusion coefficients as measured by DOSY given in μm^2 / s. 79

Figure 3-16. ^{31}P NMR spectrum of a Pb-TMPPA solution synthesised by a reaction of PbO with TMPPA in d8-toluene. Asterisks (*) denote organophosphorus impurities. 79

Figure 3-17. ^{31}P NMR spectrum of a $CsPbI_3$-TMPPA solution washed twice to remove all TMPPA species. Note 5 hours scan duration. 81

Figure 3-18. 1H NMR spectrum of a concentrated solution of $CsPbI_3$-TMPPA NCs washed once (top) and washed twice (bottom). 81

Figure 3-19. (a) UV-Vis absorption and (b) PL spectra of as prepared $CsPbI_3$-TMPPA and OA-added $CsPbI_3$-TMPPA solutions. (c) UV-Vis absorption and (d) PL spectra of these samples after 24 h under ambient conditions. 82

Figure 3-20. $CsPbI_3$-TMPPA solution with oleylammonium-oleate added (left) and as-prepared $CsPbI_3$-TMPPA solution (right). 83

Figure 3-21. (a) UV-Vis absorption and (b) PL spectra for original $CsPbI_3$-OA and TMPPA-added $CsPbI_3$-OA solutions after 2 days. 83

Figure 3-22. TEM images, size distribution histograms and SADP for $CsPbI_3$ synthesised with OA+OLA ligands at (a) 5 seconds, (b) 5 minutes, (c) 10 minutes, (d) 1 hour. 84

Figure 3-23. TEM images, size distribution histograms and SADP for $CsPbI_3$ synthesised with TMPPA+OLA ligands at (a) 5 seconds, (b) 5 minutes, (c) 1 hour, (d) 9 hours, inset of d: The Fast-Fourier-Transform of the NWs region, showing its δ-phase. 85

Figure 3-24. UV-Vis absorption and PL spectra for $CsPbI_3$ NCs synthesised at different reaction times with (a) OA and (b) TMPPA ligands. 87

Figure 3-25. Chemical formulas for (a) 2-hexyldecanoic acid (HLA), (b) 2-decyltetradecaonic acid (DTA), (c) Diisooctyl phosphinic acid (DPA). 88

Figure 3-26. The TEM images, UV-vis absorption and PL spectra for the $CsPbI_3$ NCs synthesised with OLA and (a),(b) 2-heptylnonanoic acid (C16), (c), (d) 2-decyltetradecaonic acid (C24), (e), (f) Diisooctyl phosphinic acid. 89

Figure 3-27. XRD pattern for the $CsPbI_3$ PNCs synthesised from OA, HLA, DTA and DPA at day 7 of storage. 90

Figure 3-28. The TEM images, absorption & PL spectrum, XRD pattern for (a), (b), (c) $CsPbCl_3$ and (d), (e), (f) $CsPbBr_3$ NCs, respectively. 91

Figure 3-29. Photo of the $CsPbX_3$ NCs solution with various halide composition under the UV lamp. 92

Figure 4-1. (a) Chemical structures of diisooctyl phosphinic acid (DPA) and oleylamine (OLA). (b) UV-Vis absorption and photoluminescence spectra for the CsPbI3 NC crude solution. (c) TEM of $CsPbI_3$ NCs synthesized with DPA after one wash cycle with the insets showing STEM of single $CsPbI_3$ NCs with the lattice spacing (left) and histogram of the size distribution of the NC ensemble (right). 98

Figure 4-2. UV-Vis absorption and PL spectra of NCs after the 1st, 2nd, and 3rd washing cycle with (a) no additive additions, (b) OLA, (c) DPA, (d) OLA and DPA, (e) hexadecylammonium iodide (RNH_3I), (f) RNH_3I with OLA and DPA, referred to as "RNH_3I solution," and (g) PbI_2 with OLA and DPA, referred to as "PbI_2 solution." 99

Figure 4-3. TEM images for the $CsPbI_3$ NCs after various additions of washing additives during purification. (a) 1st wash, no additions, and 2nd wash with (b) no additions, (c) OLA, (d) DPA, (e) OLA+DPA, (f) RNH_3I, (g) RNH_3I solution, and (h) PbI_2 solution. 100

Figure 4-4. Correlation between (a) the PLQY and (b) the absorption changes of NCs after the 3rd wash against different molar ratios of added PbI_2 in the "PbI_2 wash solution"and the concentration of the NCs after the 1st wash. Time resolved photoluminescence (TRPL) measurements and the fitting

curves for $CsPbI_3$ NCs after (c) the 1st and 2nd washing steps with no additional additives and (d) after the 1st, 2nd, and 3rd washing steps with the PbI_2 solution. 101

Figure 4-5. Schematic illustration of how different additives used for purifying α-$CsPbI_3$ NCs from within a toluene solvent and IPA antisolvent mixture affect the nanocrystal dispersion. 102

Figure 5-1. Schematic illustration of the NCs to SCs assembling strategies relying on (a) Intermolecular forces, (b) template and (c) External field. [2] 120

Figure 5-2. TEM images of $CsPbI_3$ NCU showing (a) the presence of Pb^0 black dots (red circles) within the modified $CsPbI_3$ NCU method, and SCs at (b) low, (c) medium, and (d) high magnifications. Inset of (d) includes the SADP of the SCs. 122

Figure 5-3. Schematic illustration for the synthesis of (a) Normal $CsPbX_3$ NCs, (b) 3D-ordered $CsPbX_3$ SCs..... 123

Figure 5-4. DLS size measurements for $CsPbCl_3$ NCs and SCs. 124

Figure 5-5. STEM- EDX mapping of Cs, Pb and halide elements for (a) $CsPbCl_3$, (b) $CsPbBr_3$ and (c) $CsPbI_3$ SCs. 125

Figure 5-6. XRD patterns of $CsPbCl_3$, $CsPbBr_3$ and $CsPbI_3$ super-crystals. Standard PDF number for the cubic phase of $CsPbCl_3$, $CsPbBr_3$ and $CsPbI_3$ are 00-018-0365, 00-054-0752, 01-080-4039, respectively. 125

Figure 5-7. TEM images of $CsPbI_3$ NCs synthesised at different Cs:Pb:I molar ratios: (a) 1:4:8, (b) 1:2:4, (c) 1:1:2, (d) 1:4:16, (e) 1:2:8, and (f) 1:1:4. All images were taken immediately after synthesises. 127

Figure 5-8. The SADP of $CsPbI_3$ SCs synthesised at a Cs:Pb:I = 1:1:2 ratio. The pattern is indexed to the Cs_4PbI_6 phase. 127

Figure 5-9. Absorption spectra of the $CsPbI_3$ SC crude solution synthesised at different Cs:Pb:I ratio. 128

Figure 5-10. ^{31}P-NMR spectra of the SC dispersions of (top to bottom) $CsPbCl_3$, $CsPbBr_3$, $CsPbI_3$, which were washed 2 times. 130

Figure 5-11. Low and high magnification TEM images for $CsPbI_3$ synthesised at Cs: Pb: I= 1:1:4 with the (a), (b) TMPPA and OLA ligands and (c), (d) OA and HDA ligands. 131

Figure 5-12. TEMs of $CsPbI_3$ NCs (top) and the associated histograms of the inter-NC surface distance (bottom) synthesised (a) with HDA surface chemistry, (b) as SCs with HDA surface chemistry, and (c) with an OLA surface chemistry. 132

Figure 5-13. Proposed intermolecular interactions between $CsPbX_3$ NCs capped with (a) hexadecylamine (HDA), and (b) oleylamine (OLA) ligands. 133

Figure 5-14. TEM images and photos for the $CsPbI_3$ crude solution synthesised with HDA ligands and Cs: Pb: I= 1 :4: 8 stoichiometry that is (a) as synthesised, (b) stored for 10 days. (c) evolution of corresponding absorption & PL spectra with time (inset: zoom-in PL spectra showing the red shift of the PL peaks). 134

Figure 5-15. (a)-(d) Low to high magnification TEM images. (e) Schematic illustration of NPLs within SC structure. (f) Absorption and PL spectra for $CsPbI_3$ SCs synthesized at 100 °C, diluted in hexane. Inset: Zoomed-in region for the NPLs absorption and emission. 136

Figure 5-16. TEM images of $CsPbI_3$ SCs synthesised at 180 °C under (a) low and (b) high magnification. 136

Figure 5-17. TEM images of $CsPbI_3$ synthesised at Cs: Pb: I= 1:1:4 at low and high magnification with TMPPA and various alkyl amine ligands: (a,b) octylamine, (c,d) dodecylamine, (e,f) octadecylamine. 138

Figure 5-18. (a) DLS size distribution measurement for $CsPbCl_3$ under different conditions: original NCs, original SCs, SCs sonicated for 1 hr, SCs sonicated and rested for 4 hours and 7 days; TEM images of $CsPbCl_3$ SCs (b) original, (c) as-sonicated, (d) sonicated and rested for 7 days. 140

Figure 5-19. Photo of $CsPbCl_3$ SCs dispersed in hexane with: no treatment, sonicated for 1 hour, sonicated and rested 4 hours. 140

Figure 5-20. (a) DLS size distribution measurements for $CsPbCl_3$ hexane dispersions with 25 vol% various polar solvents after 1-hour sonication. TEM images of these samples with (b) methyl acetate, (c) acetone, (d) tert-butanol, (e) tetrahydrofuran, (f) iso-propanol addition. 141

Figure 5-21. Absorption and PL spectra for NC and SC films of (a) $CsPbCl_3$, (b) $CsPbBr_3$ and (c) $CsPbI_3$. (d) The emission of the NCs and SCs plotted on the colour gamut spectrum (CIE 1976), the PL is transformed into the u' v' through the chromaticity application in Origin software. (e) The PL spectra of the down conversion LED devices fabricated from the SC-PMMA composites (left) and photos of the LEDs (right). 143

Chapter 1. Introduction to $CsPbX_3$ Perovskite Nanocrystals

1.1 Synopsis

Inorganic metal halide perovskite nanocrystals (PNCs) possessing the chemical formula $CsPbX_3$ ($X=Cl^-, Br^-, I^-$) have emerged as an extensively researched topic since being first reported in 2015.[1],[2] Such PNCs possess excellent optoelectronic properties, including photoluminescent quantum yields (PLQY) approaching unity (>95 %),[3] readily tuneable emission across the entire visible spectrum,[4] narrow emission full-width-half-maximum (FWHM) of 12 to 45 nm,[5] and suppressed photoluminescence (PL) blinking.[6] These superior properties have made PNCs a very promising candidate material for various optoelectronic applications, such as light emitting diodes (LEDs),[7] lasers,[8] photodetectors,[9] and solar cells.[10]

This introductory chapter will review the birth of the $CsPbX_3$ NC field, their optoelectronic and physical properties, diverse synthetic methods, nucleation and growth dynamics, and the role of surface ligand chemistry. Across each of these areas, major research challenges will be highlighted, which will serve to define the scope of this thesis.

1.2 Perovskites

The term "perovskite" was named after the mineralogist Lev Perovski, and it was first applied to the calcium titanium oxide ($CaTiO_3$) mineral in 1840.[11] Subsequently, it became a general term for all the compounds that have the same chemical formula ABX_3, in which A and B are cations, and X is an anion.[12] To predict the exact crystal phase of the perovskites, one can use the Goldschmidt tolerance factor (*t*) as given by **Formula 1-1**. Herein, r_A, r_B and r_X stands for the ionic radius for the A, B and X ions, respectively.[13] For *t* values close to 1, the perovskite adopts a cubic phase. As shown in **Figure 1-1** a, for cubic phase perovskites the corner-sharing polymorphs formed by BX_6 octahedra are occupied by the A cation.[14] If the *t* value is larger than 1, perovskites will adopt either a hexagonal or tetragonal phase. If *t* is small (~ 0.8), the perovskite will exist either in a rhombohedral or orthorhombic phase.[15] Interestingly, the orthorhombic phase can be exist in two types; if the *t* is too small, the perovskite adopts the totally distorted δ-orthorhombic phase (**Figure 1-1** b), otherwise it forms the slightly distorted γ-orthorhombic phase (**Figure 1-1** c), which is similar to the cubic phase.

$$t = \frac{r_A + r_X}{\sqrt{2}(r_B + r_X)}$$

Formula 1-1. the calculation of the Goldschmidt tolerance factor (t).

1.2.1 Metal Halide Perovskite

Although metal halide perovskites were discovered decades ago,[16] they have only drawn pronounced research attention since 2009, when the organic-inorganic hybridized methylammonium lead halides ($MAPbX_3$) were first used in dye-sensitised solar cells as the sensitiser.[17] Since that time, many compositional variants have been explored to yield metal halide perovskites with vast optical tuneability (**Figure 1-1** d). This has been afforded by exploiting a wide range of A-site cations (e.g. methylammonium (MA^+), formamidinium (FA^+) or Caesium (Cs^+)), B-site cations (e.g. lead (Pb^{2+}), manganese (Mn^{2+}), bismuth (Bi^{3+}), tin (Sn^{2+}), antimony (Sb^{3+}) or lanthanides), and X-site anions (e.g.

chloride (Cl^-), bromide (Br^-), iodide (I^-)) that have been reported. In addition, apart from single elements occupying one site, mixed composition perovskites at either the A, B or X-site have also been shown.[18] This variation in perovskite composition has caused their *t* value to usually deviate from 1, rendering their ambient-condition stable phase to be either cubic, tetragonal or orthorhombic.[19]

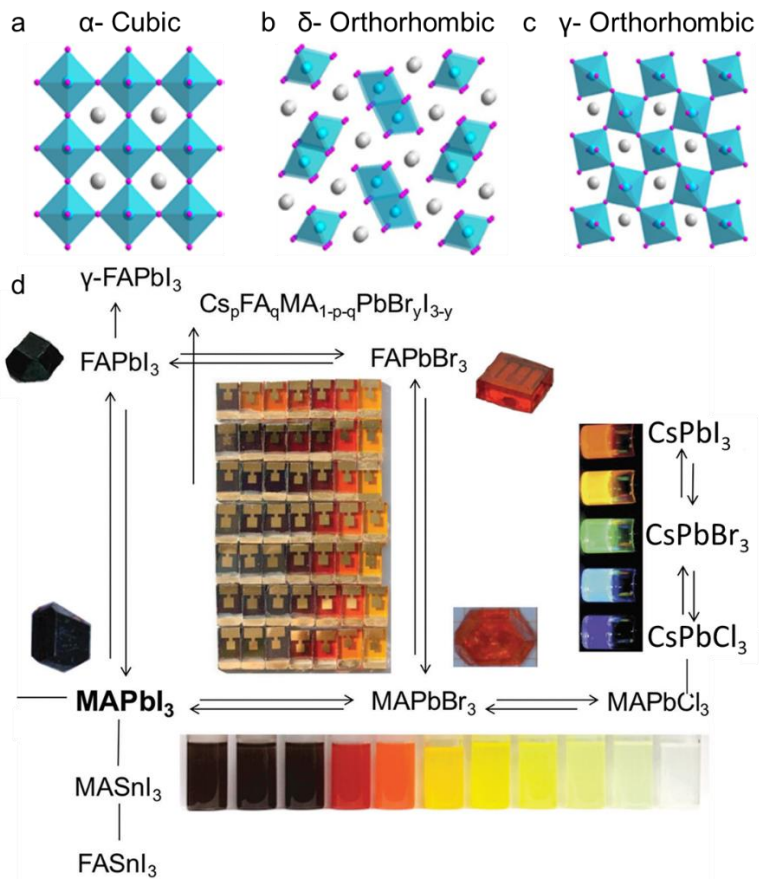

Figure 1-1. Unit cell of ABX_3 perovskite with (a) cubic, (b) γ-orthorhombic, (c) δ-orthorhombic phases. (d) A range of perovskite materials with different A, B, X elements or molecules, demonstrating their compositional versatility and optoelectronic tenability.

1.2.2 Inorganic Metal Halide Perovskite

For inorganic $CsPbX_3$, the corresponding *t* factor values for $CsPbCl_3$ and $CsPbBr_3$ fall within the range 0.9 – 1, while for $CsPbI_3$ it approaches 0.8.[20] These subtle differences allow the bulk $CsPbCl_3$

to have a $Pm\overline{3}m$ α-cubic and $CsPbBr_3$ to have either a $Pm\overline{3}m$ α-cubic or slightly distorted Pnma γ-orthorhombic phase under ambient conditions,[21] both of which are functional phases.

In contrast, the phase transformation of the bulk $CsPbI_3$ is much more complicated (**Figure 1-2** a). Its functional α-cubic phase is only stable at elevated temperature of 583K,[22] if the α-phase is cooled down rapidly to room temperature, the $CsPbI_3$ could be trapped in the metastable Pnma γ-orthorhombic phase,[23] which has identical functionality as the α-phase. However, when stored under ambient condition further, the γ phase eventually transforms into the highly distorted Pnma δ-orthorhombic phase, which has a wide bandgap (~2.7 eV) and no photoluminescent emission. Such a structural instability problem of $CsPbI_3$ is due to the radius of the Cs^+ ions being too small to fill the interstitial sites between the corner-sharing PbI_6 polyhedra, even though Cs^+ is already the largest non-radioactive ion. This provides practical limits to the use of iodide derivatives in their bulk state, despite its appeal for use in various optoelectronic applications, e.g. solar cells.

Interestingly, according to a recent computational study, the γ- orthorhombic and δ-orthorhombic have a different surface Gibbs free energy (**Figure 1-2** b).[24] As a result, when the grain size of the $CsPbI_3$ is below 100 nm, the free energy of the δ- phase becomes larger than the γ- phase, which makes the functional γ- phase thermodynamically stable at room temperature. Inspired by this mechanism, a surface ligand driven stabilization of the functional phase of $CsPbI_3$ will be presented in Chapter 3 of this thesis. Deeper insights into the phase transformation will also be provided, and the role of nanostructuring and surface chemistry towards preserving the functional phase will also be discussed.

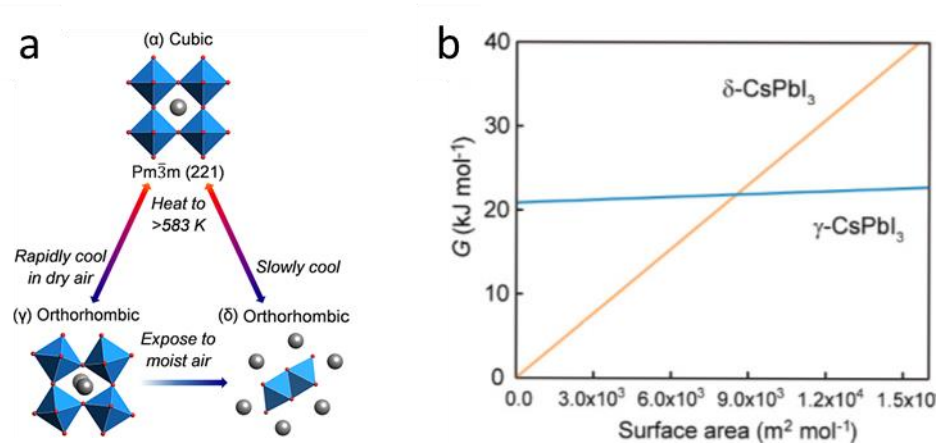

Figure 1-2. (a) The different phase structures of the $CsPbI_3$ during the phase transformation.[23] (b) Simulated Gibbs free energy for the δ- $CsPbI_3$ and the γ-$CsPbI_3$ as a function of the surface area per molar of the $CsPbI_3$.[24]

A key advantage of inorganic perovskites is in their thermal and chemical stability. Compared to conventional organic-inorganic hybridized metal halide perovskites, which experience poor thermal (start to decompose at 85 °C) and chemical stabilities (MA^+ ions are vulnerable to deprotonation to water molecules),[25],[26] the all-inorganic $CsPbX_3$ perovskites possess a dramatically improved thermal stability of up to 400 °C before thermal decomposition,[27] as well as better chemical stability, as demonstrated by the greatly enhanced resistance to moisture.[28] Such thermal and chemical robustness of $CsPbX_3$, coupled with its exceptional optoelectronic properties, has made it among the most attractive perovskite material classes for the study of its nanocrystal derivatives.

1.2.3 Optical Properties of $CsPbX_3$

All-inorganic $CsPbX_3$ possess bulk optical bandgaps of ~1.73 eV ($CsPbI_3$), ~2.43 eV ($CsPbBr_3$) and ~2.90 eV ($CsPbCl_3$). [29] While their conduction band is determined by Pb p-orbitals, their valence band positions are influenced by the hybridized Pb s-orbitals and halide p-orbitals,[1] which makes spectral tunability achievable simply by controlling the halide composition. As nanocrystals, their bandgap can also be influenced through the quantum confinement effect. This allows for a further shift of ~ 0.3 eV to the blue through size control.[30] Therefore, through both halide composition and

size control, $CsPbX_3$ readily exhibits tuneable absorption and PL features across the entire visible spectrum (**Figure 1-3** a-d).

As shown in the transmission electron microscopy (TEM, **Figure 1-3** e), $CsPbX_3$ PNCs can be made monodisperse and with well passivated surfaces to render them with very high PLQYs of 50 to 90 %, narrow PL emission FWHM of 12 to 45 nm and PL lifetimes between 1 to 29 ns.[1] Such impressive optical properties are further attributed to the superior electronic properties of the perovskite itself, which includes high absorption coefficients (>10^4 cm^{-1}),[31] long charge carrier lifetimes (~10^3 ns), [32] and low trap state densities (~10^{16} cm^{-3}).[33] The broader versatility of PNCs has also been demonstrated through simple doping approaches. As shown in **Figure 1-3** f, g, dual emission peaks have been achieved through the introduction of Mn^{2+} into $CsPbCl_3$.[34],[35] These originated from the intrinsic emission of $CsPbCl_3$ at ~400nm and the $^4T_1$ -$^6A_1$ transition of the Mn^{2+} at ~ 580 nm following energy transfer.[36] Except from manganese, a number of other elements could also be doped into the PNC lattice, which introduces different energy states and hence emission peaks. The doping of the PNCs will be discussed in greater detail in Section 1.3.1.

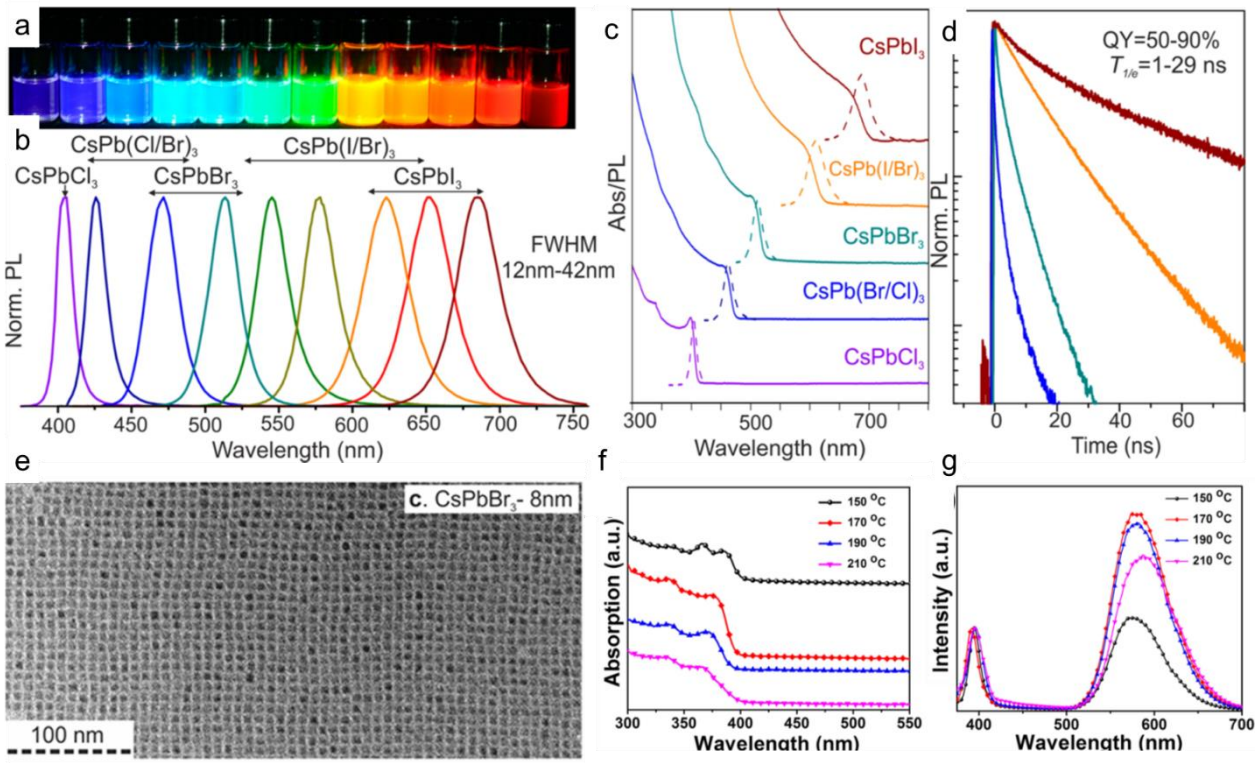

Figure 1-3. (a) Colloidal dispersions of all-inorganic $CsPbX_3$ perovskite nanocrystals under UV light (λ = 365 nm), (b) their tuneable PL emission depending on halide composition, (c) their full UV-Vis absorption and PL spectra, (d) their Time-Resolved PL spectra, (e) the transmission electron microscopy (TEM) image for the $CsPbBr_3$ PNCs,[1](f), (g) The Absorption and PL spectra for the Mn doped $CsPbCl_3$ PNCs synthesised at 150- 210 °C.[34]

1.3 Synthesis of $CsPbX_3$ PNCs

The methods for synthesising $CsPbX_3$ PNCs can be divided into two categories: injection and non-injection. Injection methods refer to the mixing of precursor solutions to induce supersaturation and drive formation of NCs. The injection synthesis has been widely studied for the traditional NCs system, and its nucleation and growth dynamics are well described by the LaMer model.[37] Meanwhile, non-injection methods involve the reaction of all the precursors in a single reaction medium through a thermally or chemically driven change in precursor stability to cause supersaturation. To date, injection methods have been the most well-developed techniques for

producing $CsPbX_3$ PNCs. Herein, the most representative synthetic methods of the $CsPbX_3$ will be reviewed.

1.3.1 Hot-Injection

The high temperature hot-injection (HI) method refers to when individual precursors are firstly dissolved separately through the use of appropriate ligands, then one precursor solution is injected into the other at an elevated temperature to initiate a chemical reaction. The HI method was first established by Murray and co-workers in 1993, which promoted the synthesis of high-quality semiconducting cadmium chalcogenide nanocrystals with high-crystallinity and narrow size-distributions down to 5 %.[38] Afterwards, the HI approach was applied to numerous semiconducting nanocrystal systems to gain precise control over their size, morphology, and phase, such as II-VI (e.g. CdS, CdSe, ZnS, ZnSe),[39] III-V (e.g. GaAs, GaSb, InP, InAs, InSb),[40] IV-VI (e.g. PbS, PbSe),[41] I-III-VI (e.g. $CuInS_2$, $CuInSe_2$, $AgInS_2$),[42] as well as core-shell structures (e.g. CdS/ZnS, InAs/CdSe).[43] In 2015, the HI route was applied to the synthesis of $CsPbX_3$ PNCs for the first time by the group of Kovalenko. [1]

Simple $CsPbX_3$ PNCs

The synthetic approach for the hot-injection synthesis of $CsPbX_3$ developed by the Kovalenko group has emerged as the archetypical method in the field. [1] Typically, caesium carbonate (Cs_2CO_3) is reacted with oleic acid (OA) as the ligand in octadecene (ODE) as the solvent under a nitrogen environment at 120 °C to produce the Cs-oleate precursor (**Formula 1-2**). In the meantime, lead halide (PbX_2) is dissolved in ODE with both OA and oleylamine (OLA) ligands (**Formula 1-3**). In the case of $PbCl_2$, trioctylphosphine (TOP) has been found necessary to facilitate the dissolution of the metal salt in ODE. The Cs-oleate precursor solution is then injected into the PbX_2 precursor solution at a temperature between 140 to 200 °C for the formation of $CsPbX_3$ PNCs (**Formula 1-4**). The reaction is terminated in a water bath at ~ 5s after the injection of Cs-oleate precursor to prevent excessive coarsening and to maintain a narrow size distribution of the PNC product. Following this

HI protocol, the PNCs have a nanocube (NCU) shape and are 4 to 15 nm in size. By adjusting the temperature and halide precursor composition, the resulting $CsPbX_3$ PNCs can exhibit tuneable absorption and PL spectra across the entire visible spectrum, as previously shown in **Figure 1-3** a-c.

$$Cs_2CO_3 + 2OA \rightarrow 2CsOA + H_2O + CO_2$$

Formula 1-2. The Cs precursor dissolution reaction.

$$PbX_2 + 2OA + 2OLA \rightarrow PbOA_2 + 2OLA\ X$$

Formula 1-3. The Pb precursor dissolution reaction.

$$CsOA + PbOA_2 + 3OLA\ X \rightarrow CsPbX_3 + 3OA^- + 3OLA^+$$

Formula 1-4. The hot injection reaction.

During the HI synthesis, there are several parameters that influences the size, morphology and quality of the $CsPbX_3$ PNC product, namely reaction temperature, time, ligands and precursor ratios. Herein, their effects will be discussed.

Reaction temperature plays a dominant role in the HI synthesis of $CsPbX_3$. At injection temperatures of 150 to 200 °C, the formation of cube shaped $CsPbX_3$ PNCs are thermodynamically favoured (**Figure 1-4** a) .[44],[45] Meanwhile, at lower injection temperatures of 90 to 130 °C, 2D nanoplatelets (NPLs) or nanosheets (NSs) form (**Figure 1-4** b, c). The enhanced quantum confinement induced by the reduced Z-axis height for the NPLs causes their PL to be blue shifted compared to NCU. PLQYs of the resulting NPLs ranged from 84 % to 10 %, with the thinner NPLs exhibiting lower PLQYs due to the increased amount of surface trap state. For lower injection temperatures of 70 °C, a transparent suspension of amorphous, micrometre-sized sheets formed, which was presumably unreacted precursors.

Reaction time is another important parameter in HI synthesis.[46] At a standard reaction time of 5 s (**Figure 1-5** a), NCU shaped PNCs tend to form for reaction temperatures of 150 to 200 °C. However, if the reaction time is extended to 10 minutes (**Figure 1-5** b), it has been shown that elongated nanowires (NWs) with ~20 nm width and ~5 µm length form (**Figure 1-5** c-e). This has been attributed to the oriented attachment of NCU PNCs along ⟨110⟩ preferential directions. If the reaction time was further prolonged to more than 180 mins, completely coarsened micron-sized crystals resulted (**Figure 1-5** f).

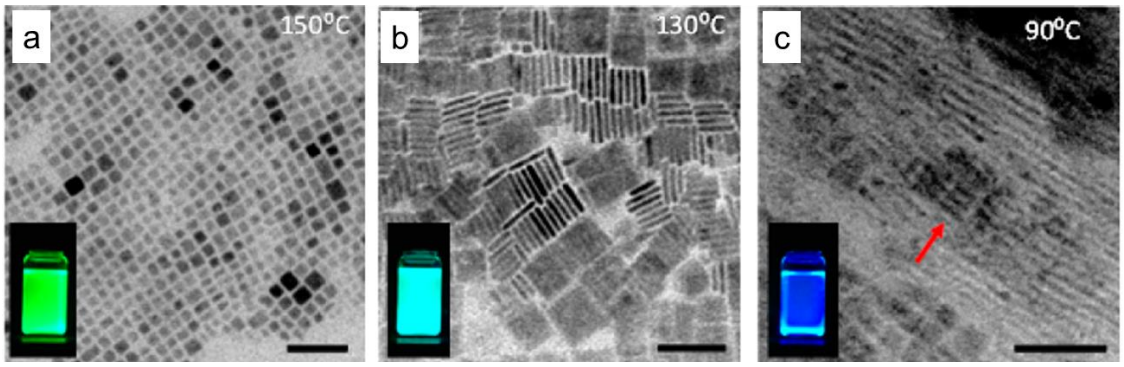

Figure 1-4. HI synthesised $CsPbB_3$ PNCs at reaction temperature of (a) 150 °C, (b) 130 °C, (c) 90 °C. [44] scale bar: 50 nm.

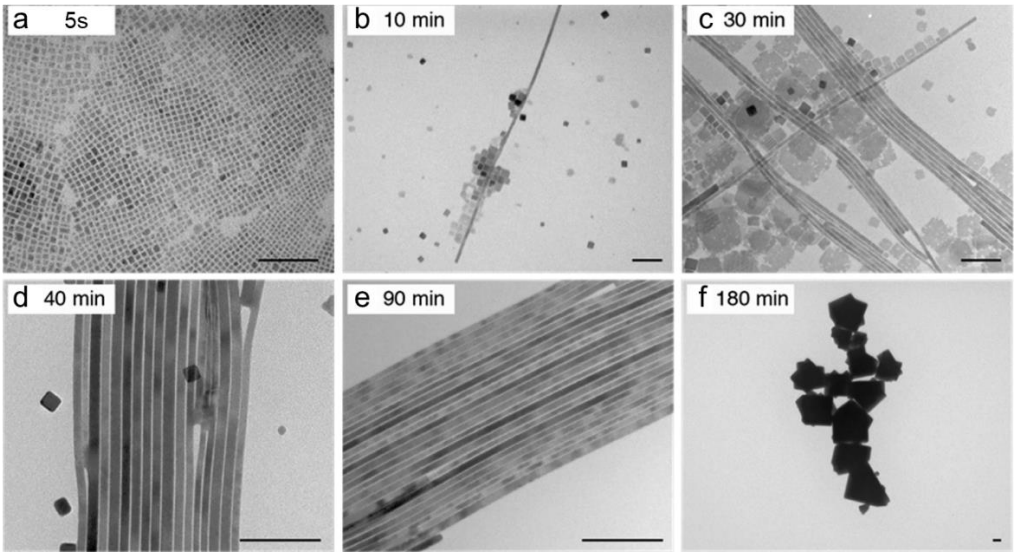

Figure 1-5. HI synthesised $CsPbB_3$ PNCs at reaction time of (a) 5 s, (b) 10 mins, (c) 30 mins, (d) 40 mins, (e) 90 mins, (f) 180 mins. [46] scale bar: 100 nm.

For a given reaction temperature, the precursor concentrations, their stoichiometries and associated ligands play dominant roles in defining the nucleation and growth events. The high temperatures involved in HI require high-boiling point solvents, such as ODE, which consequently result in a need for alkyl ligands. As such, long chain ligands, such as OA and OLA, are chosen to ensure good colloidal stability and to tailor the size, shape and ensemble distribution of the PNCs.[47] In general, it has been found that using acid ligands shorter than OA results in an increased size of the cube-shaped PNCs, while using amine ligands shorter than OLA has caused the PNCs to adopt NPL morphologies.

The ternary nature of $CsPbX_3$ creates challenges in achieving balanced precursor reactivities. Therefore, judicious control of the reaction precursor stoichiometries is critical to achieve high quality PNCs.[48] At the simplest level, it has been shown that at a Cs:Pb ratio between 1:2 to 1:4, monodispersed PNCs is mostly favoured, with the FWHMs of the emission for these PNCs being around 20 to 40 nm. However, when the Cs content was increased to reach a Cs : Pb ratio of 1:1.5 or lower, PNCs with very poor colloidal stabilities and significant amounts of by-products were formed. Conversely, if the Cs:Pb ratio was above 1:4.5, the PNCs had broad size distributions and ensuing poor optical properties. Alongside Cs and Pb, the halide stoichiometry is also a critical reaction variable. In a slightly modified HI synthesis of the $CsPbX_3$ PNCs, PbO and NH_4X were used as the Pb^{2+} and X^- sources, instead of solely PbX_2, to tune the X:Pb ratio.[49] By increasing the X:Pb ratio from 2:1 to 4:1, the PNC products exhibited significantly higher PLQYs, narrower FWHMs and higher PL lifetimes. Such an improvement was attributed to two factors: (1). higher halide content decreased the surface halide vacancies, which act as non-radiative trap states on the PNCs and (2). the extent of heterogeneous nucleation and growth processes was reduced under high halide content, giving the product much smaller average size and also narrower size distributions.[50]

In addition to the precursor stoichiometry, concentration is another factor that influences the final morphology of the PNCs. It has been shown that when the precursor concentration is increased ten-fold in the synthesis of $CsPbBr_3$, the formed PNCs spontaneously assemble into a super-lattice, or so called super-crystal (SC) structures, with a size in the 100's nm and a red-shifted PL compared to isolated PNCs due to enhanced electronic coupling.[51] Such self-assembly behaviour is similar to the traditional cadmium chalcogenide NCs or gold nanoparticles.[52] The formation of SCs can also happen via post-synthetic treatments,[53] which will be introduced in section 1.6.4.

Compositional alloyed $CsPbX_3$ PNCs

The versatility of the HI method enables the precursor ratios to be modified readily in order to allow for the synthesis of mixed A- or B- site $CsPbX_3$ PNCs. As mentioned before, the Goldschmidt tolerance factor for $CsPbI_3$ PNCs is much smaller than 1, which makes its functional cubic phase not stable at room temperature.[20] One effective method to stabilize the functional cubic phase of $CsPbI_3$ is to alloy a larger A-site cation (e.g. FA^+) into the lattice to shift the average *t* value towards 1.[54],[55] By simply injecting the FA-oleate together with the Cs-oleate during the HI synthesis, FA:$CsPbI_3$ has been shown to readily form.[56] The resulting cubic-phased $FA_{0.1}Cs_{0.9}PbI_3$ PNCs exhibit a PL emission located at a peak of ~ 685 nm and with a PLQY of ~70 % (**Figure 1-6** a). Moreover, if the injection of the A-site precursor was all FA-oleate, the resulting $FAPbI_3$ PNCs possessed a red-shifted PL at 770 nm. Both the $FA_{0.1}Cs_{0.9}PbI_3$ and $FAPbI_3$ exhibited stabilities of more than 6 months under ambient storage.

Compositional alloying has been more widely explored for the B-site cation doping. Due to the same valence and similar ionic radius to Pb^{2+}, Mn^{2+} has emerged as a suitable B-site dopant.[35] By simply dissolving the MnX_2 precursor within the PbX_2 precursor solution and following the same injection protocol as for the archetypical $CsPbX_3$, Mn:$CsPbX_3$ PNCs have been readily synthesised. In this approach, a higher MnX_2 precursor amount resulted in a progressively higher level of Mn^{2+}

incorporation in the PNCs, with the highest Mn/Pb being at 46 % when using a 10:1 Mn:Pb precursor ratio.[34] Notably, pristine $CsPbCl_3$ had a PLQY of merely 5 %, whereas the Mn-doped $CsPbCl_3$ had a boosted PLQY of 80 %. This was ascribed to the passivation of defects enhancing band-edge emission and the existence of a highly-luminescent secondary emission peak, as previously shown in **Figure 1-3** f, g. In addition to boosting the PLQY, Mn doping has also improved the thermal and ambient condition stabilities of $CsPbBr_3$ NCs, which was ascribed to the Mn^{2+} increasing the overall formation energy of the perovskite.[57],[58]

Except from Mn^{2+}, lanthanide ions (Ce^{3+}, Sm^{3+}, Eu^{3+}, Tb^{3+}, Dy^{3+}, Er^{3+}, Yb^{3+}) can also be doped into the $CsPbCl_3$ PNCs. Similar with previous methods, lanthanide chloride was mixed into the $PbCl_2$ precursor solution during the HI process.[59] Owing to the tri-valence of the lanthanide ions and their much smaller ionic radius vs Pb^{2+}, the doped $CsPbCl_3$ had a decreased lattice constant (3.96 Å for undoped $CsPbCl_3$ and 3.87 Å for $CsPbCl_3$:Yb^{3+}, **Figure 1-6** b) and also distorted perovskite structure. Similar to the Mn-doped $CsPbCl_3$, all the lanthanide doped $CsPbCl_3$ have a secondary emission peak depending on the band structure of the dopant element. As shown in **Figure 1-6** c, the secondary PL peak ranged from 500 nm to the near infrared, while the PLQY varied from 15 % to 30 %. Currently, the record PLQY of 146 % at 988 nm was found in a cerium and ytterbium co-doped $CsPbCl_{1.5}Br_{1.5}$ PNCs.[60] Such a PLQY over 100 % was attributed to the quantum cutting effect of the lanthanide dopants.

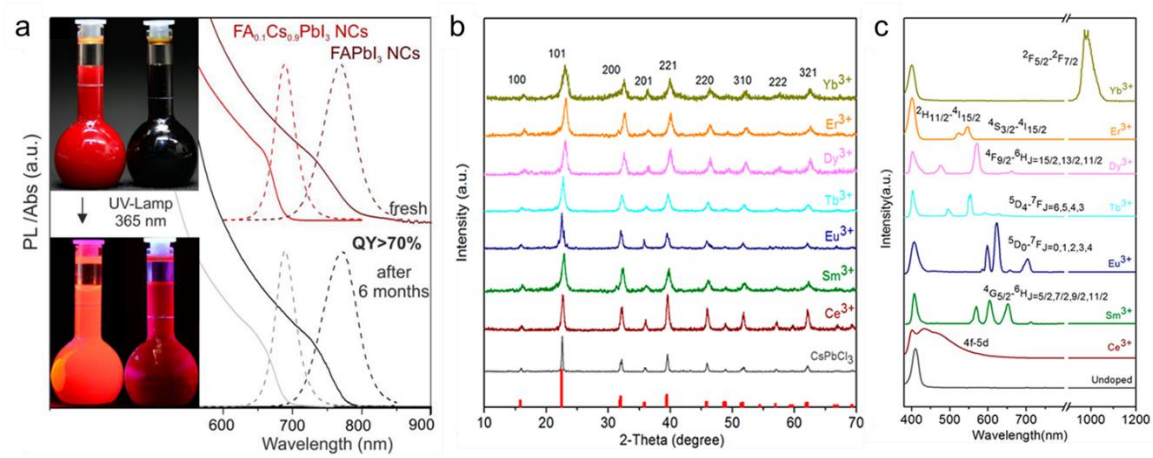

Figure 1-6. (a) Absorption and PL spectra of $FA_{0.1}Cs_{0.9}PbI_3$ and $FAPbI_3$ PNCs freshly synthesized and 6 months later. Insets show photographs of their respective solutions under sunlight and λ = 365 nm UV light.[56] (b) XRD and (c) PL characterization of Lanthanide doped $CsPbCl_3$ PNCs.[59]

Lead-Free PNCs

Due to the toxicity of Pb, there is an on-going need to find a non-toxic replacement that can provide comparable optical and electric properties. The first attempt to achieving this was using Sn^{2+} as the B-site cation to achieve lead-free PNCs. Following the HI route and simply substituting PbX_2 with SnX_2 yielded $CsSnX_3$ NCs with ~10 nm size.[61] Similar to $CsPbX_3$, these $CsSnX_3$ NCs exhibited an orthorhombic (X = Br, I) or cubic (X = Cl) perovskite phase and also tuneable bandgaps according to their halide composition (**Figure 1-7** a-c). However, comparing with lead halide PNCs, they only had a maximum PLQY of 0.14 %, largely because the distortion of their lattice was thought to induce higher trap state densities.

Another feasible element to substitute Pb is Bi. Similarly, by using a BiX_3 precursor within the HI synthesis, hexagonal phase $Cs_3Bi_2X_9$ NCs of 18 nm size could be produced (**Figure 1-7** d).[62] Unlike for $CsPbX_3$, the band structure for the hexagonal $Cs_3Bi_2X_9$ NCs was shown to consist of a direct exciton transition and also an indirect phonon transition. This unique band structure allowed the $Cs_3Bi_2I_9$ NCs to have dual peak emissions centred at 580 nm and 605 nm (**Figure 1-7** e). However,

such an indirect bandgap also introduced more non-radiative trap states, and the PLQY of these $Cs_3Bi_2X_9$ NCs was very low at 0.017 %.

Last but not the least, Sb^{3+} has been another explored candidate. Similar to above, $SbCl_3$ was used within the HI protocol, yielding trigonal $Cs_3Sb_2Cl_9$ NWs with widths of 20 nm and also tuneable lengths from 290 nm to 3.4 µm.[63] This control of length was achieved by adjusting the $SbCl_3$ precursor concentration and OA : hexadecylammonium ligand pair ratios in the synthesis. For the $Cs_3Sb_2Cl_9$ NWs, the emission peak position was at 436 nm with a PLQY of ~4 %. Although not comparable to the lead-based derivatives, this value represents a major step forward compared to the Sn and Bi analogues.

Except from single B-site substitution, monovalent Ag^+ and trivalent Bi^{3+} have been co-used in the HI synthesis to prepare double perovskites.[64],[65],[66] In the first report, $Cs_2AgBiBr_6$ PNCs were synthesized from a slightly changed HI protocol. Basically, $BiBr_3$ and $AgNO_3$ were dissolved in ODE at 200 °C using OA, OLA and HBr, then the Cs-oleate was injected and the reaction was quenched after 5 s.[65] The produced $Cs_2AgBiBr_6$ double perovskite had a cube shape with 9.5 nm average size. In another report, the stoichiometry of the reaction was more precisely controlled by dissolving Cs, Ag and Bi acetate salts in ODE, OA and OLA mixture, then injecting trimethylsilyl halide at 140 °C to yield Cs_2AgBiX_6. [66] The product was also NCU with 8.1 nm size. The highest PLQY for these double perovskites was still low (0.3 %), but possessed improved thermal, photo and moisture stability.

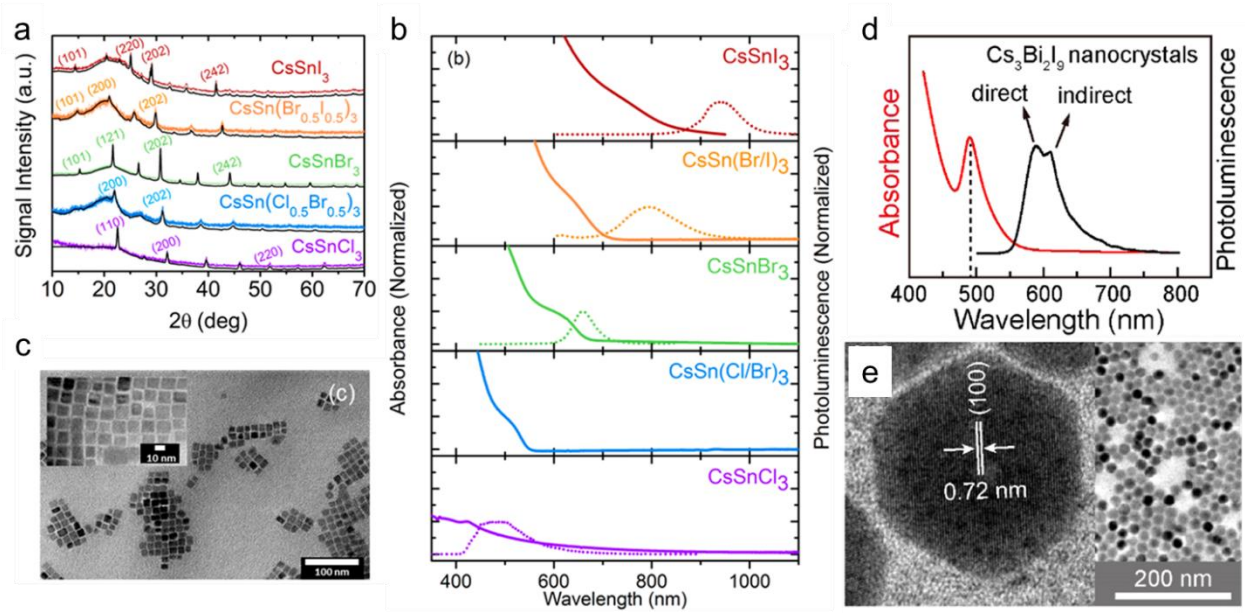

Figure 1-7. (a) XRD and (b) UV-Vis absorption spectra of $CsSnX_3$ (X = Cl, Br, I or mixed $Cl_{0.5}Br_{0.5}$, $Br_{0.5}I_{0.5}$) PNCs, (c) TEM of $CsSnI_3$ PNCs,[61] (d) UV-Vis absorption and PL spectra of $Cs_3Bi_2I_9$ PNCs showing dual emission peaks and (e) Corresponding TEM of hexagonal shape $Cs_3Bi_2I_9$ PNCs with size of ~18 nm.

1.3.2 Low-Temperature Injection

The HI synthesis mixes the precursors at an elevated temperature to drive the supersaturation and PNC formation. Low temperature (LI) injection techniques have also emerged for the synthesis of PNCs. To a large extent, these utilize solvent polarity changes to drive the supersaturation. To perform the LI synthesis of $CsPbX_3$ PNCs, all precursor materials (CsX, PbX_2) and ligands (OLA, OA) are dissolved together in a polar solvent (dimethylformamide, DMF or dimethyl sulfoxide, DMSO). Then the non-polar solvent (toluene) is added under vigorous stirring to decrease the solubility of the precursors and drive the precipitation of the PNCs close to room temperature and ambient conditions. [67],[68],[69] Under these conditions, the resulting PNCs are typically cuboid in shape with a size of ~ 9 to 20 nm. In general, their optical properties are comparable to the HI analogues, with the PLQY reaching values of up to 95 % and the PL FWHMs being around 12 to 35

nm.[68] Through halide compositional engineering, tuning of the emission wavelength from 405 to 680 nm across the visible region has also been demonstrated (**Figure 1-8** a-c).[68],[69]

Similar to the HI method, ligands also play a dominant role in determining the morphology of the product in the LI method. By combining alkyl acid and amine ligands of different chain lengths, multiple morphologies (quantum dots, NCUs, NPLs, nanorods (NRs)) have been realized for $CsPbX_3$ PNCs (**Figure 1-8** d).[70] It was speculated that the ligands influenced the nucleation stage and hence induced morphology control of the PNCs, although detailed experimental work to elucidate this stage of formation was not carried out.

Since the LI is carried out at close to room temperature, its reaction kinetics tend to be much slower than for HI, which make it more controllable for scaled-up reactions. [71] By using propionic acid and butylamine as a ligand pair, and isopropanol (IPA) and hexane as a solvent and anti-solvent, respectively, it has been shown that the LI synthesis of the $CsPbBr_3$ PNCs can be scaled up to volumes as high as 900 mL. This is much larger than the typical 5 to 10 mL scales used in HI syntheses. The sizes of the resulting PNCs ranged from 2.6 to 7.2 nm by simply changing the supersaturation level of the precursors through adjusting the volume ratio between the polar and non-polar solvent.[67] PLQYs for such a scale-up synthesized $CsPbBr_3$ PNCs lied between 80 to 92 %, with larger PNCs size showing a decreasing PLQY.

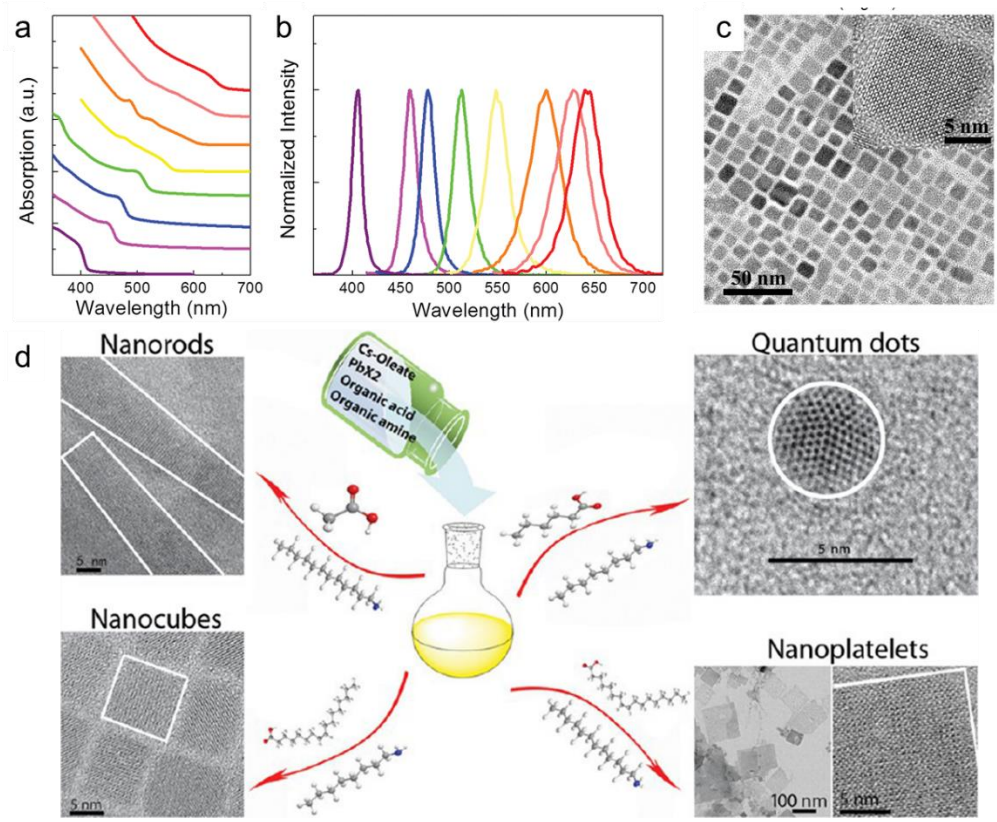

Figure 1-8. (a), (b) UV-Vis Absorption and PL spectra for the $CsPbX_3$ PNCs synthesized from the LI method, (c) TEM and HRTEM images for the $CsPbBr_3$ prepared via the LI method,[68] (d) $CsPbX_3$ with different morphologies synthesized via the LI method using acid and amine ligand with different chain lengths. [70]

1.3.3 Non-Injection

Compared with injection syntheses, the non-injection methods for $CsPbX_3$ PNCs are still in their infancy. In the most typical non-injection method, the so-called "heat-up" approach, all the Cs, Pb, X precursors, acid and amine ligands are dissolved in the solvent in one pot, and the entire mixture is heated up to drive the reaction and subsequent formation of $CsPbX_3$ PNCs.[72] There are also other non-injection synthesis techniques, depending on the energy source used, that can be divided into several categories:

(1). Solvothermal. All the precursors, ligands and solvents sealed in an autoclave and heated under pressurized condition.[73]

(2). Microwave. All the precursors and ligands are mixed in a microwave radiation absorbing solvent medium and then the microwave is used as the heat source to ensure rapid and uniform heating profile on the mixture.[74]

(3). Ultrasonication. Applying energy to the reaction solution via the acoustic cavitation caused by the ultrasonication. [75]

These non-injection synthetic methods hold the promise of enabling facile scale-up of PNC synthesis with an enhanced reproducibility. While this thesis does not cover these approaches in any depth, it is noted that for such methods to achieve comparable quality nanocrystals as for injection methods, achieving controlled reaction kinetics across each of these non-injection variants through tailored reaction chemistries will need to fulfilled.

1.4 Nucleation & Growth of PNCs

The nucleation and growth processes of colloids are most commonly described within the context of the LaMer model (**Figure 1-9** a),[37] which can be divided into three stages: (i) build-up of monomers; (ii) nucleation of the monomers due to their supersaturation; (iii) growth of the nuclei through the monomer addition and Ostwald ripening.[38],[76]

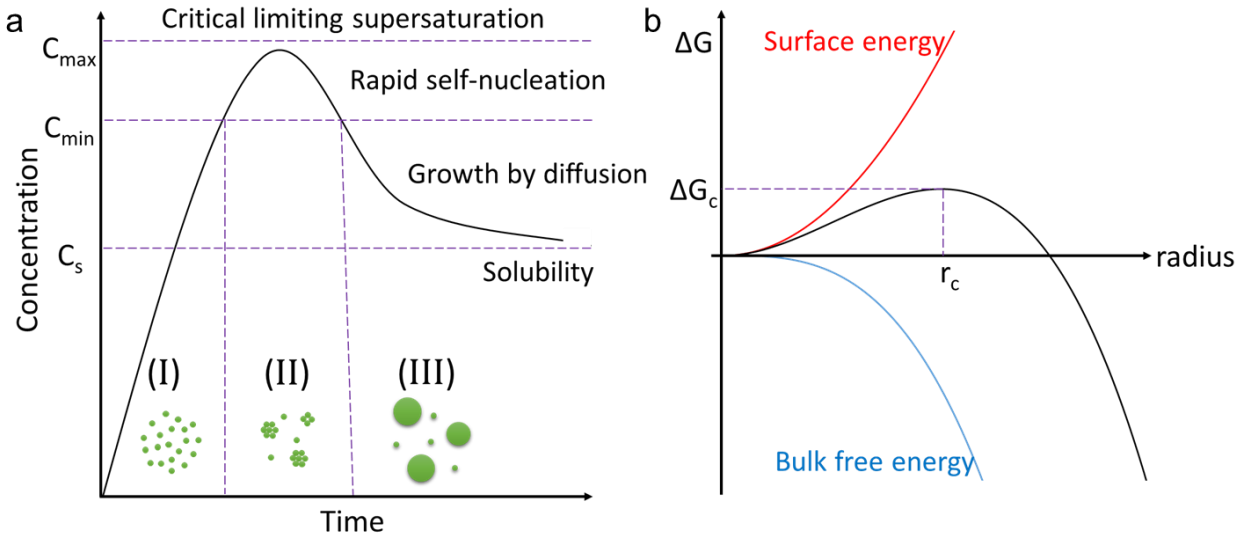

Figure 1-9. (a) Classical LaMer nucleation model of nanoparticles consisting three stages: (i) monomer accumulation, (ii) nucleation after reaching a critical monomer supersaturation and (iii) growth of the nuclei through nuclei attachment. (b) The surface, bulk and total free energies as a function of cluster radius, where the critical radius, r_c is the minimum stable radius.

1.4.1 Nucleation

The nucleation process requires the build-up of monomers within a precursor solution to a level that exceed a critical supersaturation threshold. As shown in **Figure 1-9** b, clusters, which under normal conditions continuously form and dissolve, with a size larger than the critical nucleation radius (r_c) become thermodynamically viable for growth from monomer attachment.[77] The precursor chemistries, reactant concentration, reaction temperature, the conversion rates of precursors to monomers, nucleation rates and growth rates all impact the degree of supersaturation and the dynamics of the nucleation and early-growth stages.

For the LI synthesis of PNCs, a supersaturation state is simply created by the addition of the anti-solvent to the solution. When the anti-solvent is added, the solubility of the precursors could be reduced down to 10^{-7} g/mL,[78] which triggers nucleation. In case of the HI methods, which are typically performed at 100 to 200 °C for PNCs, its success is largely dependent on the nucleation and

growth dynamics being slower than the complete mixing of the precursor solution after the injection. In conventional metal chalcogenide and pnictides synthesis,[79],[80] this can be readily achieved at lab-scale reaction volumes through delicate precursor and ligand combination.[81],[82] However, for PNCs this is extremely hard to achieve as the experimentally determined nucleation stage is within 0.4 s (**Figure 1-10** a,b).[48] Recent theoretical works have even proposed that the nucleation processes occur on a sub-microsecond timeframe.[83] These ultrafast kinetics cause great difficulties in studying the nucleation of PNCs, and to date there is still a lack of authoritative explanation on the nucleation mechanism, although several models have been proposed.

One model of PNC nucleation divided the process into two steps; first, the Pb^{2+} and X^- ions form the corner sharing PbX_6 polyhedra as nuclei, then the interstitial voids are filled with Cs^+ ions.[84] This is similar to the intramolecular exchange processes that has been reported for bulk perovskites.[85] In another theory, Pb^0 nanoparticles of ~2 nm in size act as heterogeneous nucleation seeds within the reaction solution. This has been suggested based on evidence from TEM (**Figure 1-10** c-e), which has shown dark-contrast Pb^0 nanoparticles in several different PNC samples following LI synthesis,[86][67],[69] HI synthesis, [87],[88] or non-injection synthesis.[75],[89] Interestingly, this Pb^0 particles were seen within PbX_2 precursor solutions even before the Cs injection and any PNCs nucleation.[90],[91] Since Pb^{2+} can be easily reduced (E^0 = -0.13 V),[92] the presence of Pb^0 seeds within the PNC reaction is feasible because the amine ligands used in the reaction are also mild reducing agents. However, such a Pb^0 feature have also been reported as a degradation product under the TEM electron beam irradiation.[93] Further investigations are necessary to unambiguously examine this mechanism of nucleation.

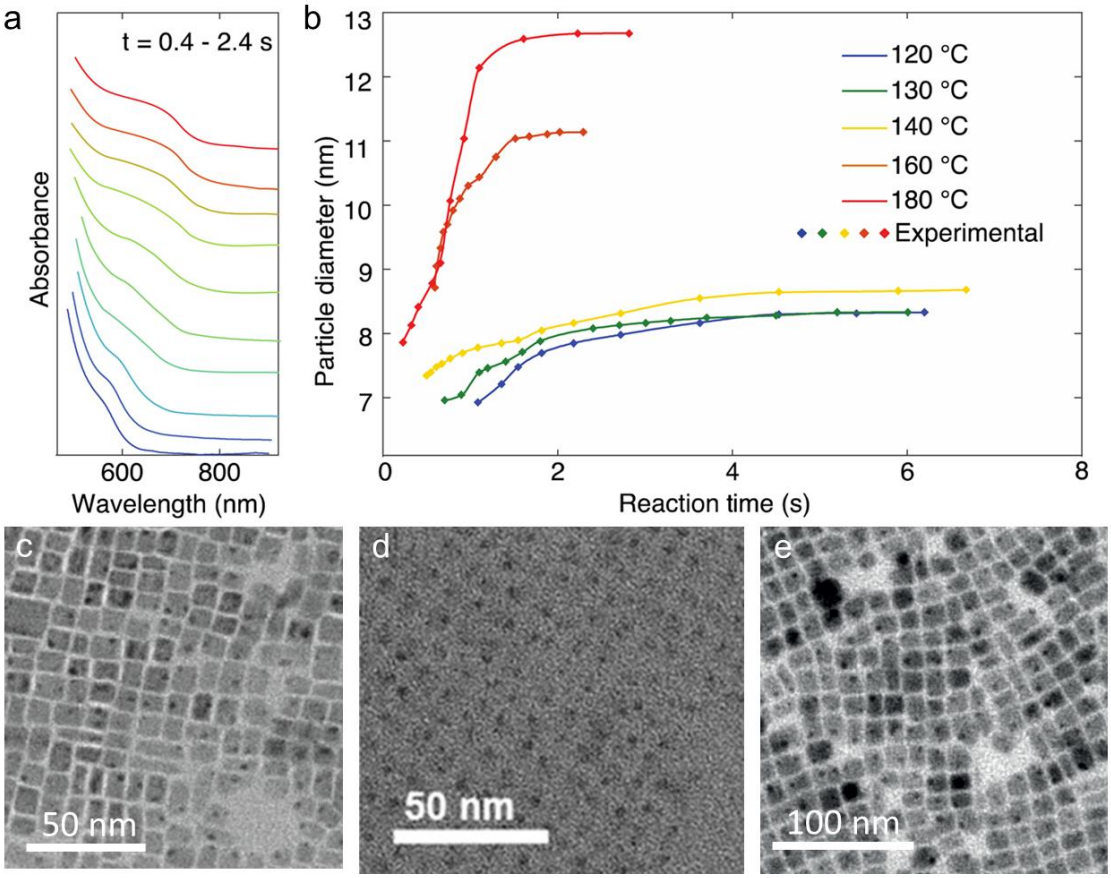

Figure 1-10. (a) Evolution of $CsPbI_3$ absorption spectra at reaction times between 0.4 to 2.4 seconds, (b) Evolution of PNC sizes at different reaction times with various reaction temperatures,[48]TEM images showing the black dots for PNCs prepared from (c) LI synthesis, [70](d) HI synthesis, [90](e) non-injection synthesis.[75]

1.4.2 Growth

As mentioned before, in a typical HI synthesis of PNCs the reaction is terminated after 5 seconds. This arises due to the extremely fast nucleation and growth dynamics for these reactions.[48] As a consequence, available monomer in solution is rapidly consumed in the early stage of the reaction. According to the LaMer model, the dominant growth mechanism after most free-monomer is consumed is Ostwald ripening. To illustrate the ripening process, HI synthesis of $CsPbI_3$ PNCs following different reaction times was carried out (**Figure 1-11** a-e). Within the first few seconds after the injection, the products showed high quality NCU morphologies, with some evidence of size

focusing.[94] When the reaction time was prolonged, a defocusing of the size distribution was seen, which was ascribed to the coarsened NCs.

The growth stage of PNCs in LI synthesis has been reported to finish within 10 to 20 seconds.[71] This can be ascribed to the comparatively slower monomer diffusion rates and lowered reaction kinetics at these low temperatures compared to HI approaches. Despite this, Ostwald ripening is also profound in the LI method. This arises because the crude solution of the LI synthesized PNCs contains up to 30 vol % of polar solvents, such as DMF, DMSO or IPA.[71],[68] In such a polar environment the perovskite lattice has a considerable solubility, therefore the Ostwald ripening process is accelerated.[95][96]

Orientated attachment is the other major growth mechanism observed in PNCs.[97] As previously mentioned in Section 1.3.1, the PNCs undergo orientated attachment to form NWs during HI processes at extended reaction times. Such a process can also be induced post-synthetically. As shown in **Figure 1-11** f-h, when a PNC dispersion is destabilized upon the addition of a polar anti-solvent, e.g. ethanol, orientated attachments would occur and result in NW formation. This arises due to the surface ligand shell being disrupted by the polar solvents,[90] although it is not clear why such a preferential attachment is observed. Notably, orientated attachment has also been ascribed for the formation of other heterogeneous PNC morphologies, such as NPLs and NSs.[44]

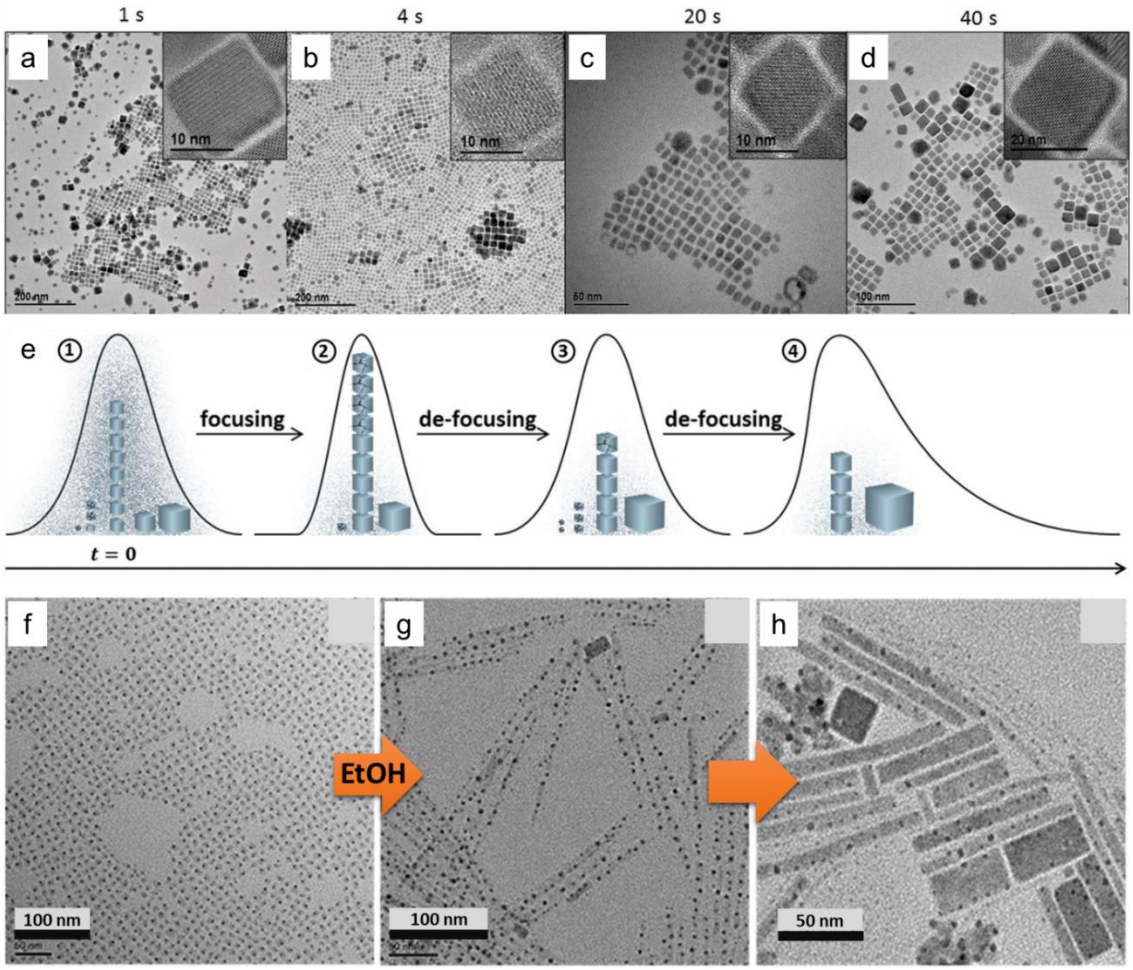

Figure 1-11. TEM images for (a-d) $CsPbI_3$ PNCs synthesized with different times, (e) The evolution of the corresponding PL spectra and the size distribution of the PNCs, [94] TEM images for $CsPbBr_3$ PNCs that has been (f) Original, (g) added with 20 vol % ethanol and underwent oriented growth into nanowires, (h) further grew into the nanorods and nanoplates. [90]

Apart from fast dynamics of the nucleation and growth processes of PNCs, their synthetic window is also sensitive to factors such as solvent,[90] acid-base equilibria,[86] reagent species,[73] ligand species[70],[69] and even mixing rates.[98] Among these factors, the ligand is the most important. Being the outer shell of the PNCs, the surface capping ligands dominant the chemical and physical behaviour of the NCs, which will be discussed in the following section.

1.5 Ligand Interactions with PNCs

The surface capping ligands have multiple roles in the NCs system.[99] First of all, they are surfactants that help to solubilize the precursor salts in the reaction solution. Secondly, they cap the outer layer of the NCs to ensure colloidal dispersibility and prevent them from coarsening. Thirdly, they passivate the surface dangling bonds of the NCs, decrease the surface trap states and enhance the optical properties of the NCs. For traditional semiconductor NCs, common types of ligands include: alkyl-amines, carboxylic acids, phosphonic or phosphinic acids, phosphine oxides, alkyl-thiols or metal chalcogenide complexes.[100],[101],[102],[103] Till now, almost all these ligand species have been adopted in the synthesis of PNCs,[78],[104],[105] while the alkyl amine (OLA) and carboxylic acid (OA) being the most widely-used.[47]

Surface characterizations (Nuclear Magnetic Resonance, NMR and Fourier Transform Infrared Spectroscopy, FTIR) of PNCs synthesized following the OA and OLA combinations confirmed that the oleyl-ammonium(OLA^+) and oleate (OA^-) species were the pre-dominant surface binding species,[106],[107] which were the product of the acid-base reaction between OLA and OA in the reaction solution.[108] Importantly, in PNC dispersions, the ligands species were found to exist in a dynamic exchange process between two stages: binding to the PNCs surface or free floating among the dispersion.[107] This behaviour causes difficulties in the stabilization and purification of the PNCs, which will be a main topic in Chapter 4.

Ligands other than the standard OA and OLA have also been used in the PNC synthesis. Typically, longer acidic ligand chain lengths could yield PNCs with better stability and colloidal dispersibility, whereas decreasing acid chain lengths produces PNCs with increasing size.[47],[109],[110] As a result, PNCs synthesized with longer chain acids, such as OA or tetradecanoic acid, typically had a PLQY up to 80 %, which was higher than the shorter chained derivatives.[69] The reason is that the longer chain ligand provided stronger steric stabilization and therefore prevented the monomer uptake during

the growth stage, thus the resulting PNCs had a smaller size and narrower size distribution.[111] Moreover, decreasing the amine's carbon chain length resulted in the PNCs showing NPL morphologies rather than cubes, with the thickness of the NPLs being proportional to the amine chain-length. A minimum thickness of 1.8 nm for the NPLs was seen when using the hexylamine. [47]

Alkyl phosphorus ligands have also been found to facilitate the synthesis of high-quality PNCs. TOP was first used as a surfactant to help dissolve $PbCl_2$.[1] When used alongside OA and OLA in the $CsPbI_3$ synthesis, the resulting PNCs exhibited a near unity PLQY.[3] Interestingly, NMR measurements revealed that it is not directly binding to the PNC surface, and the surface ligands were determined to still be the OLA^+ and OA^- species. The use of trioctylphosphine oxide (TOPO) has also yielded PNCs with better size uniformity and long-term stability. In contrast to TOP, TOPO was confirmed to be a surface binding species and effectively passivated the PNCs.[112],[89]

Other less common ligands were also investigated, among the most notable one was the sulfobetaine zwitterion ligand.[113] The use of only this zwitterion ligand produced PNCs that experienced longer storage stability and enhanced chemical resistance comparing to the standard OA and OLA PNCs. Such an improvement was ascribed to the sulfobetaine molecule forming strong bonds simultaneously with both the surface anion and cations of the PNCs. Investigations into other ligands have included secondary to quaternary amines,[69],[114] bidentate ammoniums,[115],[114] aniline derivatives,[116] etc. However, generally these ligands have yielded PNCs of worse quality compared to conventional OA and OLA, due to factors that they had either lower steric stabilization, changed precursor/monomer solubilities, or worse prevention of the Ostwald ripening.[115]

1.6 Post-Synthetic Treatments

Due to the ionic nature of the perovskite lattice and the labile binding between the PNCs and ligands, they can undergo a variety of post-synthetic treatments, which includes purification, anion and cation

exchanges, and self-assembly.[117] In this section, the major post-synthetic treatments of PNCs will be introduced.

1.6.1 Purification

The crude reaction solution of PNCs contains many unwanted impurities, such as unreacted precursors, residual solvent, excess ligands and so on. These impurities are detrimental for long term storage stability or device fabrication, thus it is necessary to purify the PNCs.[71],[30],[118] Typically, the purification process is carried out by adding a polar anti-solvent (e.g. tert-butanol, IPA, methyl-acetate, etc) to the crude solution to precipitate the PNCs, then subjecting the flocculated dispersion to high speed centrifugation (typically > 6000 rpm) to isolate the PNCs, followed by discarding the supernatant and finally re-dispersing the PNCs in a non-polar solvent (e.g. toluene, hexane).

Selection of the anti-solvent must be carefully considered in order to effectively precipitate the PNCs and at the same time not destroy the perovskite lattice. Typically, moderately polar anti-solvents with a dipole moment around 1.66-2.88 D (i.e. isopropanol, butanol, acetone, acetonitrile) have been found to be suitable.[106] Of these, methyl acetate was found to successfully maintain the cubic phase of $CsPbI_3$ after purification.[30] If the anti-solvents were too polar, such as DMF or DMSO (~4.0 D), or protic (methanol, ethanol), the perovskite lattice would be disrupted which caused degradation to the PNCs.[106]

Usually, only one purification cycle is not sufficient to remove all the impurities, hence multiple purification cycles are required to achieve high purity PNC dispersions.[119] However, multiple purification cycles can also cause the progressive loss of the PNCs' surface ligands, and consequently the coarsening of the PNCs to induce degradation of their optical properties. This arises because the dynamic ligand exchange between bound and unbound ligands results in free ligands being lost after every wash cycle. To compensate for this ligand loss and maintain the PNCs' quality during the

purification process, an effective strategy is to add extra OA and OLA ligands before every purification cycle to preserve colloidal stability and PL during multiple purification cycles.[107]

More detailed surface chemistry studies and a more reliable purification strategy will be discussed in Chapter 4.

1.6.2 Anion Exchange

PNCs can undergo facile anion exchange reactions to enable their bandgap to be post-synthetically tuned (**Figure 1-12**). [120] Because of the high diffusivity of halide vacancies in the perovskite lattice,[121] rapid $Cl^- \leftrightarrow Br^-$ or $Br^- \leftrightarrow I^-$ exchange occurs upon exposure to an external halide source (e.g. ammonium halide solution or halide salt solution). [4],[69],[120] By adjusting the ratio between the original and additional halide, the degree of the halide exchange can be controlled.[121] Generally, varying the original to additional halide ratio from 1:3 to 3:1 results in complete covering of the PL spectrum region in-between of the pristine PNCs. Importantly, the PNCs after the exchange possess the same morphology and high optical properties as those directly synthesized PNCs of equivalent composition.[74],[121] Moreover, PNCs with NWs or NPLs morphology can also undergo this exchange process.[86],[122]

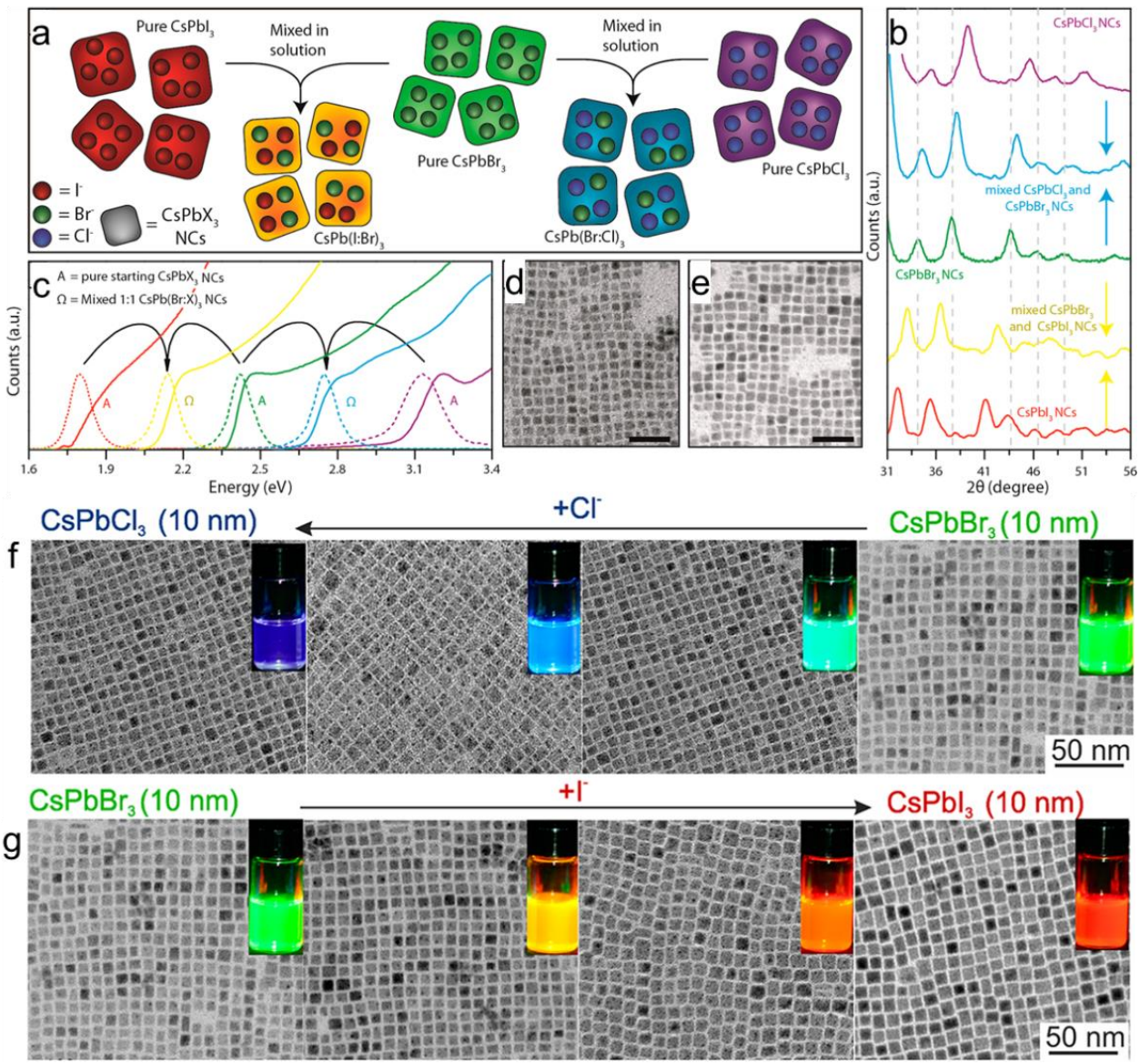

Figure 1-12. Post-synthesis anion exchange for $CsPbX_3$ PNCs; (a) schematic illustration of the anion exchange process, (b) XRD spectra and (c) UV-Vis absorption and PL spectra for the PNCs after exchange, TEM images of (d) $CsPb(Br_{1.5}Cl_{1.5})$ and (e) $CsPb(Br_{1.5}I_{1.5})$,[120](f),(g) TEM images of $CsPbX_3$ PNCs exchange transitions and their associated solutions under UV-light.[121]

1.6.3 Cation Exchange

In addition to anion exchange, cation exchange (mostly on the Pb) for $CsPbX_3$ PNCs is also feasible, which allows for further tuning of their optical properties. By simply mixing the $CsPbBr_3$ PNC dispersion with a M^{2+} cation precursor solution (MBr_2, M = Sn^{2+}, Zn^{2+}, and Cd^{2+}) in toluene, cation

exchange readily occurs, with the resulting $CsPb_{1-x}M_xBr_3$ PNCs exhibiting a blue-shift in the PL according to the type of M^{2+} dopant and its concentration (**Figure 1-13**). [123] In contrast to anion exchange, which can result in almost complete substitution of the original element, the cation exchange has only reached a maximum of 10 % substitution, even when the M^{2+} has been in great excess. This was attributed to the cation exchange requiring higher activation energy,[121] and the rigid perovskite lattice formed by the cation backbone limiting the cation exchange to the outer surface.

Using ultrasonication as the energy source and a saturated solution of $CdCl_2$ in ethanol and OLA as the secondary B site element source, a maximum substitution of 40 % Cd^{2+} has been achieved for the $CsPbCl_3$ PNCs.[124]. This much higher exchange level was attributed to the more polar ethanol solvent breaking the rigid $PbCl_6$ polyhedra lattice, which promoted $CdCl_2$ diffusion into not just the surface but also the bulk of the lattice. After this high-percentage cation exchange, the PLQY of the $CsPbCl_3$ also increased from 3 % to nearly 100 %, which was attributed to the smaller Cd^{2+} ions reducing the distortion of the $PbCl_6$ polyhedra and consequently removing the chloride vacancies and their associated non-radiative trap states. Such $CsPb_xCd_{1-x}Cl_3$ PNCs also exhibited an enhanced photo-stability with their PLQYs being maintained at 90 % for several months.

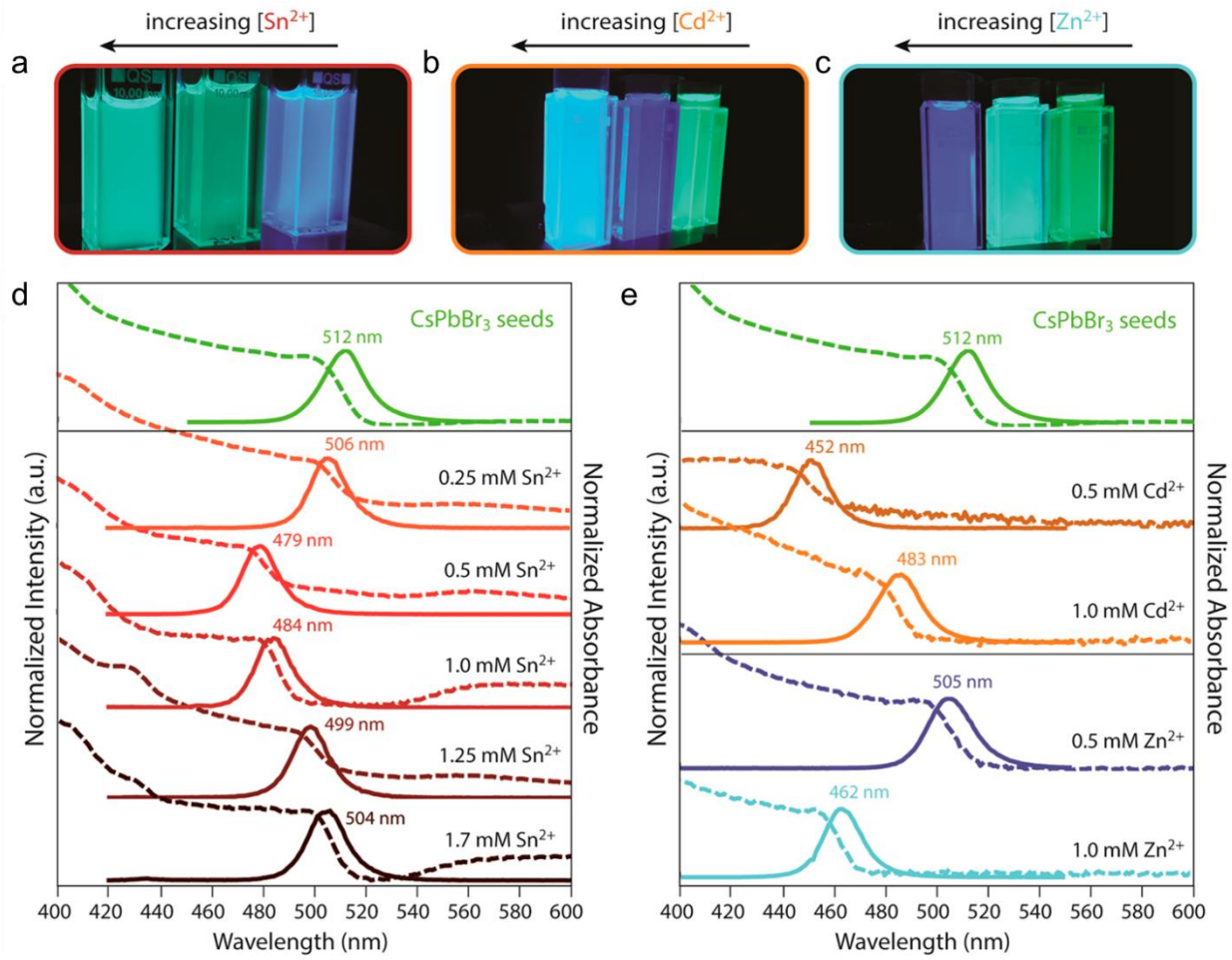

Figure 1-13. $CsPbBr_3$ PNCs dispersion under UV light after the cation exchange with increasing additions of (a) $SnBr_2$, (b) $CdBr_2$, (c) $ZnBr_2$, UV-Vis absorption and PL emission spectra of $CsPbBr_3$ dispersions with (d) Sn^{2+}, (e) Cd^{2+} and Zn^{2+} additions.[123]

1.6.4 Post-synthetic Self-assembly of PNCs

As mentioned in Chapter 1.3.1, the PNCs can also undergo self-assembly and form a SC structure directly after synthesis. Alternatively, the SCs can also be post-synthetically assembled from neat PNCs.[125] This has been shown by slowly evaporating the solvent of purified $CsPbBr_3$ PNCs with narrow size distribution to form 1–10 µm sized SCs (**Figure 1-14** a). SCs prepared by this manner also had a coherent super-fluorescence, which was demonstrated by its red-shifted PL, narrower PL FWHM and decreased PL lifetime (**Figure 1-14** b,c). Notably, even for PNCs that did not have a narrow size distribution, they could also be assembled into SCs via the addition of polar anti-solvent

or complexing agents, which exerted inter-molecular forces on the PNCs to drive their assembly.[126],[127] Apart from the NCU shape PNCs, other morphologies, such as NPLs,[128] NRs,[129] and NSs,[130] can also undergo similar post-synthetic self-assembling processes to form super lattice structures (**Figure 1-14** d-f).

A new self-assembling strategy of the PNCs relying on the hydrophobic interaction will be discussed in Chapter 5.

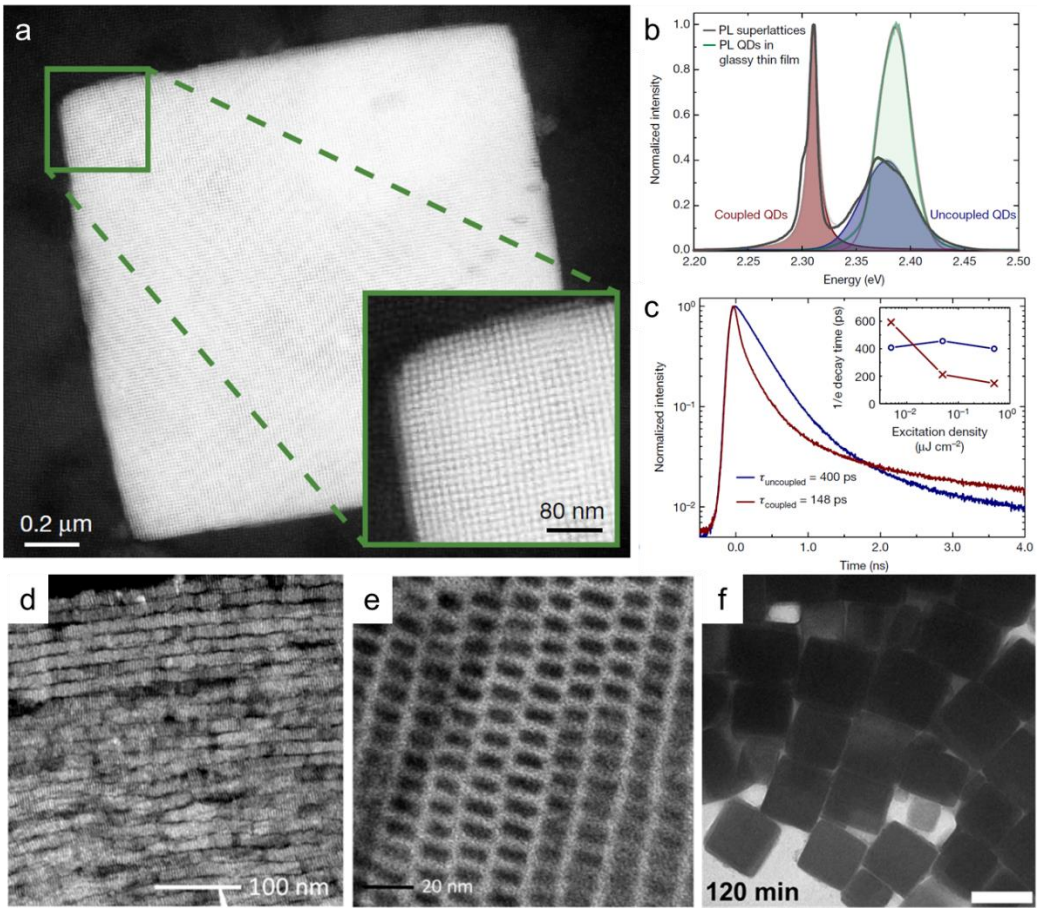

Figure 1-14. (a) TEM images, (b), (c) PL and TRPL spectra for the $CsPbBr_3$ super-lattice,[125] The self-assembled super-lattice structures for the $CsPbBr_3$ (d) Nanoplatelets,[128] (e) Nanorods,[129] (f) Nanosheet,[130] scale bar 500nm.

1.7 Thesis Overview

In this chapter, the properties and synthetic approaches for $CsPbX_3$ PNCs have been reviewed. The excellent optoelectronic properties of such materials make them a highly promising candidates for a variety of optoelectronic applications. However, to ensure that such PNCs can reach their full potential, it is essential that they can be synthesised with high quality and good reproducibility. This is particularly the case for $CsPbI_3$, which has continued to suffer from structural instability, despite great synthetic advances across both injection and non-injection synthetic approaches.

This thesis is focused on developing high quality $CsPbX_3$ PNC materials by: stabilizing the functional cubic phase of $CsPbI_3$ under ambient conditions via understanding its phase transformation mechanism and then controlling its surface ligand chemistry; establishing an effective purification protocol for a $CsPbX_3$ PNC as-synthesised solution to achieve high quality and high purity ink while retaining optical properties and long term stability; utilizing the intermolecular forces among the PNCs to drive self-assembly into SC structures with modified optical properties. It addresses these goals through targeted research efforts across the following themes:

1. The cubic phase stability of the $CsPbI_3$. *The bandgap for the cubic phase $CsPbI_3$ is 1.73 eV, which is suitable for solar cell or red-light LED applications. However, this functional cubic phase of $CsPbI_3$ is only stable above 300 °C. Below room temperature, this material would spontaneously transform into the non-functional orthorhombic phase, which has a much wider band gap 2.9 eV and no PL.*

In chapter 3, a novel reaction ligand chemistry has been explored to probe the influence between ligand chemistry and $CsPbI_3$ PNC phase stability. It was found that the traditionally used oleic acid enabled structural instability of such PNCs, with more sterically prohibitive ligands preventing phase transformation. This knowledge was applied to all the $CsPbX_3$ analogues to achieve a high-quality PNCs compositional library.

2. The purification of the $CsPbX_3$ PNCs*. The as-synthesized crude solution of $CsPbX_3$ PNCs is not suitable for film deposition or device fabrication because it contains many unwanted impurities, therefore purification is always necessary. To date, most purification studies have been on $CsPbBr_3$ PNCs, which is the most robust across all the $CsPbX_3$ family.*

In chapter 4, a suitable purification protocol for $CsPbX_3$ PNCs was developed, which made use of an additive solution featuring both ligands and compositional ions to balance the surface chemistry during the purification process. With this additive solution, multiple purification cycle could be realised while maintaining the PNC phase, microstructure and optical properties.

3. Formation of $CsPbX_3$ PNC super-crystals. *Self-assembly of the NCs into SC structures with nanoscale ordering could effectively tune their optical and electronic properties. Although the synthesis of $CsPbX_3$ PNCs has been extensively investigated, their self-assembly into super-crystals has received much less attention, with current methods to assemble the PNCs being complex and not well understood.*

In Chapter 5, a facile direct synthesis method of $CsPbX_3$ super-crystals is reported. The self-assembly was realised by the special surface chemistry design leveraging from the work in Chapter 3, as well as stoichiometry tunning. The hydrophobic interaction was found to be the key inter-molecular force to drive the self-assembly process. Through disrupting the hydrophobic interaction, such super-crystals structure would collapse and recover back over time. Such super-crystals were harnessed within down-converting light-emitting structures.

References

[1] L. Protesescu, S. Yakunin, M. I. Bodnarchuk, F. Krieg, R. Caputo, C. H. Hendon, R. X. Yang, A. Walsh, M. V. Kovalenko, *Nano Lett.* **2015**, *15*, 3692.

[2] Q. A. Akkerman, G. Rainò, M. V. Kovalenko, L. Manna, *Nat. Mater.* **2018**, *17*, 394.

[3] F. Liu, Y. Zhang, C. Ding, S. Kobayashi, T. Izuishi, N. Nakazawa, T. Toyoda, T. Ohta, S. Hayase, T. Minemoto, K. Yoshino, S. Dai, Q. Shen, *ACS Nano* **2017**, *11*, 10373.

[4] Y. Zhang, M. I. Saidaminov, I. Dursun, H. Yang, B. Murali, E. Alarousu, E. Yengel, B. A. Alshankiti, O. M. Bakr, O. F. Mohammed, *J. Phys. Chem. Lett.* **2017**, 8, 961.

[5] L. C. Schmidt, A. Pertegás, S. González-Carrero, O. Malinkiewicz, S. Agouram, G. Mínguez Espallargas, H. J. Bolink, R. E. Galian, J. Pérez-Prieto, *J. Am. Chem. Soc.* **2014**, *136*, 850.

[6] A. Swarnkar, R. Chulliyil, V. K. Ravi, M. Irfanullah, A. Chowdhury, A. Nag, *Angew. Chemie - Int. Ed.* **2015**, *54*, 15424.

[7] Z. Xiao, R. A. Kerner, L. Zhao, N. L. Tran, K. M. Lee, T.-W. Koh, G. D. Scholes, B. P. Rand, *Nat. Photonics* **2017**, *11*, 108.

[8] S. Yakunin, L. Protesescu, F. Krieg, M. I. Bodnarchuk, G. Nedelcu, M. Humer, G. De Luca, M. Fiebig, W. Heiss, M. V Kovalenko, *Nat. Commun.* **2015**, *6*, 8056.

[9] L. Lv, Y. Xu, H. Fang, W. Luo, F. Xu, L. Liu, B. Wang, X. Zhang, D. Yang, W. Hu, A. Dong, *Nanoscale* **2016**, *8*, 13589.

[10] E. M. Sanehira, A. R. Marshall, J. A. Christians, S. P. Harvey, P. N. Ciesielski, L. M. Wheeler, P. Schulz, L. Y. Lin, M. C. Beard, J. M. Luther, *Sci. Adv.* **2017**, *3*, eaao4204.

[11] G. Rose, *J. Prakt. Chemie* **1840**, *19*, 459.

[12] H.-R. Wenk, A. Bulakh, *Minerals: Their Constitution and Origin*; Cambridge University Press, 2003.

[13] V. M. Goldschmidt, *Naturwissenschaften* **1926**, *14*, 477.

[14] Z. Cheng, J. Lin, *CrystEngComm* **2010**, *12*, 2646.

[15] J.-P. Correa-Baena, M. Saliba, T. Buonassisi, M. Grätzel, A. Abate, W. Tress, A. Hagfeldt, *Science.* **2017**, *358*, 739.

[16] C. K. Møller, Crystal Structure and Photoconductivity of Cæsium Plumbohalides. *Nature* **1958**, *182*, 1436–1436.

[17] A. Kojima, K. Teshima, Y. Shirai, T. Miyasaka, *J. Am. Chem. Soc.* **2009**, *131*, 6050.

[18] J.-P. Correa-Baena, A. Abate, M. Saliba, W. Tress, T. Jesper Jacobsson, M. Grätzel, A. Hagfeldt, *Energy Environ. Sci.* **2017**, *10*, 710.

[19] Y. Fu, H. Zhu, C. C. Stoumpos, Q. Ding, J. Wang, M. G. Kanatzidis, X. Zhu, S. Jin, *ACS Nano* **2016**, *10*, 7963.

[20] W. Travis, E. N. K. Glover, H. Bronstein, D. O. Scanlon, R. G. Palgrave, *Chem. Sci.* **2016**, *7*, 4548.

[21] P. Cottingham, R. L. Brutchey, *Chem. Commun. Chem. Commun* **2016**, *5246*, 5246.

[22] A. Dutta, N. Pradhan, *ACS Energy Lett.* **2019**, *4*, 709.

[23] R. J. Sutton, M. R. Filip, A. A. Haghighirad, N. Sakai, B. Wenger, F. Giustino, H. J. Snaith, *ACS Energy Lett.* **2018**, *3*, 1787.

[24] B. Zhao, S. Jin, S. Huang, N. Liu, J.-Y. Ma, D.-J. Xue, Q. Han, J. Ding, Q.-Q. Ge, Y. Feng, J.-S. Hu, *J. Am. Chem. Soc.* **2018**, *140*, 11725.

[25] B. Conings, J. Drijkoningen, N. Gauquelin, A. Babayigit, J. D'Haen, L. D'Olieslaeger, A. Ethirajan, J. Verbeeck, J. Manca, E. Mosconi, F. De Angelis, H.-G. Boyen, *Adv. Energy Mater.* **2015**, *5*, 1500477.

[26] Y. Hu, T. Bein, P. Docampo, M. van Schilfgaarde, M. Campoy-Quiles, M. T. Weller, P. Azarhoosh, A. M. A. Leguy, M. I. Alonso, O. J. Weber, P. R. F. Barnes, J. Nelson, *Chem. Mater.* **2015**, *27*, 3397.

[27] S. Dastidar, C. J. Hawley, A. D. Dillon, A. D. Gutierrez-Perez, J. E. Spanier, A. T. Fafarman, *J. Phys. Chem. Lett.* **2017**, *8*, 1278.

[28] M. Kulbak, S. Gupta, N. Kedem, I. Levine, T. Bendikov, G. Hodes, D. Cahen, *J. Phys. Chem. Lett.* **2016**, *7*, 167.

[29] M. Maqbool, G. Rehman, L. Ali, M. Shafiq, R. Iqbal, R. Ahmad, T. Khan, S. Jalali-Asadabadi, M. Maqbool, I. Ahmad, *J. Alloys Compd.* **2017**, *705*, 828.

[30] A. Swarnkar, A. R. Marshall, E. M. Sanehira, B. D. Chernomordik, D. T. Moore, J. A. Christians, T. Chakrabarti, J. M. Luther, *Science.* **2016**, *354*, 92.

[31] W. J. Yin, T. Shi, Y. Yan, *Adv. Mater.* **2014**, *26*, 4653.

[32] D. W. DeQuilettes, S. M. Vorpahl, S. D. Stranks, H. Nagaoka, G. E. Eperon, M. E. Ziffer, H. J. Snaith, D. S. Ginger, *Science.* **2015**, *348*, 683.

[33] S. D. Stranks, H. J. Snaith, *Nat. Nanotechnol.* **2015**, *10*, 391.

[34] H. Liu, Z. Wu, J. Shao, D. Yao, H. Gao, Y. Liu, W. Yu, H. Zhang, B. Yang, *ACS Nano* **2017**, *11*, 2239.

[35] W. Liu, Q. Lin, H. Li, K. Wu, I. Robel, J. M. Pietryga, V. I. Klimov, *J. Am. Chem. Soc.* **2016**, *138*, 14954.

[36] D. Parobek, B. J. Roman, Y. Dong, H. Jin, E. Lee, M. Sheldon, D. H. Son, *Nano Lett.* **2016**, *16*, 7376.

[37] V. K. LaMer, R. H. Dinegar, *J. Am. Chem. Soc.* **1950**, *72*, 4847.

[38] C. B. Murray, D. J. Norris, M. G. Bawendi, *J. Am. Chem. Soc.* **1993**, *115*, 8706.

[39] X. Peng, L. Manna, W. Yang, J. Wickham, E. Scher, A. Kadavanich, A. P. Alivisatos, *Nature* **2000**, *404*, 59.

[40] X. Peng, J. Wickham, A. P. Alivisatos, *J. Am. Chem. Soc.* **1998**, *120*, 5343.

[41] N. C. Anderson, M. P. Hendricks, J. J. Choi, J. S. Owen, *J. Am. Chem. Soc.* **2013**, *135*, 18536.

[42] D. Aldakov, A. Lefrançois, P. Reiss, *J. Mater. Chem. C* **2013**, *1*, 3756.

[43] D. V Talapin, J. S. Lee, M. V Kovalenko, E. V Shevchenko, *Chem. Rev.* **2010**, *110*, 389.

[44] Y. Bekenstein, B. A. Koscher, S. W. Eaton, P. Yang, A. P. Alivisatos, *J. Am. Chem. Soc.* **2015**, *137*, 16008.

[45] S. Yang, Y. C. Zheng, Y. Hou, X. Chen, Y. Chen, Y. Wang, H. Zhao, H. G. Yang, *Chem. Mater.* **2014**, *26*, 6705.

[46] D. Zhang, S. W. Eaton, Y. Yu, L. Dou, P. Yang, *J. Am. Chem. Soc.* **2015**, *137*, 9230.

[47] A. Pan, B. He, X. Fan, Z. Liu, J. J. Urban, A. P. Alivisatos, L. He, Y. Liu, *ACS Nano* **2016**, *10*, 7943.

[48] I. Lignos, S. Stavrakis, G. Nedelcu, L. Protesescu, A. J. Demello, M. V. Kovalenko, *Nano Lett.* **2016**, *16*, 1869.

[49] P. Liu, W. Chen, W. Wang, B. Xu, D. Wu, J. Hao, W. Cao, F. Fang, Y. Zeng, R. Pan, S. Chen, W. Cao, X. W. Sun, K. Wang, *Chem. Mater.* **2017**, *29*, 5168.

[50] Y. Dong, T. Qiao, D. Kim, D. Parobek, D. Rossi, D. H. Son, *Nano Lett.* **2018**, *18*, 3716.

[51] Y. Tong, E. Yao, A. Manzi, E. Bladt, K. Wang, M. Döblinger, S. Bals, P. Müller-buschbaum, A. S. Urban, L. Polavarapu, *Adv. Mater.* **2018**, *1801117*, 1.

[52] M. A. Boles, M. Engel, D. V. Talapin, *Chem. Rev.* **2016**, *116*, 11220.

[53] Z. Nie, A. Petukhova, E. Kumacheva, *Nat. Nanotechnol.* **2010**, *5*, 15.

[54] M. R. Linaburg, E. T. McClure, J. D. Majher, P. M. Woodward, *Chem. Mater.* **2017**, *29*, 3507.

[55] C. Wang, Y. Zhang, A. Wang, Q. Wang, H. Tang, W. Shen, Z. Li, Z. Deng, *Chem. Mater.* **2017**, *29*, 2157.

[56] L. Protesescu, S. Yakunin, S. Kumar, J. Bär, F. Bertolotti, N. Masciocchi, A. Guagliardi, M. Grotevent, I. Shorubalko, M. I. Bodnarchuk, C.-J. Shih, M. V. Kovalenko, *ACS Nano* **2017**, *11*, 3119.

[57] S. Zou, Y. Liu, J. Li, C. Liu, R. Feng, F. Jiang, Y. Li, J. Song, H. Zeng, M. Hong, X. Chen, *J. Am. Chem. Soc.* **2017**, *139*, 11443.

[58] A. Swarnkar, W. J. Mir, A. Nag, *ACS Energy Lett.* **2018**, *3*, 286.

[59] G. Pan, X. Bai, D. Yang, X. Chen, P. Jing, S. Qu, L. Zhang, D. Zhou, J. Zhu, W. Xu, B. Dong, H. Song, *Nano Lett.* **2017**, *17*, 8005.

[60] D. Zhou, D. Liu, G. Pan, X. Chen, D. Li, W. Xu, X. Bai, H. Song, *Adv. Mater.* **2017**, *29*, 1704149.

[61] T. C. Jellicoe, J. M. Richter, H. F. J. Glass, M. Tabachnyk, R. Brady, S. E. Dutton, A. Rao, R. H. Friend, D. Credgington, N. C. Greenham, M. L. Böhm, *J. Am. Chem. Soc.* **2016**, *138*, 2941.

[62] Y. Zhang, J. Yin, M. R. Parida, G. H. Ahmed, J. Pan, O. M. Bakr, O. F. Mohammed, *J. Phys. Chem. C* **2017**, *8*, 3173.

[63] S. Acharya, S. Sain, G. S. Kumar, B. Pradhan, A. Dalui, S. K. Pradhan, U. K. Ghorai, *Chem. Mater.* **2018**, *30*, 2135.

[64] E. T. McClure, M. R. Ball, W. Windl, P. M. Woodward, *Chem. Mater.* **2016**, *28*, 1348.

[65] L. Zhou, Y. F. Xu, B. X. Chen, D. Bin Kuang, C. Y. Su, *Small* **2018**, *14*, 1703762.

[66] S. E. Creutz, E. N. Crites, M. C. De Siena, D. R. Gamelin, *Nano Lett.* **2018**, *18*, 1118.

[67] H. Huang, F. Zhao, L. Liu, F. Zhang, X. G. Wu, L. Shi, B. Zou, Q. Pei, H. Zhong, *ACS Appl. Mater. Interfaces* **2015**, *7*, 28128.

[68] X. Li, Y. Wu, S. Zhang, B. Cai, Y. Gu, J. Song, H. Zeng, *Adv. Funct. Mater.* **2016**, *26*, 2435.

[69] S. Wei, Y. Yang, X. Kang, L. Wang, L. Huang, D. Pan, *Chem. Commun.* **2016**, *52*, 7265.

[70] S. Sun, D. Yuan, Y. Xu, A. Wang, Z. Deng, *ACS Nano* **2016**, *10*, 3648.

[71] Q. A. Akkerman, M. Gandini, F. Di Stasio, P. Rastogi, F. Palazon, G. Bertoni, J. M. Ball, M. Prato, A. Petrozza, L. Manna, *Nat. Energy* **2016**, *2*, 16194.

[72] X. Chen, L. Peng, K. Huang, Z. Shi, R. Xie, W. Yang, *Nano Res.* **2016**, *9*, 1994.

[73] M. Chen, Y. Zou, L. Wu, Q. Pan, D. Yang, H. Hu, Y. Tan, Q. Zhong, Y. Xu, H. Liu, B. Sun, Q. Zhang, *Adv. Funct. Mater.* **2017**, *1701121*, 1701121.

[74] Z. Long, H. Ren, J. Sun, J. Ouyang, N. Na, *Chem. Commun.* **2017**, *53*, 9914.

[75] Y. Tong, E. Bladt, M. F. Aygüler, A. Manzi, K. Z. Milowska, V. A. Hintermayr, P. Docampo, S. Bals, A. S. Urban, L. Polavarapu, J. Feldmann, *Angew. Chemie - Int. Ed.* **2016**, *55*, 13887.

[76] C. B. Murray, C. R. Kagan, M. G. Bawendi, *Annu. Rev. Mater. Sci.* **2000**, *30*, 545.

[77] D. J. Shaw, *Introduction to Colloid and Surface Chemistry*; 4th Editio.; Butterworth-Heinemann, 1992.

[78] X. Li, Y. Wu, S. Zhang, B. Cai, Y. Gu, J. Song, H. Zeng, *Adv. Funct. Mater.* **2016**, *26*, 2435.

[79] Z. A. Peng, X. Peng, *J. Am. Chem. Soc.* **2001**, *123*, 183.

[80] M. A. Olshavsky, A. N. Goldstein, A. P. Alivisatos, *J. Am. Chem. Soc.* **1990**, *112*, 9438.

[81] A. Sahu, L. Qi, M. S. Kang, D. Deng, D. J. Norris, *J. Am. Chem. Soc.* **2011**, *133*, 6509.

[82] F. Wang, W. E. Buhro, *J. Am. Chem. Soc.* **2012**, *134*, 5369.

[83] P. Ahlawat, P. Piaggi, M. Grätzel, M. Parrinello, U. Röthlisberger, *arXiv preprint arXiv*. **2018**, *1810*, 00759.

[84] Y. Li, H. Huang, Y. Xiong, S. V. Kershaw, A. L. Rogach, *Angew. Chemie - Int. Ed.* **2018**, *57*, 5833.

[85] J. S. Manser, M. I. Saidaminov, J. A. Christians, O. M. Bakr, P. V. Kamat, *Acc. Chem. Res.* **2016**, *49*, 330.

[86] Q. A. Akkerman, S. G. Motti, A. R. Srimath Kandada, E. Mosconi, V. D'Innocenzo, G. Bertoni, S. Marras, B. A. Kamino, L. Miranda, F. De Angelis, A. Petrozza, M. Prato, L. Manna, *J. Am. Chem. Soc.* **2016**, *138*, 1010.

[87] L. Protesescu, S. Yakunin, M. I. Bodnarchuk, F. Bertolotti, N. Masciocchi, A. Guagliardi, M. V. Kovalenko, *J. Am. Chem. Soc.* **2016**, *138*, 14202.

[88] O. Vybornyi, S. Yakunin, M. V. Kovalenko, *Nanoscale* **2016**, *8*, 6278.

[89] Q. Pan, H. Hu, Y. Zou, M. Chen, L. Wu, D. Yang, X. Yuan, J. Fan, B. Sun, Q. Zhang, *J. Mater. Chem. C* **2017**, 5, 10947.

[90] T. Udayabhaskararao, M. Kazes, L. Houben, H. Lin, D. Oron, *Chem. Mater.* **2017**, *29*, 1302.

[91] Y. H. Ko, P. Prabhakaran, M. Jalalah, S. J. Lee, K. S. Lee, J. G. Park, *J. Mater. Chem. C* **2018**, *6*, 7803.

[92] S. G. Bratsch, *J. Phys. Chem. Ref. Data* **1989**, *18*, 1.

[93] J. A. Sichert, Y. Tong, N. Mutz, M. Vollmer, S. Fischer, K. Z. Milowska, R. García Cortadella, B. Nickel, C. Cardenas-Daw, J. K. Stolarczyk, A. S. Urban, J. Feldmann, *Nano Lett.* **2015**, *15*, 6521.

[94] M. Koolyk, D. Amgar, S. Aharon, L. Etgar, *Nanoscale* **2016**, *8*, 6403.

[95] A. Kirakosyan, S. Yun, S.-G. Yoon, J. Choi, *Nanoscale* **2018**, *10*, 1885.

[96] M. P. Pileni, *Nat. Mater.* **2003**, *2*, 145.

[97] J. Zhang, F. Huang, Z. Lin, *Nanoscale* **2010**, *2*, 18.

[98] H. Huang, J. Raith, S. V. Kershaw, S. Kalytchuk, O. Tomanec, L. Jing, A. S. Susha, R. Zboril, A. L. Rogach, *Nat. Commun.* **2017**, *8*, 996.

[99] Y. Yin, A. P. Alivisatos, *Nature* **2005**, *437*, 664.

[100] M. J. Greaney, R. L. Brutchey, In *Materials Today* **2015**, 18, 31.

[101] C. Jiang, J. S. Lee, D. V Talapin, *J. Am. Chem. Soc.* **2012**, *134*, 5010.

[102] M. V Kovalenko, M. Scheele, D. V. Talapinl, *Science.* **2009**, *324*, 1417.

[103] M. A. Boles, D. Ling, T. Hyeon, D. V Talapin, *Nat. Mater.* **2016**, *15*, 141.

[104] H. Huang, A. S. Susha, S. V. Kershaw, T. F. Hung, A. L. Rogach, *Adv. Sci.* **2015**, *2*, 1500194.

[105] S. Bhaumik, S. A. Veldhuis, Y. F. Ng, M. Li, S. K. Muduli, T. C. Sum, B. Damodaran, S. Mhaisalkar, N. Mathews, *Chem. Commun.* **2016**, *52*, 7118.

[106] Y. Kim, E. Yassitepe, O. Voznyy, R. Comin, G. Walters, X. Gong, P. Kanjanaboos, A. F. Nogueira, E. H. Sargent, *ACS Appl. Mater. Interfaces* **2015**, *7*, 25007.

[107] J. De Roo, M. Ibáñez, P. Geiregat, G. Nedelcu, W. Walravens, J. Maes, J. C. Martins, I. Van Driessche, M. V. Kovalenko, Z. Hens, *ACS Nano* **2016**, *10*, 2071.

[108] G. Almeida, L. Goldoni, Q. Akkerman, Z. Dang, A. H. Khan, S. Marras, I. Moreels, L. Manna, *ACS Nano* **2018**, *12*, 1704.

[109] J. Cho, H. Jin, D. G. Sellers, D. F. Watson, D. H. Son, S. Banerjee, *J. Mater. Chem. C* **2017**, *5*, 8810.

[110] F. Di Stasio, S. Christodoulou, N. Huo, G. Konstantatos, *Chem. Mater.* **2017**, *29*, 7663.

[111] J. Shamsi, Z. Dang, P. Bianchini, C. Canale, F. Di Stasio, R. Brescia, M. Prato, L. Manna, *J. Am. Chem. Soc.* **2016**, *138*, 7240.

[112] L. Wu, Q. Zhong, D. Yang, M. Chen, H. Hu, Q. Pan, H. Liu, M. Cao, Y. Xu, B. Sun, Q. Zhang, *Langmuir* **2017**, *33*, 12689.

[113] F. Krieg, S. T. Ochsenbein, S. Yakunin, S. ten Brinck, P. Aellen, A. Süess, B. Clerc, D. Guggisberg, O. Nazarenko, Y. Shynkarenko, S. Kumar, C.-J. Shih, I. Infante, M. V. Kovalenko, *ACS Energy Lett.* **2018**, *3*, 641.

[114] J. Cho, S. Banerjee, *Chem. Mater.* **2018**, *30*, 6144.

[115] F. Zhu, L. Men, Y. Guo, Q. Zhu, U. Bhattacharjee, P. M. Goodwin, J. W. Petrich, E. A. Smith, J. Vela, *ACS Nano* **2015**, *9*, 2948.

[116] M. Aamir, M. D. Khan, M. Sher, M. A. Malik, J. Akhtar, N. Revaprasadu, *ChemistrySelect* **2017**, *2*, 5595.

[117] M. V Kovalenko, L. Protesescu, M. I. Bodnarchuk, *Science.* **2017**, *750*, 745.

[118] T. Chiba, K. Hoshi, Y.-J. Pu, Y. Takeda, Y. Hayashi, S. Ohisa, S. Kawata, J. Kido, *ACS Appl. Mater. Interfaces* **2017**, *9*, 18054.

[119] J. Li, L. Xu, T. Wang, J. Song, J. Chen, J. Xue, Y. Dong, B. Cai, Q. Shan, B. Han, H. Zeng, *Adv. Mater.* **2017**, *29*, 1603885.

[120] Q. A. Akkerman, V. D'Innocenzo, S. Accornero, A. Scarpellini, A. Petrozza, M. Prato, L. Manna, *J. Am. Chem. Soc.* **2015**, *137*, 10276.

[121] G. Nedelcu, L. Protesescu, S. Yakunin, M. I. Bodnarchuk, M. J. Grotevent, M. V. Kovalenko, *Nano Lett.* **2015**, *15*, 5635.

[122] D. Zhang, Y. Yang, Y. Bekenstein, Y. Yu, N. A. Gibson, A. B. Wong, S. W. Eaton, N. Kornienko, Q. Kong, M. Lai, A. P. Alivisatos, S. R. Leone, P. Yang, *J. Am. Chem. Soc.* **2016**, *138*, 7236.

[123] W. van der Stam, J. J. Geuchies, T. Altantzis, K. H. W. Van Den Bos, J. D. Meeldijk, S. Van Aert, S. Bals, D. Vanmaekelbergh, C. De Mello Donega, *J. Am. Chem. Soc.* **2017**, *139*, 4087.

[124] N. Mondal, A. De, A. Samanta, *ACS Energy Lett.* **2019**, *4*, 32.

[125] G. Rainò, M. A. Becker, M. I. Bodnarchuk, R. F. Mahrt, M. V. Kovalenko, T. Stöferle, *Nature* **2018**, *1804*, 01873.

[126] J. S. Van Der Burgt, J. J. Geuchies, B. Van Der Meer, H. Vanrompay, D. Zanaga, Y. Zhang, W. Albrecht, A. V. Petukhov, L. Filion, S. Bals, I. Swart, D. Vanmaekelbergh, *J. Phys. Chem. C* **2018**, *122*, 15706.

[127] K. H. Wang, J. N. Yang, Q. K. Ni, H. Bin Yao, S. H. Yu, *Langmuir* **2018**, *34*, 595.

[128] S. K. Mehetor, H. Ghosh, N. Pradhan, *J. Phys. Chem. Lett.* **2019**, *10*, 1300.

[129] S. K. Mehetor, H. Ghosh, N. Pradhan, *ACS Energy Lett.* **2019**, *4*, 1437.

[130] Y. Liu, M. Siron, D. Lu, J. Yang, R. dos Reis, F. Cui, M. Gao, M. Lai, J. Lin, Q. Kong, T. Lei, J. Kang, J. Jin, J. Ciston, P. Yang, *J. Am. Chem. Soc.* **2019**, 33, 13028.

Chapter 2. Experimental Methods

2.1 Synopsis

This chapter describes the synthesis and purification of NCs, their characterization, as well as the optical and surface chemistry data processing approaches. All the precursors, solvents, anti-solvents, ligands and other materials are listed in Section 2.2. The syntheses of the $CsPbX_3$ NCs and SCs are introduced in Section 2.3. The syntheses follow a conventional ligand-assisted hot-injection route, which involves heating of Cs and PbX_2 precursor solutions separately, and then injecting the Cs precursor into the PbX_2 solution. The purification process of the as-synthesised NCs is included in Section 2.4. The PNCs in the as-synthesised crude solution are precipitated via the addition of a polar anti-solvent, separated through centrifugation, and redispersed in a nonpolar solvent. The preparation of the super-crystals and poly (methyl methacrylate) composites are introduced in Section 2.5.

All the characterizations techniques are listed in Section 2.6. UV-Vis and PL measurements are used to characterize the optical behaviour of the NCs and to obtain their photoluminescence quantum yield (PLQY). X-ray diffraction (XRD) determines their exact crystal phase, and the phase stability upon storage. Transmission electron microscopy (TEM) was used to observe their microstructure. Specifically, in TEM, selected area diffraction (SAD) and energy dispersive x-ray (EDX) techniques were applied to further characterize the NCs' phase and elemental distribution, respectively. Nuclear magnetic resonance (NMR) and inductively coupled plasma mass spectrometry (ICP- MS) were utilized to quantitatively study the surface chemistry and the ligand binding conditions. Dynamic light scattering (DLS) was used to approximate the size of the PNCs within the dispersion. The data processing methods are in Section 2.7, including the calculation of the PLQY, the PNCs concentration, the surface ion percentage, the diffusion coefficient and the surface ligand density.

2.2 Materials

Caesium carbonate (Cs_2CO_3, 99.995 % trace metal basis), dodecane (99 %, anhydrous), lead (II) chloride ($PbCl_2$, 99.999 % trace metals basis), lead(II) bromide ($PbBr_2$, 99.999 % trace metals basis), lead(II) iodide (PbI_2, 99.999 % trace metal basis), dodecane (anhydrous, ≥99 %), 1-octadecene (ODE, 90 %, technical grade), oleylamine (OLA, 70 %, technical grade), octylamine (OCA, 99 %), dodecylamine (DOA, 99 %), hexadecylamine (HDA, 98 %), octadecylamine (OCDA, 97 %), oleic acid (OA, 90 %, technical grade), tert-butanol (99.5 %, anhydrous), hydrochloric acid (HCl, ACS reagent, 37 wt. % in water), hydroiodic acid (HI, 57 wt. % in H_2O, distilled, stabilized, 99.95 %), tert-butanol (anhydrous, ≥99.5 %), polymethyl methacrylate (PMMA, MW~350000), diisooctylphosphinic acid (DPA, 90 %, technical grade), iodine (I_2, ACS reagent, ≥99.8 %), toluene (99.5 %, analytical reagent), Cs and Pb standard solution for ICP (1000 mg/L in 2 wt. % nitric acid), 2-hexyl-1-decanol (≥97 %), 2-decyl-1-tetradecanol (≥97 %), tetrabutylammonium bromide (ACS reagent, ≥98 %), $KMnO_4$ (ACS reagent, ≥99 %), dichloromethane (anhydrous, ≥99.8 %), Sodium sulphite (≥98 %), were purchased from Sigma-Aldrich. Bis(2,4,4-trimethylpentyl) phosphinic acid (TMPPA, 85 %) was purchased from Cytec. Hexane (99.5 % analytical reagent), hydrobromic acid (HBr, 48 wt. % in H_2O, ⩾ 99.99%), acetic acid (ACS reagent, ≥99.7 %), ethyl acetate (anhydrous, ≥99.8 %) and isopropanol (IPA, 99.5 %, analytical reagent) were purchased from Merck. Ethanol (absolute, analytical reagent) was purchased from Ajax Finechem. All reagents were used without further purification.

2.3 Synthesis of Materials

2.3.1 Synthesis of Cs Precursor

Synthesis of all precursor solutions and particles were carried out under standard Schlenk line conditions (**Figure 2-1**). For the Cs precursor solution, Cs_2CO_3 (0.1 g, 307 μmol) was suspended in a solution of ODE (5 ml) and 0.5 ml of either OA, TMPPA or DPA in a 50 mL three-neck flask, and heated to 120 °C under vacuum (~1 mbar) with stirring. The reaction solution was degassed for 1 h at the target temperature. The suspension was then heated to 100–180 °C under a N_2 atmosphere, with the temperature then maintained until all the Cs_2CO_3 had fully dissolved. The solution was then kept at 100 °C before use.

Figure 2-1. Schlenk line used in typical Cs-precursor and $CsPbX_3$ synthesis.

2.3.2 Synthesis of $CsPbX_3$ NCs

The synthesis of $CsPbX_3$ PNCs via hot injection is the main topic of Chapter 3. A schematic illustration of such a synthesis is shown in **Figure 2-2**. These reactions were carried out under standard Schlenk line conditions using N_2. In a typical reaction, PbX_2 (188 μmol, 50mg, 70mg, 87mg for $PbCl_2$, $PbBr_2$ and PbI_2, respectively) was suspended in a solution of ODE (5 ml), 0.5ml of either

OA, TMPPA or DPA, and 0.5ml of either OLA, OCA, DOA, HDA or OCDA in a 100 mL 3-neck flask, and heated to 120 °C under vacuum (~ 1 mbar) with stirring, with the temperature maintained for 1 h. For the dissolution of $PbCl_2$, the volume of both the acid and amine was doubled to 1 ml. After dissolution of PbX_2, the temperature of the reaction solution was adjusted to a target temperature within the 100–180 °C range. Then, 0.4 mL of the preheated Cs precursor solution was injected into the reaction solution, and after 5 s the flask was submerged in a water bath to quench the reaction.

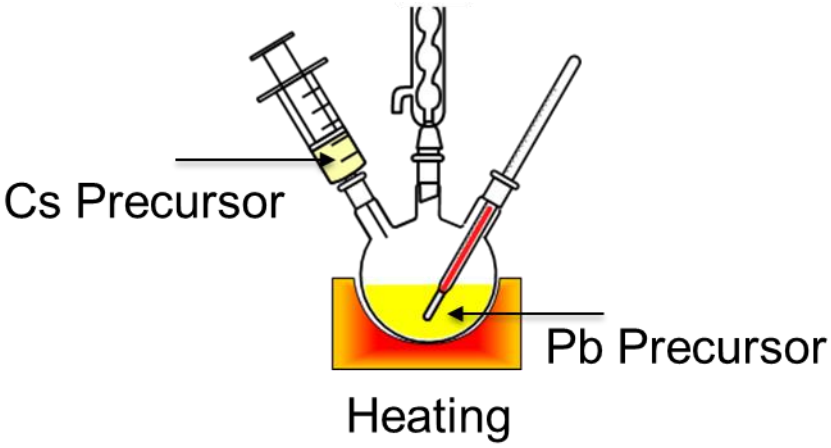

Figure 2-2. Schematic illustration for the hot injection synthesis.

2.3.3 Preparation of Mixed Halide $CsPbX_3$ PNCs Dispersion

The mixed halide $CsPbX_3$ PNCs dispersion could be readily prepared via simply mixing the pristine $CsPbCl_3$, $CsPbBr_3$, $CsPbI_3$ dispersion. Notice that such mixing could only happen between the $CsPbCl_3$ and $CsPbBr_3$, or $CsPbBr_3$ and $CsPbI_3$. By adjusting the Cl: Br or Br: I molar ratio, mixed halide $CsPbX_3$ with any desired halide ratio could be achieved.

2.3.4 Synthesis of Branched Carboxylic Acid

Branched carboxylic acids were used in Chapter 3 to explore the stabilization mechanism of the α-$CsPbI_3$. Two acids, 2-hexyldecanoic acid (HLA, 16 carbons) and 2-decyltetradecaonic acid (DTA, 24 carbons) were prepared.

To synthesise 2-hexyldecanoic acid, 2-hexyl-1-decanol (3.63 g), tetrabutylammonium bromide (2.62 g) and $KMnO_4$ (7.38 g) were added to a solution of dichloromethane (180 ml), water (60 ml) and acetic acid (23 ml). The solution was stirred vigorously and heated to reflux for 24 hours. The solution was then cooled to room temperature and neutralised with HCl in water (180 ml). Na_2SO_3 (8.34 g) was then added slowly to dissolve the MnO_2 precipitate. This solution was left to stand for 24 hours, resulting in the formation of a white precipitate. A sufficient volume of water was added to redissolve this precipitate, and the yellow dichloromethane phase containing the product was separated from the green aqueous phase. The dichloromethane phase was washed five times with water (100 ml) to remove any reactants and the acetic acid. The solvent was then removed under vacuum, yielding a viscous orange liquid. The product was recrystallised from ethyl acetate in the freezer, and then isolated as the pure product before melting at room temperature.

Synthesis of 2-decyltetradecanoic acid followed the same procedure but used 2-decyl-1-tetradecanol (5.31 g) as the starting material.

2.3.5 Synthesis of Hexadecylammonium Iodide (RNH_3I).

This salt was synthesised as an additive for the $CsPbI_3$ PNCs purification process, which is the main topic of Chapter 4. Due to the low purity of OLA (70 %), HDA was selected to synthesise the ammonium iodide salt. 0.5 ml, 3.8 mmol of 57 % aqueous HI was added to a solution of HDA (915 mg, 3.8 mmol) in ethanol (5 mL). The resulting mixture was stirred at room temperature for 1 h. The

solvent was then dried under high vacuum. The white powder product was then washed with hexane and dried and stored in a desiccator.

2.3.6 Preparation of RNH_3I solution.

The previously synthesised RNH_3I salt was prepared in a solution with the help of ligands. 137.5 mg of hexadecylammonium iodide is dissolved in a solution of 0.5 ml DPA and 0.45 ml OLA at 120 °C with stirring to achieve an iodide: acid: amine ratio of 1:5:5. After full dissolution of the RNH_3I, the solution was transferred to a glass vial and diluted with toluene (1 ml) to reduce the viscosity. The concentration of the RNH_3I solution was 0.216 mol/L.

2.3.7 Preparation of PbX_2 solution

The PbX_2 salts were dissolved with the help of ligands to prepare additive solutions for $CsPbX_3$ PNC purification. Under Schlenk line conditions, PbX_2 (1.08 mmol, 380 mg, 500 mg for $PbBr_2$ and PbI_2 or 0.54 mmol, 135 mg) was suspended in a solution of DPA (3 ml) and OLA (3 ml) in a 50 mL three-neck flask, and heated to 120 ˚C under vacuum with stirring. The temperature was maintained for 1 h. After full dissolution of the PbI_2, the solution was transferred to a glass vial and diluted with toluene (4 ml) to reduce the viscosity. The concentration of the $PbBr_2$ and PbI_2 solutions were both 0.108 mol/L, while for the $PbCl_2$ solution it was 0.54 mol/L.

2.3.8 Synthesis of $CsPbX_3$ Super-Crystals

The synthesis of $CsPbX_3$ SCs is the main topic of Chapter 5. Under standard Schlenk line conditions, PbX_2 (188 μmol, 50 mg, 70 mg, 87 mg for $PbCl_2$, $PbBr_2$ and PbI_2, respectively) was suspended in a solution of dodecane (5 ml), TMPPA (1 ml), HDA (760 mg) and HX (366 μmol, 28 μl, 34 μl, 40 μl for HCl, HBr, HI, respectively) in a 50 mL three-neck flask, and placed under vacuum with stirring for 1 h. The temperature was then raised to 140 °C under N_2. After the PbX_2 was dissolved, 1.6 mL

of the preheated Cs precursor solution was injected into the reaction solution, and after 5 s the flask was submerged in a water bath to quench the reaction.

2.4 Purification of $CsPbX_3$ PNCs

2.4.1 Washing without any additives

A schematic illustration of the PNC washing process is shown in **Figure 2-3**. The crude $CsPbI_3$ PNC solution in ODE was mixed with the anti-solvent IPA in a 1:3 (v/v) ODE:IPA ratio. The mixture was then centrifuged for 5 min at 10000 rpm in a Beckman Coulter Allegra™ X-22R Centrifuge (**Figure 2-4**). The clear supernatant was discarded and the $CsPbI_3$ precipitate was redispersed in toluene. The redispersed NC solution was reprecipitated using the same 1:3 (v/v) solvent : anti-solvent ratio with the same centrifugation conditions. One, two or three wash cycles were performed.

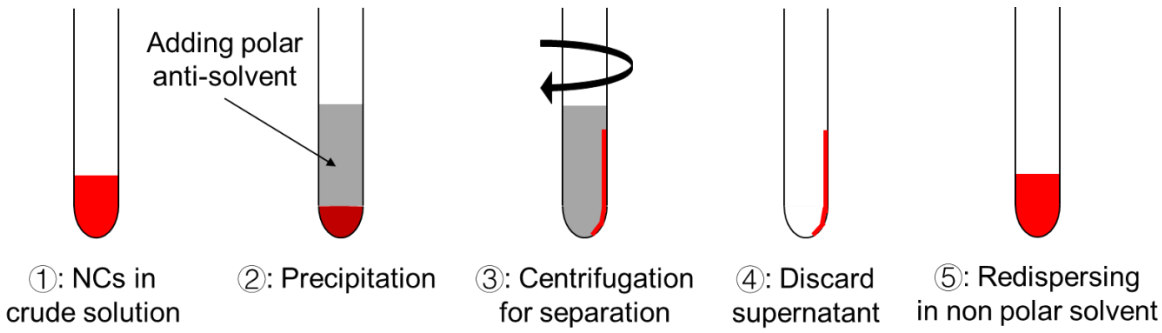

Figure 2-3. Schematic illustration for the washing process.

Figure 2-4. Photo of the Allegra^{TM} X-22R Centrifuge.

2.4.2 Washing with ligand additives

The washing procedure was the same as above, except additional ligand (DPA and/or OLA) was added before adding the anti-solvent. Generally, 50 µl of either DPA or OLA, or 50 µl DPA+ 50 µL OLA were added to 1 ml of the crude $CsPbI_3$ solution, thus the amount of ligand added was in a 1:2 molar ratio against what was in the crude solution. As above, one, two or three wash cycles were performed.

2.4.3 Washing with RNH_3I

The hexadecylammonium iodide (137.5 mg) was first dissolved in 2 ml of toluene. 120 µl of this salt solution was then added to 1 ml of the crude $CsPbI_3$ solution before adding the anti-solvent, thus the additional iodide was in a 1:2 molar ratio against what was in the crude solution. As above, one, two or three wash cycles were performed.

2.4.4 Washing with RNH_3I solution

The hexadecylammonium iodide solution in DPA/OLA/toluene was transparent at room temperature, indicating it did not require heating prior to addition. 120 µl of the RNH_3I solution was added to 1 ml

of the crude $CsPbI_3$ solution before adding anti-solvent. As above, either 1, 2, or 3 wash cycles were performed.

2.4.5 Washing with PbI_2 solution.

The solution of PbI_2 in DPA/OLA/toluene was transparent at room temperature, indicating it did not require heating prior to addition to the NC solution. Various volumes of the PbI_2 solution were added to 1 ml of the crude $CsPbI_3$ solution before adding the anti-solvent. As above, one, two or three wash cycles were performed. It was found that 120 µl of PbI_2 solution was the lowest amount required to be added to 1 ml of the $CsPbI_3$ solution to maintain the PLQY and phase stability after 3 wash cycles.

2.4.6 Washing of the Super-crystals

Due to the much larger nature of the SCs, these could be readily washed without any anti-solvent. The crude solution of the SCs (5 ml) was transferred to the centrifugal tube and centrifuged for 5 mins at 10000 rpm. The colourless supernatant was discarded and the SCs were then re-dispersed in hexane (5 ml).

2.5 Preparation of SC-PMMA composite

PMMA beads were suspended in toluene (200 mg/ml) and stirred overnight for full dissolution. 100 µl of the washed SCs solution was then mixed with 2 ml of the PMMA solution, and then transferred to a Teflon mould. The Teflon mould was then placed in a desiccator with a low vacuum (~50 mbar) applied to remove the solvent over 12 hours. The SC-PMMA composites were then lifted up from the mould and stored in ambient condition. Photo of a typical SC-PMMA composite was shown in **Figure 2-5**.

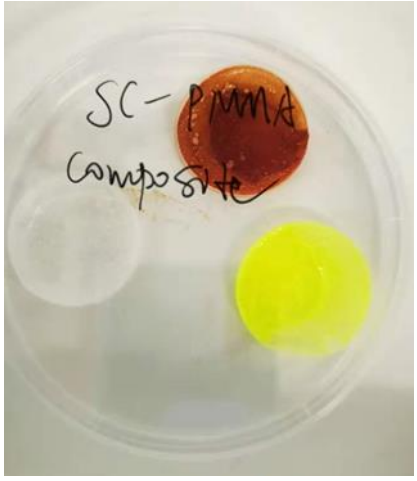

Figure 2-5. Photo of the SC-PMMA composite material. The white, yellow and brown disks consist of the $CsPbCl_3$, $CsPbBr_3$ and $CsPbI_3$ SCs-PMMA composites, respectively.

2.6 Characterization

2.6.1 UV-vis Spectroscopy

UV-vis absorbance spectra were collected using a Perkin Elmer Lambda 950 UV-Vis-NIR spectrometer (**Figure 2-6**). The absorption was measured across 300 nm to 800 nm region, with the data interval set as 1 nm and the slit width fixed at 2nm. For solution samples, 10 µl of either the NC or SC solution was diluted in 3 ml of hexane in a 1 cm pathlength quartz cuvette. For film samples, 50 µl NCs or SCs washed solution was first drop cast on thin glass slides and dried under ambient conditions to make a ~100nm thick film.

Figure 2-6. Photo of the Perkin Elmer Lambda 950 UV-Vis-NIR spectrometer.

2.6.2 Photoluminescence (PL)

Photoluminescence spectra were collected using a Horiba Fluoromax-4 spectrofluorometer (**Figure 2-7**). The excitation wavelength was 360, 440, 520 nm for the $CsPbCl_3$, $CsPbBr_3$, $CsPbI_3$ samples, respectively. The excitation and emission slit widths were both 2 nm. The concentrations of the solutions or film preparation were the same as for the absorption measurement.

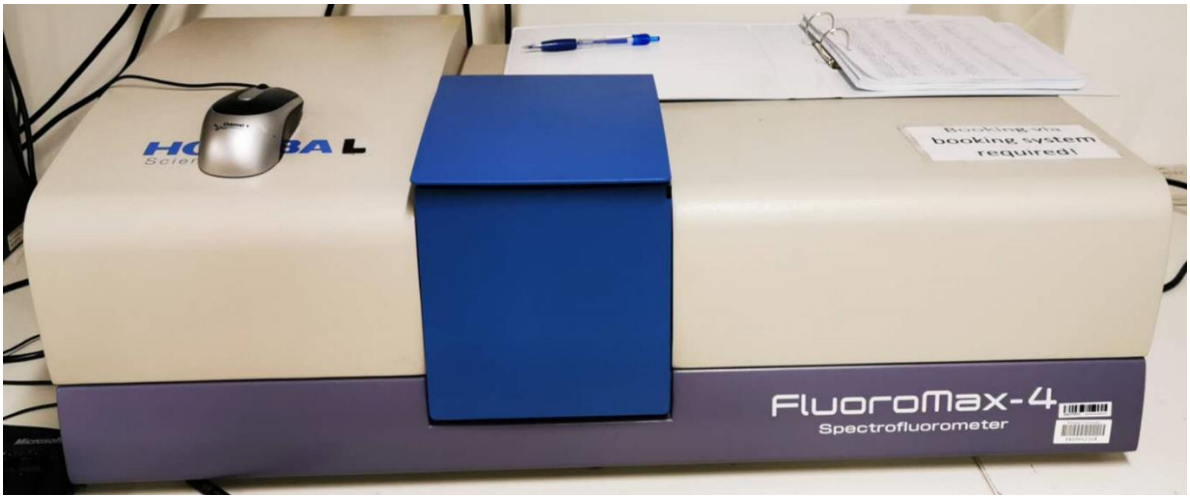

Figure 2-7. Photo of the Horiba Fluoromax-4 spectrofluorometer.

2.6.3 X-ray Diffraction (XRD)

XRD was used to characterize the phase of the PNCs. Samples were prepared for XRD measurements by depositing suspensions of $CsPbX_3$ in toluene on a glass substrate and heating the substrate at 80 °C to evaporate the toluene. XRD patterns were acquired on a Bruker D8 Advance diffractometer (**Figure 2-8**) using a Cu source (Kα = 1.54 Å) at 40 kV, 40 mA, and a LynxEye detector.

The in-situ heating XRD was also conducted on the same equipment, with an Anton Paar HTK1200N in-situ heating stage that can be heated up to 1200ºC in ambient atmosphere. Different from the normal XRD measurement, the $CsPbX_3$ sample was deposited on silicon wafer for the in-situ experiment.

Figure 2-8. Photo of the Bruker D8 Advance diffractometer.

2.6.4 Transmission Electron Microscopy (TEM)

TEM was used to characterize the nanostructure of the PNCs, their phases and their chemical composition. For sample preparation, 10µl of a $CsPbX_3$ PNC suspension following the washing as described in 2.4 was first diluted in 1 ml of toluene to give a PNCs concentration of approximately

1×10^{-8} mol/L, then an ultrathin carbon TEM grid (Ted Pella) was immersed into the diluted suspension. The solvent was subsequently evaporated under ambient conditions.

Standard TEM, high-resolution TEM (HR-TEM) and selected area diffraction measurements (SAD) of deposited PNCs were obtained on the FEI Tecnai G2 T20 transmission electron microscope (**Figure 2-9** a) equipped with a LaB_6 electron source operated at 200 kV. Images were acquired by an Orius SCD200D wide-angle CCD camera. Meanwhile, scanning TEM (STEM) and energy dispersive X-ray (EDX) mapping were obtained on a FEI Tecnai G2 F20 S-Twin transmission electron microscope (**Figure 2-9** b) equipped with a field emission gun electron source operated at 200 kV. STEM images were obtained on a Gatan Ultrascan 1000 high-resolution CCD camera. EDX was obtained by the Bruker X-Flash X-ray detector with an energy resolution of 123 eV. Finally, in-situ heating TEM was conducted on a Gatan hot stage holder on the JOEL 2100F transmission electron microscope (**Figure 2-9** c) equipped with field emission electron source operated at 200 kV. The hot stage could be heated to 300 °C.

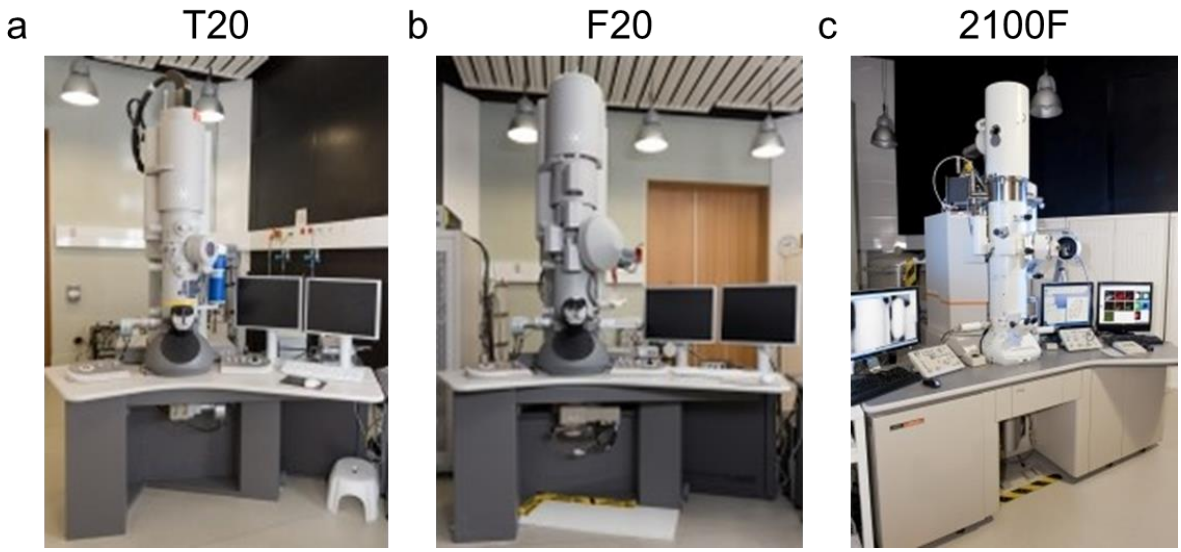

Figure 2-9. Photos of the (a) FEI Tecnai G2 T20, (b) FEI Tecnai G2 F20, (c) JOEL 2100F Transmission Electron Microscope.

2.6.5 Time-Resolved Photoluminescence (TRPL)

The TRPL measurement was used to characterize the PL lifetime of the PNCs. TRPL curves were recorded using a bespoke Time-Correlated Single Photon Counting (TCSPC) system. Samples were photoexcited by a picosecond Fianium laser passed through a 425 nm bandpass filter with a 1 MHz frequency and power of ca. 152 μW. The emitted PL was spectrally dispersed with a monochromater for each PL signal, and was collected by a fast photon multiplier tube detector (PMA 182, PicoQuant GmbH). The resulting instrumental response function was about 60 ps in full-width-half-maximum, and all of the signals were measured at the emission peak of the perovskite (670 nm for $CsPbI_3$).

2.6.6 Nuclear Magnetic Resonance Spectroscopy (NMR)

NMR was used to probe the surface chemistry of the PNCs. ^{1}H, ^{13}C, and ^{31}P NMR measurements were performed on a Bruker Bio Spin Av400H with a 9.4 T magnet and a 5 mm inverse 1H-X BBI autotuning broadband probe at a 1H frequency of 400.13 MHz. All samples were measured in d_8-toluene. Diffusion-ordered spectroscopy (DOSY) are used to obtain the diffusion coefficients of the characteristic signal of a specie (e.g. the alkene group for the OLA). The diffusion coefficient reveals the mobility of the specie within the dispersion, and could be used to quantitatively determine the binding affinity of the ligands, as tightly binging ligands give low diffusion coefficient.

2.6.7 Inductively Coupled Plasma Mass Spectrometry (ICP-MS)

ICP-MS was used to quantitatively determine the molar concentration of the elements in the $CsPbX_3$ PNC dispersions. These experiments were conducted by operating staff at the CSIRO-Clayton ICP facility. For the $CsPbI_3$ PNCs dispersed in toluene, ~0.08 g of solution was accurately weighed to 4 decimal places for solution preparation. The 0.08 g $CsPbI_3$ dispersed in toluene was then diluted by 78 g of acetonitrile. Rh and In were added as internal standards. Standards for Cs in acetonitrile were prepared by weight dilution from aqueous 1000 ppm purchased standards. Analysis was performed

with acetonitrile matched calibration standards using the analytical balance, and an Agilent 7700 ICP-MS in organic mode.

2.6.8 Dynamic Light Scattering (DLS)

DLS was used to probe the size of the PNCs within the dispersion. These experiments were performed with a Brookhaven NanoBrook Omni analyser with a 640 nm diode laser at an angle of 90 °. Toluene for dilution were filtered in 0.45 µm polytetrafluoroethylene (PTFE) prior to use with samples measured in round glass cuvettes with a path length of 1cm. The PNCs was diluted to the same level as the UV-Vis and PL measurement, with the final concentration being about 1×10^{-8} mol/L. For some measurement, the sample was sonicated for 1 h before measurement, as will be specifically indicated in Chapter 5.

2.7 Data processing

2.7.1 Photoluminescence Quantum Yield (PLQY) Measurement

The PLQY of the PNCs in solution was measured using a Rhodamine 101 dye (QY=96% at an excitation wavelength of 510 nm) as the reference.[1] Using such a reference, the QY of the PNCs can be determined through:

$$QY = QY_{REF}\frac{\eta^2 I A_{REF}}{\eta_{REF}{}^2 I_{REF} A}$$

Where η is the refractive index of the solvent, I is the integrated PL intensity, A is the absorbance at the excitation wavelength, and the terms with an associated underscored "ref" are the corresponding values for the reference sample. The η values at room temperature for the frequently used solvent in this thesis are: $\eta_{toluene}$=1.497, $\eta_{ethanol}$=1.361.[2]

2.7.2 Determination of [NC] for $CsPbX_3$ PNCs

To calculate the molar concentration of the NCs, one has to determine the concentration of total precursor in a solution and divide this value by the amount of precursor per average particle. This can be done using any element within the PNCs, provided that it can be qaunatitatively measured. Herein Cs was selected, as [Cs] could be reliably measured by ICP-MS.

The number of Cs atoms in a single NC was estimated based on the edge length (d, nm) of the PNCs acuquired from TEM mearument the and the interplanar distance of the (100) plane of the $CsPbX_3$ (**Figure 2-10**). Taking $CsPbI_3$ as an example, the (100) plane spacing is 0.62 nm, thus the number of Cs atoms in a single edge was calculated by:

$$Cs\ per\ edge = d/0.62$$

Considering the NC to be a perfect cube, the total number of Cs atoms (n_{cs}) in one cube is therefore:

$$n_{cs} = (\frac{d}{0.62})^3$$

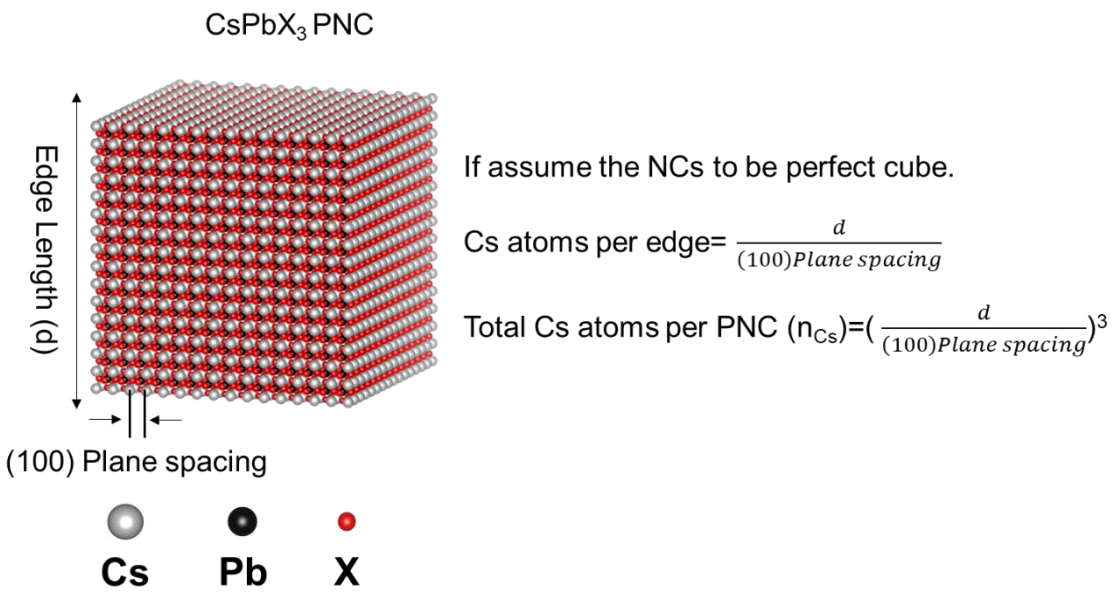

Figure 2-10. Schematic illustration for the calculation of Cs atoms per PNC.

With the n_{Cs} estimated, the [NC] can be approximated using:

$$[NC] = \frac{[Cs]}{n_{Cs}}$$

2.7.3 Determination of Extinction Coefficient

The aboved determined [NC] was then used to determine their wavelength-dependent molar extincition coefficient through the Beer-Lambert equation :

$$A = \varepsilon[NC]L$$

Where A is the absorption acquired from the UV-Vis measurment, ε (M^{-1} cm^{-1}) is the extinction coefficient to be determined, and L is the length of the cuvette (1 cm).

The ε was also converted to the the absorption coefficient α (cm^{-1}) based on the equation: [3]

$$\alpha = \frac{\varepsilon \times 1000 \times \ln(10)}{N_A \times V_{NC}}$$

where N_A is Avogadro's number and V_{NC} is the volume of the NC, which is estimated by:

$$V_{NC} = d^3$$

2.7.4 Determination of [Surface ions]

The molarity of the surface ions [Surface ions] was further estimated by the number of surface Cs ions, which is calculated from the relative percentage of these ions versus the bulk. Again, taking $CsPbI_3$ at the example, the (100) plane spacing is 0.62 nm, so the number of ions per one facet was given by:

$$Cs\ per\ facet = (\frac{d}{0.62})^2$$

When calculating the total number of surface Cs ions, the number of Cs per facet was multiplied by 6, then minus the atoms on the 12 edges that has been counted twice

$$Surface\ Cs\ per\ PNC = 6 \times (\frac{d}{0.62})^2 - 12 \times \frac{d}{0.62}$$

Then the percentage of the surface ions versus the bulk was given by:

$$\frac{Surface\ ions}{Total\ ions} = \frac{6 \times (\frac{d}{0.62})^2 - 12 \times \frac{d}{0.62}}{(\frac{d}{0.62})^3}$$

If d was 10 nm, which was common for the $CsPbX_3$ PNCs, calculation gave the surface ions percentrage to be about 30 %.

So the [Surface ions] was given by:

$$[Surface\ ions] = [Cs] \times 30\%$$

2.7.5 Estimation of Diffusion Coefficient

The diffusion coefficient D for a tightly bound oleylamine/ ammonium species was estimated via the Stokes-Einstein equation:[4],[5]

$$D = \frac{k_b T}{6\pi\eta C}$$

Where k_b is the Boltzmann constant (1.38064852 × 10-23 m^2 kg s^{-2} K^{-1}), T is the temperature (room temperature 298K), η is the viscosity for the solvent, which is 0.65 mm^2 s^{-1} for toluene at 298 K, and C=0.66d is the capacity of cube shaped objects,[6] with d being the edge length of the cube.

2.7.6 Ligand density Calculation

The ligand density of cubic $CsPbI_3$ NCs was calculated by combining the UV-vis, ICP, TEM and NMR measurements. The calculation is given below:

The [NC] was determined as per section 2.6.2.

The total surface area [S] for a given [NC] could then be determined by:

$$[S] = 6 \times d^2 \times [NC]$$

This equation simply considers that there are six equivalent faces in a cubic nanocrystal.

The molar concentration of the alkene resonance of the OLA species, e.g. the [ligand] was acquired from NMR measurements by using the Electronic reference to access in vivo concentrations (ERETIC) method, provided in the Bruker Topspin software.

Noting that ligands are in dynamic exchange at the surface, the exact value of binding ligand density could not be obtained, but the maximum ligand surface density (ρ) could be determined as:

$$\rho = \frac{[\text{ligand}]}{[\text{S}]}$$

References

[1] R. F. Kubin, A. N. Fletcher, *J. Lumin.* **1982**, *27*, 455.

[2] D. R. Huanca, W. J. Salcedo, *ECS Trans.* **2009**, *23*, 499.

[3] J. Jasieniak, L. Smith, J. Van Embden, P. Mulvaney, M. Califano, *J. Phys. Chem. C* **2009**, *113*, 19468.

[4] J. De Roo, M. Ibáñez, P. Geiregat, G. Nedelcu, W. Walravens, J. Maes, J. C. Martins, I. Van Driessche, M. V. Kovalenko, Z. Hens, *ACS Nano* **2016**, *10*, 2071.

[5] J. T. Edward, *J. Chem. Educ.* **1970**, *47*, 261.

[6] B. Hubbard, J. F. Douglas, *Phys. Rev. E* **1993**, *47*, 2983.

Chapter 3. Synthesis of $CsPbX_3$ PNCs

3.1 Declaration

Results presented in Section 3.4 of this Chapter have been published in *Chem. Commun.* **2017**, *53*, 232. DOI:10.1039/C6CC08282C. Figures of this article has been re-used, and the content of this article has been re-written to fit in the narration of this Chapter. The copy of the article has been attached in Appendix.

3.2 Introduction

All-inorganic $CsPbX_3$ PNCs possess many advanced optoelectronic properties, and are promising candidates for LED,[1] lasers,[2] and photodetectors applications.[3] However, the $CsPbI_3$ perovskite suffers from a phase instability problem, in which the functional α-cubic perovskite phase of $CsPbI_3$ (**Figure 3-1** a) is only stable at temperatures above 315 °C.[4] At room temperature, the metastable α-$CsPbI_3$ thermodynamically transforms into its stable, but non-functional, δ- orthorhombic phase (**Figure 3-1** b, also known as the "yellow phase" due to its colour),[5] causing difficulties in its study or use in any practical applications.

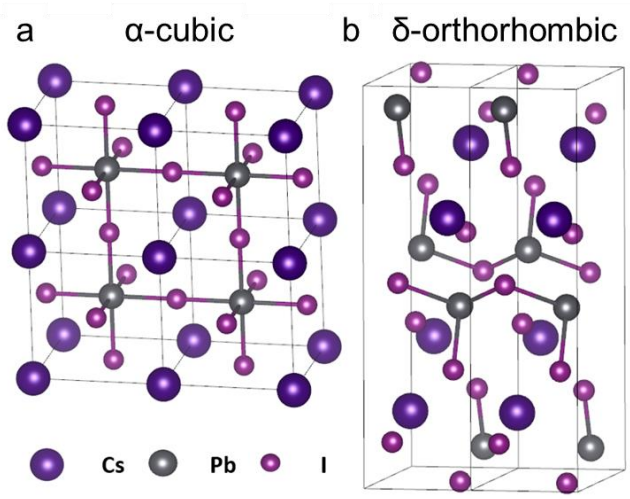

Figure 3-1. The schematic illustration of the (a) α-cubic and (b) δ- orthorhombic phases of the $CsPbI_3$.

To date, there are two strategies to stabilize the cubic phase of $CsPbI_3$:

(1). Partially substitute the A-site Cs^+ with a bigger cation (FA^+), the B-site Pb^{2+} with a smaller cation (Mn^{2+}, Sn^{2+}) , or the X site I^- with smaller Cl^- or Br^- anions,[6],[7],[8] all of which shift the tolerance factor towards 1 and thermodynamically stabilize the cubic $CsPbI_3$. However, this strategy intrinsically changes the band structure of the pristine $CsPbI_3$ and hence shifts its emission peak.

(2). Reduce the grain size of the $CsPbI_3$ to increase the lattice strain and surface energy, which effectively lowers the α-to-δ phase transformation temperature.[9],[10] It has been previously shown via computational study that when the grain size of the $CsPbI_3$ is smaller than ~100 nm, the δ phase becomes thermodynamically unfavourable at room temperature, and hence the functional phase can be stabilized.[11] For the PNCs, reducing grain size is especially applicable because NCs are already present in a nanocrystalline form with high surface energy, and all that remained is to manipulate the surface ligand chemistry to ensure robust ligand binding and prevent the NCs from coarsening. To date, α-$CsPbI_3$ PNCs could be stabilised through a careful purification process utilizing special anti-solvents that did not disturb the surface ligand chemistry,[12] or by capping the α-$CsPbI_3$ PNCs with special bidentate ligands[13] or trioctylphosphine.[14]

In this chapter, the α- to δ- phase transformation of $CsPbI_3$ PNCs is thoroughly studied, and a novel synthetic protocol that harnesses branched ligand chemistry to enable stabilized α-$CsPbI_3$ PNCs is presented. The stabilization mechanism is studied in detail and is found to be related to the modified surface chemistry arising from the use of these branched ligands. Finally, this synthetic protocol is generalized to also include $CsPbCl_3$ and $CsPbBr_3$ PNCs.

3.3 Phase Transformation of $CsPbI_3$

To preserve the cubic phase of $CsPbI_3$, its cubic to orthorhombic phase transformation process must be understood. To do so, $CsPbI_3$ PNCs synthesised according to the conventional hot-injection method developed by Protesescu et al. in 2015 has been used as a baseline.[4] This synthetic protocol,

which is described in detail in Chapter 2.3.1 to 2.3.2, uses OA and OLA as solubilising ligands within the reaction mixture. From here on, such conventionally synthesised $CsPbI_3$ PNCs will be termed as $CsPbI_3$-OA. The as-synthesised crude solution of $CsPbI_3$-OA displayed bright emission (**Figure 3-2** a). However, it exhibited poor room temperature α-phase stability - after storage under ambient condition for three days, it had completely transformed into the yellow non-functional δ-phase with no active PL (**Figure 3-2** b). To further elucidate this transformation process, XRD and TEM measurements were made.

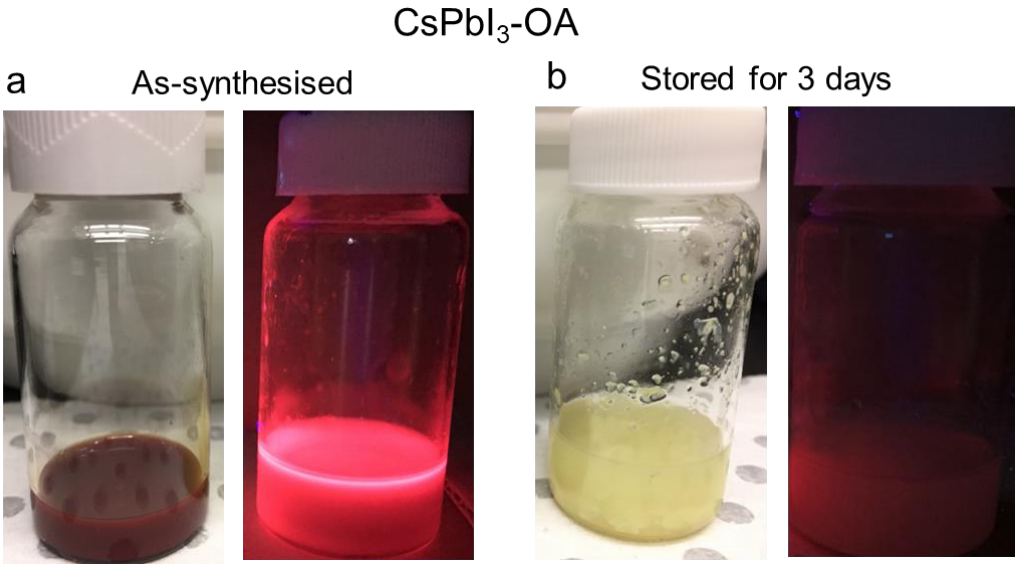

Figure 3-2. Photos under room light and UV-lamp for the $CsPbI_3$-OA crude solution that is (a) As-synthesised, (b) Stored in ambient condition for 3 days.

3.3.1 XRD

The phase transformation process of the $CsPbI_3$-OA was examined via ex-situ and in-situ XRD. As showed previously, under ambient condition, the α-$CsPbI_3$-OA spontaneously transformed into the δ-phase. To confirm this, the $CsPbI_3$-OA was deposited into film on glass substrate and stored under open air, with its phase examined by the ex-situ XRD (**Figure 3-3** a). In 3 days, the α-$CsPbI_3$ fully transformed to δ-phase. At day 2, the diffraction peaks for the α and δ phase were both present, with the α peaks being broad and the δ-peaks narrow. According to the Scherrer equation, the peak width

is inversely proportional to the grain size,[15] hence $CsPbI_3$ exhibited grain growth concurrent to the α-to-δ transformation process. Such a phenomenon is presumably because the coarsening of small cube NCs into the larger structures, which will be further confirmed via TEM study.

At higher temperatures (yet still below 315 °C), the diffusion of the atoms, and hence the coarsening and phase transformation process of the meta-stable α-$CsPbI_3$-OA should be accelerated. This was experimentally confirmed by in-situ heating XRD experiments (**Figure 3-3** b), which were conducted at ambient atmosphere on silicon wafer substrates. As the samples were prepared on silicon, additional diffraction peaks attributable to the silicon were present. To that end, only the (100) at 2θ = 14° and (200) at 2θ = 28° peaks were present due to the preferential orientation on the silicon substrate. When heated to 150 °C, it only took 10 minutes for the α-$CsPbI_3$-OA to almost completely transform into the δ phase, which is much faster than under ambient conditions. This confirms that the α- to δ- phase change of $CsPbI_3$ is indeed accelerated upon heating.

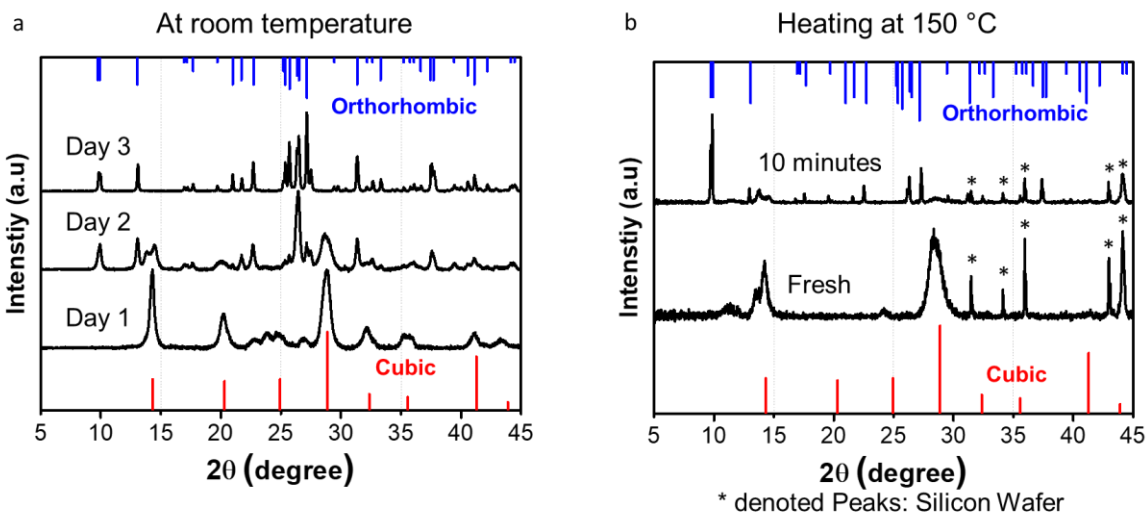

Figure 3-3. XRD patterns of the $CsPbI_3$ nanocrystals deposited as films and measured (a) at room temperature over 3 consecutive days and (b) following in-situ heating at 150°C for 10 minutes.

3.3.2 Ex-situ TEM

Ex-situ TEM was used to characterise the change of nanostructure during this phase transformation process. As shown in **Figure 3-4** a, the as-synthesised $CsPbI_3$-OA exhibited a monodisperse NCU microstructure. The α-phase was confirmed by HR-TEM, which showed an interplanar spacing of 0.62 nm, corresponding to the (100) plane of α-$CsPbI_3$. After storage in ambient condition for 3 days, the formation of δ-$CsPbI_3$ was observed (**Figure 3-4** b), as confirmed by the presence of an interplanar distance 0.91 nm, which corresponds to the (011) plane of the δ-phase.[5] These crystals no longer retained their NCU shape morphology, instead they transformed into rods and sheets that were µm in size. Notably, small NCUs of ~10 nm size, as well as NRs of ~20 nm in width and ~100 nm in length were also found among these samples. This is likely due to the presence of α-$CsPbI_3$ NCs that had not yet fully transformed, or were in a transition state during the α-to-δ transformation process. From these ex-situ TEM observations, it is reasonable to posit that the α-to-δ phase transformation involves NCs aggregating and then structurally re-arranging to form rod- and sheet-shaped crystals. Further in-situ heating TEM were carried out to probe the α-to-δ transformation process.

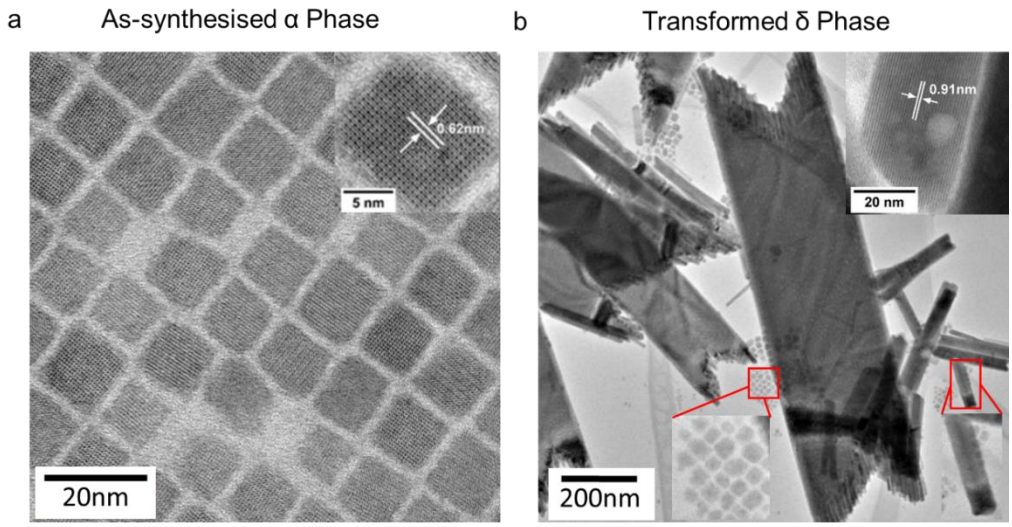

Figure 3-4. TEM images of $CsPbI_3$ NCs capped with OA and OLA ligands that are (a) as-synthesised, cubic phased and (b) after their orthorhombic phase transition following 3 days post-synthesis. Insets show high resolution TEM images of the NCs.

3.3.3 In-situ Heating TEM

To determine if the phase transformation process could be monitored directly, in-situ heating TEM experiments were conducted. This involved heating of α-$CsPbI_3$-OA at 150 °C within the TEM using an in-situ heating TEM sample stage. It took less than two minutes for the heating stage to reach 150 °C starting from room-temperature. Nonetheless, taking high quality TEM images in these in-situ experiments was extremely difficult because of electron beam damage. The high energy electrons tend to reduce the Pb^{2+} ions in the PNCs lattice back to Pb^0, hence cause the halide to evaporate away and the PNCs to degrade.[16] Worse still, the high temperature in these in-situ heating experiments greatly accelerated these processes and enhanced the beam damage. A representative example of the electron beam damage at 150 °C was displayed in **Figure 3-5**. At the beginning, the sample had a clean morphology (**Figure 3-5** a), although some Pb^0 black dots has already occurred during focusing. After being kept under electron beam for 10 seconds, the structure of the feature was severely damaged, with most of the substance being evaporated, leaving dark contrast Pb^0 particles.

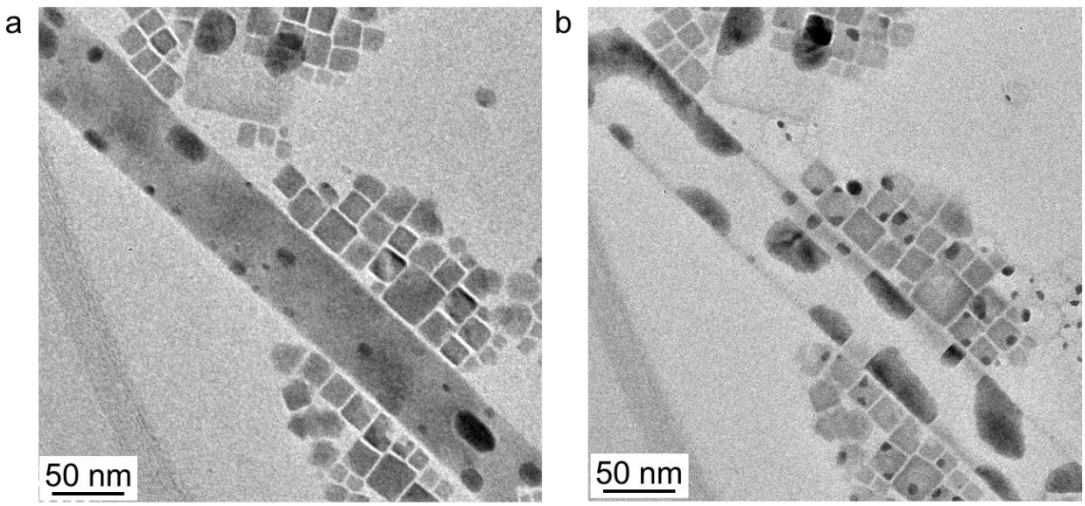

Figure 3-5. TEM images for $CsPbI_3$ NCs that have been (a) Just put under the electron beam and (b) Experienced severe electron beam damage after 10 seconds.

Under this circumstance, it is impossible to take the complete α -to- δ transition at a fixed position, as the features are destroyed easily by electron beam. Therefore, TEM images acquired at different

positions were combined together to show every representative stage of the α- to δ- phase transformation (**Figure 3-6)**. At the beginning, the PNCs were monodispersed NCU (**Figure 3-6** a), with the corresponding SADP pattern confirming the samples consisted of randomly oriented α-phase PNCs (**Figure 3-6** f). In early stage of the transformation, some of the NCU were observed to aggregate into elongated NW structures (**Figure 3-6** b). The SADP again indicated α-phase, although this time more preferential alignment was observed owing to the presence of the NWs (**Figure 3-6** g). The NWs continued to coarsen and reached lengths of several hundred nm (**Figure 3-6** c). At this stage, the SADP yielded clear scattering contributions from δ- $CsPbI_3$ in the sample (**Figure 3-6** h). Further elongation of these NW was observed concurrent with a removal of most NCU morphologies (**Figure 3-6** d). The SADP primarily displayed diffraction spots indexed to the δ-phase, indicating that the α-PNCs had transformed into δ-NWs at this stage (**Figure 3-6** i). Finally, only platelet structures on a µm scale were present (**Figure 3-6** e). The isolated spots in the SADP were indexed to the single-crystalline δ-phase (**Figure 3-6** j).

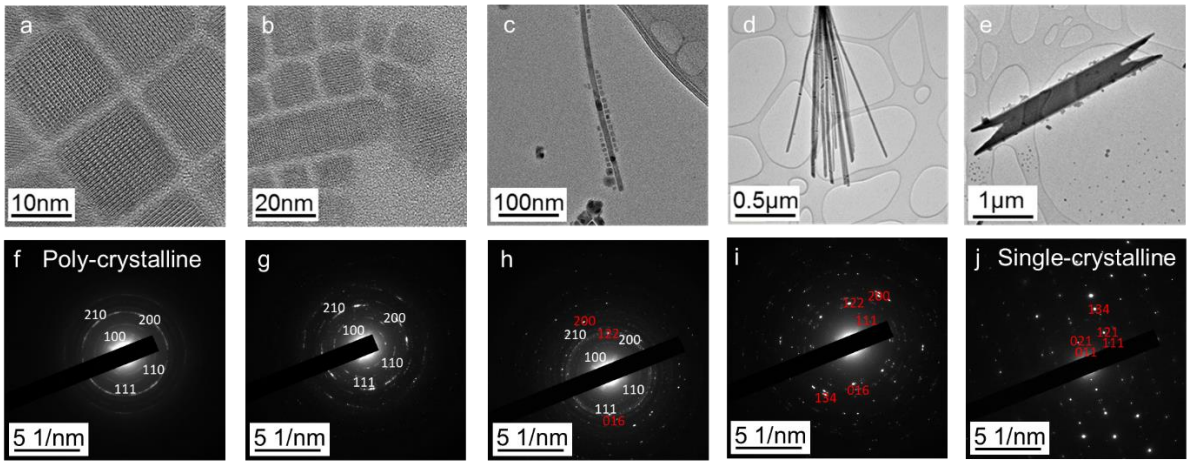

Figure 3-6. (a)- (e) In-situ TEM images and (f)-(j) the corresponding SADP for the $CsPbI_3$ NCs during the in-situ heating experiment and different stages of the α to δ phase. transformation. These images were taken of different areas on a single TEM grid to minimise any beam damage effects. The white and red label indicated the crystal planes of the α and δ phases, respectively.

Compared with the in-situ heating XRD measurement, which was conducted for only 10 minutes to yield complete phase transformation, it took almost 3 hours of in-situ heating in the TEM for the final platelet structure δ-phase to occur. This variation in time may arise from the intrinsic differences in thermal conductivity between ambient and vacuum environments, the presence of air in the XRD measurements, and/or the monolayer nature of nanocrystals used for TEM versus the thin film used for the XRD. Further elucidation of the exact origins remains as future work.

In conclusion, these observations suggest that the $CsPbI_3$ α- to δ- phase transformation occurs through a process that involves small NCs coarsening to form large NWs, NRs and NPLs structures. For grain size above 100 nm, the α-phase is no longer the stable phase,[11] rendering all these structures to be δ- phased materials. Therefore, it was postulated that key challenge to prevent the phase transformation of α-$CsPbI_3$ is to hinder NCs coarsening. To do so, developing a more robust ligand surface chemistry could be a feasible strategy.

3.4 Synthesis of Cubic Phase-stable $CsPbI_3$

3.4.1 Ligand Selection & Synthesis

The chemical and steric nature of ligands play a governing role in the synthesis of PNCs by controlling their nucleation and growth dynamics, passivating the nanocrystal surface and providing colloidal stability.[17] For the conventional OA and OLA ligand combination used in the PNCs, the OLA and its derivatives (oleylammonium halides and oleylammonium oleates) have been confirmed as the main surface binding species on the PNC surface. However, the level of co-passivation by OA remains under debate, while some researchers suggest that it directly binds to the PNCs, [18] others claim it is indirectly drawn into the ligand shell in form of the oleylammonium oleates species.[19] Despite this uncertainty, as has been previously shown in Section 3.3, the OA-OLA ligand combination fails to prevent the PNCs from coarsening, which induces the α-$CsPbI_3$ to undergo phase transformation. Further reports have suggested that removing excess OA and oleate-based precursors

from the α-$CsPbI_3$ solution can promote long-term stability of α-$CsPbI_3$.[12] Therefore, a synthesis that is free from OA in the first place could be conducive towards prolonging the α-phase stability of such materials.

To achieve this, bis-(2,2,4-trimethylpentyl) phosphinic acid (TMPPA, **Figure 3-7**) was selected as a direct OA replacement in the synthesis of $CsPbI_3$ NCs. TMPPA has been a widely used ligand in the conventional CdSe QDs synthesis owing to its strong chelating ability to metal ions.[20] The synthesis of $CsPbI_3$ followed the reaction protocols described in Chapter 2.3.1- 2.3.2. From here on, the TMPPA-synthesised PNCs will be termed as $CsPbI_3$-TMPPA.

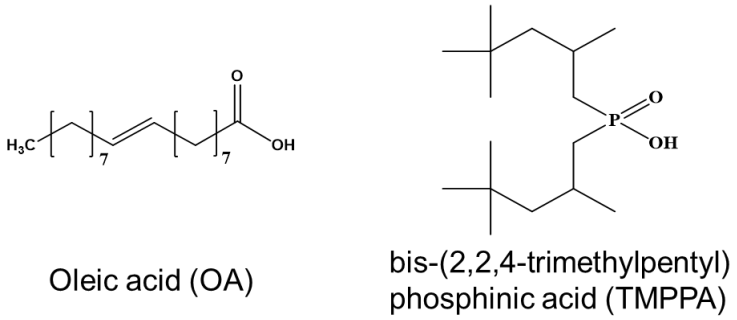

Figure 3-7. Chemical structure of oleic acid (OA) and bis-(2,2,4-trimethylpentyl) phosphinic acid (TMPPA).

The first advantage of using TMPPA is that its Cs precursor, Cs-TMPPA, can be dissolved in ODE at room temperature, while the OA-based precursor, Cs-OA, remains insoluble unless heated up to 100 °C (**Figure 3-8** a). This allows the Cs-TMPPA to be conveniently stored and used during reaction. The second and most important advantage, is that the crude solution of $CsPbI_3$-TMPPA PNCs exhibited a preserved α-phase, in this case being shown for 20 days storage (**Figure 3-8** b).

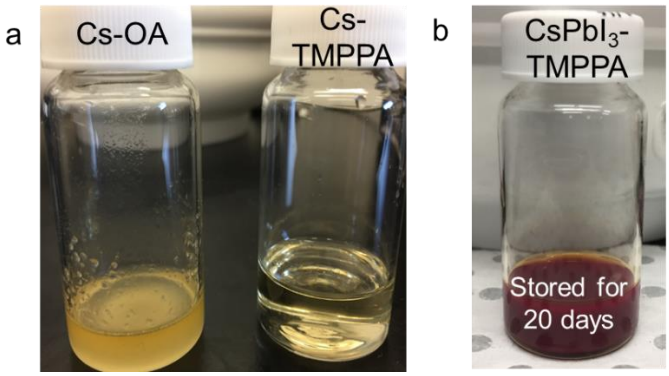

Figure 3-8. photos of (a) Cs- OA and Cs- TMPPA precursors at room temperature, (b) $CsPbI_3$ - TMPPA crude solution that has been stored for 20 days under ambient condition.

3.4.2 Optical and Structural Characterisation

The effectiveness of using TMPPA in synthesising α-$CsPbI_3$ was further examined by UV-Vis absorption, PL, XRD and TEM measurements. A comparison of the UV-Vis absorption and PL spectra of $CsPbI_3$-OA and $CsPbI_3$-TMPPA after storage for different times is shown in **Figure 3-9** a-d. The two as-synthesised samples exhibited similar band-edge absorption profiles, with a characteristic optical bandgap of ~1.8 eV. Meanwhile, both samples exhibited strong PL characteristics with peaks positions and FWHM for the $CsPbI_3$-TMPPA being 684 nm and 34 nm, respectively, and that for $CsPbI_3$-OA being 678 nm and 50 nm, respectively. Given the limited size-sorting during purification, this comparison suggests that the quality of the $CsPbI_3$-TMPPA PNCs was superior compared to the OA analogues in these syntheses. Importantly, across these samples, the $CsPbI_3$-OA PNCs showed an increased scattering upon storage over 3 days, accompanied by yellow precipitates forming from solution, which is characteristic of the δ-$CsPbI_3$. At the same time, its PL intensity also declined. In stark contrast, the absorption and PL properties of the $CsPbI_3$-TMPPA were almost perfectly preserved during these 20 days of storage under ambient environment.

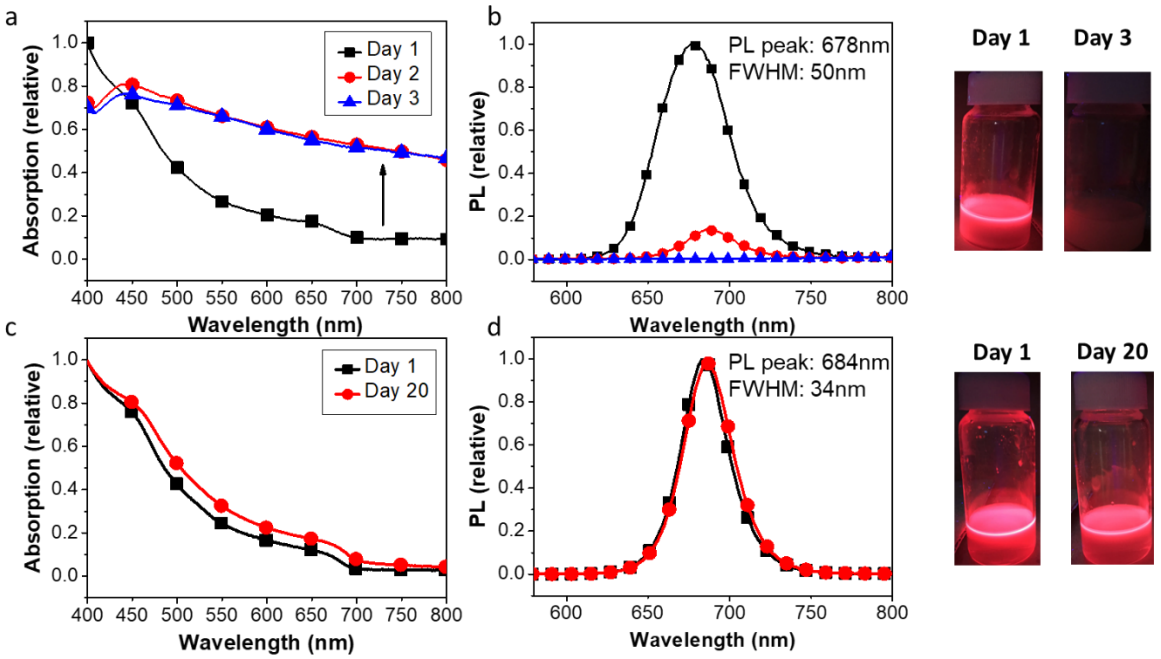

Figure 3-9. UV-Vis absorption and PL spectra for (a), (b) $CsPbI_3$-OA and(c), (d) $CsPbI_3$-TMPPA. Photos on side of (b, d): Solutions of the respective PNCs under UV light at different times following synthesis.

To confirm the structural characteristics inferred from optical measurements, XRD and in-situ heating TEM measurements were performed. As the XRD previously shown in Section 3.3.1, $CsPbI_3$-OA had very poor α-phase stability. In comparison, $CsPbI_3$-TMPPA remained in the α-phase throughout the 30 days testing period (**Figure 3-10** a). Moreover, when heated at 150 °C for 4 hours, the $CsPbI_3$-TMPPA displayed no obvious structural changes nor any evidence of coarsened PNCs (**Figure 3-10** b). This provides direct proof that the $CsPbI_3$-TMPPA had much better α-phase stability both in solution and deposited as a monolayer with heating.

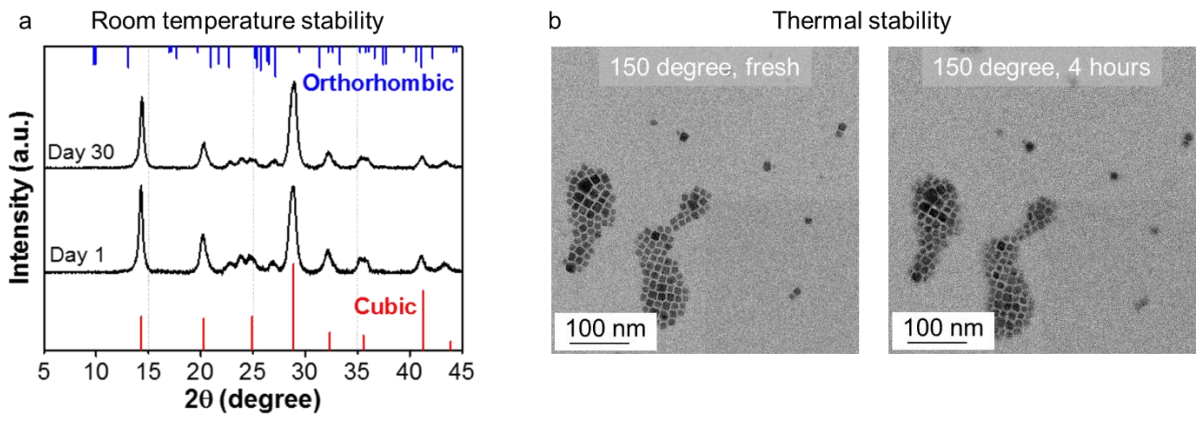

Figure 3-10. (a) XRD patterns of $CsPbI_3$-TMPPA stored in ambient condition for 30 days. Standard cubic phase is shown in red (bottom), orthorhombic phase in blue (top). (*) unidentified peaks. (b) In-situ heating TEM at 150 °C for the α-$CsPbI_3$-TMPPA at the beginning and after 4 hours.

3.4.3 NCs Size Evolution during Purification

After synthesis, the $CsPbI_3$ NCs in their crude solution must be purified or "washed". The procedure for this washing process was introduced in Chapter 2.3.1. Herein, tert-butanol was used as the anti-solvent, and the effect of different washing parameters (solvent/anti-solvent ratio, centrifuge rotation speed) on the achieved PNCs are presented in **Figure 3-11** a-d and **Table 3-1**. Generally, PNCs with a smaller size were harder to precipitate out via centrifugation. There are two approaches to promote a complete precipitation: (1) increase the polarity of the mixture by introducing greater amounts of anti-solvent, which reduces the dispersity of the PNCs; and (2) increase the rotational speed of the centrifuge to generate larger centrifugal forces. When adopting the highest solvent: anti-solvent volume ratio (1:3), and the largest centrifugal speed (10000 rpm), the washed $CsPbI_3$-TMPPA sample had the smallest average particle sizes and largest size distribution (**Figure 3-11** b, 11.9 nm ± 2.8 nm), indicating a near-complete precipitation. Using the same washing parameters gave $CsPbI_3$-OA NCs with a smaller average size (**Figure 3-11** d, 9.5 nm ± 2.3 nm). As such, a 1:3 solvent: anti-solvent volume ratio and a 10000 rpm centrifugal speed was used as a standard parameter for carrying out in-depth purification studies in Chapter 4.

Table 3-1 Summary of the size of NCs with different washing parameters

Group number	Solvent/Anti-solvent	Rotation speed (rpm)	Average size (nm)	Standard deviation (nm)
a	1:3	8000	12.1	1.8
b	1:3	10000	11.9	2.8
c	2:1	10000	13.1	2.0
d ($CsPbI_3$-OA)	1:3	10000	9.5	2.3

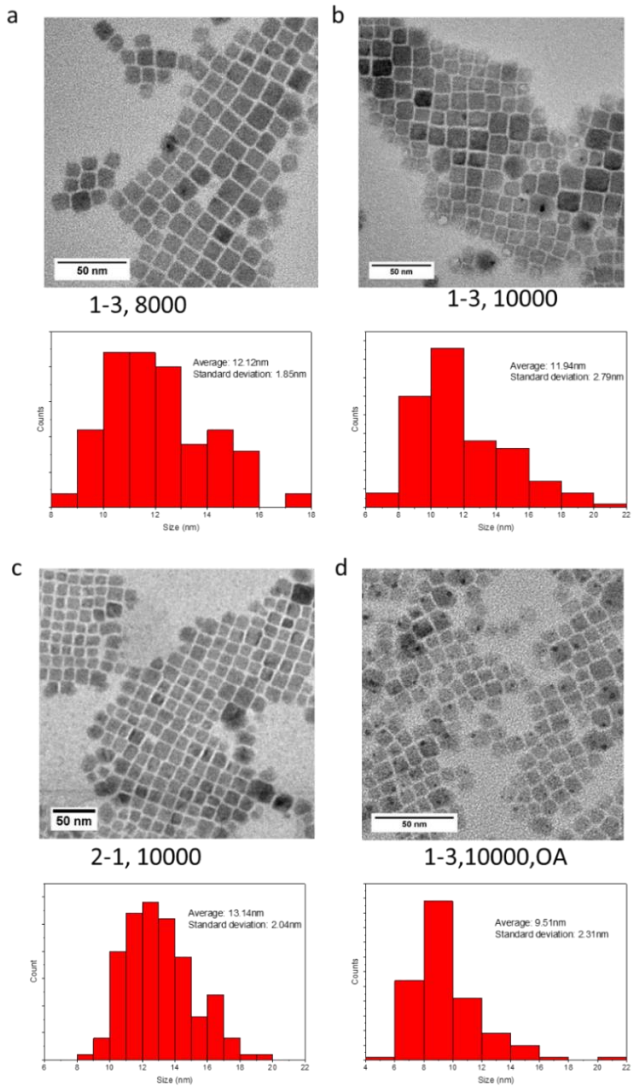

Figure 3-11. TEM images and size distributions of (a) $CsPbI_3$-TMPPA, 1:3 solvent/anti-solvent (v/v), 8000 rpm, (b) $CsPbI_3$-TMPPA, 1:3 solvent/anti-solvent (v/v), 10000 rpm, (c) $CsPbI_3$-TMPPA, 2:1 solvent/anti-solvent (v/v), 10000 rpm, (d) $CsPbI_3$-OA, 1:3 solvent/anti-solvent (v/v), 10000 rpm.

3.4.4 Surface Chemistry of $CsPbI_3$-TMPPA

To explore the potential mechanism for the TMPPA enabling α-$CsPbI_3$ PNCs, nuclear magnetic resonance (NMR) spectroscopy was used to examine the PNCs surface chemistry. Conventional ^{1}H and ^{13}C NMR measurements can be very ambiguous for the $CsPbI_3$-TMPPA mixture, as the signals from the OLA, residual ODE and tert-butanol all convolute together.[19] However, as TMPPA is the only reaction additive that contains phosphorous,[21] ^{31}P NMR measurements could be used to provide a clear insight into its chemical state.

The ^{31}P NMR spectrum of neat TMPPA is shown in **Figure 3-12** as a reference, which contains minor peaks attributable to organophosphorous impurities. The ^{31}P NMR spectrum of a once-washed, concentrated solution of $CsPbI_3$-TMPPA PNCs (**Figure 3-13**) reveals significant shifting and broadening of the signals attributed to TMPPA compared to the reference spectra of neat TMPPA. This could indicate strong bonding between TMPPA and the PNC surface.[22],[23] However, the ^{31}P NMR signal of TMPPA is also known to shift and broaden whenever it forms ion pairs in the presence of a base.[21] To differentiate between these possibilities, a solution of TMPPA that has been reacted with an excess of OLA to form the OLA-TMPPA ion pair was measured with ^{31}P NMR. The results (**Figure 3-14**) displayed a peak with the same position and width as that observed in **Figure 3-13** for the $CsPbI_3$ NCs. Similarly, when reacting PbI_2 with TMPPA and OLA (**Figure 3-15**), the characteristic signal for the TMPPA was at the same position as that observed for the $CsPbI_3$ NCs and the TMPPA/OLA control solution.

Notably, attempts to form a Pb-TMPPA solution in ODE using PbI_2 as a lead source failed, with the PbI_2 not dissolving without the aid of the Lewis base chelating agent, even at elevated temperatures. In order to form a Pb-TMPPA complex, PbO was reacted with TMPPA. The ^{31}P NMR signal for the TMPPA species in this control solution was present at 45 ppm (**Figure 3-16**), a shift of ~6 ppm in comparison to the TMPPA species in the NMR spectra of TMPPA/OLA and α-$CsPbI_3$ NCs. A shift of this magnitude is ascribed to the formation of a Pb-TMPPA species in solution. It also confirms

that in these reaction mixtures, the TMPPA in the $CsPbI_3$ NCs exists in the form of an OLA-TMPPA ion pair, rather than a pure Pb-TMPPA complex. Given this factor, it could be inferred that TMPPA is not directly binding to lead species at the surface of these PNCs. This is in contrast to typical II-VI semiconductors, for which it would form the main surface passivant.[20]

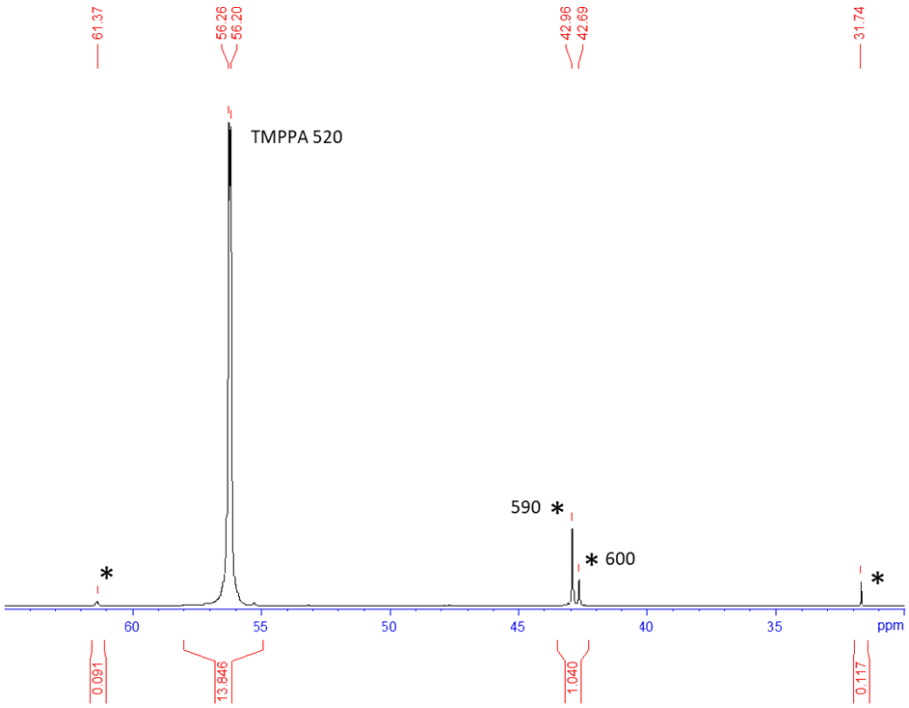

Figure 3-12. ^{31}P NMR spectrum of neat TMPPA. Asterisks (*) denote organophosphorus impurities. Annotated diffusion coefficients as measured by DOSY given in μm^2 / s.

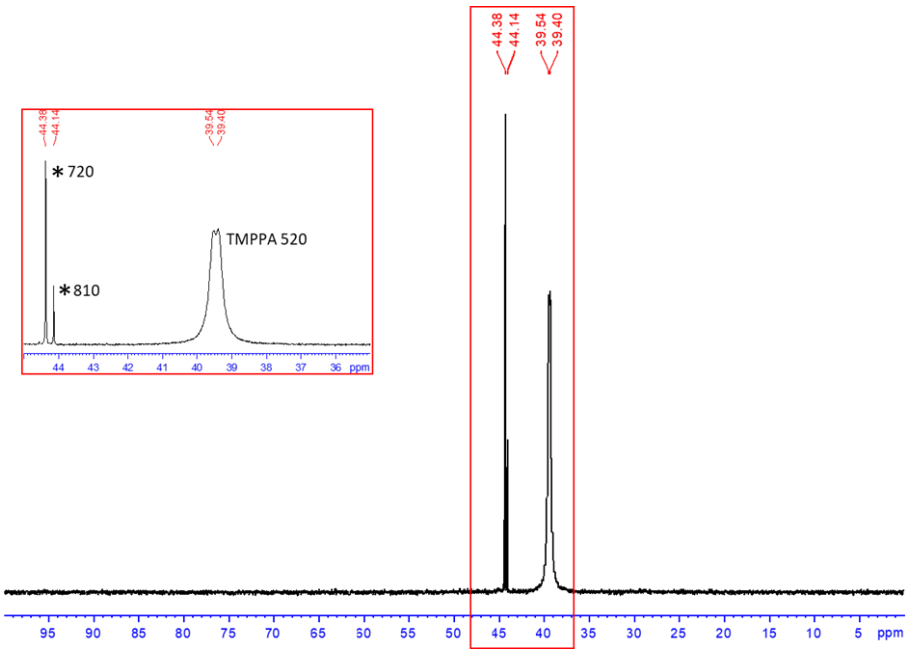

Figure 3-13. ^{31}P NMR spectrum of a concentrated solution of $CsPbI_3$-TMPPA NCs (washed once). Asterisks (*) denote organophosphorus impurities. Annotated diffusion coefficients as measured by DOSY given in μm^2 / s.

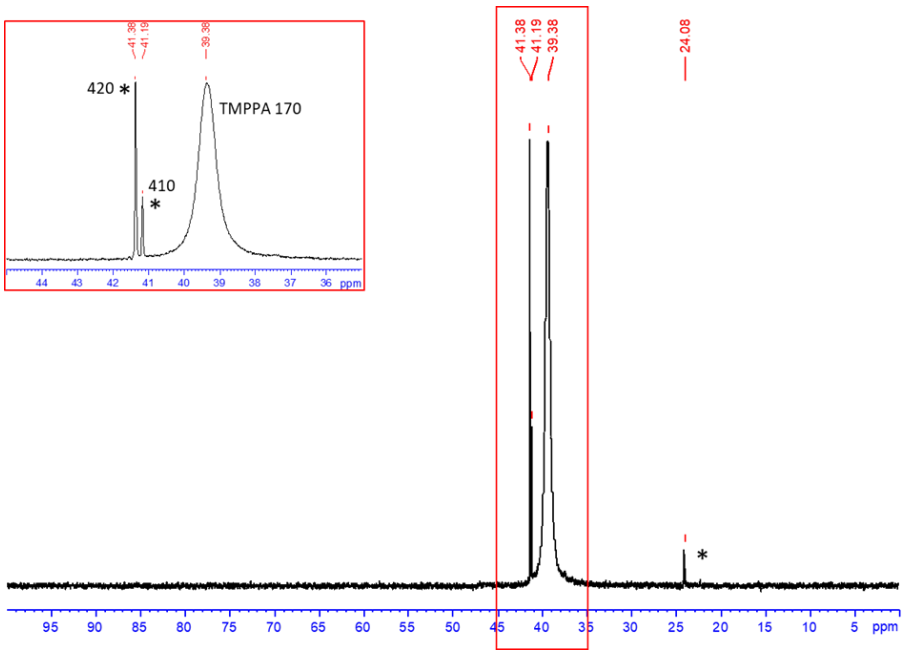

Figure 3-14. ^{31}P NMR spectrum of TMPPA with an excess of OLA present in solution. Asterisks (*) denote organophosphorus impurities. Annotated diffusion coefficients as measured by DOSY given in μm^2 / s.

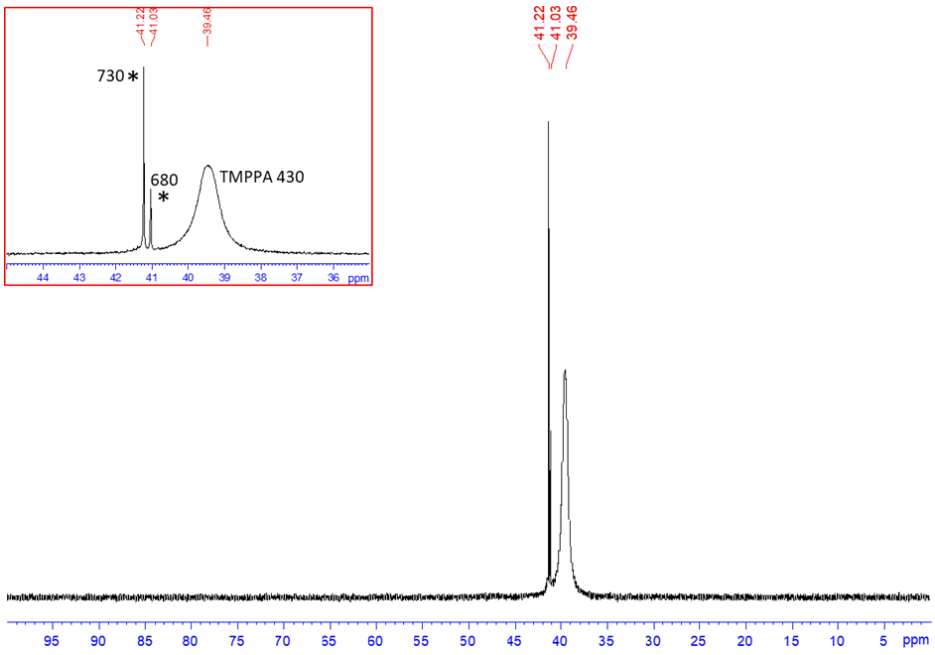

Figure 3-15. ^{31}P NMR spectrum of a PbI_2-TMPPA/OLA solution. Asterisks (*) denote organophosphorus impurities. Annotated diffusion coefficients as measured by DOSY given in μm^2 / s.

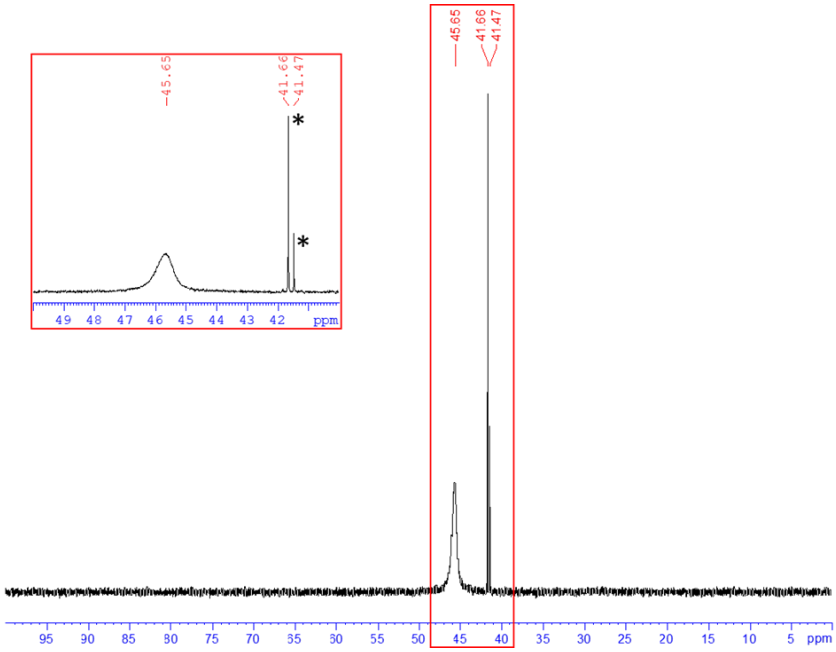

Figure 3-16. ^{31}P NMR spectrum of a Pb-TMPPA solution synthesised by a reaction of PbO with TMPPA in d8-toluene. Asterisks (*) denote organophosphorus impurities.

Diffusion coefficients measured from diffusion-ordered spectroscopy (DOSY) were also used to confirm the chemical nature of TMPPA in solution.[19] The diffusion coefficients for the characteristic signals of TMPPA in solutions of neat TMPPA, $CsPbI_3$-TMPPA, TMPPA- OLA and PbI_2-TMPPA-OLA were measured to be 520 $\mu m^2/s$, 520 $\mu m^2/s$, 170 $\mu m^2/s$ and 430 $\mu m^2/s$. All these value were much larger than the typical value for species forming bindings with ~10 nm size NCs, which should be around ~50 $\mu m^2/s$.[19] This provides further evidence that in a once-washed solution of $CsPbI_3$ NCs, TMPPA exists in solution as an ion pair with oleylammonium and does not bind to the PNCs surface.

To verify this hypothesis, the $CsPbI_3$-TMPPA PNC solution was washed an additional time attempting to remove all the residual TMPPA species. The resulting PNC dispersion was then analyzed using ^{31}P NMR, which showed that even after an extended measurement time of ~5 hours, only extremely weak ^{31}P signals could be collected (**Figure 3-17**). This confirmed that TMPPA was not present in the solution in any significant quantity after the second wash. Moreover, it further validates the notion that it does not act to stabilize the α-$CsPbI_3$ by directly coordinating to the PNC surface. To gauge at what then does coordinate the surface, ^1H NMR on the same twice washed solution was carried out (**Figure 3-18**). It showed a broad peak at 5.5 ppm, which is ascribed to the alkene resonance originating from the OLA or its quarternarised oleylammonium species. This confirms that OLA or oleylammonium are the primary passivants of $CsPbI_3$-TMPPA PNCs .[19]

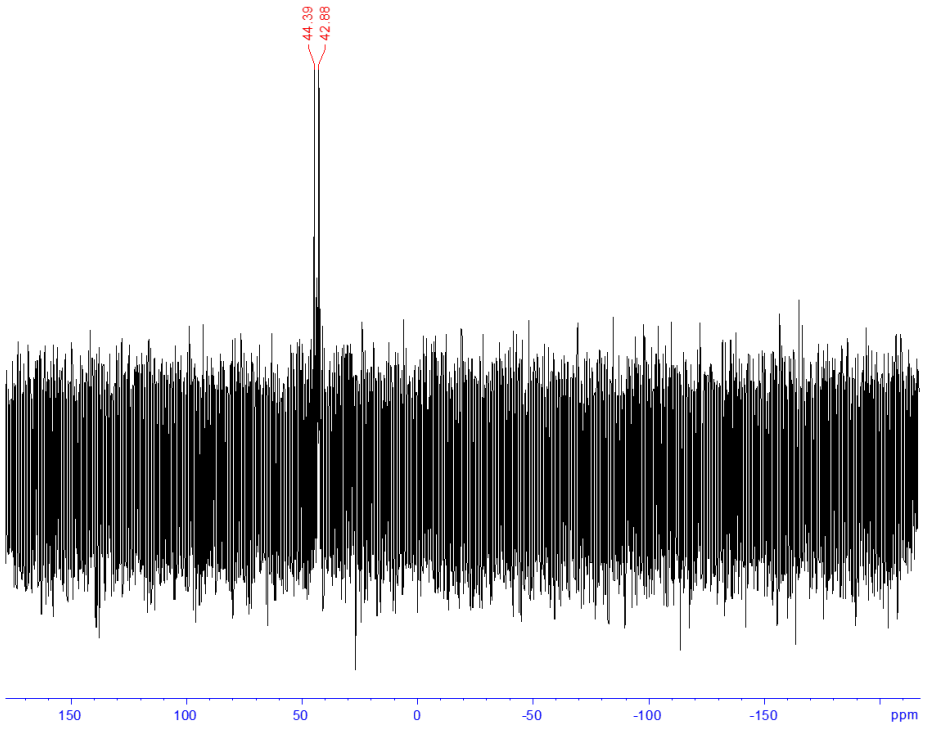

Figure 3-17. ^{31}P NMR spectrum of a $CsPbI_3$-TMPPA solution washed twice to remove all TMPPA species. Note 5 hours scan duration.

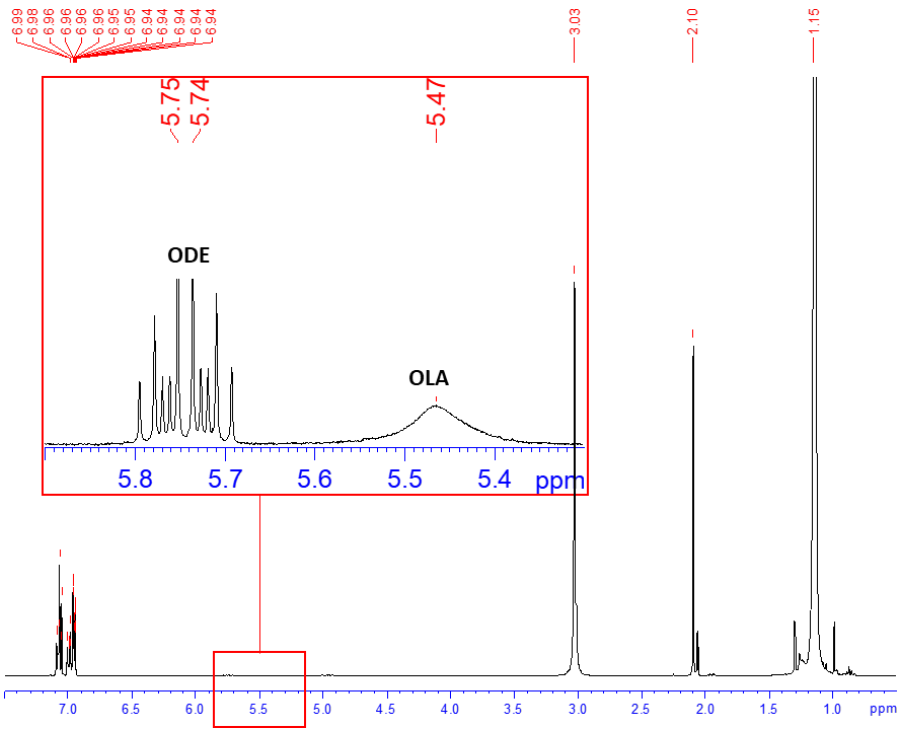

Figure 3-18. 1H NMR spectrum of a concentrated solution of $CsPbI_3$-TMPPA NCs washed once (top) and washed twice (bottom).

It has been suggested that for $CsPbBr_3$-OA, oleylammonium-oleate is a co-passivant to other OLA species at the surface.[18],[19] Given this factor, it is likely that α-to-δ phase transformation of $CsPbI_3$-OA in solution is associated with such a mixed surface chemistry. To verify this hypothesis, 50 ul of OA or oleylammonium - oleate were added to 1 ml of an as-prepared $CsPbI_3$-TMPPA solution and its stability was compared with a neat $CsPbI_3$-TMPPA solution. As demonstrated in **Figure 3-19**, adding pure OA to $CsPbI_3$-TMPPA exhibited a decreased the stability of the α-phase to less than a day. **Figure 3-20** shows a photo of the rapid phase transformation after only 3 hours following oleylammonium-oleate addition. Conversely, when 50ul of TMPPA was added to 1 ml of fresh α-$CsPbI_3$-OA at a [PNC] ~ 1×10^{-6} M, the α-$CsPbI_3$-OA solution exhibited a slower α-to-δ transformation, although it did not prevent it (**Figure 3-21**).

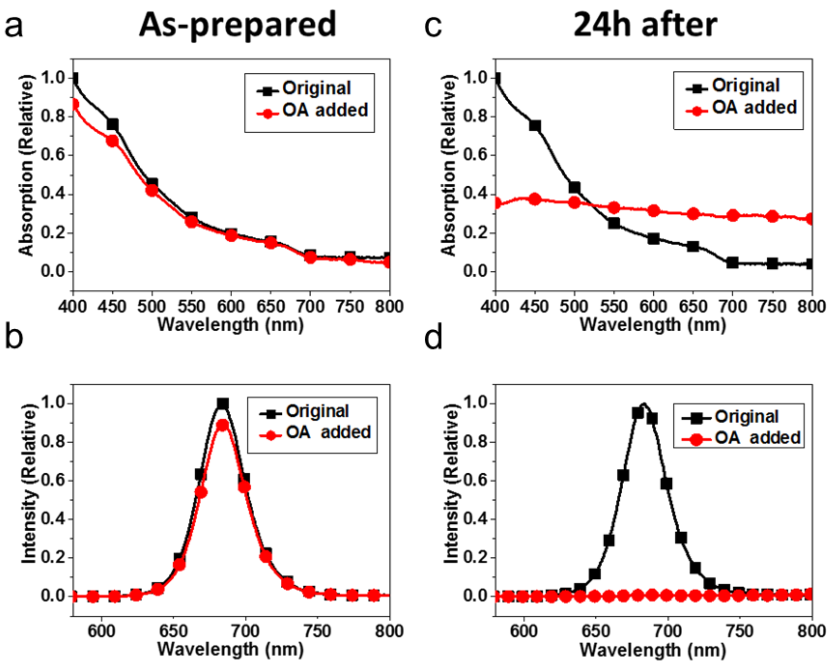

Figure 3-19. (a) UV-Vis absorption and (b) PL spectra of as prepared $CsPbI_3$-TMPPA and OA-added $CsPbI_3$-TMPPA solutions. (c) UV-Vis absorption and (d) PL spectra of these samples after 24 h under ambient conditions.

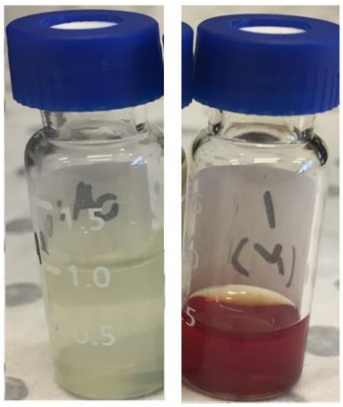

Figure 3-20. $CsPbI_3$-TMPPA solution with oleylammonium-oleate added (left) and as-prepared $CsPbI_3$-TMPPA solution (right).

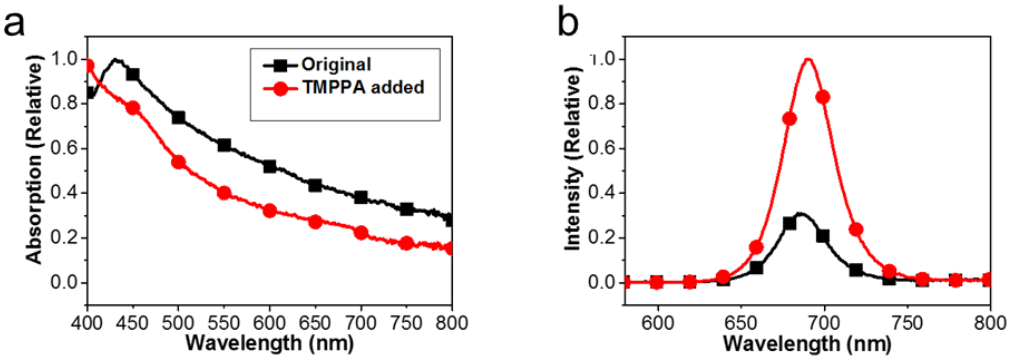

Figure 3-21. (a) UV-Vis absorption and (b) PL spectra for original $CsPbI_3$-OA and TMPPA-added $CsPbI_3$-OA solutions after 2 days.

3.4.5 TMPPA-Suppressed Coarsening of the $CsPbI_3$ PNCs

Having shown that the usage of TMPPA as a replacement to OA within a hot-injection synthesis successfully yielded long term stable α-$CsPbI_3$, its effects on other aspects of the synthesis were studied and compared with the conventional OA ligand.

When using the OA+OLA ligand combination and 140 °C as the injection temperature, the NCs coarsen significantly if the reaction time is extended. When the reaction was terminated by submerging in a water bath after 5 s, which is the conventional reaction time, the NCs were NCU with a mean size of 11.90 ± 2.85 nm (**Figure 3-22** a). Notice that in this batch, the average size and

size distribution of the PNCs was significantly larger than that presented previously in Section 3.4.3, which used the same reaction temperature and purification protocol. This indicates that the batch to batch reproducibility for the HI method is problematic. When the reaction was maintained at 140 °C for 5 minutes, however, the size of the resulting NCs greatly increased to 18.56 ± 2.04 nm (**Figure 3-22** b). When extended to 10 minutes (**Figure 3-22** c), elongated NW structures were observed in conjunction with smaller NCU, with the former exhibiting the δ-phase based on SADP measurements. When the reaction time was further extended to 1 hour (**Figure 3-22** d), only large platelet structures were observed. These were fully phase transformed, single-crystalline δ-phased $CsPbI_3$. These results suggest that the conventional OA+OLA ligand combination results in progressive coarsening of the NCs during the reaction, which necessitates rapid cooling soon after injection of the precursor to maintain a narrow ensemble distribution.

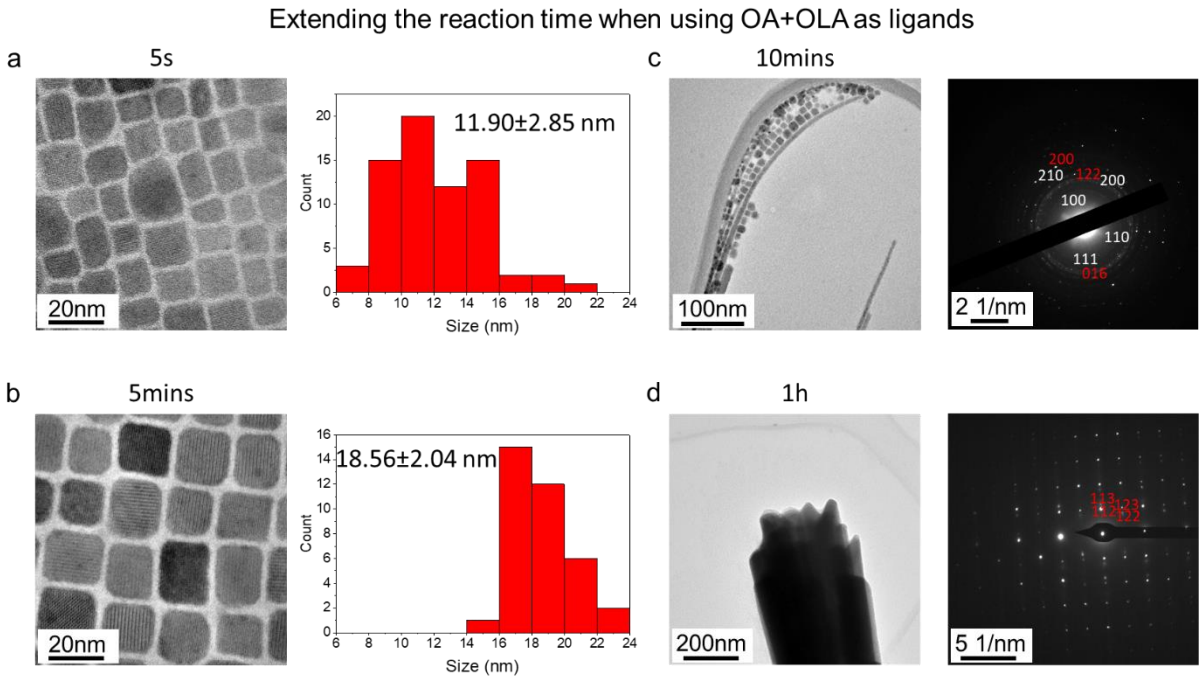

Figure 3-22. TEM images, size distribution histograms and SADP for $CsPbI_3$ synthesised with OA+OLA ligands at (a) 5 seconds, (b) 5 minutes, (c) 10 minutes, (d) 1 hour.

As a comparison, the same synthesis reaction was carried out using the TMPPA+OLA ligand system (**Figure 3-23**). The NCs were also NCU in structure and possessed a mean size of 11.10 ± 1.57 nm and 11.33 ± 1.31 nm for the samples following 5 s and 5 minutes of reaction, respectively (**Figure 3-23** a, b), which is in contrast to the OA+OLA sample. When the reaction was extended to 1 hour (**Figure 3-23** c), the mean size was slightly increased to 12.17 ± 2.23 nm, indicating little coarsening had occurred. Such a result suggests that the TMPPA indeed suppresses the coarsening of the NCs, even at high temperatures. This is likely to be associated with TMPPA not binding to the NC surface, which inherently reduces any re-dissolution of surface species back into solution and ensures a robust ligand shell on the NC surface to prevent coarsening. Despite this, when the reaction was prolonged to 9 hours, some NW structures of ~10 µm length and ~50 nm width were observed (**Figure 3-23** d) alongside the normal cube NCs. The Fast-Fourier-Transform of the NW is indexed to be the δ-phased. Therefore, although the coarsening of the NCs was suppressed by using TMPPA in the reaction, it was not fully prevented. As a result, heterogenous growth of the α-phased NCs into δ-phased NWs was still observed.

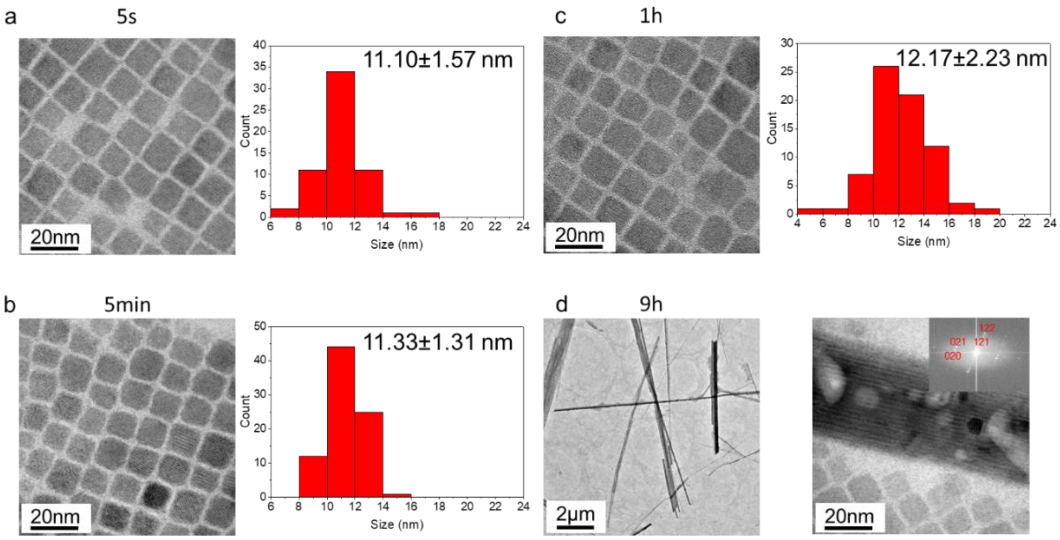

Figure 3-23. TEM images, size distribution histograms and SADP for $CsPbI_3$ synthesised with TMPPA+OLA ligands at (a) 5 seconds, (b) 5 minutes, (c) 1 hour, (d) 9 hours, inset of d: The Fast-Fourier-Transform of the NWs region, showing its δ-phase.

To further study the reaction kinetics of the PNCs, absorption and PL measurements were carried out for syntheses using OA and TMPPA by measuring quantitative aliquots of the crude reaction mixture at different reaction times (**Figure 3-24**). For the OA sample (**Figure 3-24** a), the absorption exhibited clear scattering signatures across all times, albeit with the lowest values being at 5 s and the highest being at 60 minutes. Given that the purified $CsPbI_3$-OA PNC products of the early time reactions exhibit good dispersion and limited scattering (for example, **Figure 3-9** a), these scattering contributions can be associated with larger sized biproducts forming in the reaction. They are likely to be δ-phased crystals, which exhibit NW structures, possess an optical bandgap of ~2.7 eV and are not fluorescent.[24] The large scattering contributions make any comparison of the PL spectra mis-leading, although the complete suppression of the PL after 60 minutes of reaction time was noted.

The TMPPA sample showed vastly different dynamics in its absorption and PL spectra (**Figure 3-24** b). For all the samples reacted from 5 s to 1 hour, the spectra remained similar, suggesting that the coarsening was negligible over this time period. Importantly, the spectra also showed a smaller scattering, which is in vast contrast with the OA-synthesised sample that contained larger sized side-products with significant scattering. The intensity of the absorption and PL continued to drop at 3 hours and 9 hours because of the formation of NWs. This comparison between TMPPA and OA syntheses show that the use of TMPPA unequivocally suppresses the coarsening of $CsPbI_3$ PNCs. This makes TMPPA a far more superior ligand choice for $CsPbI_3$ PNC synthesis comparing with OA, and potentially also for the broader $CsPbX_3$ PNC family.

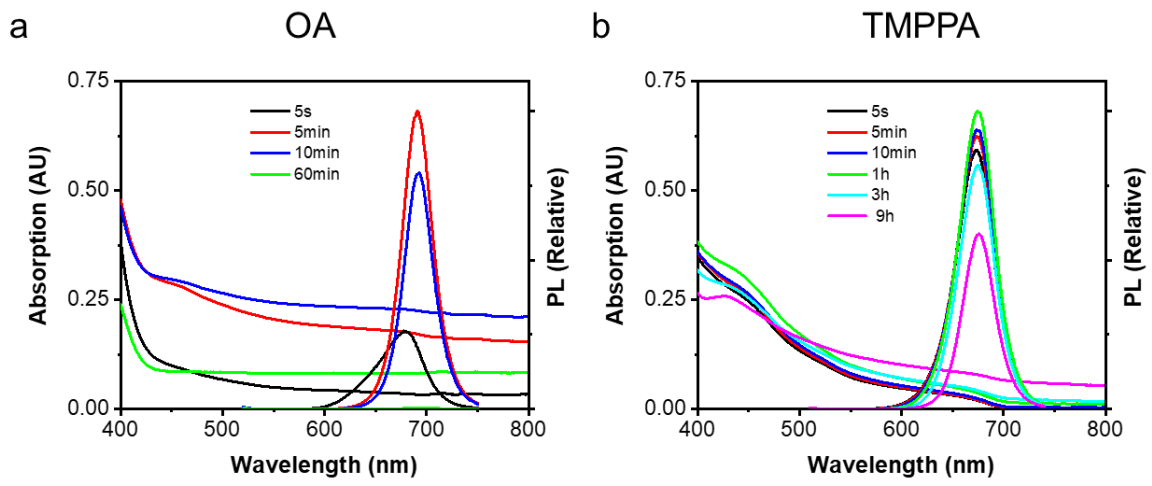

Figure 3-24. UV-Vis absorption and PL spectra for $CsPbI_3$ NCs synthesised at different reaction times with (a) OA and (b) TMPPA ligands.

3.4.6 Stabilization of the α-$CsPbI_3$ with Branching Ligands

Having shown the effectiveness of TMPPA in enabling the synthesis of α-$CsPbI_3$ NCs with suppressed coarsening characteristics, its stabilization mechanism was further investigated. Unlike OA, TMPPA and its ion-pairs do not bind to the NCs' surface. This ensures that oleylamine and/or oleylammonium iodide are the predominant surface ligands. On the contrary, it has been shown that OA binds to the surface of the PNCs and participates in a dynamic ligand exchange process,[18] which creates a more complex surface chemistry environment. Evidently, this latter surface chemistry provides a more conductive environment for undergoing a phase transformation compared to the $CsPbI_3$-TMPPA NCs.

The two major differences between the TMPPA and OA are in their acidity and steric nature. Firstly, TMPPA is a stronger acid (pKa for phosphinic acid is ~1.2, for carboxylic acid is ~5),[25] hence it is more capable of protonating the OLA in solution to ensure a higher concentration of ammonium species to cap the PNC surface. Secondly, the branching nature of TMPPA creates a greater steric hinderance. Little has been done to understand the role of steric interactions in such NCs; however,

it can be considered that large branched ligand may be physically excluded from a binding to the NCs' surface purely because of the greater steric interaction comparing with more linear ligands.

To examine the effects of the acidity and branching, two branching carboxylic acids were prepared following methods described in Chapter 2.3.4: the 2-hexyldecanoic acid (HLA, 16 carbons) and 2-decyltetradecaonic acid (DTA, 24 carbons), together with the commercially available Diisooctyl phosphinic acid (DPA, 16 carbons). Their chemical formulas are displayed in **Figure 3-25** a-c. They were then used in conjunction with OLA to synthesis $CsPbI_3$ NCs, and the longer-term stability of the NCs were monitored by TEM, UV-vis absorption, PL and XRD.

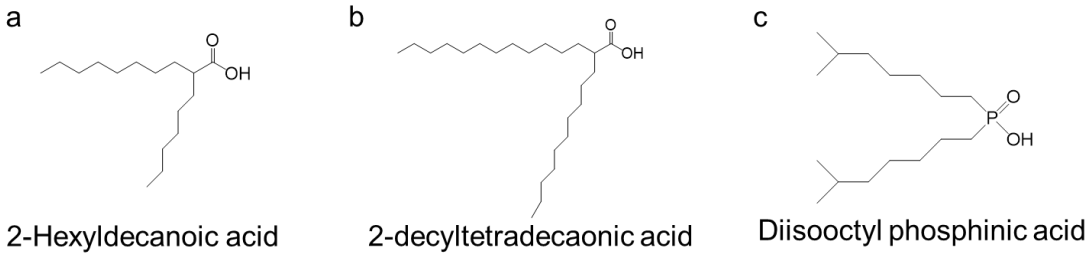

Figure 3-25. Chemical formulas for (a) 2-hexyldecanoic acid (HLA), (b) 2-decyltetradecaonic acid (DTA), (c) Diisooctyl phosphinic acid (DPA).

HLA has a similar degree of branching as TMPPA, but less acidity. After day 7 of storage, the microstructure of the $CsPbI_3$-HLA NCs displayed mostly monodisperse NCU (**Figure 3-26** a). However, some aggregated rod shape structures were observed, similar to the intermediate phase observed during the α- to δ- transformation for $CsPbI_3$-OA, as shown in **Figure 3-6** b. Furthermore, its absorption spectrum had an additional peak at around 400 nm and its PL decreased significantly after storing for 7 days (**Figure 3-26** b), which is attributed to the formation of the wider band-gap, non-emitting δ phase. This was confirmed by XRD (**Figure 3-27**), which displayed both α- and δ-scattering peaks. Such a result suggests that HLA is conducive for PNC synthesis, but is comparatively worse than TMPPA (although better than the OA) in maintaining the α-phase stability

of $CsPbI_3$. Meanwhile, DTA has longer branching, but less acidity than TMPPA. At day 7 of storage, the $CsPbI_3$-DTA PNCs still had a monodisperse nanostructure, similar to the $CsPbI_3$-TMPPA PNCs (**Figure 3-26** c). Moreover, its absorption and PL spectra had only minor differences at day 1 and day 7 (**Figure 3-26** d), and its XRD pattern displayed mostly cubic peaks. This result indicates that the greater steric interactions provided by this carboxylic acidic derivative indeed promote an enhanced α-phase stability of the $CsPbI_3$ PNCs. Finally, the DPA has similar branching and acidity as TMPPA. Not surprisingly, $CsPbI_3$-DPA exhibited a monodisperse PNC ensemble (**Figure 3-26** e). The reaction chemistry also resulted in PNCs that fully maintained their absorption, PL (**Figure 3-26** f), and structural properties at day 7.

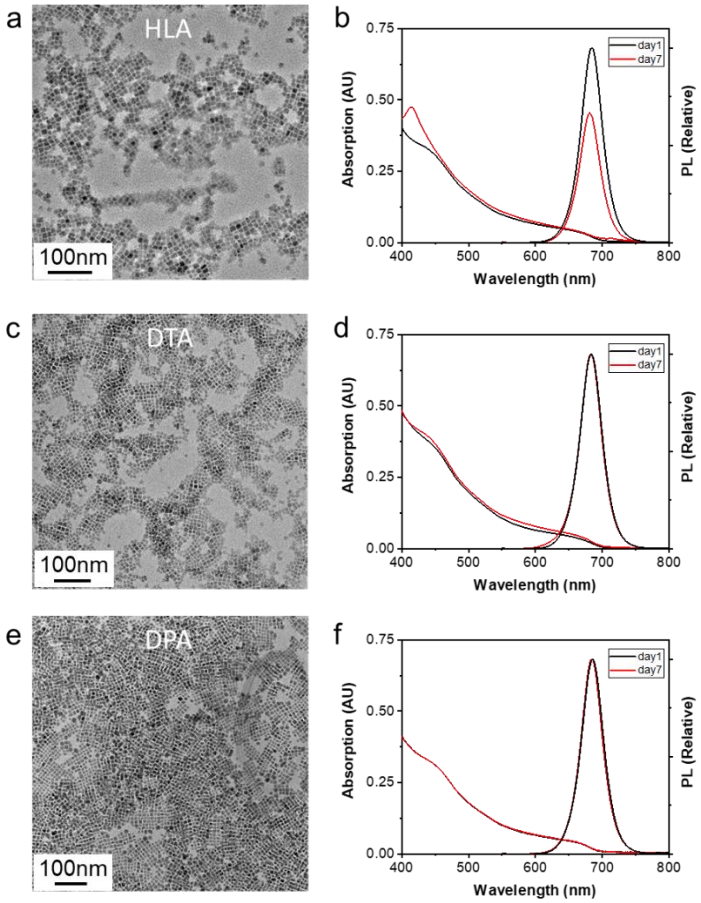

Figure 3-26. The TEM images, UV-vis absorption and PL spectra for the $CsPbI_3$ NCs synthesised with OLA and (a),(b) 2-heptylnonanoic acid (C16), (c), (d) 2-decyltetradecaonic acid (C24), (e), (f) Diisooctyl phosphinic acid.

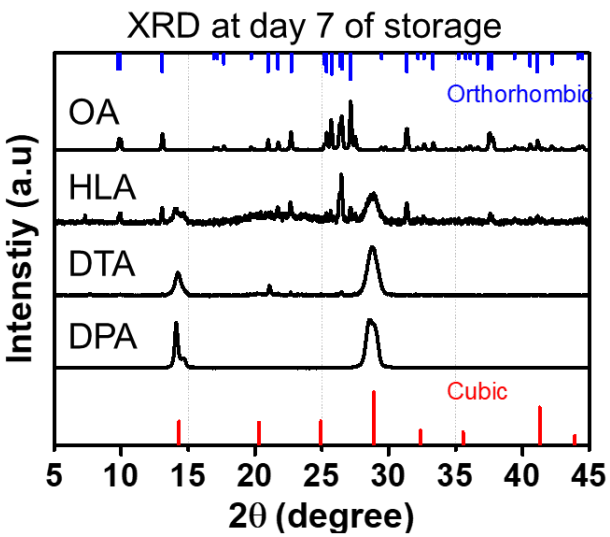

Figure 3-27. XRD pattern for the $CsPbI_3$ PNCs synthesised from OA, HLA, DTA and DPA at day 7 of storage.

The above results allow for the empirically derived conclusion that the stronger acidity and branching structure of TMPPA allows it to promote the long-term cubic phase stability of the $CsPbI_3$. Judging by the stability of the $CsPbI_3$-DTA, it could be inferred that strong steric hinderance itself is sufficiently effective to maintain the α-phase $CsPbI_3$. However, at this stage further surface chemistry and computational work are required to accurately probe the surface interactions between such a sterically hindered ligands compared to the more traditional OA in order to understand how steric interactions govern the degree of surface passivation in mixed ligand systems. This will provide some important considerations for future ligand design that are tailored for structural integrity in such NCs.

3.5 Generalized Synthesis of $CsPbX_3$ PNCs

In this chapter we have primarily focussed on the synthesis of $CsPbI_3$ PNCs using a modified HI reaction mixture containing TMPPA and OLA as solubilising ligands. Here we extend the compositional window of this reaction mixture to include $CsPbCl_3$ and $CsPbBr_3$ NCs, with the results shown in **Figure 3-28**. Synthesis of both types of PNCs displayed a monodisperse ensemble of NCU. XRD patterns of each were also indexed to their α phase's standard powder diffraction file card, yet

due to the similarity of α-cubic and γ-orthorhombic phase of $CsPbBr_3$, one can only determine their exact phase with high accuracy XRD techniques, e.g. synchrotron source XRD.[26] The $CsPbCl_3$ and $CsPbBr_3$ NCs exhibited absorption edges at 400 nm and 485nm, respectively. Meanwhile, their PL peaks were centred at 407 nm (FWHM of 11 nm) and 506 nm (FWHM of 20 nm), respectively, and possessed a PLQY of 10% and 90%, respectively. The low QY for the $CsPbCl_3$ is attributed to the high Cl deficiency levels and the corresponding high trap states density similar to other report.[27]

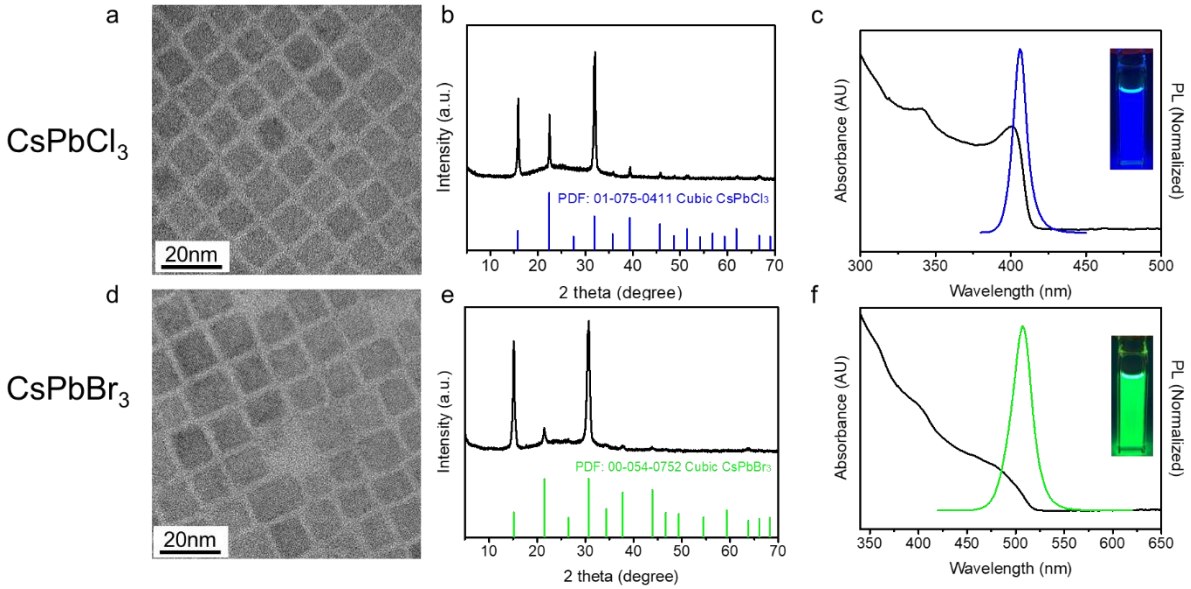

Figure 3-28. The TEM images, absorption & PL spectrum, XRD pattern for (a), (b), (c) $CsPbCl_3$ and (d), (e), (f) $CsPbBr_3$ NCs, respectively.

After synthesising pristine $CsPbCl_3$, $CsPbBr_3$, $CsPbI_3$ PNCs, by simply mixing them at different molar ratio, the $CsPbX_3$ PNCs with multiple emission colour across the entire visible spectrum could be readily prepared (**Figure 3-29**).

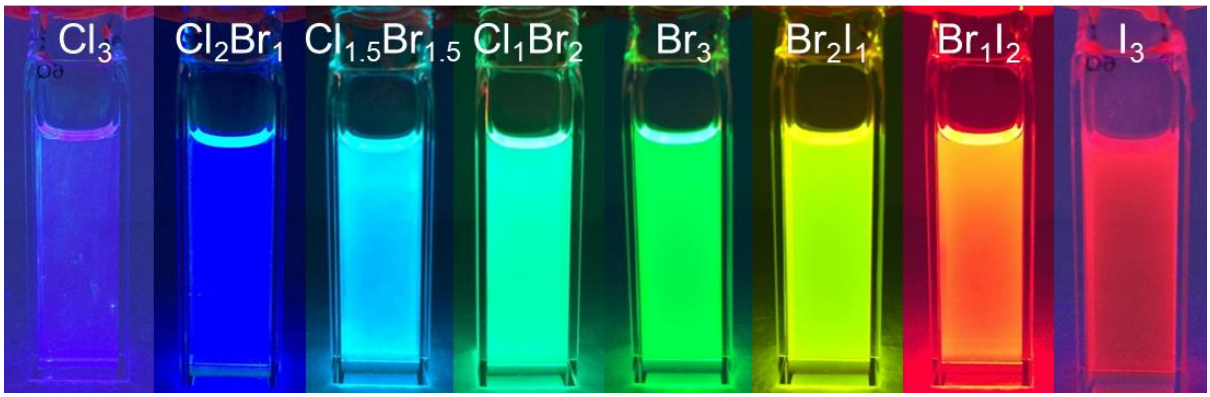

Figure 3-29. Photo of the $CsPbX_3$ NCs solution with various halide composition under the UV lamp.

3.6 Conclusions

In summary, this chapter investigated the α- to δ- phase transformation of $CsPbI_3$ PNCs. We showed that the archetypical synthesis developed by Protesescu et al. results in the progressive phase transformation of such nanocrystals over hours to days both in crude and washed solutions.[4] The driving mechanism for this transformation was found to be the gradual coarsening of α-$CsPbI_3$ PNCs into larger wires and platelets, for which the δ phase is the most stable. To suppress this coarsening mechanism, we replaced the conventionally-used oleic acid (OA) with a branched alkyl phosphinic acid (TMPPA) in the synthesis of such PNCs. In contrast to expectation based on the chemical role of this ligand for traditional II-VI semiconductor colloids, the TMPPA was found not to bind to the NC surface. Instead it was found to act as a spectator ion, primarily aiding in the solubilisation process of the Cs^+ and Pb^{2+} in the precursor solutions, and protonating the oleylamine (OLA). As a result, its use indirectly ensured a more robust surface ligand shell composed of oleylamine (OLA) and/or oleylammonium species on the NC surface. The formation of this ligand shell resulted in dramatically reduced coarsening of the NCs during the reaction at high temperatures, as well as following the reaction, both in the crude and washed solutions. Replacing the TMPPA with other branched alkyl carboxylic or phosphinic acids was also found to effectively stabilize α-$CsPbI_3$ NCs. This shows that

the use of branched ligand chemistries plays a powerful role in dictating the surface chemistry of PNCs and ultimately their structure-property relations. The versatility of this reaction approach was expanded through the demonstrated synthesis of high quality $CsPbX_3$ PNCs.

References

[1] J. Song, J. Li, X. Li, L. Xu, Y. Dong, H. Zeng, *Adv. Mater.* **2015**, *27*, 7162.

[2] S. Yakunin, L. Protesescu, F. Krieg, M. I. Bodnarchuk, G. Nedelcu, M. Humer, G. De Luca, M. Fiebig, W. Heiss, M. V Kovalenko, *Nat. Commun.* **2015**, *6*, 8056.

[3] J.-S. Lee, P. Ramasamy, D.-H. LIM, B. Kim, S.-H. Lee, M.-S. Lee, *Chem. Commun.* **2015**, *52*, 3.

[4] L. Protesescu, S. Yakunin, M. I. Bodnarchuk, F. Krieg, R. Caputo, C. H. Hendon, R. X. Yang, A. Walsh, M. V. Kovalenko, *Nano Lett.* **2015**, *15*, 3692.

[5] D. M. Trots, S. V. Myagkota, *J. Phys. Chem. Solids* **2008**, *69*, 2520.

[6] L. Protesescu, S. Yakunin, S. Kumar, J. Bär, F. Bertolotti, N. Masciocchi, A. Guagliardi, M. Grotevent, I. Shorubalko, M. I. Bodnarchuk, C.-J. Shih, M. V. Kovalenko, *ACS Nano* **2017**, *11*, 3119.

[7] Q. A. Akkerman, D. Meggiolaro, Z. Dang, F. De Angelis, L. Manna, *ACS Energy Lett.* **2017**, *2*, 2183.

[8] S. Dastidar, D. A. Egger, L. Z. Tan, S. B. Cromer, A. D. Dillon, S. Liu, L. Kronik, A. M. Rappe, A. T. Fafarman, *Nano Lett.* **2016**, *16*, 3563.

[9] A. Dutta, N. Pradhan, *ACS Energy Lett.* **2019**, *4*, 709.

[10] G. E. Eperon, G. M. Paterno, R. J. Sutton, A. Zampetti, A. A. Haghighirad, F. Cacialli, H. J. Snaith, *J. Mater. Chem. A* **2015**, *3*, 19688.

[11] B. Zhao, S. Jin, S. Huang, N. Liu, J.-Y. Ma, D.-J. Xue, Q. Han, J. Ding, Q.-Q. Ge, Y. Feng, J.-S. Hu, *J. Am. Chem. Soc.* **2018**, *140*, 11716.

[12] D. T. Moore, J. M. Luther, T. Chakrabarti, J. A. Christians, A. R. Marshall, E. M. Sanehira, A. Swarnkar, B. D. Chernomordik, *Science.* **2016**, *354*, 92.

[13] J. Pan, Y. Shang, J. Yin, M. De Bastiani, W. Peng, I. Dursun, L. Sinatra, A. M. El-Zohry, M. N. Hedhili, A. H. Emwas, O. F. Mohammed, Z. Ning, O. M. Bakr, *J. Am. Chem. Soc.* **2018**, *140*, 562.

[14] F. Liu, Y. Zhang, C. Ding, S. Kobayashi, T. Izuishi, N. Nakazawa, T. Toyoda, T. Ohta, S. Hayase, T. Minemoto, K. Yoshino, S. Dai, Q. Shen, *ACS Nano* **2017**, *11*, 10373.

[15] A. Monshi, *World J. Nano Sci. Eng.* **2012**, *02*, 154.

[16] Z. Dang, J. Shamsi, F. Palazon, M. Imran, Q. A. Akkerman, S. Park, G. Bertoni, M. Prato, R. Brescia, L. Manna, *ACS Nano* **2017**, 11, 2124.

[17] M. A. Boles, D. Ling, T. Hyeon, D. V. Talapin, *Nat. Mater.* **2016**, *15*, 141.

[18] A. Pan, B. He, X. Fan, Z. Liu, J. J. Urban, A. P. Alivisatos, L. He, Y. Liu, *ACS Nano* **2016**, *10*, 7943.

[19] J. De Roo, M. Ibáñez, P. Geiregat, G. Nedelcu, W. Walravens, J. Maes, J. C. Martins, I. Van Driessche, M. V. Kovalenko, Z. Hens, *ACS Nano* **2016**, *10*, 2071.

[20] J. Jasieniak, L. Smith, J. Van Embden, P. Mulvaney, M. Califano, *J. Phys. Chem. C* **2009**, *113*, 19468.

[21] D. Cholico-Gonzalez, M. Avila-Rodriguez, G. Cote, A. Chagnes, *J. Mol. Liq.* **2013**, *187*, 165.

[22] M. Kuno, J. K. Lee, B. O. Dabbousi, F. V Mikulec, M. G. Bawendi, *J. Chem. Phys.* **1997**, *106*, 9869.

[23] J. S. Owen, J. Park, P.-E. Trudeau, A. P. Alivisatos, *J. Am. Chem. Soc.* **2008**, *130*, 12279.

[24] T. Yang, Y. Zheng, Z. Du, W. Liu, Z. Yang, F. Gao, L. Wang, K.-C. Chou, X. Hou, W. Yang, *ACS Nano* **2018**, 12, 1611.

[25] R. Williams, *pKa Data Compil. by R. Williams* **2012**, 33.

[26] P. Cottingham, R. L. Brutchey, *Chem. Commun. Chem. Commun* **2016**, *5246*, 5246.

[27] Z. J. Yong, S. Q. Guo, J. P. Ma, J. Y. Zhang, Z. Y. Li, Y. M. Chen, B. Bin Zhang, Y. Zhou, J. Shu, J. L. Gu, L. R. Zheng, O. M. Bakr, H. T. Sun, *J. Am. Chem. Soc.* **2018**, *140*, 9942.

Chapter 4. Surface Chemistry and Purification of $CsPbI_3$ PNCs

4.1 Synopsis

In Chapter 3, it was shown that the α phase of $CsPbI_3$ PNCs could be meta-stabilized effectively using a simple ligand modification of the reaction medium. This modified reaction approach was further found to be suitable for synthesising the broader $CsPbX_3$ family of PNCs. However, the use of these nanocrystals entails post-purification requirements, which are inherently challenging owing to the sensitive nature of PNCs. To date, detailed studies on PNC purification have been mainly focused on its phase-stable $CsPbBr_3$ derivative. These have identified the most suitable anti-solvents for the purification process (methyl-acetate), [1],[2] demonstrated the use of OA and OLA as additives to retain the properties of the PNCs after multiple purification cycles,[3] and established a benzene sulfonic acid based ligand system that supresses the non-radiative trap states of the PNCs and allows the PNCs to withstand multiple purification cycle.[4] In comparison, little has been done towards developing an effective protocol that enables purification of $CsPbI_3$ PNCs while achieving high quality inks with preserved optical and structural properties.

---

[1] Y. Kim, E. Yassitepe, O. Voznyy, R. Comin, G. Walters, X. Gong, P. Kanjanaboos, A. F. Nogueira, E. H. Sargent, ACS Appl. Mater. Interfaces 2015, 7, 25007.

[2] T. Chiba, K. Hoshi, Y.-J. Pu, Y. Takeda, Y. Hayashi, S. Ohisa, S. Kawata, J. Kido, *ACS Appl. Mater. Interfaces* **2017**, *9*, 18054.

[3] J. De Roo, M. Ibáñez, P. Geiregat, G. Nedelcu, W. Walravens, J. Maes, J. C. Martins, I. Van Driessche, M. V. Kovalenko, Z. Hens, *ACS Nano* **2016**, *10*, 2071.

[4] D. Yang, X. Li, W. Zhou, S. Zhang, C. Meng, Y. Wu, Y. Wang, H. Zeng, *Adv. Mater.* **2019**, *1900767*, 1900767.

In this chapter, a facile purification protocol for $CsPbI_3$ PNCs is established through studying the role of different solvents, ligands and additives. The underlying basis of the protocol is the finding that multiple washing steps cause the gradual loss of surface ligand species. To compensate for this ligand loss, the effect of different additives is assessed during the precipitation/redispersion protocol. Ultimately, the addition of a PbI_2 solution containing ligands used with the original solution shows the most promising results, with the optical and structural properties of the NCs being maintained after multiple washing cycles. A critical minimum limit for the additive solution relative to the NCs is determined to maintain their properties. Under such conditions, this facile washing strategy was shown to allow for the production of high quality and high purity $CsPbX_3$ NCs inks. These dispersion properties form essential requirements for integrating these exciting materials into high performance optoelectronic devices.

This entire Chapter has been published as a journal article in *J. Chem. Phys.* **2019**, 151, 121105, DOI: 10.1063/1.5123306.

The Journal of Chemical Physics | COMMUNICATION | scitation.org/journal/jcp

Facile purification of $CsPbX_3$ ($X = Cl^-, Br^-, I^-$) perovskite nanocrystals

Cite as: J. Chem. Phys. 151, 121105 (2019); doi: 10.1063/1.5123306
Submitted: 4 August 2019 • Accepted: 9 September 2019 •
Published Online: 30 September 2019

View Online Export Citation CrossMark

Chujie Wang,[1] Anthony S. R. Chesman,[2] Wenping Yin,[1] Laszlo Frazer,[3] Alison M. Funston,[3] and Jacek J. Jasieniak[1,a)]

AFFILIATIONS

[1]ARC Centre of Excellence in Exciton Science, Department of Materials Science and Engineering, Faculty of Engineering, Monash University, Clayton, VIC 3800, Australia
[2]CSIRO Manufacturing, Ian Wark Laboratories, Bayview Ave., Clayton, VIC 3168, Australia
[3]ARC Centre of Excellence in Exciton Science, School of Chemistry, Monash University, Clayton, VIC 3800, Australia

Note: This paper is part of the JCP Special Topic on Colloidal Quantum Dots.
[a)]**Author to whom correspondence should be addressed:** jacek.jasieniak@monash.edu

ABSTRACT

$CsPbI_3$ perovskite nanocrystals are a promising optoelectronic material when stabilized in their cubic phase. While ongoing efforts have addressed this structural challenge through a variety of meta-stabilization approaches, the postsynthesis purification of these nanocrystal dispersions has remained a challenge. In this article, we undertake a detailed investigation into the chemical, optical, and structural changes that arise during purification of $CsPbI_3$ nanocrystals. It is found that nanocrystal degradation can only be avoided through the judicious control of additives within each purification cycle. Under optimized additive-to-nanocrystal ratios, multiple purification cycles can be readily achieved, while retaining the quality and phase stability of the $CsPbI_3$. This facile purification protocol ensures the preparation of high purity and high quality $CsPbI_3$ nanocrystal inks that are suitable for better characterization or integration in optoelectronic devices. The approach has been generalized for $CsPbX_3$ ($X = Cl^-$, Br^-, and I^-).

https://doi.org/10.1063/1.5123306

Inorganic perovskite nanocrystals (NCs) based on the chemical formula $CsPbX_3$ (X = Cl, Br, and I) have garnered significant interest due to their high photoluminescence quantum yield (PLQY),[1,2] narrow full-width half-maximum (FWHM) PL emission,[2] and defect-tolerant band structure.[3] $CsPbI_3$ is particularly attractive, as its optical bandgap lies in the red emitting region,[1] indicating it may find application in solar cell or red light-emitting diode devices.[4,5] However, for the full potential of these materials to be realized, a facile strategy for preventing their transformation from the cubic (α) perovskite phase to an orthorhombic (δ) phase at room temperature is required.[6] To date, a number of approaches have been employed for achieving phase stabilization, including doping $CsPbI_3$ with Cl^- ions,[7] using specific nonpolar antisolvents during purification,[4] incorporating stabilizing ligands during synthesis,[8] passivating NCs in solution via addition of bidentate ligand species,[9] partially substituting the Cs^+ cation with formamidinium$^+$,[10] and *in situ* polymer encapsulation of the NC film.[11] In general, these strategies act to either modify the effective Goldschmidt tolerance factor or the relative surface to bulk energies to enable α perovskite formation.[12]

Across all of these approaches used to stabilize α-$CsPbI_3$ NCs, a key element that has not been adequately addressed is the postprocessing of these materials to achieve purified NC inks that maintain their optical and structural properties. Instead, the purification studies of perovskite NCs are mainly focused on $CsPbBr_3$.[13–15] Generally, the purification or "washing" process for NCs involves (i) precipitating the NCs from the reaction solution (1-octadecene, ODE) with a polar antisolvent, (ii) isolating the precipitated NCs via centrifugation and decanting the supernatant containing impurities, and (iii) redispersing the NCs in a nonpolar solvent.[1] These three steps constitute a single wash cycle, with multiple wash cycles typically required to adequately purify the NCs of residual precursors, ligands, and solvents.[16] However, the need for multiple wash cycles presents a major challenge for metal halide perovskites because their

surfaces tend to be passivated by weakly bound ligands, typically aliphatic ammonium/amine,[17,18] and the bulk inorganic component is partially soluble in polar solvents owing to its highly ionic bonding character. As a result, during the precipitation of such NCs with an excess of polar solvent, the stabilizing ligands on the surface of the NCs are easily removed,[19] which can result in irreversible aggregation, structural transformation of the NCs to larger sizes, and/or a phase change, resulting in the degradation of their optical properties.

Herein, we report a facile $CsPbI_3$ NC purification protocol that allows for multiple washing cycles, while retaining the quality and phase stability of the NCs. The approach is based on using additives during the washing procedure to balance the surface chemistry requirements. Toward this goal, we have assessed the effects of several different additives, including the ligands used during synthesis, the alkyl ammonium salt and a lead iodide solution. UV-vis absorption and PL spectroscopy, transmission electron microscopy (TEM), scanning transmission electron microscopy (STEM), and X-ray diffraction (XRD) have been used to monitor the optical properties, nanostructure, and phase stability of the NCs after multiple washes, and inductively coupled plasma-mass spectrometry (ICP-MS) and nuclear magnetic resonance (NMR) spectroscopy have been employed to evaluate the NC molar concentration and surface chemistry.

$CsPbI_3$ NCs were synthesized using a modified hot-injection route that involved the mixing of a Cs precursor into a PbI_2-containing solution at elevated temperature (see the supplementary material for details).[1] Briefly, the synthesis used the branched diisooctyl phosphinic acid [DPA, Fig. 1(a)] and oleylamine (OLA) as the ligand sources,[8] with the final Cs:Pb:I:DPA:OLA molar ratios being 0.25:1:2:12.5:10.[20] This synthetic approach produces a crude solution of α-$CsPbI_3$ NCs that exhibits a structural stability greater than four months (Fig. S1), making it a reliable platform for this purification study. We include the absorption and PL spectra of the unwashed NCs diluted in toluene in Fig. 1(b).

To develop an optimized purification protocol, we have trialed various antisolvents for the precipitation of $CsPbI_3$ NCs from the crude reaction solution (Table S1). Methyl-acetate has been widely accepted as an antisolvent for washing the standard oleic acid (OA) synthesized $CsPbI_3$,[4] but it was found to result in phase transformation of our washed NCs within a week, presumably because our NCs have a different surface chemistry due to the usage of DPA. For these NCs, isopropanol (IPA) was found to be the most suitable antisolvent. Following the first wash with IPA, the NC dispersion exhibited a reduction in relative absorbance and a narrowing of the PL peak FWHM from ~120 meV to ~100 meV, although its overall intensity and peak position remained similar [see Fig. 1(b)]. Such an observation indicates that the excessively small NCs were removed during the washing process without any detrimental effects on the optical properties of the remaining NCs. As seen through TEM measurements, these single-washed $CsPbI_3$ NCs were monodisperse cubic particles with an average size of 11.3 ± 1.6 nm [see Fig. 1(c)]. Furthermore, STEM revealed that the NCs exhibited an interplanar spacing of 0.62 nm, which reflects the (100) plane of α phase $CsPbI_3$.

Despite IPA's suitability as an antisolvent for washing the crude $CsPbI_3$ NCs, its use within multiple washing cycles was found to cause the absorption and PL intensity of the NCs to

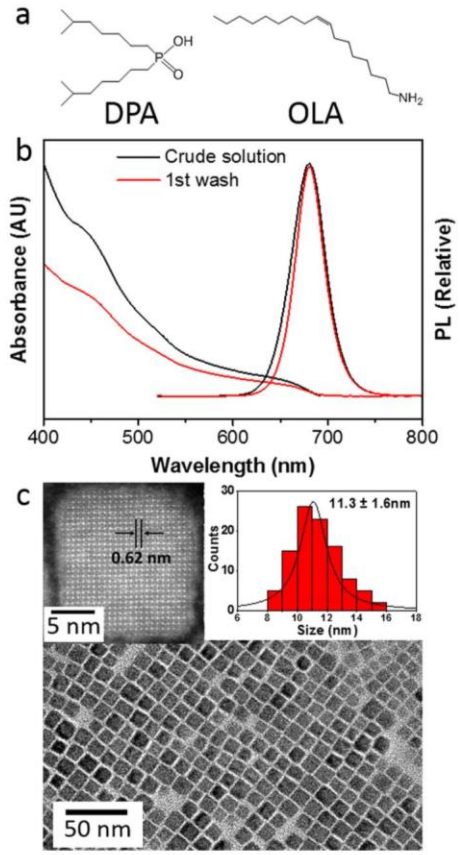

FIG. 1. (a) Chemical structures of diisooctyl phosphinic acid (DPA) and oleylamine (OLA). (b) UV-Vis absorption and photoluminescence spectra for the $CsPbI_3$ NC crude solution. (c) TEM of $CsPbI_3$ NCs synthesized with DPA after one wash cycle with the insets showing STEM of single $CsPbI_3$ NCs with the lattice spacing (left) and histogram of the size distribution of the NC ensemble (right).

gradually decrease [Fig. 2(a)] and become almost negligible after the 3rd wash. Quantitative PL measurements were performed to determine the QY of the samples using Rhodamine 101 as a reference dye.[21] These showed that the PLQY of the NCs dropped from 62% to a mere 7% between the 1st and 3rd wash (Fig. S2). For reference, the PLQY of the crude solution was 65%. The degradation of NCs during this washing process is ascribed to the progressive loss of surface ligands, which causes subsequent aggregation or dissolution. Changes to the ligand concentrations were confirmed using ^{1}H-NMR, which showed that multiple washing steps resulted in a significant reduction in the intensity of the alkene groups of the oleylamine/ammonium ligands (Fig. S3)—the dominant surface binding species in our $CsPbI_3$ NCs.[8] This phenomenon is attributed to the highly ionic nature of the perovskite, which enables the ligands on the NC surface to be in a dynamic exchange between binding and nonbinding states.[17] Because the supernatant containing unbound ligands is discarded following each washing step, a new equilibrium between the bound and unbound ligands is established upon redispersion, resulting in a lower effective bound ligand

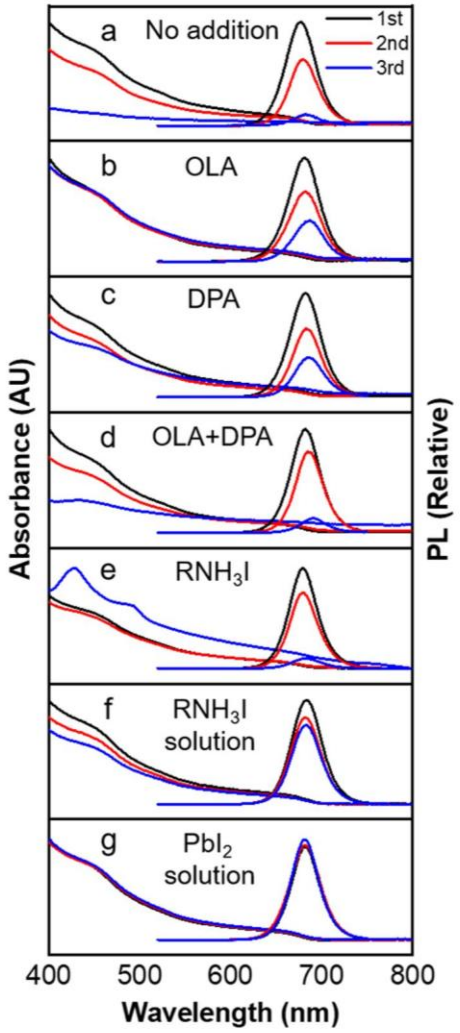

FIG. 2. UV-Vis absorption and PL spectra of NCs after the 1st, 2nd, and 3rd washing cycle with (a) no additive additions, (b) OLA, (c) DPA, (d) OLA and DPA, (e) hexadecylammonium iodide (RNH_3I), (f) RNH_3I with OLA and DPA, referred to as "RNH_3I solution," and (g) PbI_2 with OLA and DPA, referred to as "PbI_2 solution."

concentration. After multiple wash cycles, the progressive ligand loss eventually causes insufficient surface passivation on the NCs, leading to degradation of their structural and optical properties.

One simple strategy for addressing this ligand loss has been demonstrated for $CsPbBr_3$ NCs by compensating additional OLA and OA ligands during the purification process.[17] Here, we have assessed a similar strategy by using the native ligands in the form of OLA, DPA, or a mixture of both as additives within the toluene redispersion before the next wash cycle (see the supplementary material). When OLA was added, the absorption was preserved, but the PL intensity exhibited a gradual loss [Fig. 2(b)]. A similar trend in PL reduction was observed with the addition of DPA [see Fig. 2(c)], although the absorption was not preserved after multiple washes due to partial NC dissolution. When the two ligands were added together, the relative PL intensity loss and reduction in absorption was greater than for any of the individual ligands. This observation is in accordance with a previous report that indicated acid-base pairs (i.e., OLA^+-DPA^-) can effectively dissolve $CsPbX_3$ NCs.[22]

Evidently, during NC synthesis, iodide is also present in the reaction mixture. As such, we have also assessed the role of additional alkyl ammonium iodide within the solution. We synthesized hexadecylammonium iodide for this purpose owing to its higher purity compared to the OLA analog used within the synthesis. However, the addition of this RNH_3I to the washing process yielded additional absorption peaks at lower wavelengths and enhanced scattering [Fig. 2(e)], indicating a partial α-to-δ phase transformation.

Regardless of the additives introduced during the washing procedure, the first wash (precipitation directly from the crude solution) always gave the best absorption and PL characteristics. This suggests that mimicking the "crude solution condition" is the key for washing NCs multiple times. Therefore, we prepared an "RNH_3I solution" in toluene that featured a combination of RNH_3I+DPA+OLA in a similar molar ratio to the synthesis solution of 1:5:5. Unfortunately, the introduction of the RNH_3I solution into the washing process was still found to result in NC instability [Fig. 2(f)].

Given the lead-rich synthetic conditions, we then formulated a "PbI_2 solution" with a Pb:I:DPA:OLA molar ratio of 1:2:10:10 (see the supplementary material). Unlike all the other additives assessed here, the addition of the "PbI_2 solution" enabled the absorption and PL properties of the NC to be almost perfectly preserved after three wash cycles [Fig. 2(g)]. Further spectroscopic investigations into the "PbI_2 solution" washed NCs revealed that the PLQYs between the 1st and 3rd washing steps actually increased between 64% and 70%, respectively. With previous reports indicating a positive correlation between perovskite NC PLQY and halide content,[23] we have measured the iodide content of the NCs using Energy Dispersive X-ray (EDX, Fig. S4) spectroscopy. These measurements showed that the overall atomic percentage of the iodide gradually increased from 54% to 60% between the 1st and 3rd washes, confirming that a halide rich environment is indeed conducive for achieving a higher PLQY.

TEM was employed to further characterize the effect of the different additives during washing on the $CsPbI_3$ NC ensembles. As shown in Fig. 3(a), NCs washed a single time with neat IPA have a cubic structure with excellent monodispersity. Following a second washing step without any additives, the NCs were found to significantly coarsen and aggregate [Fig. 3(b)]. This is consistent with major ligand loss during this process. The extent of aggregation was reduced when different additives were used during the washing process [Figs. 3(c)–3(g)]; however, consistent with their optical measurements, the enhanced inhomogeneity of the NCs confirmed that none of the additives effectively stabilized the NCs. The use of the PbI_2 solution exhibited the most favorable washing conditions; the second wash [Fig. 3(h)] and the third wash (Fig. S5) yielded well-dispersed cubic NCs with a comparable size distribution (~11 nm) to the first wash. These TEM results demonstrate that the use of the PbI_2 solution during washing provides an advantageous chemical environment for the NCs, thus allowing for multiple washing cycles, while retaining their monodispersity. For

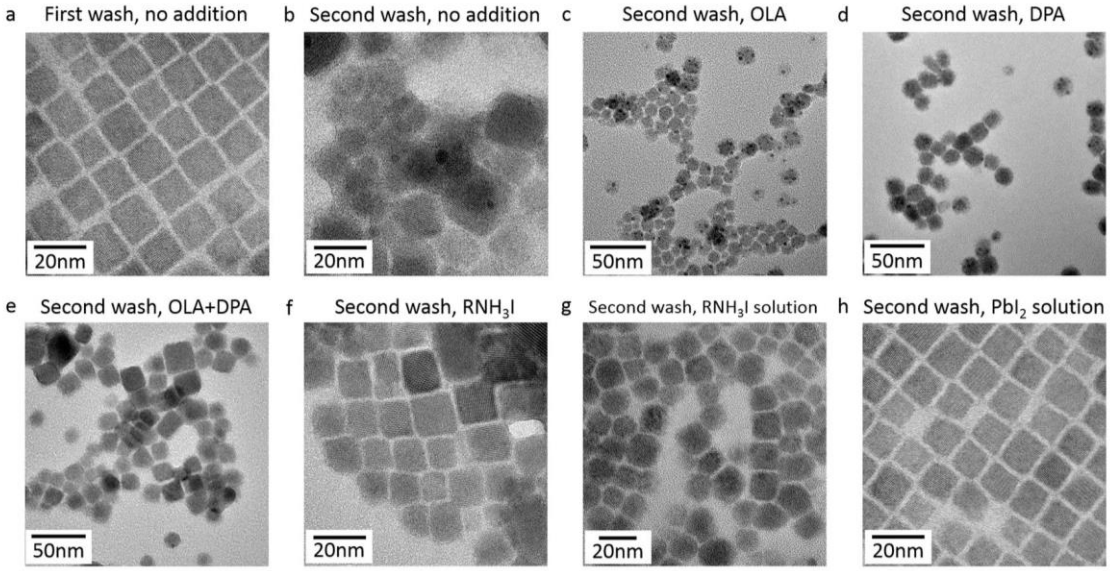

FIG. 3. TEM images for the $CsPbI_3$ NCs after various additions of washing additives during purification. (a) 1st wash, no additions, and 2nd wash with (b) no additions, (c) OLA, (d) DPA, (e) OLA+DPA, (f) RNH_3I, (g) RNH_3I solution, and (h) PbI_2 solution.

completeness, we also monitored the long term phase stability of the "PbI_2 solution" washed NCs with XRD. As shown in Fig. S6, a comparison of the XRD patterns between those freshly made and after storage for 20 days under ambient conditions exhibits identical diffraction patterns, with no δ-phase detected.

We note that under these purification conditions the structural and optical properties of the NCs could be retained even after 10 washing steps (Fig. S7), suggesting that it is a robust approach to maintain the delicate equilibrium between surface bound and solution species. Furthermore, to demonstrate the generality of this washing process, we have applied the same washing protocol to both $CsPbCl_3$ and $CsPbBr_3$ NCs using analogous $PbCl_2$ and $PbBr_2$ solutions, respectively (Fig. S8). For $CsPbCl_3$, the absorption was preserved, albeit with a slight reduction in PL, while for $CsPbBr_3$ NCs, both the absorption and PL characteristics were retained. It is important to put the slight relative PL reduction for $CsPbCl_3$ into context because its absolute PLQY is very low (<4%) compared to both $CsPbBr_3$ and $CsPbI_3$ (>60%). As such, this represents a very minor change in absolute PLQY, which is consistent with bulk defects dominating the emissions processes in $CsPbCl_3$.[24]

To examine the versatility of this purification protocol, we have also washed the conventional OA-synthesized $CsPbX_3$ NCs with an analogous PbX_2 solution, albeit using OA instead of DPA, and using the widely accepted methyl-acetate as the antisolvent. As shown in Fig. S9, this approach appears favorable for retaining the absorption and luminescence of $CsPbBr_3$; however, this is not the case for both $CsPbCl_3$ and $CsPbI_3$ NCs, which show a progressive deterioration in optical properties and, for the latter, also resulting in poor phase stability (converting in 3 days). This difference between DPA and OA based washing solutions likely arises from the variation in the steric nature of these ligands, extent of surface passivation, acidity, and/or solubility of the resulting salts, although understanding the interplay between these is outside of this work's scope.

Given that an equilibrium must exist between surface bound and solution species, we probed the effective concentration limits of these washing additives to optimize the amount of PbI_2 solution required to retain the $CsPbI_3$ NC properties following purification. To do this, we first determined the NC concentration, [NC], using ICP-MS measurements and the average NCs size (see Table S2 for calculation). We then used the concentration of the NC after the 1st wash, $[NC_{1st\ wash}]$, and the corresponding absorption measurements to approximate the wavelength-dependent molar-extinction coefficient and absorption coefficient of our $CsPbI_3$ NCs, which is shown in Fig. S10. To further probe the interaction between the additives and the NC surfaces, we estimated the molarity of the total Cs^+ or Pb^{2+} ions at the NC surface, [Surface Ions], by calculating the relative percentage of these ions vs bulk (~30%, see the supplementary material). Using these concentration values, we then assessed the PLQY of NCs washed after 3 cycles with controlled amounts of PbI_2 solution added as a function of $[PbI_2]/[NC_{1st\ wash}]$ and $[PbI_2]$/[Surface Ions] [Fig. 4(a)]. The results show that when the $[PbI_2]/[NC_{1st\ wash}] < \sim 3000$ or $[PbI_2]$/[Surface Ions] < ~1.7, the NCs exhibit instability. The reduced absorption [Fig. 4(b)] at these low additive levels confirms the partial removal of NCs through either their aggregation or dissolution during the washing process. In contrast, at higher additive levels, a PLQY of 70% was stabilized and no further changes in absorption were observed. We note that in the typical synthesis crude solution, for which the $[NC] \sim 1.1 \times 10^{-6}$ M, the $[PbI_2]/[NC]$ is around 20 000. This is consistent with the first

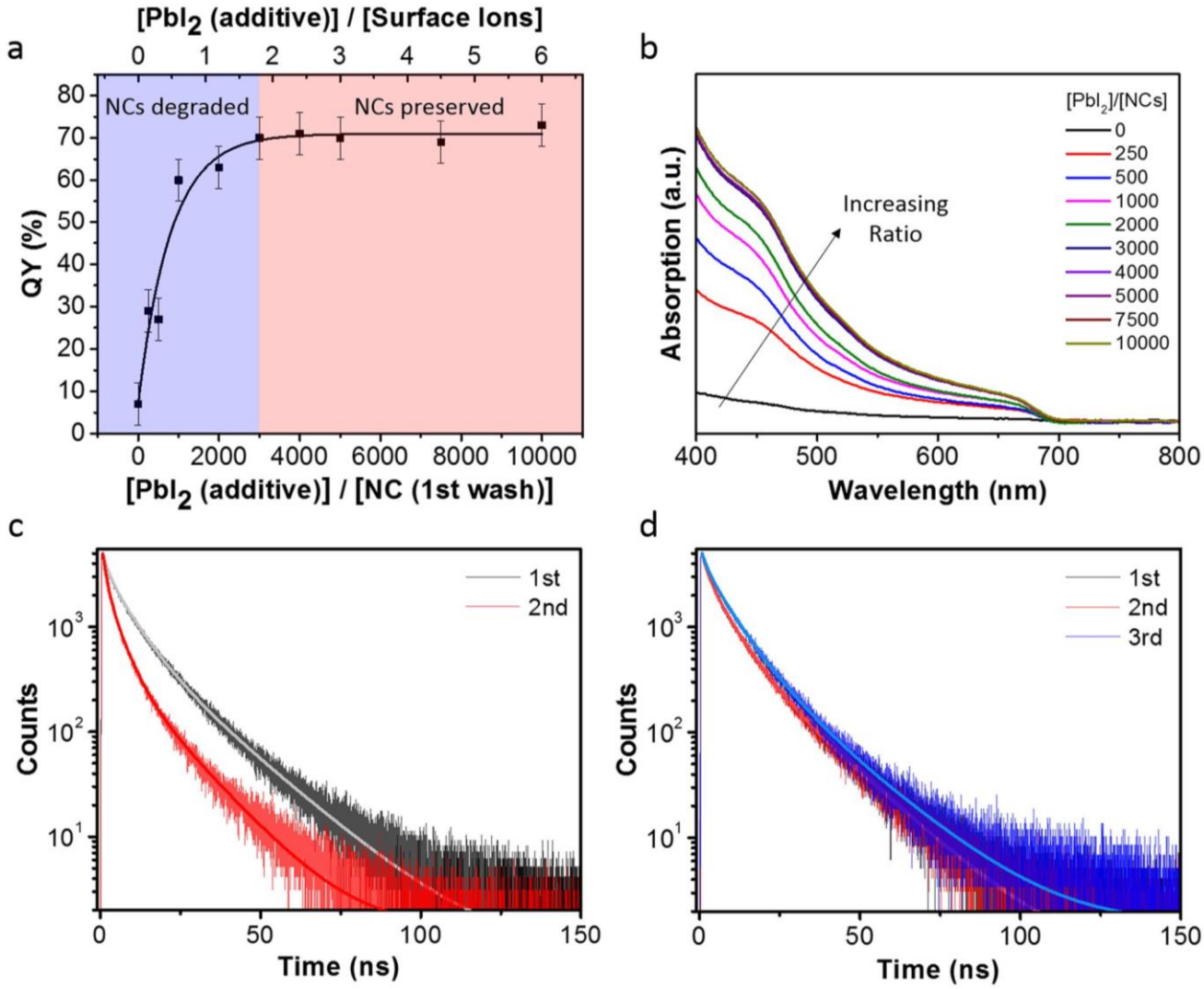

FIG. 4. Correlation between (a) the PLQY and (b) the absorption change of NCs after the 3rd wash against different molar ratios of added PbI_2 in the "PbI_2 wash solution" and the concentration of the NCs after the 1st wash. Time resolved photoluminescence (TRPL) measurements and the fitting curves for $CsPbI_3$ NCs after (c) the 1st and 2nd washing steps with no additional additives and (d) after the 1st, 2nd, and 3rd washing steps with the PbI_2 solution.

wash always yielding high quality NC dispersions that retain their optical properties.

We further tracked the impact of the washing process on the optical properties of the NCs by conducting time-resolved PL (TRPL) measurements (fitting details are in Table S3). For cycles featuring no additives during washing [Fig. 4(c)], the average lifetime significantly decreased between the 1st and 2nd washing steps from 6.7 ns to 3.0 ns. After the 3rd wash, the degradation of NCs was extremely fast under the required dilution preventing effective TRPL measurements. In contrast, but consistent with the slight increase in PLQY, processing using an optimal $[PbI_2]/[NC_{1st\ wash}] = 30\,000$, yielded similar PL lifetimes after the 1st, 2nd, and 3rd wash [Fig. 4(d)] of 5.8, 6.0, and 7.5 ns, respectively. These results confirm that washing with neat IPA yields an increase in nonradiative trap states, while employing the PbI_2 solution acts to preserve the NC bulk and surface properties.

Having shown that the use of PbI_2 solution effectively preserves the optical properties and nanostructure of the $CsPbI_3$ NCs over multiple washing cycles, we further investigated the surface chemistry of the NCs with NMR spectroscopy. First, as the presence of ODE creates difficulties in characterizing OLA species,[17] we monitored its removal by performing ^{1}H-NMR spectroscopy on NC dispersions after the 1st, 2nd, and 3rd washing cycles with the PbI_2 solution at a $[PbI_2]/[NC_{1st\ wash}]$ of 30 000 (Fig. S11 and full spectra in Figs. S12–S14). The distinct NMR resonance peaks of the terminal alkene group of ODE located at 5.0 and 5.8 ppm remain after the

1st wash but become negligible after the 3rd wash, indicating the successful removal of ODE. Meanwhile, the presence of OLA was confirmed by the broad peak at 5.5 ppm (denoted as * in Fig. S11), arising from its alkene resonance.[25] The average binding affinity of the oleylamine/oleylammonium species was measured with diffusion ordered NMR spectroscopy (DOSY), and diffusion coefficients of 524 and 345 $\mu m^2\ s^{-1}$ were obtained for the species contained in solutions of NCs washed once and three times, respectively. As a comparison, the diffusion coefficient for free oleylamine was measured as 1068 $\mu m^2\ s^{-1}$. Meanwhile, using the Stokes-Einstein equation and considering NCs with a tightly bound oleylamine shell of an overall diameter of ~12 nm, we calculated the nominal diffusion coefficient to be only 49 $\mu m^2\ s^{-1}$ (see the supplementary material). As the experimentally obtained diffusion coefficient is the weighted average between the tightly bound and free species, the decrease in diffusion coefficient demonstrates that after multiple washes the portion of OLA which is free is reduced.[26] For completeness, we have also calculated the effective total ligand density of the 1st and 3rd washed samples to be 4.6 nm^{-2} and 2.9 nm^{-2}, respectively (see the supplementary material for details). This effective decrease in ligand density supports the notion of a lower concentration of free ligands within the 3rd washed sample, reaching a value that is consistent with those reported for $CsPbBr_3$.[17]

The above analyses highlight the sensitivity of $CsPbI_3$ nanocrystals to their purification conditions. We consolidate these results in Fig. 5 by schematically depicting the effect of the different additives investigated here on the NC dispersion. Evidently, in the crude solution of $CsPbI_3$ NCs, free OLA, DPA, their conjugates, alkyl ammonium iodide, and DPA-lead complexes act to stabilize the NC surface. We have shown that unless all of these chemical species are introduced into the washing solution, and at a sufficient concentration, the NCs tend to lose their surface capping ligands, causing them to dissolve, aggregate, or transform into the δ-phase. This indicates that a complicated equilibrium involving ligands, lead ions, and iodide species must exist between the surface and solution, and only by preserving its balance, can the optical and structural properties of the NCs be maintained. This purification approach has been extended across the $CsPbX_3$ NC family, demonstrating its generalized and facile nature for the production of high quality and high purity perovskite NC inks. Achieving this dispersion state is essential to carrying out reliable fundamental studies of perovskite NC structure-property relations and, ultimately, their integration into high-efficiency and reproducible optoelectronic devices.

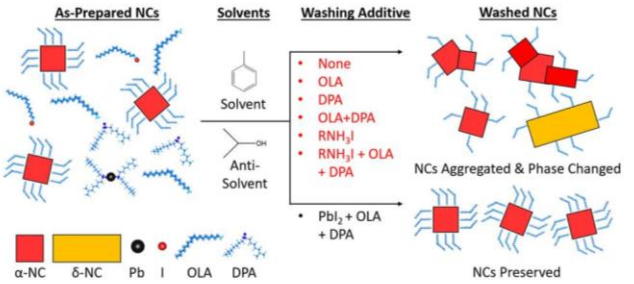

FIG. 5. Schematic illustration of how different additives used for purifying α-$CsPbI_3$ NCs from within a toluene solvent and IPA antisolvent mixture affect the nanocrystal dispersion.

See the supplementary material for experimental methods of the synthesis, purification procedure, characterization techniques, additional tables, photos, and data of UV-vis absorption and PL spectra, TEM, EDX, ICP, NMR, XRD, etc. (PDF).

This work was funded by the Australian Research Council funded Center of Excellence in Exciton Science (Grant No. CE170100026). We thank the staff in the Monash Centre of Electron Microscopy, Monash X-ray platform, and CSIRO NMR and ICP facility for their support.

The authors declare no competing financial interests.

REFERENCES

[1] L. Protesescu, S. Yakunin, M. I. Bodnarchuk, F. Krieg, R. Caputo, C. H. Hendon, R. X. Yang, A. Walsh, and M. V. Kovalenko, Nano Lett. **15**, 3692 (2015).
[2] A. Swarnkar, R. Chulliyil, V. K. Ravi, M. Irfanullah, A. Chowdhury, and A. Nag, Angew. Chem., Int. Ed. **54**, 15424 (2015).
[3] J. Kang and L. W. Wang, J. Phys. Chem. Lett. **8**, 489 (2017).
[4] A. Swarnkar, A. R. Marshall, E. M. Sanehira, B. D. Chernomordik, D. T. Moore, J. A. Christians, T. Chakrabarti, and J. M. Luther, Science **354**, 92 (2016).
[5] C. C. Lin, A. Meijerink, and R. S. Liu, J. Phys. Chem. Lett. **7**, 495 (2016).
[6] S. Dastidar, C. J. Hawley, A. D. Dillon, A. D. Gutierrez-Perez, J. E. Spanier, and A. T. Fafarman, J. Phys. Chem. Lett. **8**, 1278 (2017).
[7] S. Dastidar, D. A. Egger, L. Z. Tan, S. B. Cromer, A. D. Dillon, S. Liu, L. Kronik, A. M. Rappe, and A. T. Fafarman, Nano Lett. **16**, 3563 (2016).
[8] C. Wang, A. S. R Chesman, and J. J. Jasieniak, Chem. Commun. **53**, 232 (2017).
[9] J. Pan, Y. Shang, J. Yin, M. De Bastiani, W. Peng, I. Dursun, L. Sinatra, A. M. El-Zohry, M. N. Hedhili, A. H. Emwas, O. F. Mohammed, Z. Ning, and O. M. Bakr, J. Am. Chem. Soc. **140**, 562 (2018).
[10] L. Protesescu, S. Yakunin, S. Kumar, J. Bär, F. Bertolotti, N. Masciocchi, A. Guagliardi, M. Grotevent, I. Shorubalko, M. I. Bodnarchuk, C.-J. Shih, and M. V. Kovalenko, ACS Nano **11**, 3119 (2017).
[11] K. Chen, X. Deng, G. Dodekatos, and H. Tüysüz, J. Am. Chem. Soc. **139**, 12267 (2017).
[12] A. Dutta and N. Pradhan, ACS Energy Lett. **4**, 709 (2019).
[13] Y. Kim, E. Yassitepe, O. Voznyy, R. Comin, G. Walters, X. Gong, P. Kanjanaboos, A. F. Nogueira, and E. H. Sargent, ACS Appl. Mater. Interfaces **7**, 25007 (2015).
[14] T. Chiba, K. Hoshi, Y.-J. Pu, Y. Takeda, Y. Hayashi, S. Ohisa, S. Kawata, and J. Kido, ACS Appl. Mater. Interfaces **9**, 18054 (2017).
[15] D. Yang, X. Li, W. Zhou, S. Zhang, C. Meng, Y. Wu, Y. Wang, and H. Zeng, Adv. Mater. **31**, 1900767 (2019).
[16] C. K. Ng, C. Wang, and J. J. Jasieniak, Langmuir **35**, 11609 (2019).
[17] J. De Roo, M. Ibáñez, P. Geiregat, G. Nedelcu, W. Walravens, J. Maes, J. C. Martins, I. Van Driessche, M. V. Kovalenko, and Z. Hens, ACS Nano **10**, 2071 (2016).
[18] V. K. Ravi, P. K. Santra, N. Joshi, J. Chugh, S. K. Singh, H. Rensmo, P. Ghosh, and A. Nag, J. Phys. Chem. Lett. **8**, 4988 (2017).
[19] J. Li, L. Xu, T. Wang, J. Song, J. Chen, J. Xue, Y. Dong, B. Cai, Q. Shan, B. Han, and H. Zeng, Adv. Mater. **29**, 1603885 (2016).
[20] I. Lignos, S. Stavrakis, G. Nedelcu, L. Protesescu, A. J. Demello, and M. V. Kovalenko, Nano Lett. **16**, 1869 (2016).
[21] R. F. Kubin and A. N. Fletcher, J. Lumin. **27**, 455 (1982).
[22] G. Almeida, L. Goldoni, Q. Akkerman, Z. Dang, A. H. Khan, S. Marras, I. Moreels, and L. Manna, ACS Nano **12**, 1704 (2018).

Supplementary Figures and information

$CsPbI_3$ Crude solution Stability

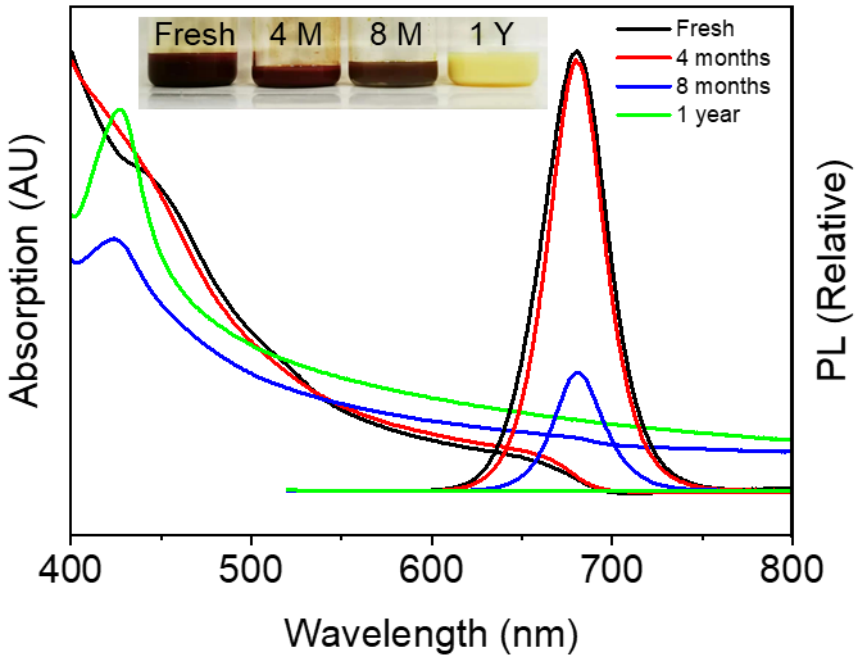

Figure 4S- 1. UV-Vis absorption and photoluminescence spectra for $CsPbI_3$ NC crude solutions that hves been stored for different times, inset: the corresponding photos for the different crude solutions.

Anti-Solvent Treatments

Table 4S- 1. The effect of different polar anti-solvents after the first wash. Ratio of crude solution to anti-solvent is 1:3 for all candidates.

	Anti-Solvent	Effect	Supernatant Transparency	Cubic phase Stability
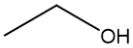	Ethanol	Caused aggregation	Slight Yellow	N/A
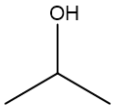	Iso-propanol	Preserved NCs	Slight Yellow	10 days+
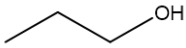	1-butanol	Caused phase transformation	N/A	N/A
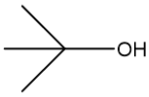	Tert-Butanol	Preserved NCs	Light red	10 days
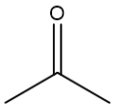	Acetone	Caused phase transformation	N/A	N/A
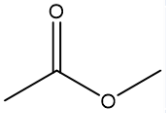	Methyl-Acetate	Preserved NCs	Colourless	7 days
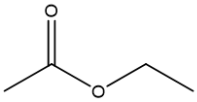	Ethyl-Acetate	Preserved NCs	Red	7 days
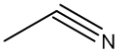	Acentonitrile	Preserved NCs	Red	10 days+

PLQY of NC solutions featuring different Additives

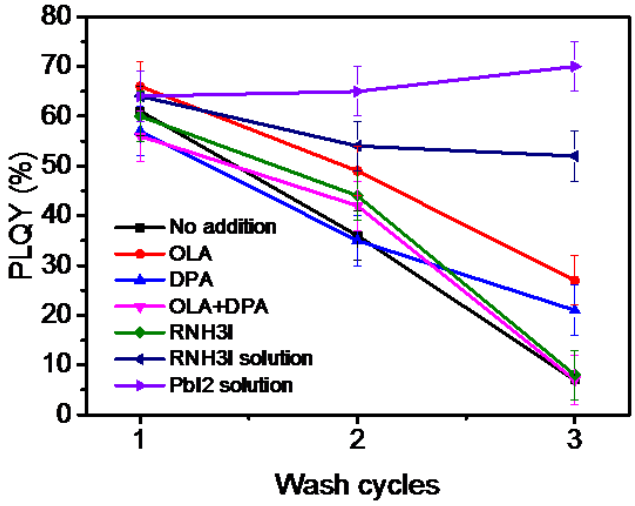

Figure 4S- 2. Evolution of the photoluminescence quantum yield of the $CsPbI_3$ NCs after the 1st, 2nd and 3rd washes with no, OLA, DPA or both, and PbI_2 solution as additive.

NMR Tracking of ODE content

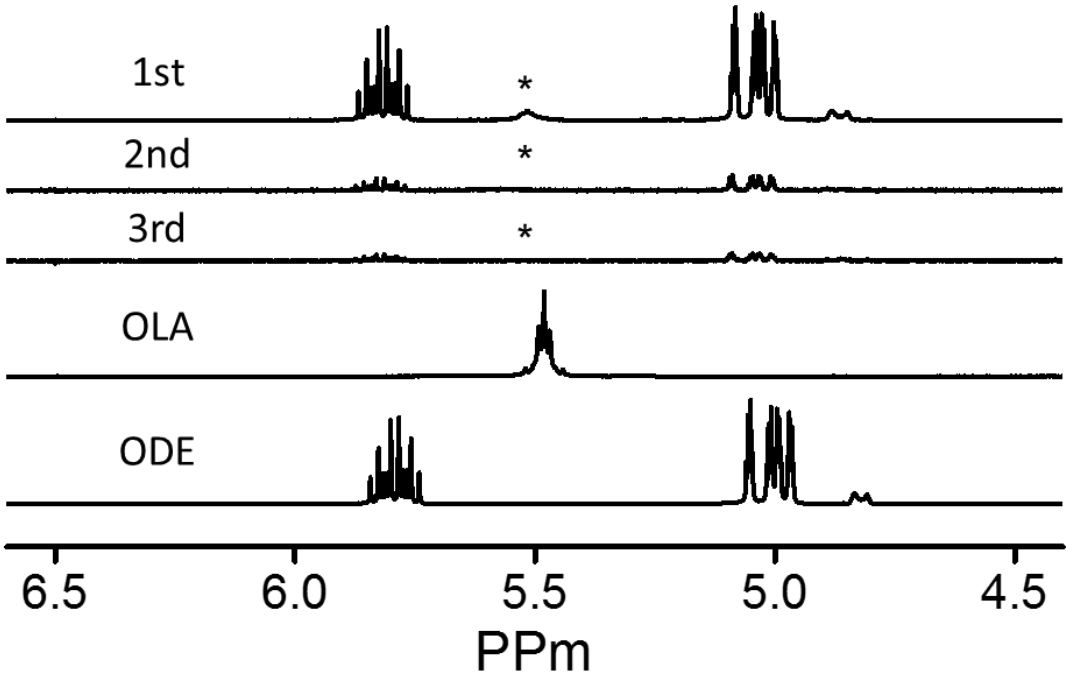

Figure 4S- 3. ^{1}H-NMR spectra $CsPbI_3$ NC solution after 1st, 2nd, and 3rd wash cycles, and the characteristic peaks of neat OLA and ODE.

EDX of $CsPbI_3$ NCs

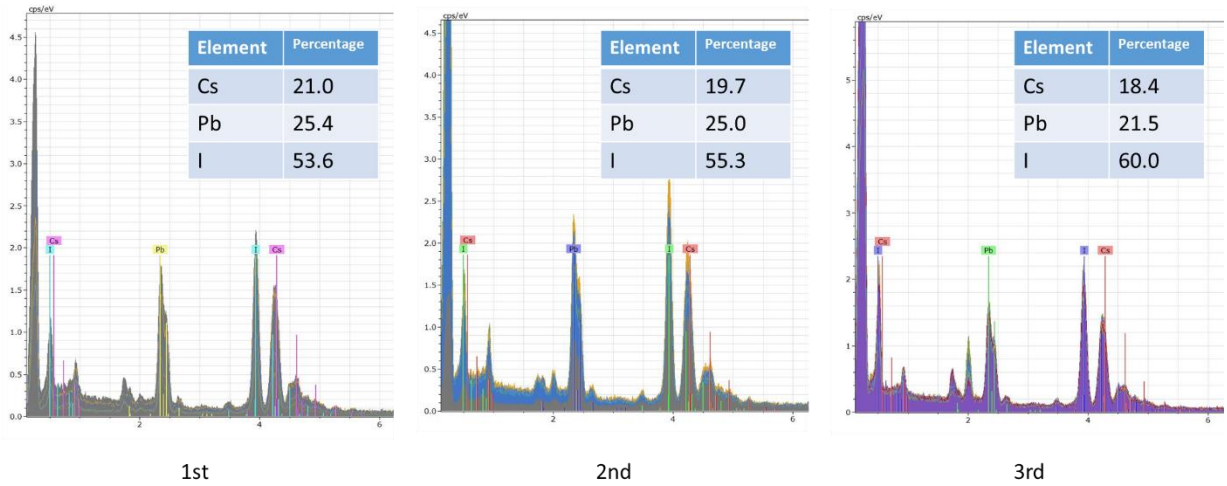

Figure 4S- 4. Energy Dispersive X-ray (EDX) measurements of $CsPbI_3$ NC solutions washed 1, 2 or 3 times with PbI_2 solution.

TEM of $CsPbI_3$ multiple Washing Steps

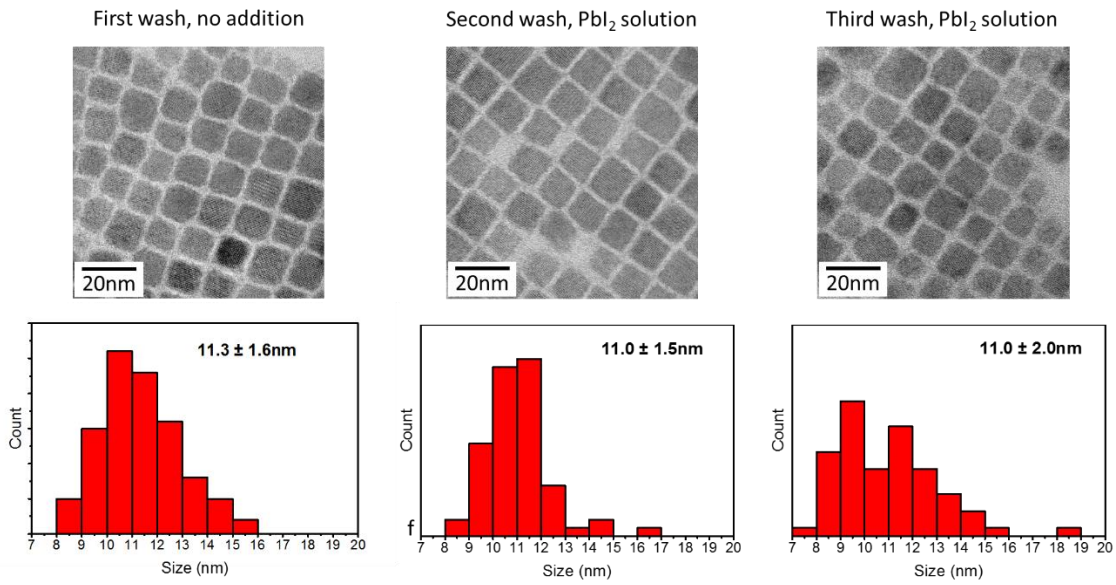

Figure 4S- 5. Size distribution of the $CsPbI_3$ NCs after 1, 2 and 3 wash cycles with the PbI_2 additive solution.

XRD Patterns of $CsPbI_3$ after multiple Washing cycles

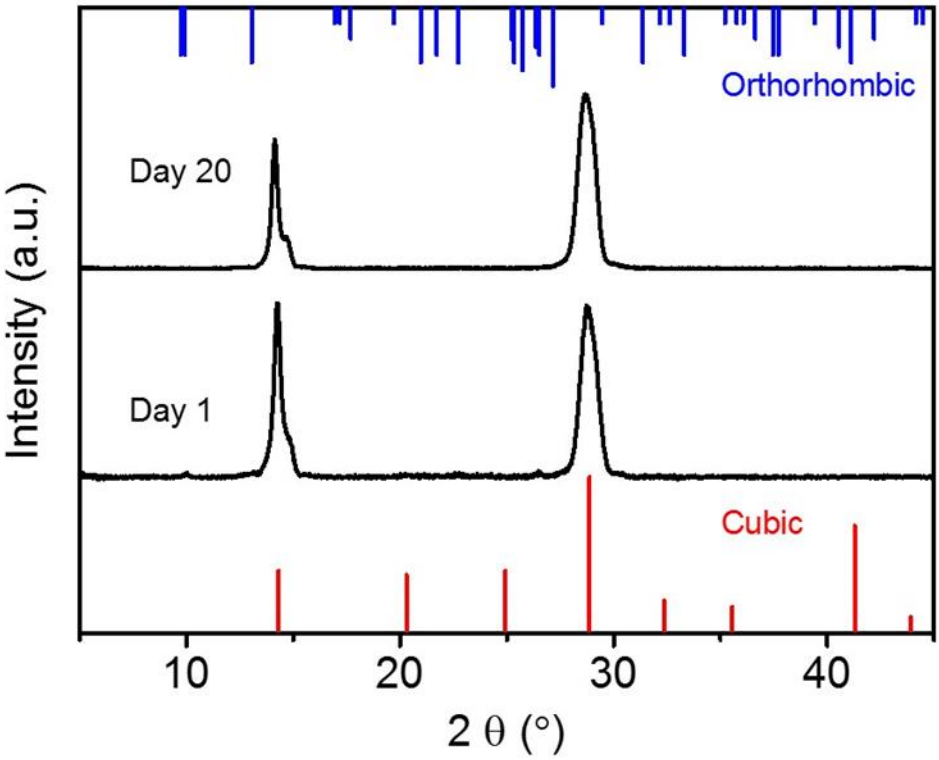

Figure 4S- 6. XRD patterns of $CsPbI_3$ NCs washed three times with PbI_2 added during the washing procedure. PDF card for standard orthorhombic phase $CsPbI_3$: 00-018-0376, cubic phase $CsPbI_3$: 01-080-4039. Notably, only the (100) and (200) planes at 2θ = 14° and 28° were observed, which is consistent with preferential alignment of the crystals.[1],[2] This presumably arose from the oriented attachment of the NCs during the deposition process, which requires further investigation.

Absorption, PL and TEM of $CsPbI_3$ NCs Washed 1 and 10 times

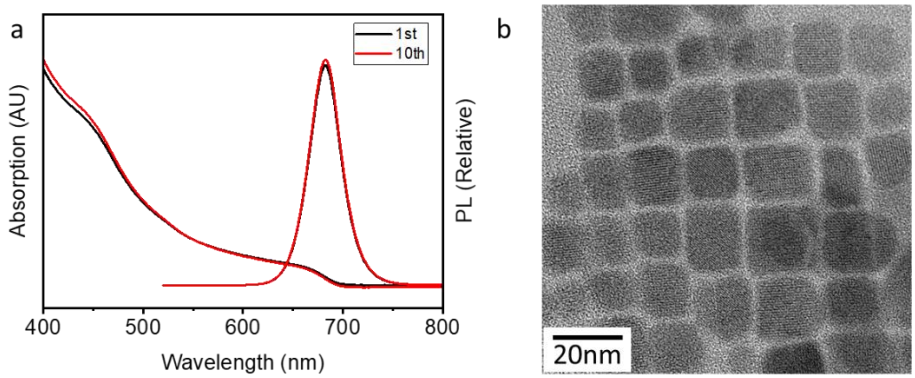

Figure 4S- 7. (a) Absorption and PL spectra of $CsPbI_3$ NC solutions that have been washed 1 (black) and 10 (red) times with PbI_2 solution, (b) the corresponding TEM image for the 10 times washed NCs. For this washing procedure we utilised a $[PbI_2]/[NC_{1st\ wash}]$ ratio of 6000.

Comparison of Washing Effectiveness for $CsPbX_3$

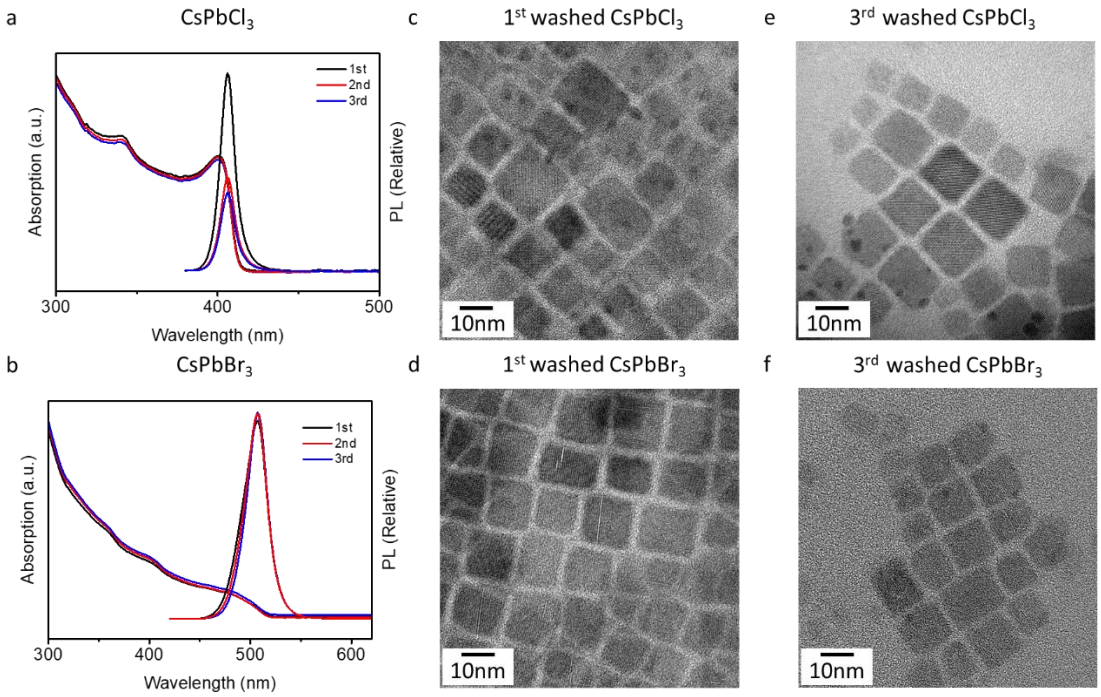

Figure 4S- 8. Absorption and PL spectra of the (a) $CsPbCl_3$ and (b) $CsPbBr_3$ NCs that have been washed 1, 2 and 3 times with $PbCl_2$ and $PbBr_2$ solutions as the additives, respectively. TEM for the corresponding 1st wash and 3rd wash (c), (e) $CsPbCl_3$, (d), (f) $CsPbBr_3$ NCs.

Washing of the conventional $CsPbX_3$-OA

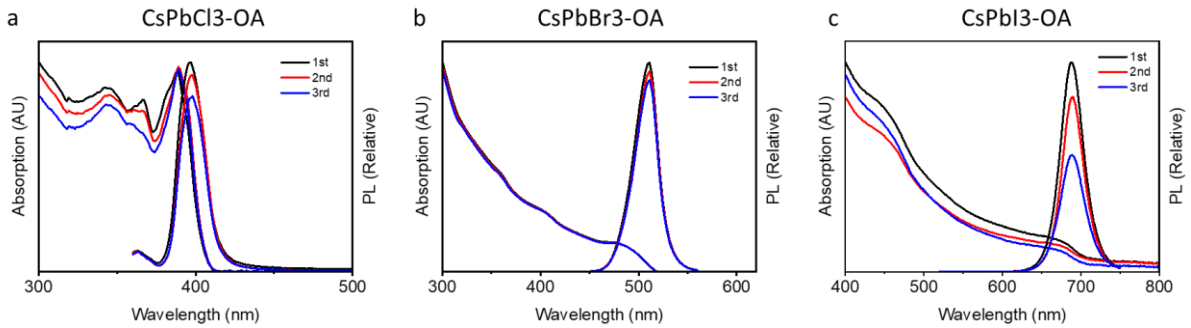

Figure 4S- 9. The absorption and PL spectra for (a) $CsPbCl_3$-OA NCs, (b) $CsPbBr_3$-OA NCs, (c) $CsPbI_3$-OA NCs that have been washed 1st, 2nd and 3rd times with the $PbCl_2$, $PbBr_2$ and PbI_2 solution, respectively. The PbX_2 is dissolved in OA and OLA at the same salt: acid: amine ratio as described in the main text.

ICP-MS

Table 4S- 2. The concentration of Cs element measured using ICP-MS data for $CsPbI_3$ NC washed after different washing cycles with the TEM measured nanocrystals size, calculated number of Cs^+ ions per nanocrystals and the corresponding NC concentration.

Washing cycles	Cs concentration (mol/L)	Size (nm)	Number of Cs atoms in single NC	NC molar concentration (mol/L)
1st	6.32E-03	11.3±1.6	6100	1.03E-06
2nd	6.19E-03	11.0±1.5	5640	1.09E-06
3rd	6.12E-03	11.0±2.0	5640	1.08E-06

Determination of [NC] and [Surface States]

Because no Cs is introduced during the washing process, the Cs concentration [Cs] is measured to monitor the change in $CsPbI_3$ concentration. The [Cs] is 6.81mmol/L and 6.32 mmol/L for the crude and first wash sample, thus 90% of the NC is retained after the first wash.

To calculate the molar concentration of NC, the number of Cs atom in a single NC need to be estimated. Based on the size (d) of the NCs and the 0.62nm interplanar distance of the (100) plane of $CsPbI_3$, the number of Cs atoms in a single edge is calculated by:

$$Cs\ per\ edge = d/0.62$$

Considering the NC to be a perfect cube, the total number of Cs atoms (n_{cs}) in one cube is therefore:

$$n_{cs} = (\frac{d}{0.62})^3$$

With the n estimated, the [NC] is then given by:

$$[NC] = \frac{[Cs]}{n_{Cs}}$$

The 1st washed NC molar concentration [$NC_{1st\ washed}$] is then used to determine their wavelength dependent molar extincition coefficient through the Beer-Lambert equation :

$$A = \varepsilon[NC]L$$

Where A is the absorption, ε (M^{-1} cm^{-1}) is the extinction coefficient, L is the length of the cuvette (1cm).

The ε is also converted to the the absorption coefficient α (cm^{-1}) based on the equation: [3]

$$\alpha = \frac{\varepsilon \times 1000 \times \ln(10)}{N_A \times V_{NC}}$$

In which N_A is the Avogadro number, V_{NC} is the volume of the NC. The calculated ε and α are given in **Figure 4S- 10**. The calculated α value is in line with other report on the $CsPbI_3$ thin film.[4]

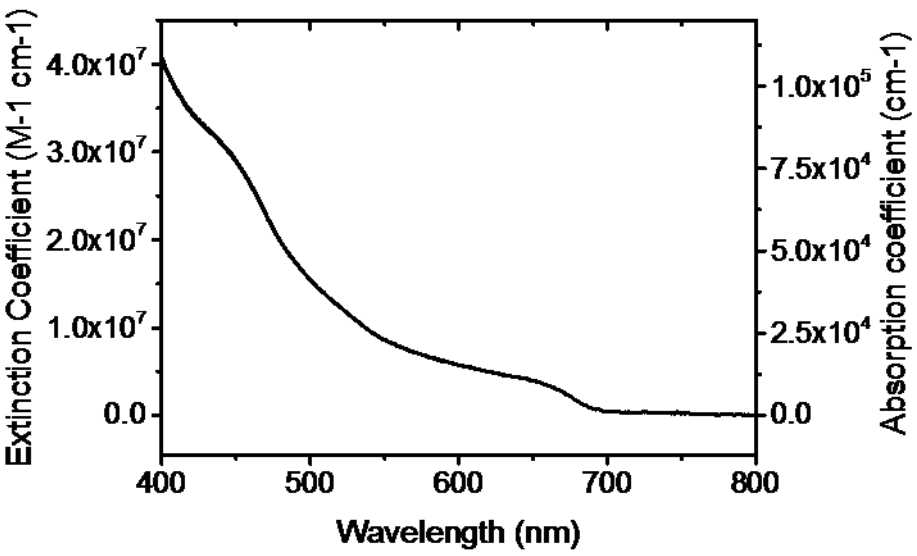

Figure 4S- 10. Wavelength dependent molar extinction coefficient and absorption coefficient spectrum for the 1st washed $CsPbI_3$ NCs.

The molarity of surface ions [Surface ions] are estimated by the number of surface Cs/Pb ions, which is calculated from the relative percentage of these ions versus bulk:

$$\frac{Surface\ ions}{Total\ ions} = \frac{6 \times (\frac{d}{0.62})^2 - 12 \times \frac{d}{0.62}}{(\frac{d}{0.62})^3} \approx 30\%$$

So the [Surface ions] is given by:

$$[Surface\ ions] = [Cs] \times 30\%$$

TRPL Analysis

Table 4S- 3. The fitting result and the calculation of the average lifetime for the NCs that has been washed 1st and 2nd with no additions, or washed 1st, 2nd and 3rd times with the PbI_2 additive solution.

Samples		A_1(%)	τ_1(ns)	A_2(%)	τ_2(ns)	A_3(%)	τ_3(ns)	τ_{avg}(ns)
No addition	1st	35.55	1.68	48.06	6.84	16.39	16.92	6.66
	2nd	57.17	1.13	36.01	4.06	6.82	13.13	3.00
	3rd	--	--	--	--	--	--	--
PbI_2 solution addition	1st	38.51	1.28	42.54	5.86	18.95	14.98	5.82
	2nd	38.82	1.77	48.02	6.62	13.16	16.43	6.02
	3rd	26.23	1.86	59.56	7.65	14.21	17.55	7.54

The fitting is done through a triple exponential model:

$$I(t) = A_1\exp(-t/\tau_1) + A_2\exp(-t/\tau_2) + A_3\exp(-t/\tau_3).$$

Where I(t) is the intensity, τ_1, τ_2, τ_3 are the lifetime of the first and second component, A_1, A_2, A_3 are the amplitude of the first and second component.

And the average lifetime τ_{avg} is given by:

$$\tau_{avg} = A_1\tau_1 + A_2\tau_2 + A_3\tau_3$$

NMR Results

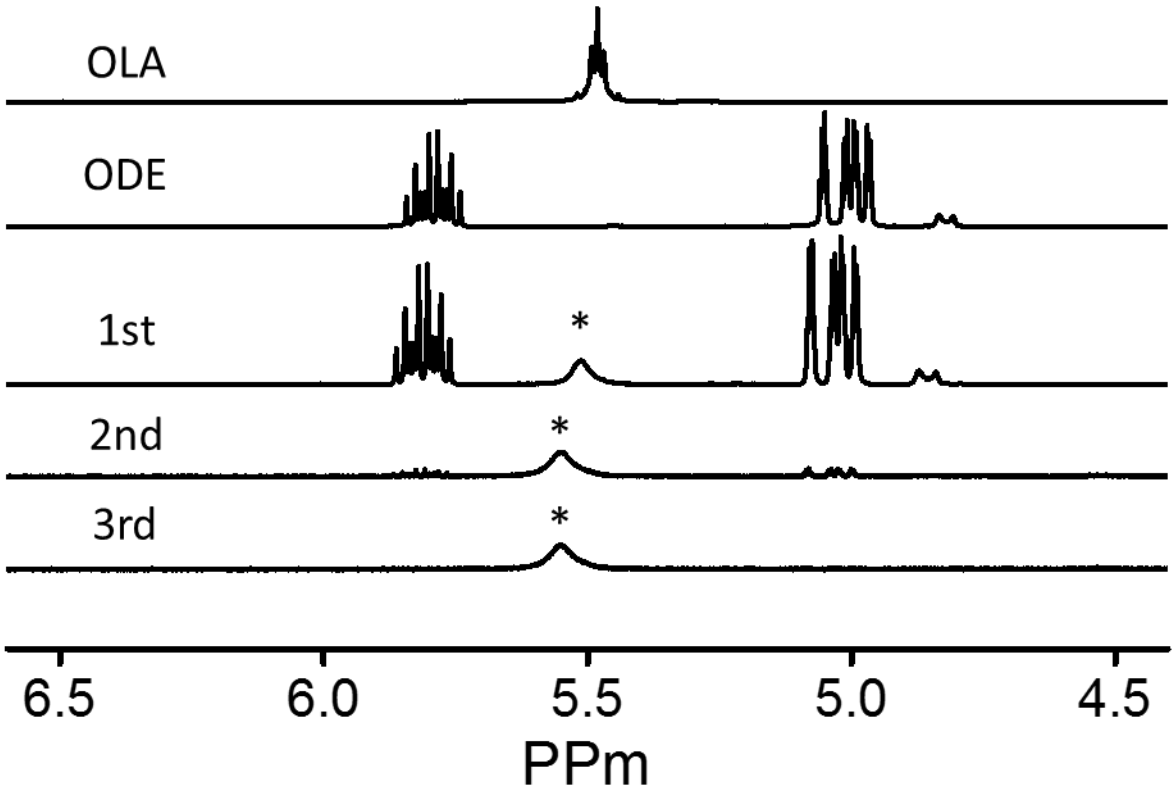

Figure 4S- 11. ^{1}H NMR spectra for neat OLA and neat ODE, $CsPbI_3$ NCs solution washed 1st, 2nd and 3rd times with PbI_2 solution. * denotes peaks attributed to the alkene resonance of OLA.

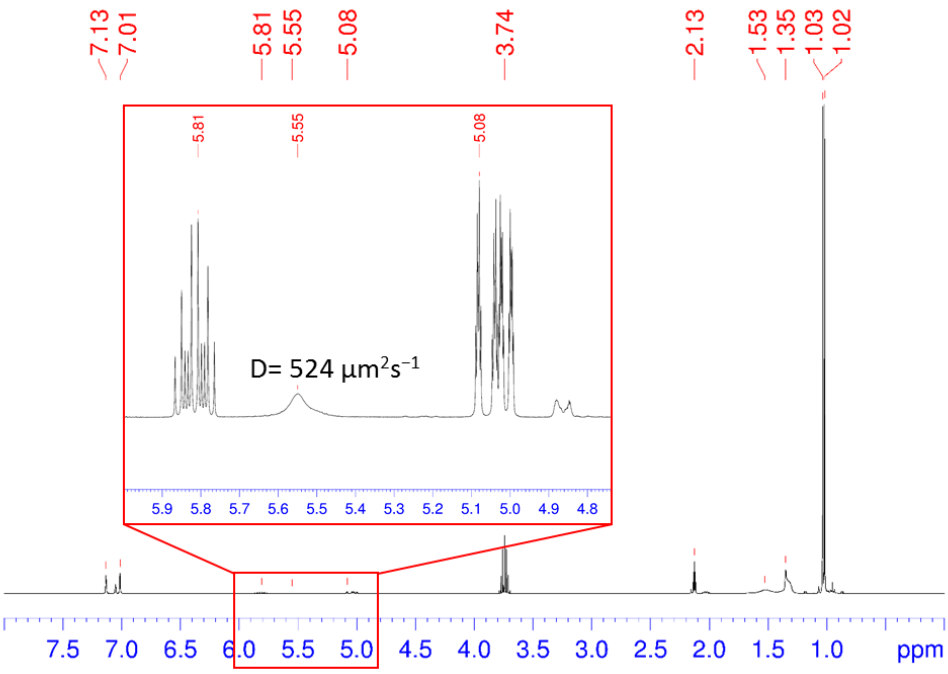

Figure 4S- 12. ^{1}H NMR spectrum of $CsPbI_3$ NC solution, washed once with PbI_2 additive solution. Diffusion coefficient of the 5.5 ppm species determined by the DOSY measurement.

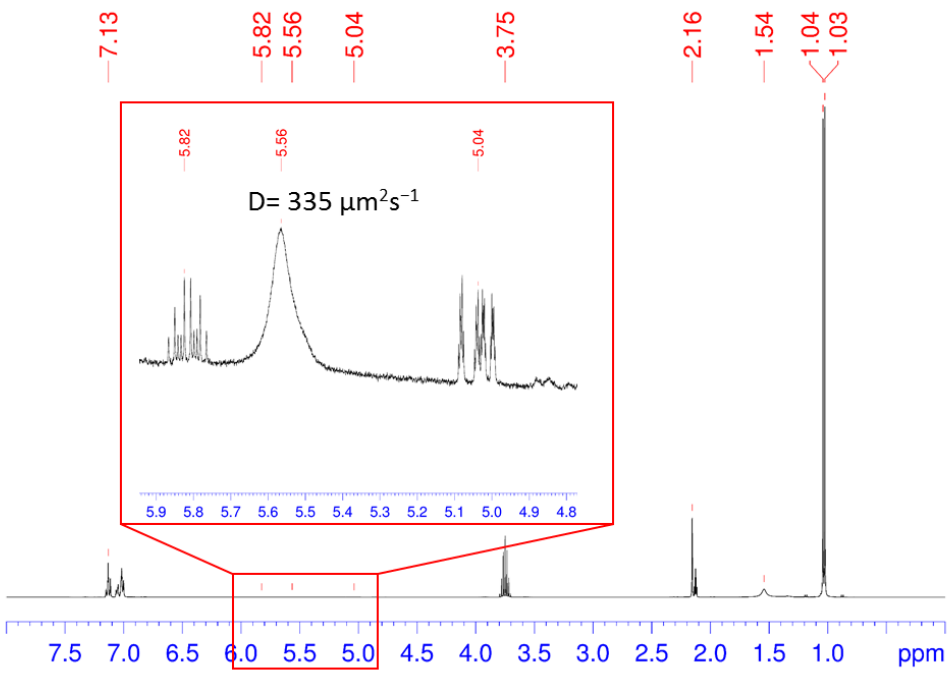

Figure 4S- 13. ^{1}H NMR spectrum of $CsPbI_3$ NC solution, washed twice with PbI_2 additive solution. Diffusion coefficient of the 5.5 ppm species determined by the DOSY measurement.

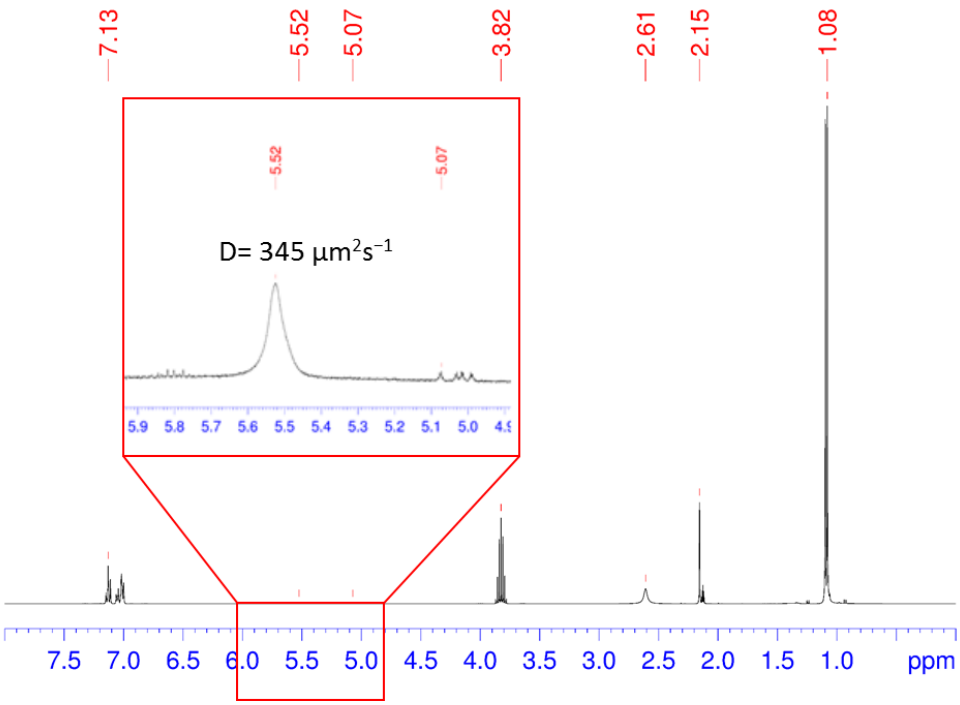

Figure 4S- 14. ^{1}H NMR spectrum of $CsPbI_3$ NC solution, washed thee times with PbI_2 additive solution. Diffusion coefficient of the 5.5 ppm species determined by the DOSY measurement.

The diffusion coefficient of the alkene species for the free oleylamine D_0 is measured to be 1068 $\mu m^2 s^{-1}$. The diffusion coefficient D_1 for a tightly bound oleylamine/ ammonium species is estimated via the Stokes-Einstein equation,[5],[6]

$$D = \frac{k_b T}{6\pi\eta C}$$

In which k_b is the Boltzmann constant, T is the temperature 298K, η is the viscosity for the solvent, which is 0.65 $mm^2\ s^{-1}$ for toluene at 298 K, and C=0.66d is the capacity of cube shaped objects,[7] where d is the edge length of the cube.

Therefore, based on equation 2, assuming an edge length of 12 nm for the NCs plus the ligand shell, D= 49 $\mu m^2 s^{-1}$ for the tightly bounded oleylamine/ ammonium species.

Surface Ligand density

The ligand density of our 1st and 3rd washed $CsPbI_3$ NCs is calculated by combining the UV-vis, ICP, TEM and NMR measurements. The calculation is given below:

The [NC] is taken from section 16 of the supplementary information.

The total surface area [S] for unit molar of NCs is calculated by:

$$[S] = 6 \times d^2 \times [NC]$$

In which d is the edge length of one NC, as derived from the TEM measurement.

The molar concentration of the alkene resonance of the OLA species, e.g. the [ligand] is acquired from NMR measurement by using the ERETIC method, provided in the Bruker Topspin software.

The ligand density (ρ) is therefore given by:

$$\rho = \frac{[\text{ligand}]}{[\text{S}]}$$

The result is given in the table below:

Table 4S- 4. The fitting result and the calculation of the average lifetime for the NCs that has been washed 1st and 2nd with no additions, or washed 1st, 2nd and 3rd times with the PbI_2 additive solution.

	[NC] (mol/L)	[S] (nm^2 mol/L)	[ligand] (mmol/L)	ρ (nm^{-2})
1st	1.03E-6	7.9E-4	3.6±2.3	4.6±2.9
3rd	1.08E-6	7.8E-4	2.2±1.5	2.8±1.9

The result for the 1st and 3rd washed $CsPbI_3$ NCs are 4.6±2.9 and 2.8±1.9 nm^{-2}, respectively. The decrease of the ligand density after the 3rd wash is mainly ascribed to the removal of the excess amount of free ligand species in the 1st wash sample. Although the magnitude is similar to what has been reported in the literature for conventional $CsPbBr_3$ NCs, (2.9 nm^{-2} from Reference [5], 6.7 nm^{-2} from Reference [8]), there were still concerns regarding the large standard deviation of this calculation, which is mainly due to the large standard deviation of the [ligand] measurement. Note that elsewhere in the literature others have not presented the standard deviation for their measurements, so it is difficult to determine how accurate they are and how our results compare.

Also, this result is calculated based on the concentration of all the OLA species, whereas some OLA containing species, such as unbound OLA-DPA ion pairs, are present in solution in unknown quantities, which makes it impossible to quantitatively determine the ratio of free vs. bound ligand species in solution or to get a real binding ligand density. Therefore, the result here is only an indication of the maximum ligand density.

References

[1] Y. Fu, M. T. Rea, J. Chen, D. Morrow, M. P. Hautzinger, Y. Zhao, D. Pan, L. H. Manger, J. C. Wright, R. H. Goldsmith, S. Jin, *Chem. Mater.* **2017**, 29,a 8385.

[2] Y. Kim, E. Yassitepe, O. Voznyy, R. Comin, G. Walters, X. Gong, P. Kanjanaboos, A. F. Nogueira, E. H. Sargent, *ACS Appl. Mater. Interfaces* **2015**, *7*, 25007.

[3] J. Jasieniak, L. Smith, J. Van Embden, P. Mulvaney, M. Califano, *J. Phys. Chem. C* **2009**, *113*, 19468.

[4] E. M. Hutter, R. J. Sutton, S. Chandrashekar, M. Abdi-Jalebi, S. D. Stranks, H. J. Snaith, T. J. Savenije, *ACS Energy Lett.* **2017**, *2*, 1901.

[5] J. De Roo, M. Ibáñez, P. Geiregat, G. Nedelcu, W. Walravens, J. Maes, J. C. Martins, I. Van Driessche, M. V. Kovalenko, Z. Hens, *ACS Nano* **2016**, *10*, 2071.

[6] J. T. Edward, *J. Chem. Educ.* **1970**, *47*, 261.

[7] B. Hubbard, J. F. Douglas, *Phys. Rev. E* **1993**, *47*, 2983.

[8] J. Li, L. Xu, T. Wang, J. Song, J. Chen, J. Xue, Y. Dong, B. Cai, Q. Shan, B. Han, and H. Zeng, Adv. Mater. **2016**, 29, 1603885.

Chapter 5. $CsPbX_3$ PNC Super-crystals

5.1 Introduction

Following the development of a synthetic protocol that enabled stable cubic-phased $CsPbX_3$ PNCs in Chapter 3 and the establishment of a facile protocol for their purification in Chapter 4, herein the self-assembly behavior of such NCs into super-lattice structures, also known as Supercrystals (SCs), are systematically studied.

SCs are composed of assembled nanocrystal (NCs) building blocks in long-range ordered structures.[1] Because of this ordering, such materials exhibit properties that are different from the isolated NC, including exitonic, plasmonic or magnetic coupling, [2] narrower bandgap due to the miniband formation, [3] or coherent super-fluorescence.[4] These unique properties have been harnessed across many applications, such as bio-chemical sensors, [5] nanoscale thermometers, [6] plasmon rulers, [7] data storage devices, [8],[9] as well as various optoelectronic devices.[10]

The assembly of PNCs into SCs has also been achieved through a number of synthetic pathways, including: increasing the precursor concentration during a NC synthesis that utilizes ultrasonication as an energy source;[11] slowly evaporating the solvent from a NC dispersion with a narrow size distribution to increase their concentration;[12] introducing polar anti-solvent or complexing agents into a NC dispersion to reduce their solubility;[13],[14] and placing perovskite NC powders under high pressure to force ordering.[15] Importantly, the assembly of perovskites has not limited to just NCU shaped NCs, with reports extending the assembly to other morphologies, such as NPLs,[16] NRs,[17] and NSs.[18] However, these SC assembly methods have been limited to $CsPbBr_3$, required complex procedures and equipment, and/or required extended periods of time.

As displayed in **Figure 5-1**, the self-assembly of NCs into SC structures can be driven by attractive inter-molecular forces (hydrogen bond, dipole-dipole interaction (Van Der Waals force, VDW),

electrostatic attraction), structural templates or external fields (magnetic or electric).[2],[19] The assembling of the PNC-SCs has been largely reliant on inter-molecular forces. However, one inter-molecular force that should be universal for all alkyl ligand stabilized NCs system, but have not been well understood in the PNCs-SCs formation is the hydrophobic interaction .[20] In gold nanoparticle system, the hydrophobic interaction between the long chain hydrocarbon capping ligands on the nanoparticle surface has been reported to effectively modulate their assembly.[21] The hydrophobic interaction originates from the tendency of two hydrophobes (e.g. hydrocarbon ligands) mutually attracting, resulting in the rearrangement of nearby solvent molecules and hence increasing of the system's overall entropy. The strength of the hydrophobic interaction can be an order of magnitude larger than the Van der Waals force, [22] and is dependent on two primary factors:

(1). The length and shape of the hydrophobes, with long and straight hydrocarbon chains ensuring greater hydrophobicity and less steric hindrance, giving rise to stronger hydrophobic interaction.

(2). The polarity of the solvent, with more polar solvents decreasing the solubility of the hydrophobes, leading to increased hydrophobic interactions. [23]

Although the perovskite NCs are typically capped with long-chain hydrocarbon ligands (OA and OLA), their direct assembly into SCs after synthesis through hydrophobic interaction has not yet been reported.

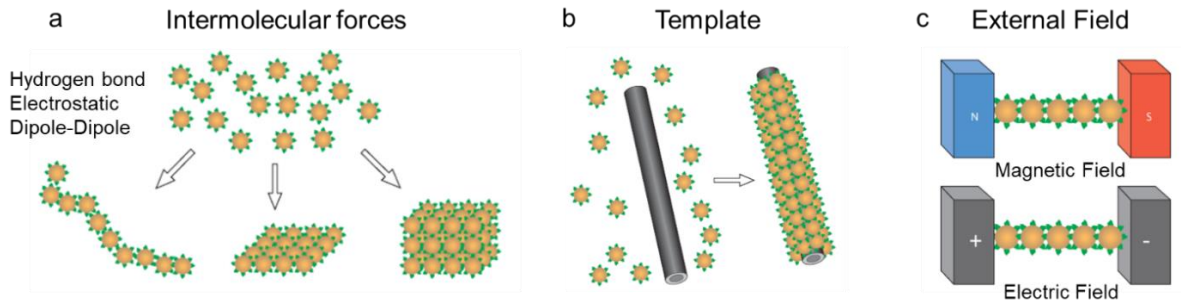

Figure 5-1. Schematic illustration of the NCs to SCs assembling strategies relying on (a) Intermolecular forces, (b) template and (c) External field. [2]

In this chapter, a facile direct synthetic method for perovskite SCs of $CsPbCl_3$, $CsPbBr_3$ and $CsPbI_3$ is reported. The SCs are up to ~1 μm in size, and are assembled from 10 nm-sized NC building blocks. The synthesis of the SCs follows the conventional hot-injection method of the PNCs, with slight modifications to the solvent, ligands and stoichiometry employed in the reaction. It is found that these tailored reaction conditions, enhance the effective hydrophobic interactions between the PNCs to drive their assembly into SCs. The degree of this hydrophobic interaction could be manipulated through modifying the ligand hydrocarbon chain structure and length, which eventually influences the SCs formation. Optical characterizations of these SCs show greatly red-shifted PL emission and narrowed PL FWHM. Such $CsPbX_3$ PNC-SCs are further shown to be readily introduced into hybrid polymer-SC matrices that can be used within colour tuneable down converting LEDs.

5.2 Synthesis of $CsPbX_3$ SCs

5.2.1 Reaction Chemistry

The synthetic protocol for $CsPbI_3$ SCs was established "by accident". Initially, the target was to achieve homogenous nucleation of PNCs via eliminating the Pb^0 black dots within the PNCs, which have been proposed as heterogeneous nucleation seeds as described in Section 1.3.1. To do so, several changes were made to the typical NCU synthetic method developed in Chapter 3:

(1). Iodine (I_2) was added in the reaction mixture as an oxidizing agent to oxidize residual Pb^0 into Pb^{2+};

(2). To avoid the I_2 being consumed through reaction with the alkene groups in the conventional ODE solvent and OLA ligands, these were substituted with the saturated dodecane and hexadecylamine (HDA), while the acid ligand was still the saturated TMPPA;

(3). To fully convert the Pb precursors into the $CsPbI_3$ and minimize the potential formation of Pb^0, the conventional reaction elemental stoichiometry of Cs: Pb: X = 1:4:8 was changed to 1:1:4. The effect of stoichiometry will be discussed in greater detail later.

After such a modified synthesis, TEM showed that the Pb^0 black dots still existed within the PNCs (**Figure 5-2** a). Hence these features are more likely to be aroused from the inherent electron beam damage rather than nuclei, which has been discussed in Chapter 3.3.3. More importantly, alongside the normal NCU shaped PNCs, there were some µm scale features (**Figure 5-2** b). When further magnified (**Figure 5-2** c, d), these features could be readily resolved as being composed of individual $CsPbI_3$ PNC building blocks with a size of around 10 nm. According to the darker contrast of these assemblies compared to the monolayer NCU, it can be further concluded that these features consist of several layers of the PNCs with 3D ordering. This was further proved by SADP (**Figure 5-2** d inset) of these SCs, which was indexed to be the cubic phase of $CsPbI_3$, while the isolated spot pattern indicated the individual NC building blocks were preferentially oriented.

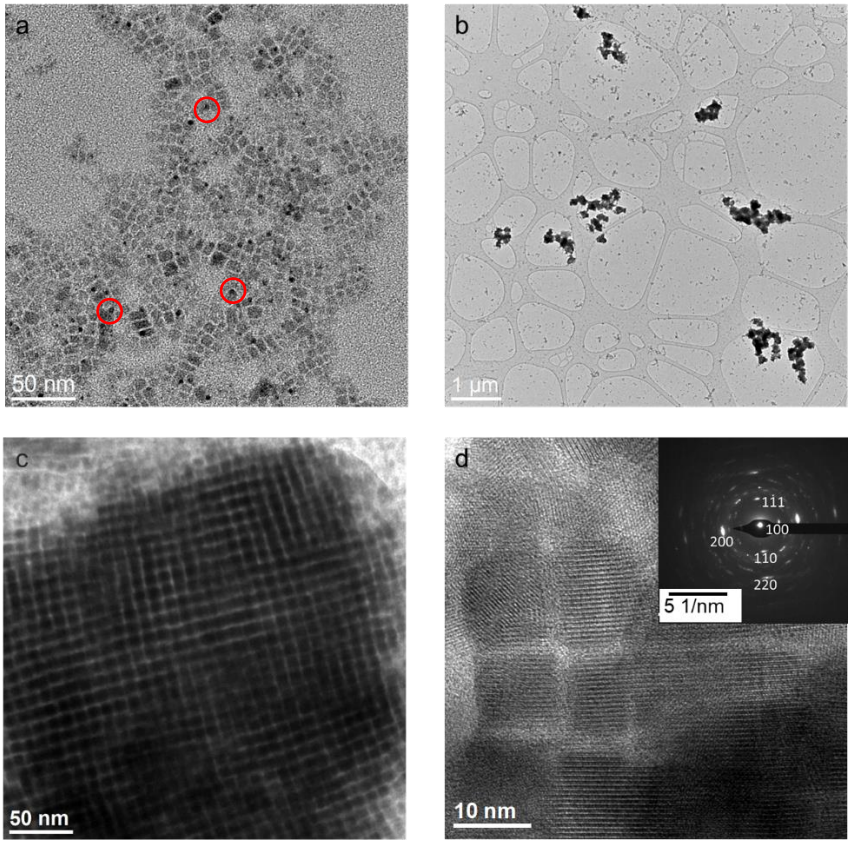

Figure 5-2. TEM images of $CsPbI_3$ NCU showing (a) the presence of Pb^0 black dots (red circles) within the modified $CsPbI_3$ NCU method, and SCs at (b) low, (c) medium, and (d) high magnifications. Inset of (d) includes the SADP of the SCs.

In the synthesis mixture, if the iodine were replaced with RNH_3I salt or hydroiodic acid with the same molar amount of iodine element, the same SCs structure could be achieved. Moreover, using the same protocol for $CsPbCl_3$ and $CsPbBr_3$ PNCs synthesis by adopting the hydrochloric and hydrobromic acid as the extra halide source, the $CsPbCl_3$ and $CsPbBr_3$ SCs could also be produced. The generalized schematic illustration for the synthesis of the NCs and SCs are summarized in **Figure 5-3**.

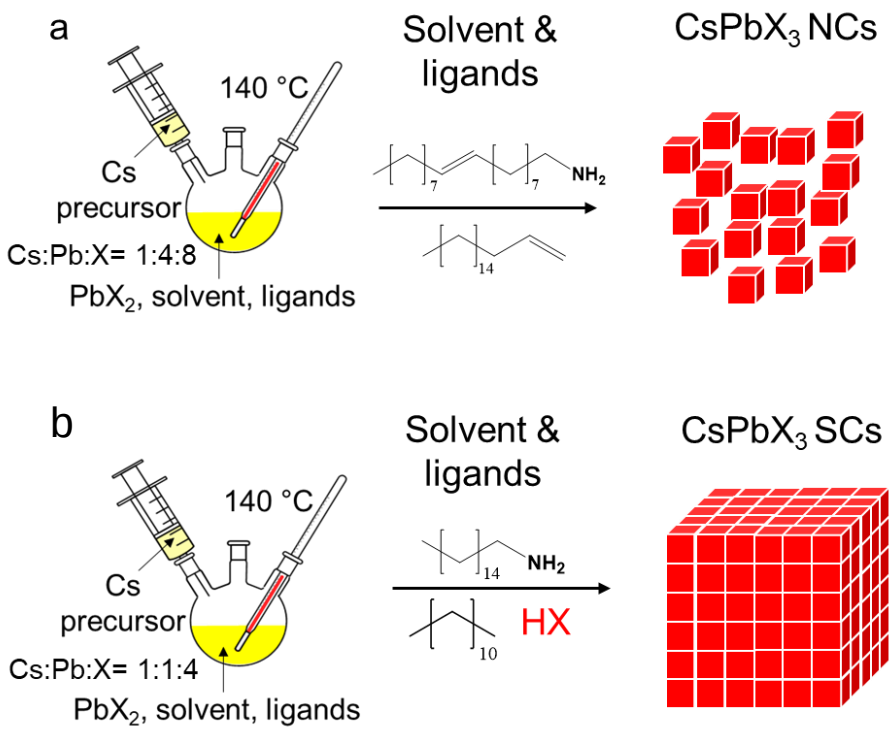

Figure 5-3. Schematic illustration for the synthesis of (a) Normal $CsPbX_3$ NCs, (b) 3D-ordered $CsPbX_3$ SCs.

5.2.2 SCs Characterizations

After synthesis, the SCs could be separated from the reaction solution via centrifugation without any anti-solvent. Such sedimentation properties are consistent with the SCs forming immediately after the synthesis. To probe the size dimensions of the SCs, dynamic light scattering (DLS) measurements were performed on purified $CsPbCl_3$ SC dispersions. The results (**Figure 5-4**) show a size distribution

of around 1 µm, in contrast to the normal NC dispersions which are around 10-100 nm. These dimensions are consistent with the TEM results, as well as the $CsPbBr_3$ SCs reported by others.[11],[14]

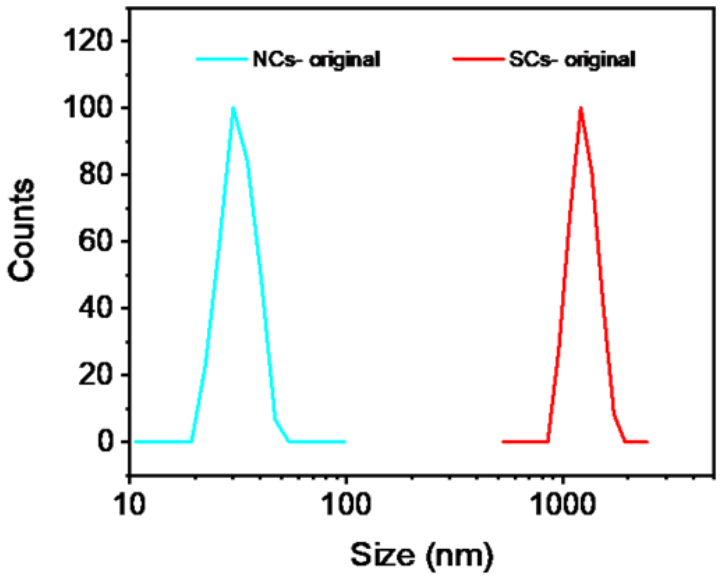

Figure 5-4. DLS size measurements for $CsPbCl_3$ NCs and SCs.

Energy Dispersive X-ray (EDX) elemental mapping and X-ray Diffraction (XRD) were carried out for all Cl, Br, I SC analogues to probe their chemical and structural properties. As shown in **Figure 5-5** by EDX mapping, the Cs, Pb and X elements were evenly distributed throughout the SCs. This is consistent with a homogeneously distributed ensemble of PNCs. Meanwhile, the corresponding XRD patterns shown in **Figure 5-6** could be readily indexed to either cubic or γ-orthorhombic phased PNCs, which are hard to distinguish using normal XRD.

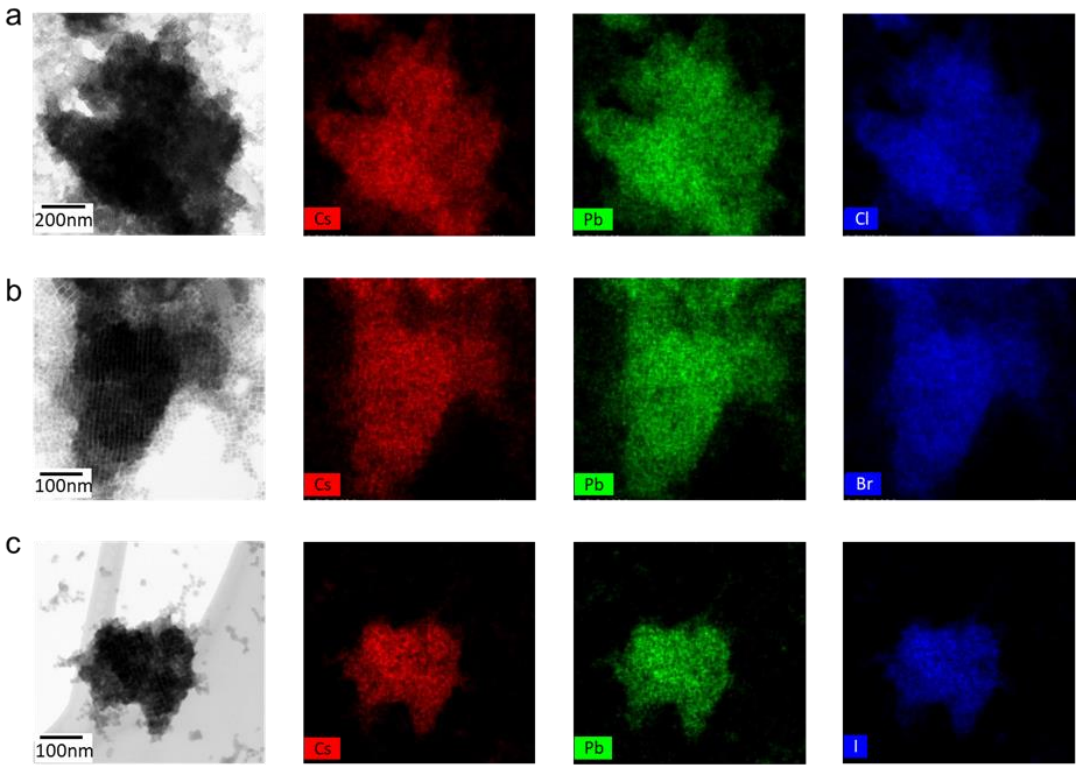

Figure 5-5. STEM- EDX mapping of Cs, Pb and halide elements for (a) $CsPbCl_3$, (b) $CsPbBr_3$ and (c) $CsPbI_3$ SCs.

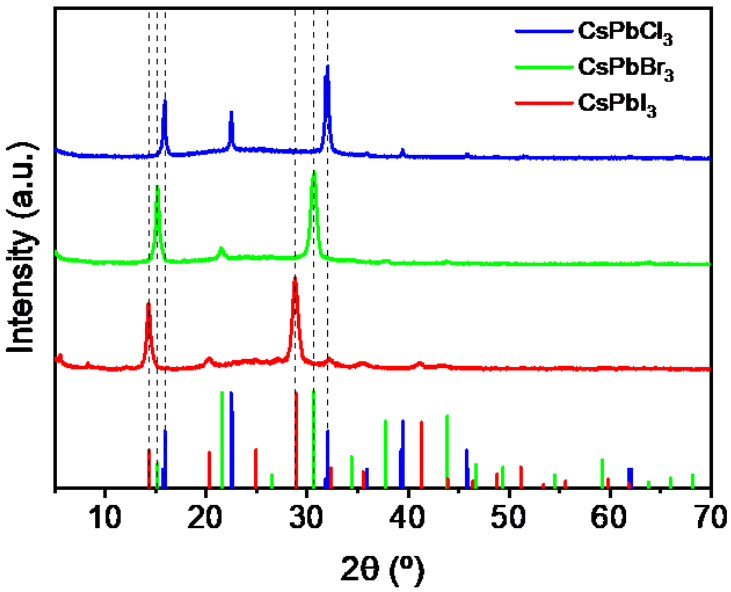

Figure 5-6. XRD patterns of $CsPbCl_3$, $CsPbBr_3$ and $CsPbI_3$ super-crystals. Standard PDF number for the cubic phase of $CsPbCl_3$, $CsPbBr_3$ and $CsPbI_3$ are 00-018-0365, 00-054-0752, 01-080-4039, respectively.

5.2.3 Effect of Stoichiometry

In addition to using saturated solvent and the correct type of ligands, another critical parameter affecting the formation of SCs was reactant stoichiometry. Experiments were conducted in which the concentration of the Pb precursor was fixed, but the Cs and X content was adjusted by varying the volume of Cs-precursor injected or the amount of HX added. The TEM images in **Figure 5-7** illustrate the effect of tuning the reactant stoichiometry on SC formation immediately after synthesis. In a conventional hot-injection synthesis of NCs, the Cs: Pb: I molar ratio is 1:4:8, which yields monodisperse cube-shape NCs (**Figure 5-7** a).[1] When the Cs content was doubled, the majority of the NCs retained the same morphology, however, a small portion of hexagonal shaped particles also formed (**Figure 5-7** b). Doubling the Cs content again yielded only hexagonal shape particles (**Figure 5-7** c), which was ascribed to the Cs_4PbI_6 phase according to SADP (**Figure 5-8**). This phase has been reported to form at high Cs: Pb ratios. [30] Doubling the iodide content of the original reaction stoichiometry did not change the morphology of the product (**Figure 5-7** d), however, doubling both the iodide and Cs content (Cs: Pb: I=1:2:8) gave rise to ~100 nm ordered aggregates (**Figure 5-7** e). Finally, at a 1:1:4 Cs: Pb: I ratio, the formation of SCs was mostly favoured (**Figure 5-7** f).

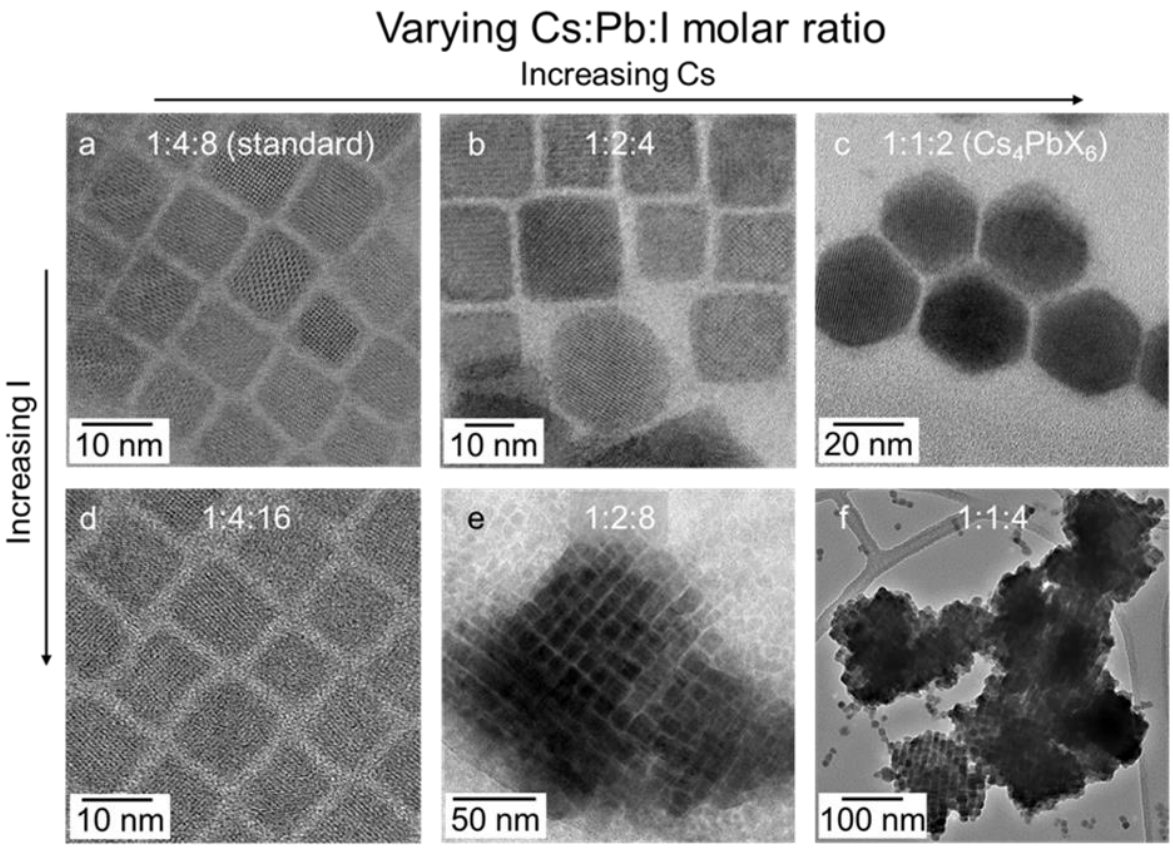

Figure 5-7. TEM images of $CsPbI_3$ NCs synthesised at different Cs:Pb:I molar ratios: (a) 1:4:8, (b) 1:2:4, (c) 1:1:2, (d) 1:4:16, (e) 1:2:8, and (f) 1:1:4. All images were taken immediately after synthesises.

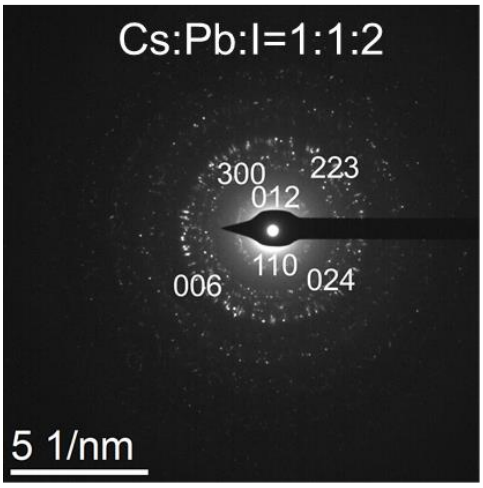

Figure 5-8. The SADP of $CsPbI_3$ SCs synthesised at a Cs:Pb:I = 1:1:2 ratio. The pattern is indexed to the Cs_4PbI_6 phase.

5.2.4 Reaction Yield

To further explain the effect of stoichiometry on SC formation, the yield of the synthesis was quantitatively determined. First, the UV-vis absorption spectra of the samples were measured and showed in **Figure 5-9**. According to the extinction coefficient of the $CsPbI_3$ NCs reported in Chapter 4,[31] the concentration of $CsPbI_3$ NCs could be calculated to derive the yield of the reactions with Cs as the limiting reagent.

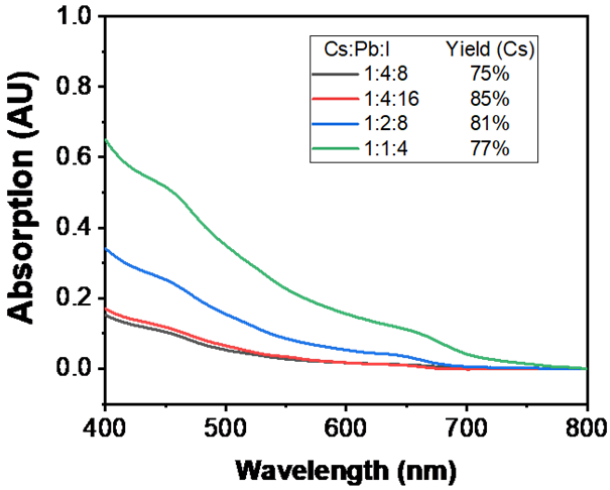

Figure 5-9. Absorption spectra of the $CsPbI_3$ SC crude solution synthesised at different Cs:Pb:I ratio.

The extinction coefficient (ε) for ~11nm sized $CsPbI_3$ NCs is 4.07×10^6 M^{-1} cm^{-1} at 400 nm. The absorption spectra were taken by diluting 10µl of the crude solutions in 3 ml of hexane, and residual scattering contribution was excluded from the spectrum by subtracting the absorbance at 800 nm across the entire spectrum (varied from 0.01 to 0.10 for different samples).

Following this process, the maximum concentration of PNCs (C) could be determined according to the Beer-Lambert law:

$$A = \varepsilon CL$$

Where C is the [PNC] in mol/L, L is the pathlength (1 cm), and A is the absorbance.

From a known concentration of PNCs, the total [Cs] could be determined, and the yield of the synthesis reaction in terms of Cs precursor could thus be calculated. These results are summarized in the **Table 2**.

Table 2. Calculations of the reaction yield (by Cs content) for different Cs: Pb: I ratios.

Cs:Pb:I	Absorbance at 400nm	Concentration of NC (M)	Concentration of Cs (M)	Total Molar of Cs (Mol)	Total Cs injection (Mol)	Reaction Yield of Cs (%)
1:4:8	0.15	1.1E-6	5.5E-3	3.3E-5	4.4E-5	75
1:4:16	0.17	1.26E-6	6.3E-3	3.7E-5	4.4E-5	85
1:2:8	0.34	2.5E-6	1.2E-2	7.2E-5	8.8E-5	81
1:1:4	0.65	4.8E-6	2.4E-2	1.4E-4	1.8E-4	77

The yield of NCs (in terms of Cs injection) across these samples were all around 70–85% (Table 2). It is also worth mention that based on the same calculation process, the reaction yield in terms of Cs for the conventional OA synthesised $CsPbI_3$ is around 65%. Thus, the usage of TMPPA could also slightly lift up the reaction yield in the HI synthesis. Meanwhile, the $CsPbI_3$ concentration and yield of Pb for the 1:1:4 sample increased almost fourfold compared to the conventional 1:4:8 sample after increasing the amount of Cs and I during reaction. Such a high $CsPbI_3$ concentration is in accordance with a previous report that suggested a high NC concentration is fundamental to SC formation.[11]

5.3 Surface Interactions

5.3.1 NMR Characterization

To unravel the formation mechanism of the SCs, it was necessary to study the surface interactions between NCs within the SCs, which required the determination of their surface chemistry. As reported in Chapter 3, the TMPPA used in the synthesis does not bind to the surface of the NCs.[24] To determine whether this holds in the SCs, ^{31}P NMR spectroscopy was used to monitor the presence of TMPPA in solution. After the 2nd wash, ^{31}P NMR spectra (**Figure 5-10**) were collected for the $CsPbCl_3$, $CsPbBr_3$ and $CsPbI_3$ SCs, with no phosphorus signals detected after an extended data

collection period (10 hours). This indicates that all TMPPA species have been removed. Such a result is consistent with the NMR characterizations in Chapter 3.4.4. [1] Therefore, it can be concluded that the only ligands present on the surface of the NCs are the straight-chain hydrophobic HDA and/or its ammonium derivative.

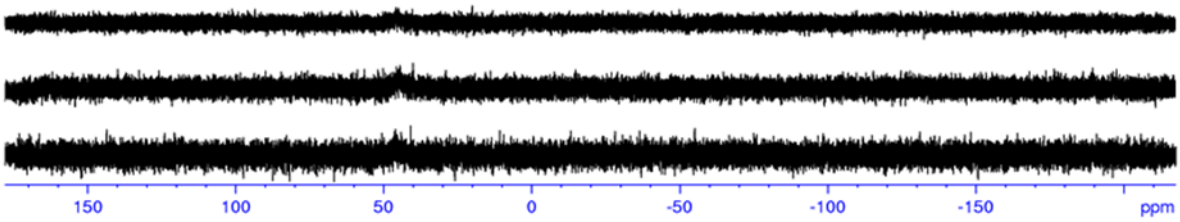

Figure 5-10. ^{31}P-NMR spectra of the SC dispersions of (top to bottom) $CsPbCl_3$, $CsPbBr_3$, $CsPbI_3$, which were washed 2 times.

5.3.2 Role of Ligands Interaction

Syntheses were than carried out using ligands with different chain structures to explore the SCs formation requirements. Following the SC synthetic protocol, when the straight chain HDA was replaced with bent OLA, the product did not demonstrate the formation of ordered SCs, but retained its isolated NCU structure (**Figure 5-11** a, b).[26] This is presumably because the bent OLA introduced a stronger steric hinderance than the straight HDA, which prevented the PNCs from close packing into the SCs. Also, if the TMPPA in the reactions was replaced by the conventionally used OA, no SCs were observed to form either (**Figure 5-11** c, d). Instead, polydisperse NCU structures were observed, this is attributed to the fact that OA is binding to the NCs surface, [25] which would disrupt the HDA-only surface chemistry that is provided by the TMPPA synthesis. Besides, the OA also has a bent structure that hindered the contact of the PNCs. Alongside the NCU, some particularly large particles were found, which could be either the coarsening product as presented in Chapter 3.4.5, or some unknown side product resulting from the changes of reaction stoichiometry. The identity of this large particle is not related to the main theme of this Chapter and thereby not further investigated.

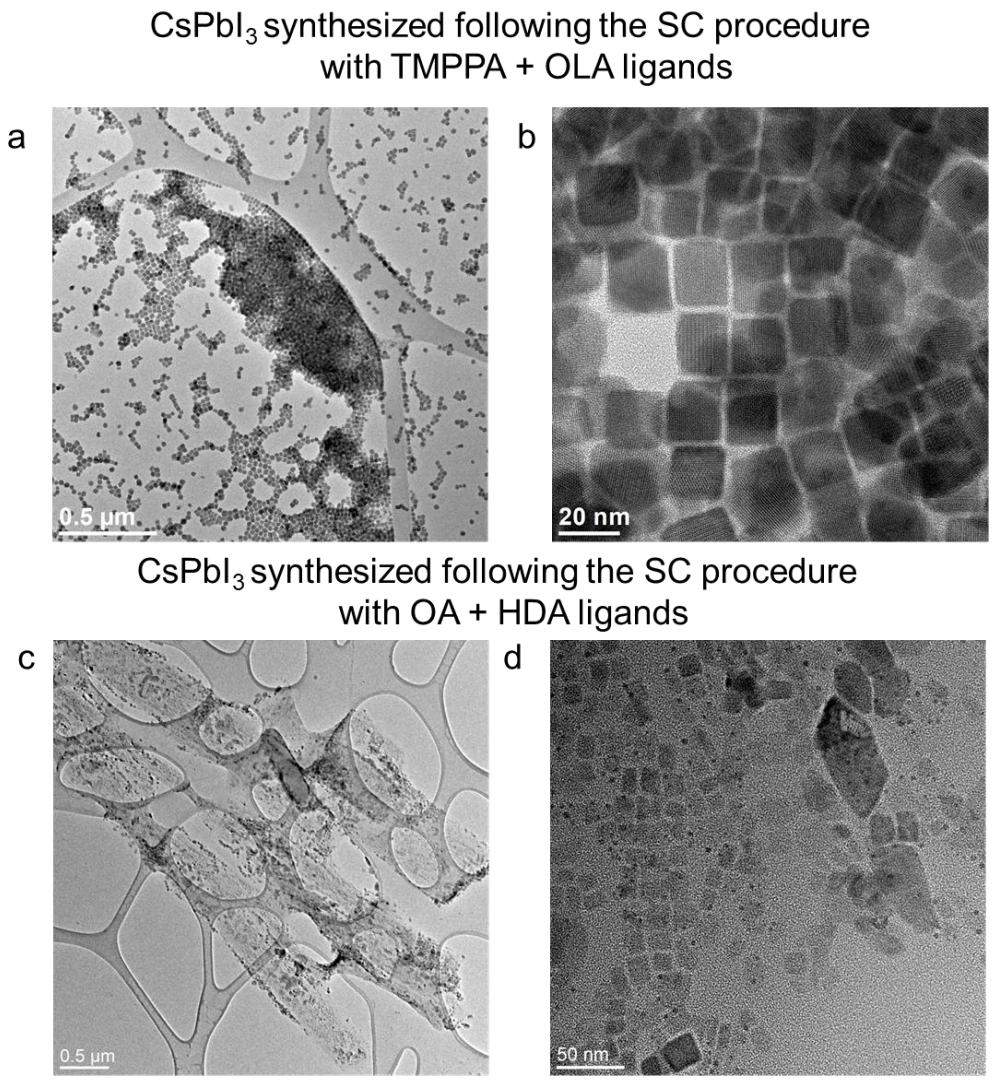

Figure 5-11. Low and high magnification TEM images for $CsPbI_3$ synthesised at Cs: Pb: I= 1:1:4 with the (a), (b) TMPPA and OLA ligands and (c), (d) OA and HDA ligands.

To gauge the origins of these differences between straight and bent ligands, quantitative measurements of the inter-NC distance of PNCs synthesised using HDA and OLA ligands were made using TEM. As shown in **Figure 5-12** a, b, the inter-NC distance for the HDA sample, either in the NC or the SC form, was determined to be around 2 nm, which corresponds to the full length of HDA (2.18 nm),[27] indicating that the HDA ligands were interdigitated between adjacent NC surfaces (**Figure 5-13** a). Such a configuration would ensure close contact of the hydrocarbon chains of HDA, thus favouring strong hydrophobic interactions, [20] which evidently favour the arrangement of NCs into SCs.

In comparison, the bent OLA has a higher degree of rotational freedom, which reduces the extent that it can interdigitate.[28] As a result, the distance between the OLA-capped $CsPbBI_3$ NCs was ~2.5 nm (**Figure 5-12** c), which is much larger than the full length of a OLA molecule (2.0 nm).[29] Such a ligand structure is evidently arising from the increased steric hinderance of OLA, which consequently would yield decreased hydrophobic interactions (**Figure 5-13** b). In support of this, other reports utilizing OLA as the capping ligand describe extra requirements, such as ultra-high NCs concentration or close NCs size distribution, for SC formation.[11],[12] When comparing the intermolecular forces arising between the HDA or OLA capped NCs, the dipole-dipole interactions should be similar across these because the two types of NCs have the same composition and surface ions. Meanwhile, the steric hinderance provided by the HDA-NCs is expected to be much smaller, suggesting that hydrophobic interactions are the driving force of PNC SC formation in this reaction system.

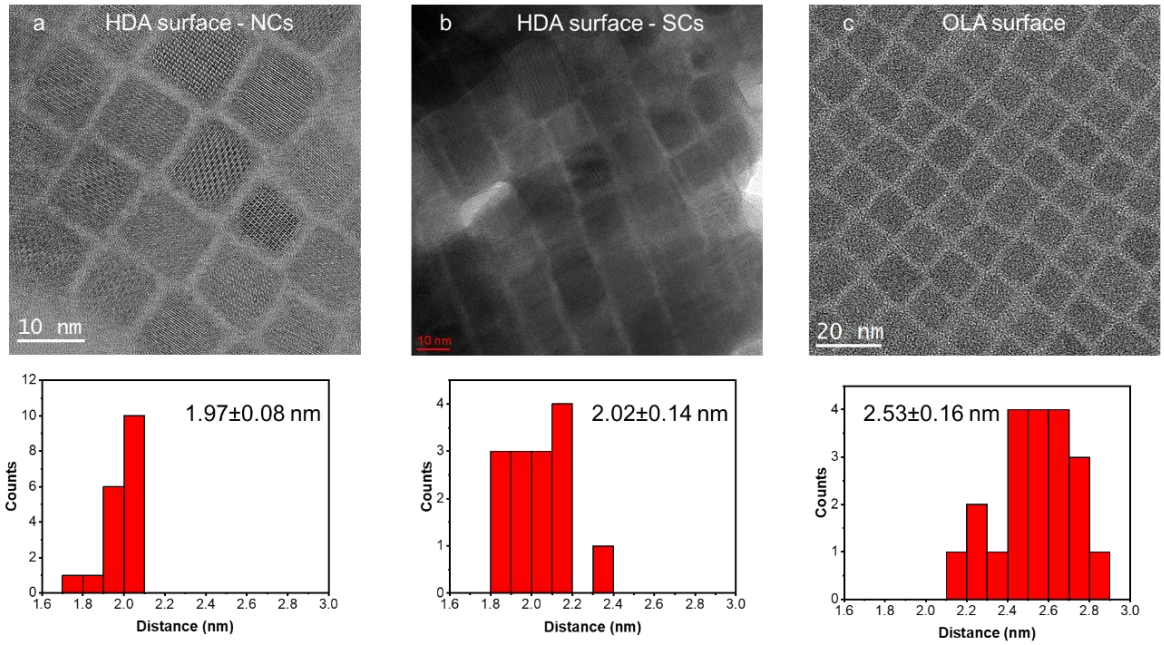

Figure 5-12. TEMs of $CsPbI_3$ NCs (top) and the associated histograms of the inter-NC surface distance (bottom) synthesised (a) with HDA surface chemistry, (b) as SCs with HDA surface chemistry, and (c) with an OLA surface chemistry.

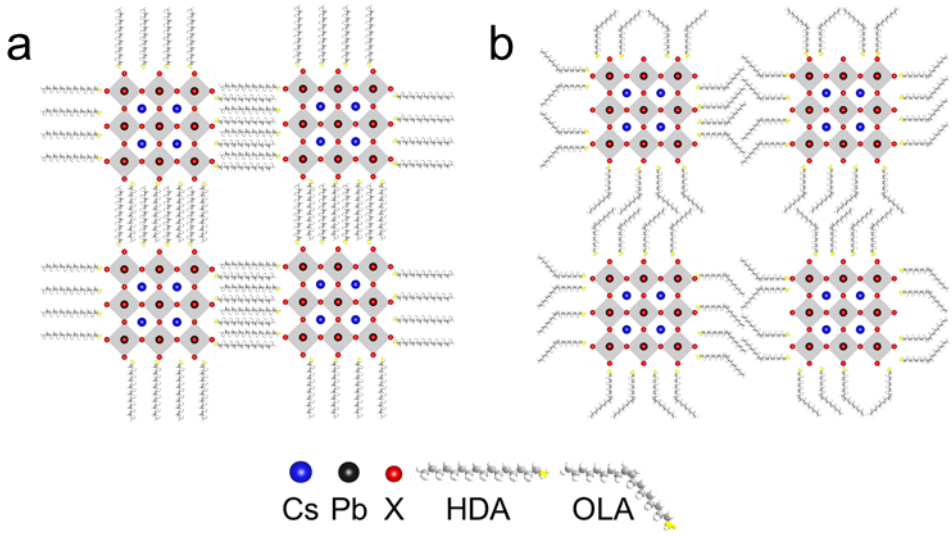

Figure 5-13. Proposed intermolecular interactions between $CsPbX_3$ NCs capped with (a) hexadecylamine (HDA), and (b) oleylamine (OLA) ligands.

5.3.3 Self- assembly of HDA-NCs

If the conclusions drawn from Section 5.3.2. are indeed true, NCs with the same HDA surface ligand should always self-assemble into SCs regardless of the synthetic conditions because of the enhanced hydrophobic interactions. Indeed, when the 1:4:8 sample (Figure 5-7 a) was stored in ambient condition, it was observed to self-assemble into SCs after a certain period of time. As shown in Figure 5-14 a, b, immediately after synthesis and purification, the sample contained well dispersed NCs, whereas after 10 days of storage at ambient condition, the sample transformed into a SC structure. During this process, a significant amount of precipitate accumulated at the bottom of the vial, presumably because the much heavier SCs could no longer remain colloidally dispersed. With the larger size SCs gradually forming, the absorption (Figure 5-14 c) of this sample showed an increasing scattering over time, indicating the formation of SCs, which are larger in size and consequently scatter light in the visible range. Also, the PL peak of this sample red shifted during this time, accompanied by a decreasing of low wavelength emission. This is consistent with the progressive enhancement of particle electronic coupling and cascading energy transfer in the evolving SCs. [3] These results

suggest that the hydrophobic interaction is universal for all the NCs with the same HDA ligand environment, and it is strong enough to drive SCs formation even at low NCs concentration in hexane.

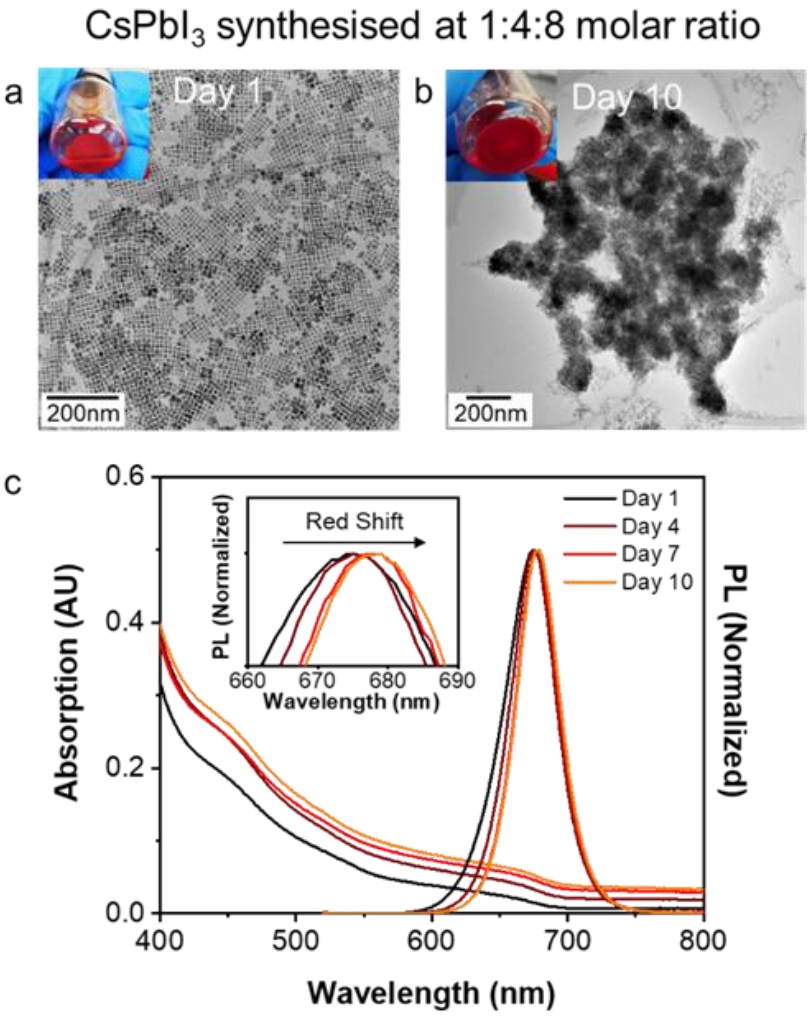

Figure 5-14. TEM images and photos for the $CsPbI_3$ crude solution synthesised with HDA ligands and Cs: Pb: I= 1 :4: 8 stoichiometry that is (a) as synthesised, (b) stored for 10 days. (c) evolution of corresponding absorption & PL spectra with time (inset: zoom-in PL spectra showing the red shift of the PL peaks).

5.4 Hydrophobic Interaction

5.4.1 Assembling of Heterogeneous Structures

To further prove that the hydrophobic interaction can effectively drive SC assembly, another widely accepted requirement for SC formation was examined, which is the uniform morphology and close size distribution of the NCs building block.[12] The $CsPbI_3$ was synthesised following the SCs procedure at 100 °C, which promotes NPL formation.[32] At this temperature, ordered SCs still formed (**Figure 5-15** a), with the elongated NPLs also accommodated into the SC structure (**Figure 5-15** b-e). As shown in **Figure 5-15** d, up to 8 NPLs were assembled together alongside the normal cube-shape NCs. The absorption and PL spectra of this sample showed additional peaks at ~550 nm, which are characteristic of quantum confined NPLs (**Figure 5-15** f).[10] In addition, a synthesis was performed at 180 °C to give a broader NC size distribution,[33] which still resulted in SC formation with large size NCs incorporated into the ordered aggregate (**Figure 5-16**). These results suggest that neither a narrow size distribution nor uniform morphology is required for SC assembly, and the hydrophobic interaction is indeed strong enough to drive even the heterogeneous structures to be packed into the SCs. Notably, as displayed **Figure 5-16** b, the contrast of such SCs are brighter than the previously shown SCs (**Figure 5-2**). This suggests the number of monolayers and thereby the long-range ordering in these SCs are less. Presumably because of the less monodisperse ensembled morphology still weakened the hydrophobic interaction and hence SCs packing.

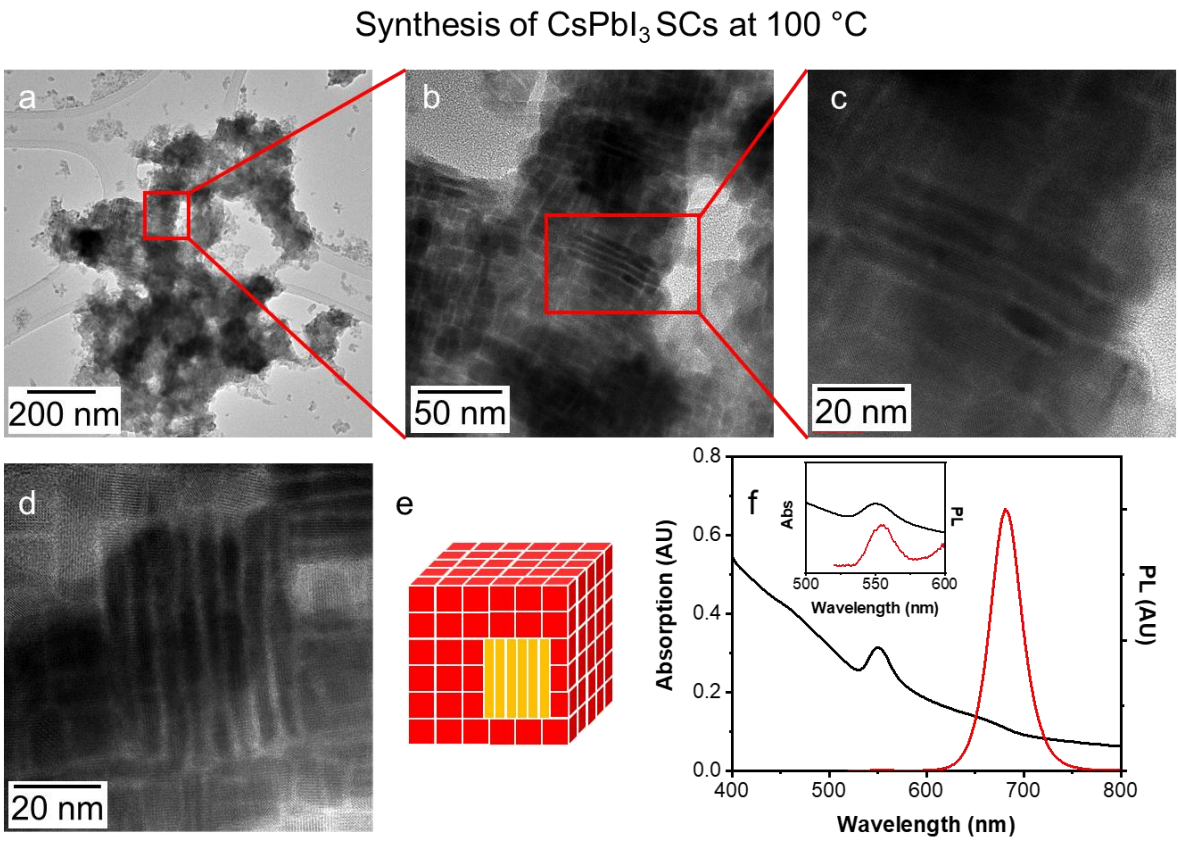

Figure 5-15. (a)-(d) Low to high magnification TEM images. (e) Schematic illustration of NPLs within SC structure. (f) Absorption and PL spectra for $CsPbI_3$ SCs synthesized at 100 °C, diluted in hexane. Inset: Zoomed-in region for the NPLs absorption and emission.

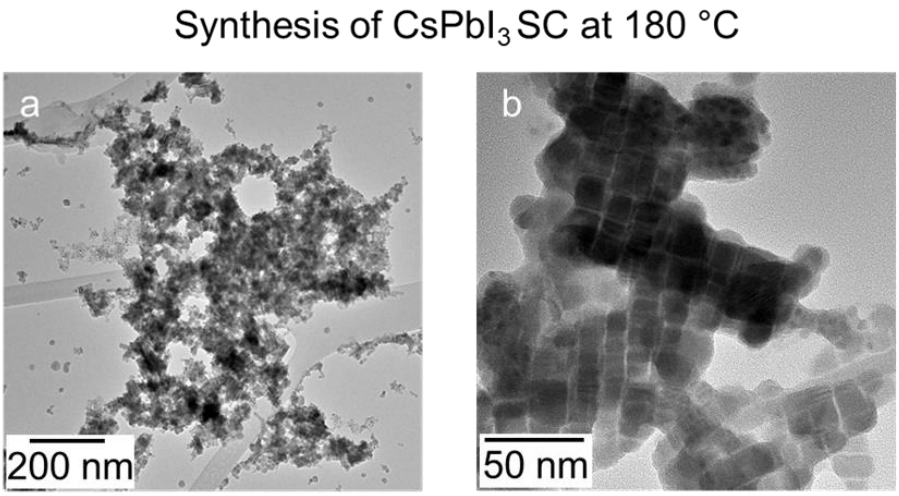

Figure 5-16. TEM images of $CsPbI_3$ SCs synthesised at 180 °C under (a) low and (b) high magnification.

5.4.2 Role of Saturated Amine Ligand Chain Length

In theory, the length of the hydrophobes would affect the strength of the hydrophobic interaction, and hence it should also affect SCs formation. To demonstrate this, $CsPbI_3$ was synthesised with saturated amine ligands of varying chain lengths following the SCs procedure. When using short octylamine (C8, **Figure 5-17** a, b) and dodecylamine (C12, **Figure 5-17** c, d) as ligands, aggregated structures similar to SCs were observed, but at higher magnification it was hard to distinguish individual NC, and the ensembles are only random aggregates showing no ordering of the building blocks. This was presumably because the short chain ligand could not sufficiently separate the PNCs apart, which caused the PNCs to coarsen and lose their monodispersity. As such, the degree of long-range ordering in their SCs was very limited, similar to the SCs previously shown that contains heterogenous structure (**Figure 5-15**, **Figure 5-16**). In stark contrast, octadecylamine (C18), which has a similar chain length to HDA, resulted in products that had a similar shape and ordered- structure to the HDA-SCs (**Figure 5-17** e, f), with the PNCs building blocks unambiguously recognized. These results suggested that the length of the hydrophobes influences the SCs formation through adjusting the monodispersity of the PNCs building blocks, while whether the strength of hydrophobic has been directly impacted remains to be further studied.

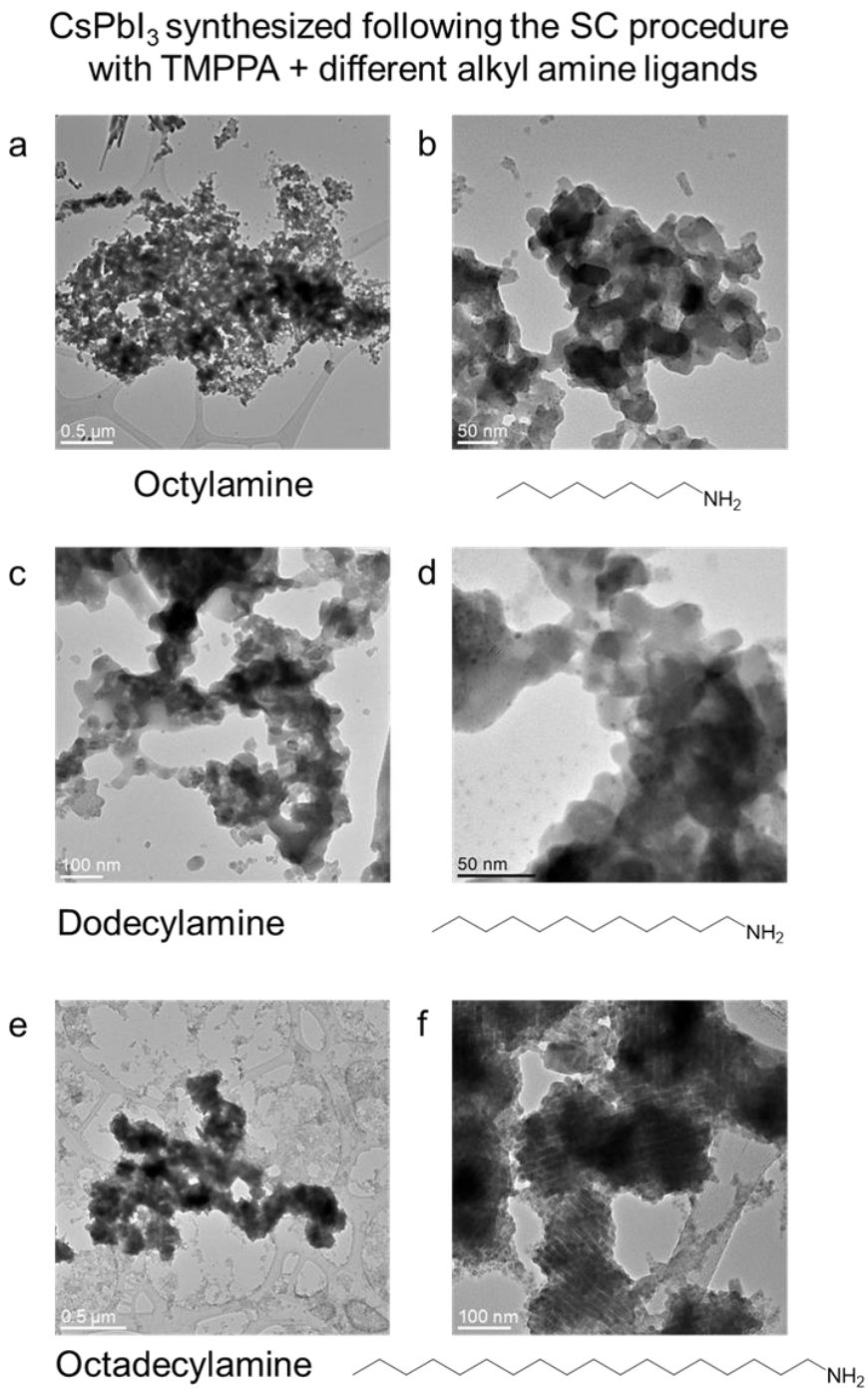

Figure 5-17. TEM images of $CsPbI_3$ synthesised at Cs: Pb: I= 1:1:4 at low and high magnification with TMPPA and various alkyl amine ligands: (a,b) octylamine, (c,d) dodecylamine, (e,f) octadecylamine.

5.4.3 Breaking and Reassembling of the SCs

Another parameter known to affect the nature of hydrophobic interactions, and hence SC formation, is solvent polarity. Theoretically, the hydrophobic interaction is weakest in the most non-polar solvent, hexane, [23] therefore it should be readily disrupted upon the application of external energy (thermal, vibration), which would then cause a reduction in SC size. To verify this hypothesis, a dispersion of $CsPbCl_3$ SCs in hexane was sonicated, with the SCs size monitored by DLS (**Figure 5-18**). After one-hour of sonication, the size of most SCs aggregates was reduced from 1 µm to around 100 nm, which is evidence of SC collapse due to the disruption of hydrophobic interactions. Such a reduction of the SC's size was supported by TEM measurements (**Figure 5-18** b-c). However, if this sonicated solution was stored under ambient conditions, the hydrophobic interaction would spontaneously drive the reassembly of the SCs, whereupon the size of the SCs increased over time, and after storing for 7 days, it reached a similar value as before sonication (**Figure 5-18** d). As evidence of this collapse-recovery process, the appearance of the SC dispersions changed from white to transparent immediately after sonication, then returned to slightly opaque when stored for 4 hours (**Figure 5-19**). Such re-assembly behaviour is in line with the previously demonstrated self-assembling process of the 1:4:8 sample, once again proving that the hydrophobic interaction is universal and would drive the SCs formation spontaneously.

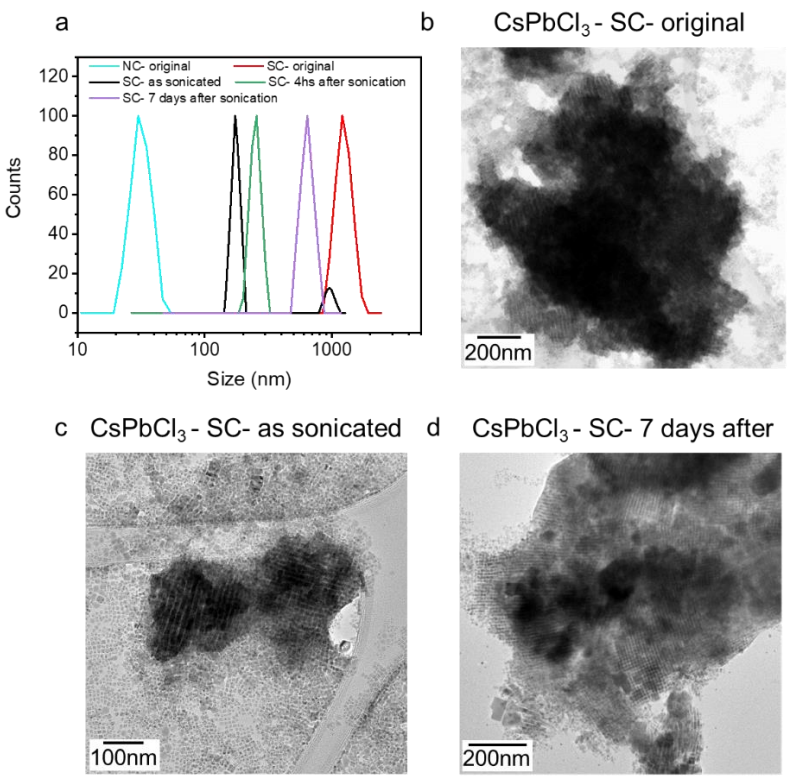

Figure 5-18. (a) DLS size distribution measurement for $CsPbCl_3$ under different conditions: original NCs, original SCs, SCs sonicated for 1 hr, SCs sonicated and rested for 4 hours and 7 days; TEM images of $CsPbCl_3$ SCs (b) original, (c) as-sonicated, (d) sonicated and rested for 7 days.

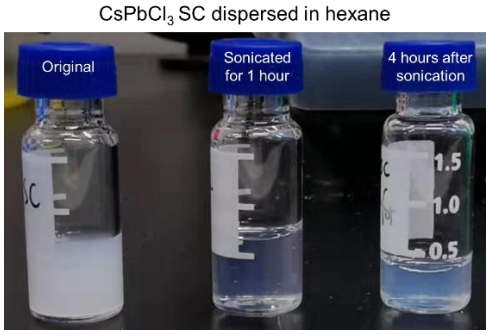

Figure 5-19. Photo of $CsPbCl_3$ SCs dispersed in hexane with: no treatment, sonicated for 1 hour, sonicated and rested 4 hours.

5.4.4 Solvent Polarity

In theory, if a polar solvent is introduced to the solution to increase the overall polarity of the dispersion, the hydrophobic interaction would be stronger and the SCs should be more difficult to

disrupt. 25 vol % of several different polar solvents were added to the hexane dispersion of $CsPbCl_3$ SCs, sonicated for 1 hour, and then characterised. As shown by DLS and TEM images (**Figure 5-20**), upon addition of almost any polar solvent, the size of the SCs after sonication was larger than that with neat hexane. Specifically, some polar solvents (tetrahydrofuran, tert-butanol) fully preserved the size of the SC after sonication, whereas IPA caused the SCs to coarsen. These results further suggest that the SC formation relies on hydrophobic interactions, which can be disrupted and recovered easily, or be enhanced in higher polarity solvent systems. Future work is still necessary to unravel the interaction between the polar molecules and the SCs, especially for the IPA which was shown as a good anti-solvent to wash the $CsPbI_3$ PNCs in Chapter 4.

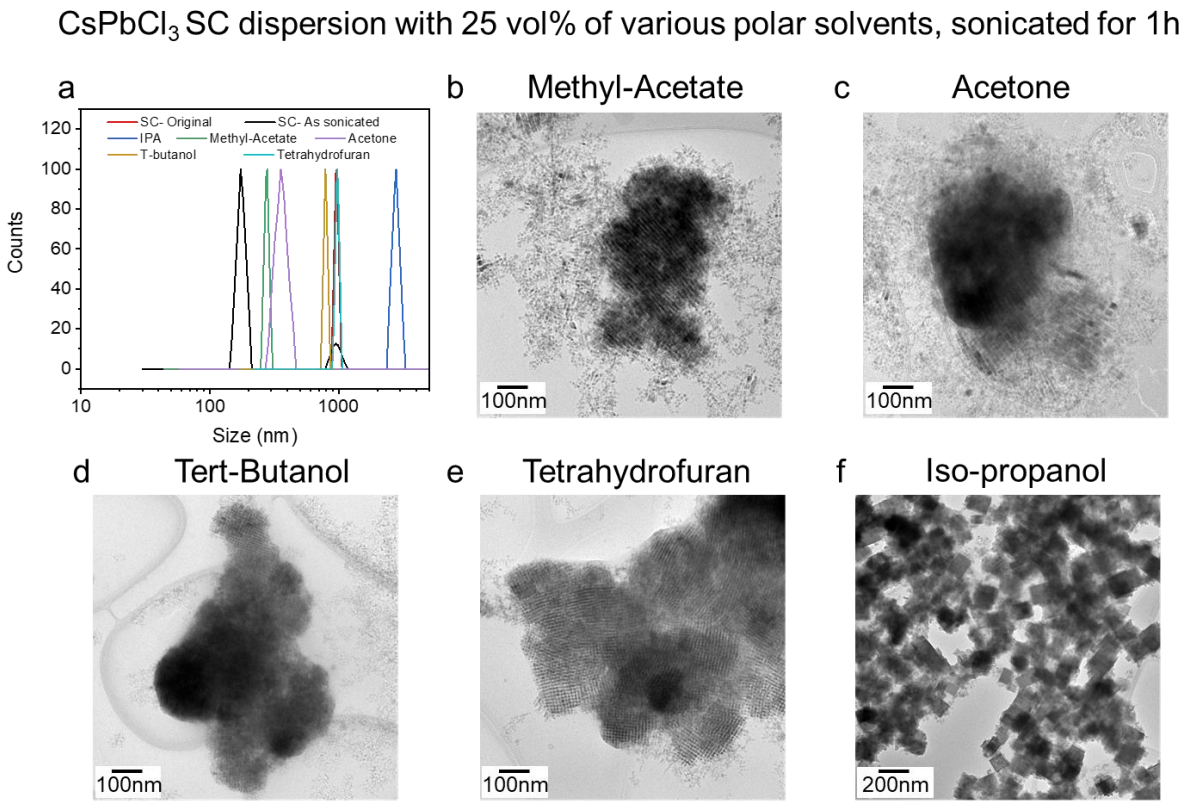

Figure 5-20. (a) DLS size distribution measurements for $CsPbCl_3$ hexane dispersions with 25 vol% various polar solvents after 1-hour sonication. TEM images of these samples with (b) methyl acetate, (c) acetone, (d) tert-butanol, (e) tetrahydrofuran, (f) iso-propanol addition.

5.5 Optical Characterizations

Having examined the effect of the hydrophobic interaction on SC formation, the optoelectronic properties of the SCs were then tested. The absorption and PL spectra of $CsPbX_3$ SC drop-cast films were compared with the corresponding NC films (**Figure 5-21** a-c). All the SC samples demonstrated a greater degree of scattering in their absorption spectra, a red shifted PL, and a narrower PL FWHM. Specifically, the emission wavelengths were 417 nm, 527 nm, 707 nm, and the FWHMs were 11 nm, 19 nm and 29 nm for the Cl, Br, I SCs, respectively. Compared with their NC analogues, the PL red shifted by 5 nm, 9 nm and 23 nm and the PL FWHM narrowed by 1 nm, 2 nm and 6 nm for the Cl, Br and I SCs. These results are consistent with previous reports that show SCs having strong electronic coupling and forming mini-bands which reduce their band gap to cause a red-shift in their PL. [11],[34] A comparison of the emission wavelengths of the NCs and SCs on the colour gamut spectrum shows the red-shifted PL of the SCs slightly extends the area of emission colour beyond what can be rendered from conventional inorganic PNCs (**Figure 5-21** d).

Finally, as a proof of concept, SC-PMMA composite films were fabricated and used in front of a commercially available UV torch to make down-conversion-LED devices (**Figure 5-21** e). The SC-PMMA composite was prepared via dispersing the SCs solution among the PMMA toluene solution, then evaporate the toluene in the recessed Teflon mould, with more details included in Chapter 2.4. The peak PL wavelength for these SCs composite LEDs was at 414 nm, 522 nm and 700 nm for the Cl, Br and I PNC samples, respectively. These were less red shifted comparing with the previous film samples, presumably because the electronic-coupling and the degree of re-absorption was less profound within the PMMA matrix. Such high quality down conversion prototype LED devices provide good test cases for PNC deployment, but stability is also a key consideration. Further work is required to assess and compare the long-term stability of $CsPbX_3$ PNCs to their SC derivates within such devices.

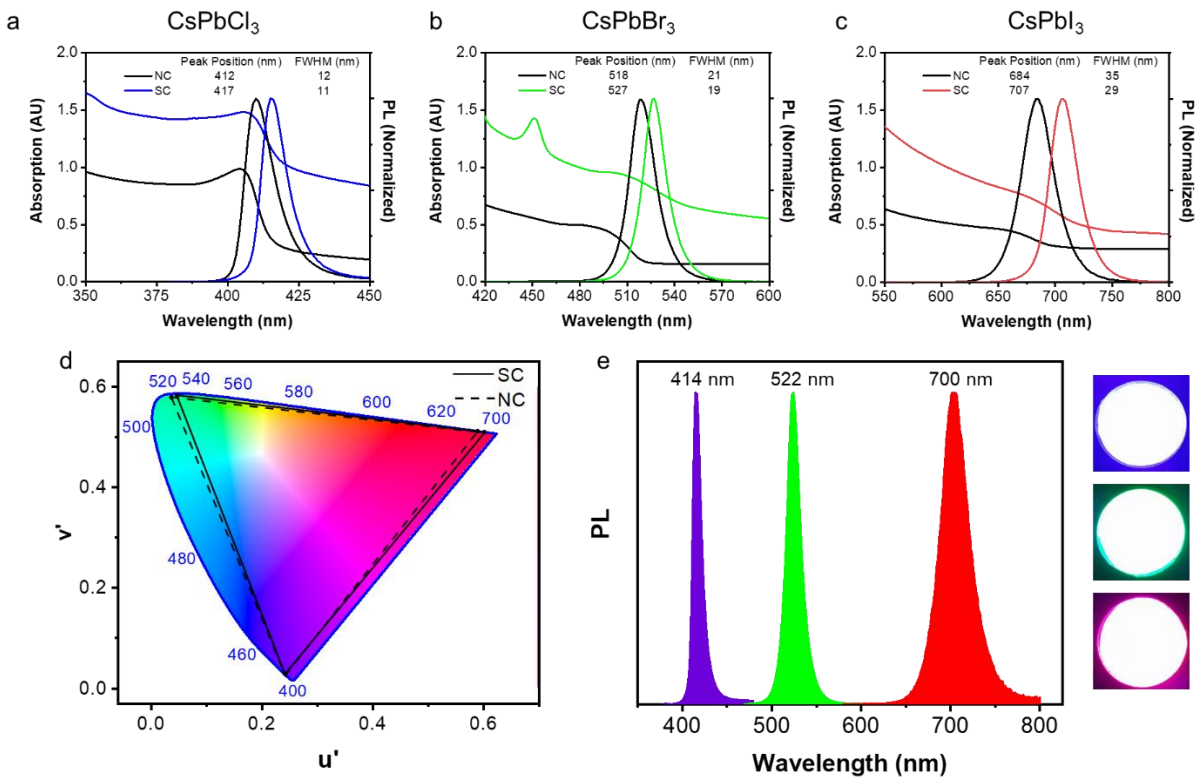

Figure 5-21. Absorption and PL spectra for NC and SC films of (a) $CsPbCl_3$, (b) $CsPbBr_3$ and (c) $CsPbI_3$. (d) The emission of the NCs and SCs plotted on the colour gamut spectrum (CIE 1976), the PL is transformed into the u' v' through the chromaticity application in Origin software. (e) The PL spectra of the down conversion LED devices fabricated from the SC-PMMA composites (left) and photos of the LEDs (right).

5.6 Conclusion

In conclusion, this chapter described the facile direct synthesis of $CsPbX_3$ perovskite supercrystals of around 1 µm in size that consisted of 10 nm NC building blocks. The synthesis generally followed the well-developed hot injection method, albeit with the conventional unsaturated solvent and ligands replaced with saturated analogues, and the stoichiometry of the precursors being tuned to increase the concentration of the PNCs. It was found that smaller inter-particle distances were observed between PNCs containing saturated vs unsaturated alkyl amine ligands of similar chain length, with the latter not yielded SCs formation. These factors suggest that enhanced hydrophobic interactions within the

saturated ligand system provides the dominant driving force for PNC assembly. These hydrophobic interactions are sufficiently strong to drive even heterogenous structure (NPL, extra-large NCU) to form the SCs. Meanwhile, these interactions could also be disrupted through sonication and recovered with time, or enhanced with higher polarity solvent systems. Such SCs exhibited red-shifted PL compared to the discrete NC analogues, which was conducive in achieving expanded colour-gamut down conversion prototype light-emitting devices. Overall, the facile synthesis of SCs presented here opens up a new strategy to manipulate the assembly of PNCs into ordered structures, with potential for real-world applications.

Reference

[1] X. Zhang, L. Lv, L. Ji, G. Guo, L. Liu, D. Han, B. Wang, Y. Tu, J. Hu, D. Yang, A. Dong, *J. Am. Chem. Soc.* **2016**, *138*, 3290.

[2] Z. Nie, A. Petukhova, E. Kumacheva, *Nat. Nanotechnol.* **2010**, *5*, 15.

[3] T. Sugaya, T. Amano, M. Mori, S. Niki, *Appl. Phys. Lett.* **2010**, *97*, 2.

[4] R. Bonifacio, L. A. Lugiato, *Phys. Rev. A* **1975**, *12*, 587.

[5] J. S. Lee, M. S. Han, C. A. Mirkin, *Angew. Chemie - Int. Ed.* **2007**, *46*, 4093.

[6] J. Lee, A. O. Govorov, N. A. Kotov, *Angew. Chemie - Int. Ed.* **2005**, *44*, 7439.

[7] C. Sönnichsen, B. M. Reinhard, J. Liphardt, A. P. Alivisatos, *Nat. Biotechnol.* **2005**, *23*, 741.

[8] R. J. Tseng, C. Tsai, L. Ma, J. Ouyang, C. S. Ozkan, Y. Yang, *Nat. Nanotechnol.* **2006**, *1*, 72.

[9] S. Sun, C. B. Murray, D. Weller, L. Folks, A. Moser, *Science (80-.).* **2000**, *287*, 1989.

[10] A. S. Baimuratov, I. D. Rukhlenko, V. K. Turkov, A. V. Baranov, A. V. Fedorov, *Sci. Rep.* **2013**, 3,1727.

[11] Y. Tong, E. Yao, A. Manzi, E. Bladt, K. Wang, M. Döblinger, S. Bals, P. Müller-buschbaum, A. S. Urban, L. Polavarapu, *Adv. Mater.* **2018**, 1801117, 1.

[12] G. Rainò, M. A. Becker, M. I. Bodnarchuk, R. F. Mahrt, M. V. Kovalenko, T. Stöferle, *Nature* **2018**, 563, 671.

[13] J. S. Van Der Burgt, J. J. Geuchies, B. Van Der Meer, H. Vanrompay, D. Zanaga, Y. Zhang, W. Albrecht, A. V. Petukhov, L. Filion, S. Bals, I. Swart, D. Vanmaekelbergh, *J. Phys. Chem. C* **2018**, 122, 15706.

[14] K. H. Wang, J. N. Yang, Q. K. Ni, H. Bin Yao, S. H. Yu, *Langmuir* **2018**, 34, 595.

[15] Y. Nagaoka, K. Hills-Kimball, R. Tan, R. Li, Z. Wang, O. Chen, *Adv. Mater.* **2017**, 29, 1606666.

[16] S. K. Mehetor, H. Ghosh, N. Pradhan, *J. Phys. Chem. Lett.* **2019**, 10, 1300.

[17] S. K. Mehetor, H. Ghosh, N. Pradhan, *ACS Energy Lett.* **2019**, 4, 2353.

[18] Y. Liu, M. Siron, D. Lu, J. Yang, R. dos Reis, F. Cui, M. Gao, M. Lai, J. Lin, Q. Kong, T. Lei, J. Kang, J. Jin, J. Ciston, P. Yang, *J. Am. Chem. Soc.* **2019**, 141, 13028.

[19] J. Liu, K. Song, Y. Shin, X. Liu, J. Chen, K. X. Yao, J. Pan, C. Yang, J. Yin, L. J. Xu, H. Yang, A. M. El-Zohry, B. Xin, S. Mitra, M. N. Hedhili, I. S. Roqan, O. F. Mohammed, Y. Han, O. M. Bakr, *Chem. Mater.* **2019**, 31, 6642.

[20] H. A. Scheraga, J. Biomol. *Struct. Dyn.* **1998**, 16, 447.

[21] M. Grzelczak, T. Altantzis, B. Goris, J. Pe, A. Sa, S. Bals, G. Van Tendeloo, S. H. Donaldson, B. F. Chmelka, *ACS Nano* **2012**, 6, 11059.

[22] J. Israelachvili, R. Pashley, *Nature* **1982**, 300, 341.

[23] P. Atkins, J. De Paula, *Physical Chemistry for the Life Sciences*, **2011**.

[24] C. Wang, A. S. R. Chesman, J. J. Jasieniak, *Chem. Commun*. **2017**, 53, 232.

[25] A. Pan, B. He, X. Fan, Z. Liu, J. J. Urban, A. P. Alivisatos, L. He, Y. Liu, *ACS Nano* **2016**, 10, 7943.

[26] Herein, the pre-made hexadecylammonium iodide is used as the extra iodide source, avoiding the hydroiodic acid being consumed by the alkene of OLA.

[27] D. Gidalevitz, Z. Huang, S. A. Rice, *Biophys. J.* **1999**, 76, 2797.

[28] A. Vivien, M. Guillaumont, L. Meziane, C. Salzemann, C. Aubert, S. Halbert, H. Gérard, M. Petit, C. Petit, *Chem. Mater.* **2019**, 31, 960.

[29] Z. Wang, X. D. Wen, R. Hoffmann, J. S. Son, R. Li, C. C. Fang, D. M. Smilgies, T. Hyeon, *Proc. Natl. Acad. Sci. U. S. A.* **2010**, 107, 17119.

[30] W. Zhai, J. Lin, Q. Li, K. Zheng, Y. Huang, Y. Yao, X. He, L. Li, C. Yu, C. Liu, Y. Fang, Z. Liu, C. Tang, *Chem. Mater.* **2018**, 30, 3714.

[31] C. Wang, A. S. R. Chesman, W. Yin, L. Frazer, A. M. Funston, *J. Chem. Phys.* **2019**, 151, 121105.

[32] Y. Bekenstein, B. A. Koscher, S. W. Eaton, P. Yang, A. P. Alivisatos, *J. Am. Chem. Soc.* **2015**, 137, 16008.

[33] I. Lignos, S. Stavrakis, G. Nedelcu, L. Protesescu, A. J. Demello, M. V. Kovalenko, *Nano Lett.* **2016**, 16, 1869.

[34] D. Baranov, S. Toso, M. Imran, L. Manna, *J. Phys. Chem. Lett.* **2019**, 10, 655.

Chapter 6. Conclusion and Perspective

6.1 Conclusions

Inorganic $CsPbX_3$ perovskite nanocrystals (PNCs) have near unity photoluminescence quantum yield, pure emission color, readily tunable band gap through halide engineering, and defect tolerant band structure.[1] Owing to these superior properties, they have attracted great research interest since being firstly reported in 2015, particularly due to their tremendous promise for use in a variety of optoelectronic applications. However, for the PNCs to reach their full potential, it is essential that they can be synthesised with high quality, high reproducibility and long-term structural stability, which have been the main targets of this thesis. In this regard, research has been focused on the synthesis, purification and self-assembly of $CsPbX_3$ PNCs, where X = Cl^-, Br^- and I^-.

To date, the hot injection method is the most widely used method for the synthesis of PNCs.[2] Upon controlling the reaction time, temperature, ligands combination and stoichiometry, high quality PNCs with tuneable morphologies (nanocubes, nanoplatelets, nanorods, nanosheet) can be achieved. By selecting different precursors, doped PNCs, lead free PNCs or double-perovskite NCs can be synthesised. However, despite these successes, the Achilles heel for PNCs has remained the instability of the functional α-phase of $CsPbI_3$ PNCs, which spontaneously transform into the non-perovskite δ-phase at room temperature to lose an important candidate for applications requiring a red colour coordinate.

Chapter 3 is focused on solving this problem. Ex-situ and in-situ experiments have revealed that the α-to-δ transformation happens in PNCs only upon the coarsening of the synthesised ~10 nm NCs into larger nanostructures. To stop this coarsening process, the HI method was modified by replacing the conventional oleic acid (OA) ligand with the branched bis-(2,2,4- trimethylpentyl) phosphinic acid (TMPPA). This slight change to the reaction chemistry prevented the coarsening and stabilized the functional α-phase of the $CsPbI_3$ PNCs for a prolonged time. Interestingly, the TMPPA ligand was

found to not bind to the PNCs surface, which was instead passivated solely by oleylamine (OLA) and oleylammonium species. By adopting other branched carboxylic ligands with similar branching structures and steric hinderance effects as the TMPPA, the α-$CsPbI_3$ could also be stabilized. This suggest that steric interactions cause the exclusion of the acidic ligand species within the surface ligand shell of the PNCs, which is opposite to the typically used OA that co-passivates the surface. Notably, the use of TMPPA was also found to suppress the coarsening of the PNCs during the synthesis reaction, which made it a reliable ligand choice for synthesising high quality $CsPbX_3$ PNCs.

The use of such PNCs in practical applications requires their purification from the crude reaction solution to remove unreacted precursors, ligands and inert solvents. Underlying this purification process is the need to preserve the ensemble quality, colloidal dispersion, optical properties and phase of the PNCs. Until now, most purification studies have been on the structurally robust $CsPbBr_3$ PNCs,[3] whereas achieving sufficient purification of $CsPbI_3$ has remained challenging owing to its phase instability.

In Chapter 4, a facile purification protocol of the $CsPbI_3$ PNCs was developed. In conventional purification protocols, the PNCs exhibit a gradual loss of their surface ligands, thus after multiple purification cycles the PNCs always coarsen and degrade. One feasible strategy to complement this ligand loss is to use additives during the purification. After testing a series of additives, a lead iodide and ligand based additive solution was prepared, which balanced the delicate surface chemistry during the following purification process. Following thorough quantitative surface chemistry characterization, a critical minimum value for the additive solution was determined, which allowed multiple washings cycles to be carried out while retaining the structural integrity and optical properties of the $CsPbI_3$ PNCs. Through the determination of the wavelength dependent molar extinction coefficients, surface ions concentrations and surface ligands densities, a quantitative insight into this washing process and underlying surface chemistry of such PNCs was achieved. The

generality of the purification protocol was also applied to the entire $CsPbX_3$ family to achieve high quality and high purity PNCs inks.

Compared with the extensive research on $CsPbX_3$ PNCs synthesis, the self-assembly of such materials in ordered structures has received comparatively less attention. Supercrystals (SCs) are one such structure, which have been shown to possess interesting properties, such as electronic coupling, miniband formation or coherent PL.[4] However, current studies across reported PNC SCs are mostly focused on $CsPbBr_3$, while limiting insights have been presented on the fundamental driving force for the assembly process.

In Chapter 5, a facile SC synthesis protocol for all the $CsPbX_3$ analogues was reported. The synthesis generally followed the procedure established in Chapter 3, but possessed modifications in the choice of solvent, amine ligand and stoichiometry. The hydrophobic interaction between straight, long chained surface ligands, was found to be the key inter-molecular force to drive the SC assembly process. Through controlling the chain length and structure of the hydrophobic ligands, adjusting the solvent polarity, or exerting external energy, the degree of the hydrophobic interaction could be manipulated to control the size and morphology of the SCs, or even break apart the SCs which could spontaneously reassemble back to their original structure. The assembled $CsPbX_3$ SCs possessed red-shifted PL and narrower emission peak width, suitable for development of prototype down-conversion LED devices featuring SCs-poly (methyl methacrylate) composites.

6.2 Perspectives

After successfully synthesizing high-quality phase stable $CsPbX_3$ PNCs, establishing their purification protocol and demonstrating their assembly into SCs structure, there are still plenty of future researches that can be carried on for this material. With the ultimate goals being the fabrication of high-performance devices, the future works are listed here as an end mark of this thesis.

Extinction coefficient

After being first reported in 2015, the investigations on the $CsPbX_3$ PNCs has been fast advancing. However, in most works to date, only qualitative approaches have been adopted to study the evolution of such materials. It is essential to transition into more quantitative methodologies to truly understand and compare different reaction conditions for this field. Towards this goal, progress has been made in Chapter 4, with the calculation of extinction coefficients for the ~11nm $CsPbI_3$ PNCs at different wavelengths determined via TEM, UV-Vis absorption and ICP characterizations. A clear opportunity is to establish a library of extinction coefficients for all the $CsPbX_3$ PNCs with various sizes. The extinction coefficient would allow convenient determination of the PNCs' molar concentration in solution, which is essential for calculating the reaction yield, quantitatively determining the surface chemistry and precisely preparing stock solution.

Modelling

Modelling and computational works are critical to deeply understand the experimental finding and to further give prediction to guide future works. This thesis has been experimental at its core. However, modelling across many of the chapters is still required to validate the conclusions being drawn and to provide greater insights into the molecular processes at hand.

As is mentioned in the Chapter 1, the dynamics of the nucleation and growth process during the PNCs synthesis has not been well understood. One crucial obstacle in studying the nucleation and growth process are their fast kinetics. As such, it is essential to conduct more detailed computational work to study these processes, for instance, directly modelling the behaviour of the monomer within the reaction mixture. Only through better understanding on the nucleation and growth, can the synthesis of the PNCs be truly controlled, which ultimately promotes the quality and reproducibility of the PNCs.

Until now, the long chain OA and OLA are still the major ligands used for synthesizing high quality PNCs. Several other ligands with different chain length, functional group, and stereochemistry has been applied and shown effects of tuning the morphology or enhancing the optical properties of the PNCs. However, there is still a lacking in understanding of the role of ligands in controlling the kinetics of the nucleation and growth process in the synthesis reaction. Further studies could be focused on conducting more modelling works to understand the intricate PNC - ligands interactions, which would expand the library of ligands for the PNC system.

In Chapter 3, the branching nature of the TMPPA and other carboxylic acid was proposed as the main reason for their exclusion in the ligand shell on the PNCs. Models that directly probe the surface interaction between the PNCs and different ligand mixtures could effectively verify this mechanism.

Finally, in Chapter 5, the self-assembly of the SCs was attributed to the surface hydrophobic interaction on the NCs surface arising from the straight chain interdigitating HDA ligands. Although results indeed indicated that the hydrophobic interaction could be manipulated to influence the SC formation, it is still arbitrary to directly affirm that the hydrophobic interaction is the decisive driving force. Herein, the modelling work would be ultimately helpful if it could directly calculate the strength of the hydrophobic interaction. The model could also be set on two adjacent NCs surfaces to calculate whether the system would have the lowest free energy when the HDAs are closely interdigitated together, which would then drive SCs assembly.

Film Deposition

An essential step in the fabrication of $CsPbX_3$ PNCs devices is the formation of high-quality thin films. The purification protocol developed in Chapter 4 provides high-purity and structurally stable PNC inks for such film deposition studies. Until now, the most widely used $CsPbX_3$ film deposition technique remains spin coating, which is a good starting point for assessment. The structural, optical and electronic properties of the achieved films should be systematically investigated. As the PNCs

are capped with long chain, non-conductive ligands, it is also imperative to conduct ligand exchange processes to decorate them with shorter ligands while retaining their optical properties and structural integrity. Limited by its inherently low material deposition yield, the spin coating processes will ultimately need to be replaced by other more advanced film deposition approaches, e.g. the slot-die coating technique, inkjet printing, transfer printing, etc. to meet the real-world deposition requirements. This will require complete ink development approaches to be developed for materials.

Device fabrication

The exciting $CsPbX_3$ class of materials is promising for a variety of optoelectronic applications, such as LED, solar cell, laser or photodetector. Among these applications, the LED is the one which could take full advantages of the high PLQY and tunable emission wavelength of the PNCs. Recent progress in this area has seen the external quantum efficiency of $CsPbBr_3$ LEDs jumping from 0.12% in 2015 to 16.48% in 2018.[5],[6] Further efficiency gains are expected through continuing material and device engineering.

As a proof of concept, the $CsPbX_3$ SCs have already been implanted into down conversion LED devices in Chapter 5. This prototype LED allows tracing of the long-term stability of the material in a real device environment. However, the essential target should be the fabrication of electroluminescence LEDs of a single color using one kind of $CsPbX_3$ PNCs or white emitting by harnessing numerous colors coordinators. Such PNCs LEDs could utilize the conventional structure design, in which PEDOT:PSS and ZnO are the hole and electron transport layers, respectively, ITO is the transparent conductor and Ag is the metal electrode.[7],[8] However, interfacial instability, ion accumulation and moisture instability would need to be addressed. Concurrently, the efficiency and brightness of the electroluminescence LEDs would need to be enhanced through modification of the film deposition process, improvement of the charge carrier injection through electron and hole injection material selection, as well as optimization of the device structure.

6.3 Ending remarks

It took CdSe NCs over 20 years of study to reach PLQYs of over 90%. In comparison, such high values were achieved almost immediately when the perovskite NCs were born in 2015. This highlights that such materials are not only tolerant to defects, but are also relatively easy to synthesise compared to the more traditional II-VI and III-V semiconductors. Indeed, efforts are still required to better understand how to precisely control PNC structure and sizes, as well as move beyond toxic lead derivatives for practical applications. However, the degree of progress made in only five years and the large interest in such materials today provides tremendous scope that such factors will get addressed in a timely manner. This will entail a new era, one that will result in highly efficient synthetic methods for the controllable size and morphology of PNCs to be developed, and then used within excellent optoelectronic devices that will hopefully play a major role in everyone's daily life.

References

[1] L. Protesescu, S. Yakunin, M. I. Bodnarchuk, F. Krieg, R. Caputo, C. H. Hendon, R. X. Yang, A. Walsh, M. V. Kovalenko, *Nano Lett.* **2015**, *15*, 3692.

[2] C. K. Ng, C. Wang, J. J. Jasieniak, *Langmuir* **2019**, *35*, 11609.

[3] Y. Kim, E. Yassitepe, O. Voznyy, R. Comin, G. Walters, X. Gong, P. Kanjanaboos, A. F. Nogueira, E. H. Sargent, *ACS Appl. Mater. Interfaces* **2015**, *7*, 25007.

[4] M. A. Boles, M. Engel, D. V. Talapin, *Chem. Rev.* **2016**, *116*, 11220.

[5] J. Song, J. Li, X. Li, L. Xu, Y. Dong, H. Zeng, *Adv. Mater.* **2015**, *27*, 7162.

[6] J. Song, T. Fang, J. Li, L. Xu, F. Zhang, B. Han, Q. Shan, H. Zeng, *Adv. Mater.* **2018**, *1805409*, 1805409.

[7] C. Zhang, B. Wang, W. Zheng, S. Huang, L. Kong, Z. Li, G. He, L. Li, *Nano Energy* **2018**, *51*, 358.

[8] M. Lu, J. Guo, P. Lu, L. Zhang, Y. Zhang, Q. Dai, Y. Hu, V. L. Colvin, W. W. Yu, *J. Phys. Chem. C* **2019**, DOI 10.1021/acs.jpcc.9b06144.

Appendix

ChemComm

COMMUNICATION

View Article Online
View Journal | View Issue

Cite this: *Chem. Commun.*, 2017, **53**, 232

Received 16th October 2016,
Accepted 21st November 2016

DOI: 10.1039/c6cc08282c

www.rsc.org/chemcomm

Published on 23 November 2016. Downloaded on 11/02/2018 23:19:14.

Stabilizing the cubic perovskite phase of $CsPbI_3$ nanocrystals by using an alkyl phosphinic acid†

Chujie Wang,[a] Anthony S. R. Chesman[b] and Jacek J. Jasieniak*[a]

$CsPbI_3$ nanocrystals suffer from a facile cubic perovskite to orthorhombic phase transformation, which deteriorates their appealing optoelectronic properties. Here, we report a new colloidal synthesis that replaces the conventionally used oleic acid with an alkyl phosphinic acid to grow high-quality, phase-stable cubic perovskite $CsPbI_3$ nanocrystals.

All-inorganic cesium lead halide perovskite ($CsPbX_3$, X = Cl^-, Br^-, I^-) nanocrystals (NCs) exhibit near-unity photoluminescence (PL) quantum yields, narrow emission peak widths,[1] and anion-tuneable absorption/emission wavelengths.[2] In addition, these materials have been shown to possess negligible electron/hole trapping and undergo ultra-fast charge transfer to suitable acceptor/donor species.[3] All these advantages make the $CsPbX_3$ perovskites attractive materials for applications such as light emitting diodes,[4] lasers,[5] and photodetectors.[6]

The group of Kovalenko was the first to report the synthesis of nearly monodisperse $CsPbX_3$ NCs using a hot-injection approach,[7] with a host of alternative synthetic methods having since been developed.[8,9] Despite their promise, a major drawback of $CsPbX_3$ perovskites is their chemical instability when exposed to polar solvents, moisture, or an external halide source.[10] The $CsPbI_3$ perovskite, which is a particularly promising candidate for red-emitting LEDs[11] and solar cells[12] owing to its 1.73 eV optical band-gap,[13] also has an inherent phase instability. Unlike $CsPbCl_3$ and $CsPbBr_3$, the functional cubic perovskite (α) phase of $CsPbI_3$ is only stable at temperatures above 315 °C.[7] The metastable α-$CsPbI_3$ spontaneously transforms into the non-functional orthorhombic (δ) phase, also known as the "yellow phase" due to its colour, at room temperature (Fig. 1),[14] preventing it from being effectively studied and harnessed in practical applications.

[a] *Department of Materials Science and Engineering, Faculty of Engineering, Monash University, Clayton, VIC 3800, Australia. E-mail: jacek.jasieniak@monash.edu*
[b] *CSIRO Manufacturing, Ian Wark Laboratories, Bayview Ave, Clayton, VIC 3168, Australia*

† Electronic supplementary information (ESI) available: Experimental information, NMR spectra, and additional experimental results. See DOI: 10.1039/c6cc08282c

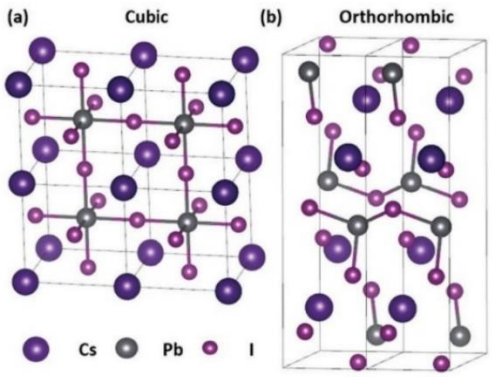

Fig. 1 Crystal structures of the $CsPbI_3$ (a) cubic perovskite and (b) orthorhombic phases.

Efforts to stabilize α-$CsPbI_3$ have mainly focussed on thin film coatings. The use of excess hydroiodic acid in its deposition has been shown to yield smaller $CsPbI_3$ grain sizes with an induced lattice strain, which has lowered the α-to-δ phase transformation temperature and, thus, enhanced the α-phase stability at room-temperature.[15] Additionally, sintering nanocrystalline mixtures of α-$CsPbCl_3$ with α-$CsPbI_3$ has been shown to create polycrystalline thin films of α-$CsPbI_{3-x}Cl_x$ that are phase-stable at room-temperature.[16] Only recently has it been shown that α-$CsPbI_3$ NCs can be stabilized through the purification of the growth solution to remove excess precursors and ligands, which were shown to drive the destabilisation process.[17]

As a critical component of NC synthesis, the surface capping ligands not only control the nucleation and growth dynamics and prevent NC aggregation, but also determine their physical and chemical behaviour,[18] as well as the final NC phase.[19,20] Conventionally, oleic acid (OA) and oleylamine (OLA) ligands have been used in the preparation of $CsPbX_3$ NCs. It has been suggested that OLA, oleylammonium halides and oleylammonium oleates are the main surface complexing agents of $CsPbX_3$ NCs, with the

This journal is © The Royal Society of Chemistry 2017

Published on 23 November 2016. Downloaded on 11/02/2018 23:19:14.

level of co-passivation by OA still under debate.[21,22] While effective for synthesising high quality NCs, this ligand mixture encourages α-$CsPbI_3$ NCs to undergo a phase transformation when the crude reaction solution is cooled to room temperature. The necessity of removing excess OA and oleate-based precursors from the solution suggests that a synthesis that is free from OA could be conducive towards enhancing phase stability.[17]

In this communication we report the use of bis-(2,2,4-trimethylpentyl)phosphinic acid (TMPPA) as an OA replacement in the synthesis of $CsPbI_3$ NCs. This novel synthesis is found to yield high quality NC ensembles and, importantly, preserve the phase of α-$CsPbI_3$ to produce stable colloidal dispersions.

Our synthetic protocol for $CsPbI_3$ was adapted from a hot-injection procedure developed by Kovalenko *et al.*[7] PbI_2 was dissolved in OLA and OA or TMPPA with 1-octadecene (ODE) as the solvent at 140 °C, which is our hot injection temperature. The Cs-precursor solution was prepared separately by dissolving Cs_2CO_3 in OA or TMPPA in ODE at 120 °C. This was subsequently injected into the Pb-precursor solution and heated for 5 s, after which it was quenched. Purification of the NCs from the reaction solution was performed *via* precipitation using *tert*-butanol as the *anti*-solvent. The washed NCs were then re-dispersed in toluene. From herein, $CsPbI_3$ synthesised in TMPPA (OA) will be termed $CsPbI_3$–TMPPA (–OA).

The first advantage of using TMPPA is that the respective Cs precursor, Cs–TMPPA, can be readily formed in ODE at room temperature, while the OA-based precursor, Cs–oleate, requires heating up to 100 °C before dissolution occurs (Fig. S1, ESI†). This allows for the convenient storage of Cs–TMPPA. The second major advantage, and the focus of this paper, is that $CsPbI_3$–TMPPA NCs retain the α-phase in both crude and washed solutions (Fig. S2, ESI†).

A comparison of the UV-Vis absorption and PL spectra of $CsPbI_3$–OA and $CsPbI_3$–TMPPA over a period of time are shown in Fig. 2a–d. As-synthesised samples exhibit band-edge absorption in the near-infrared region that approach the α-$CsPbI_3$ bulk optical bandgap of ~1.73 eV. PL characteristics are also similar, albeit with the $CsPbI_3$–TMPPA samples exhibiting a narrower FWHM of

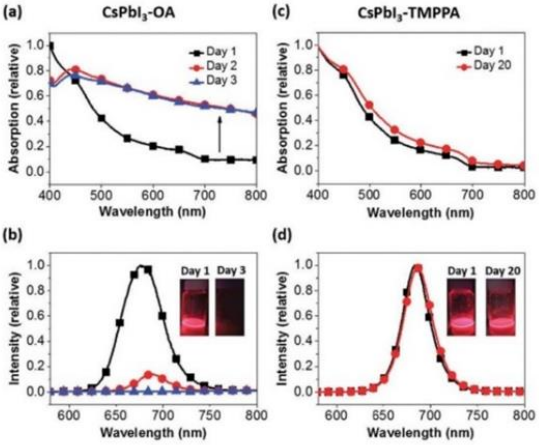

Fig. 2 UV-Vis absorption and PL spectra for $CsPbI_3$–OA (a and b) and $CsPbI_3$–TMPPA (c and d). Insets of (b and d): solutions of the respective washed NCs under UV light at different times following synthesis.

34 nm *versus* 50 nm for $CsPbI_3$–OA. The absorption spectra of $CsPbI_3$–OA show a progressively larger scattering contribution upon storage over only 3 days, with yellow precipitates forming in that period, characteristic of δ-$CsPbI_3$. The PL intensity simultaneously declines during this time. In contrast, the absorption and PL properties of $CsPbI_3$–TMPPA are almost perfectly preserved after 20 days of storage under ambient conditions. Similar findings were observed for $CsPbI_3$–TMPPA synthesised at lower reaction temperatures (Fig. S3, ESI†).

To confirm the potential structural stability and changes inferred from optical measurements, powder X-ray diffraction (PXRD) measurements were performed on $CsPbI_3$–TMPPA and $CsPbI_3$–OA NCs (Fig. 3a and b). $CsPbI_3$–TMPPA retained the α phase throughout the seven-day testing period (further measurements show the samples are stable for months). In stark contrast, $CsPbI_3$–OA had already partially transformed from the cubic to orthorhombic phase within one day. Not surprisingly, by day 7

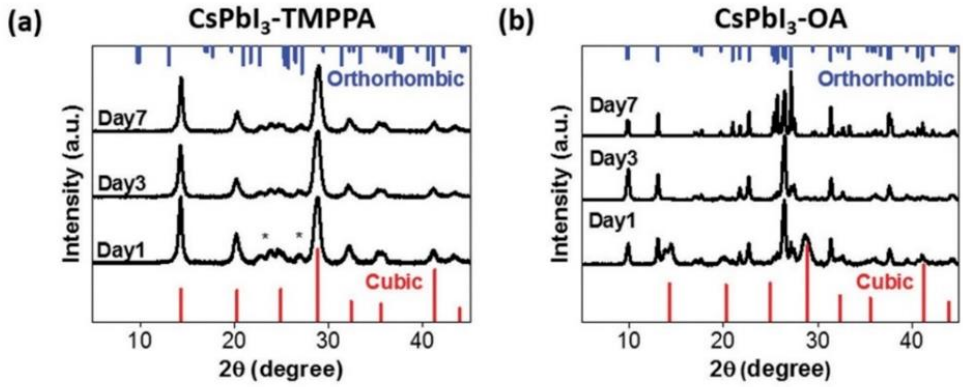

Fig. 3 XRD patterns of (a) $CsPbI_3$–TMPPA and (b) $CsPbI_3$–OA. Standard cubic phase is shown in red (bottom), orthorhombic phase in blue (top). (*) unidentified peaks.

Published on 23 November 2016. Downloaded on 11/02/2018 23:19:14.

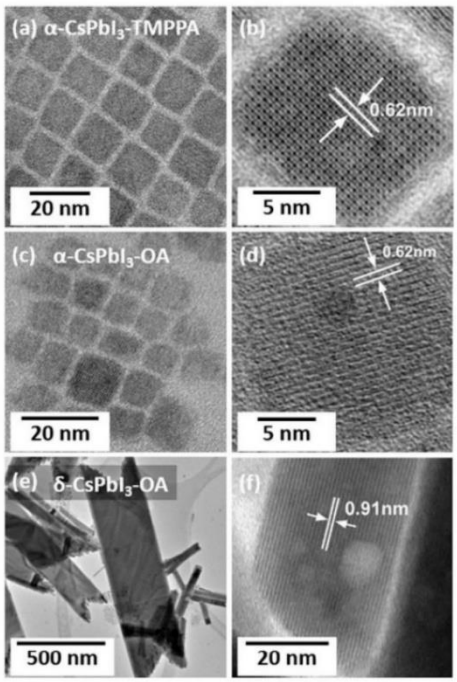

Fig. 4 TEM and HRTEM images of α-$CsPbI_3$–TMPPA (a and b), α-$CsPbI_3$–OA (c and d) and δ-$CsPbI_3$–OA (e and f).

the sample had completely transformed into the orthorhombic phase. Notably, the peak widths in Fig. 3b progressively decrease over time, indicating that $CsPbI_3$–OA is exhibiting grain growth throughout the phase transformation process.[23]

Transmission electron microscopy (TEM) was performed to verify the structural characteristics of the as-prepared and phase transformed $CsPbI_3$ samples. Nanocrystals of α-$CsPbI_3$–TMPPA and α-$CsPbI_3$–OA exhibited a cubic shape (Fig. 4a–d), and were measured to have an edge length of approximately 12 nm and 10 nm, respectively (Fig. S4, ESI†). Consistent with the (100) plane of the α-phase, these samples possess inter-planar distances of 0.62 nm (Fig. 4b and d).[13,14] The formation of δ-$CsPbI_3$ was only observed in $CsPbI_3$–OA (Fig. 4e and f), as confirmed by the presence of an inter-planar distance of 0.91 nm, which corresponds to the (011) plane.[14] These crystals no longer retain their cubic morphology and instead transform into nanorods and sheets that are hundreds of nanometers in size. Notably, small cubes of ~10 nm width were also found in these samples, likely due to the presence of α-$CsPbI_3$ NCs that have not yet fully transformed. From these observations, it is reasonable to posit that the α-to-δ phase transformation involves NCs aggregating and then structurally re-arranging to form the rod- and sheet-shaped crystals.

To explore the potential mechanism for TMPPA stabilising α-$CsPbI_3$, we examined solutions of washed NCs using Nuclear Magnetic Resonance (NMR) spectroscopy. As TMPPA is the only significant phosphorous-containing component of the reaction,[24] ^{31}P NMR measurements provide a clear insight into its chemical state, in contrast to ^{1}H and ^{13}C NMR measurements, where the convolution of signals from the OLA ligand and residual ODE and *tert*-butanol[21] makes the unambiguous identification of TMPPA impossible (Fig. S5 and S6, ESI†).

The ^{31}P NMR spectrum of a concentrated solution of once-washed $CsPbI_3$–TMPPA NCs revealed that the signal attributed to TMPPA had significantly shifted and broadened compared to the reference spectra of TMPPA (Fig. S7 and S8, ESI†). While this can be a sign of strong bonding to a NC surface,[25,26] the ^{31}P NMR signal of TMPPA is also known to shift and broaden in the presence of a base, due to the formation of ion pairs in solution.[24] To differentiate between these possibilities, a measurement of a solution in which TMPPA was reacted with an excess of OLA to form an oleylammonium–TMPPA$^-$ ion pair resulted in a spectrum that contained a peak with the same position and width as that observed for the $CsPbI_3$ NCs (Fig. S9 and S10, ESI†). Furthermore, a control measurement of a Pb–TMPPA complex showed the TMPPA signal is in an unambiguously different position compared to the $CsPbI_3$–TMPPA NC solution (Fig. S11, ESI†). These results confirmed that TMPPA was not binding to Pb on the surface of the nanocrystal.

Diffusion coefficients, as measured by 2D diffusion-ordered spectroscopy (DOSY), were also used to determine whether TMPPA was interacting with surface of the $CsPbI_3$ NCs.[21] The diffusion coefficients of TMPPA and the TMPPA species present in a concentrated solution of $CsPbI_3$ NCs were both measured to be ~520 $\mu m^2\ s^{-1}$. These diffusion coefficients are approximately one order of magnitude larger than that expected for a species binding to the surface of NCs of a size synthesised in this study.[21] Notably, while it was expected that the solution containing the ion pair would give a lower diffusion coefficient compared to the free TMPPA species, dialkyl phosphinic acids are known to form hydrogen bond dimers in apolar solvents,[27] which would give a species with a comparable solvodynamic radius. Overall, these results indicated that in a once-washed solution of $CsPbI_3$ NCs, TMPPA exists in an ion pair with oleylammonium and does not bind to the NC surface.

To test this hypothesis, a solution of $CsPbI_3$ NCs was washed a second time in an attempt to remove all TMPPA species. Remarkably, an extended ^{31}P NMR measurement (~5 h) of a twice-washed solution of phase stable α-$CsPbI_3$ NCs only yielded extremely weak signals due to P containing species (Fig. S12, ESI†). In comparison, a broad peak at 5.5 ppm, which has been attributed to OLA species dynamically interacting with the NC surface, could be detected in the same solution with a standard ^{1}H NMR measurement (Fig. S5, ESI†).[21] This indicates that after two washes, TMPPA was not present in the solution in any significant quantity and that it does not play a role in stabilising the phase of α-$CsPbI_3$ by coordinating to the NC surface.

This finding is in contrast to syntheses utilising OA, in which oleylammonium-oleate and OA are co-passivants with oleylammonium bromide and OLA for $CsPbBr_3$ NCs.[21,22] We hypothesise that the α-to-δ phase transformation in NCs is associated with this surface chemistry. This is supported by the addition of OA or oleylammonium-oleate to an α-$CsPbI_3$–TMPPA

 This journal is © The Royal Society of Chemistry 2017

solution, which resulted in a rapid transformation to the δ-phase (Fig. S13 and S14, ESI†). Conversely, the addition of TMPPA to α-$CsPbI_3$–OA solution resulted in a slower α-to-δ transformation, although it did not prevent it (Fig. S15 and S16, ESI†).

In conclusion, we have developed a new synthesis for high-quality $CsPbI_3$ nanocrystals that harnesses an alkyl phosphinic acid as a replacement for conventionally used oleic acid. Importantly, the NCs retain their cubic perovskite phase in solution, which has been a significant challenge to date. We have found that, unlike for oleic acid, the phosphinic acid and its ion-pairs do not bind to the NC surface. This ensures that in our synthesis oleylammonium iodide and/or oleylamine are the predominant surface ligands. Based on this, we suggest that the phase instability in this system is directly associated with the destabilisation of this surface chemistry. Further research is required to understand precisely why oleic acid and/or its ion pair drive this instability and what factors prevent the alkyl phosphinic acid used in this study from binding to the α-$CsPbI_3$ nanocrystal surface.

Notes and references

1 A. Swarnkar, R. Chulliyil, V. K. Ravi, M. Irfanullah, A. Chowdhury and A. Nag, *Angew. Chem., Int. Ed.*, 2015, **54**, 15424–15428.
2 Q. A. Akkerman, V. D'Innocenzo, S. Accornero, A. Scarpellini, A. Petrozza, M. Prato and L. Manna, *J. Am. Chem. Soc.*, 2015, **137**, 10276–10281.
3 K. Wu, G. Liang, Q. Shang, Y. Ren, D. Kong and T. Lian, *J. Am. Chem. Soc.*, 2015, **137**, 12792–12795.
4 J. Song, J. Li, X. Li, L. Xu, Y. Dong and H. Zeng, *Adv. Mater.*, 2015, **27**, 7162–7167.
5 S. Yakunin, L. Protesescu, F. Krieg, M. I. Bodnarchuk, G. Nedelcu, M. Humer, G. De Luca, M. Fiebig, W. Heiss and M. V. Kovalenko, *Nat. Commun.*, 2015, **6**, 8056.
6 J.-S. Lee, P. Ramasamy, D.-H. Lim, B. Kim, S.-H. Lee and M.-S. Lee, *Chem. Commun.*, 2015, **52**, 3–6.
7 L. Protesescu, S. Yakunin, M. I. Bodnarchuk, F. Krieg, R. Caputo, C. H. Hendon, R. X. Yang, A. Walsh and M. V. Kovalenko, *Nano Lett.*, 2015, **15**, 3692–3696.
8 D. Zhang, S. W. Eaton, Y. Yu, L. Dou and P. Yang, *J. Am. Chem. Soc.*, 2015, **137**, 9230–9233.
9 I. Lignos, S. Stavrakis, G. Nedelcu, L. Protesescu, A. J. Demello and M. V. Kovalenko, *Nano Lett.*, 2016, **16**, 1869–1877.
10 F. Palazon, Q. A. Akkerman, M. Prato and L. Manna, *ACS Nano*, 2016, **10**, 1224–1230.
11 C. C. Lin, A. Meijerink and R. S. Liu, *J. Phys. Chem. Lett.*, 2016, **7**, 495–503.
12 M. Saliba, T. Matsui, J.-Y. Seo, K. Domanski, J.-P. Correa-Baena, M. K. Nazeeruddin, S. M. Zakeeruddin, W. Tress, A. Abate, A. Hagfeldt and M. Grä Tzel, *Energy Environ. Sci.*, 2016, **9**, 1989–1997.
13 C. K. Møller, *Nature*, 1958, **182**, 1436.
14 D. M. Trots and S. V. Myagkota, *J. Phys. Chem. Solids*, 2008, **69**, 2520–2526.
15 G. E. Eperon, G. M. Paterno, R. J. Sutton, A. Zampetti, A. A. Haghighirad, F. Cacialli and H. J. Snaith, *J. Mater. Chem. A*, 2015, **3**, 19688–19695.
16 S. Dastidar, D. A. Egger, L. Z. Tan, S. B. Cromer, A. D. Dillon, S. Liu, L. Kronik, A. M. Rappe and A. T. Fafarman, *Nano Lett.*, 2016, **16**, 3563–3570.
17 A. Swarnkar, A. R. Marshall, E. M. Sanehira, B. D. Chernomordik, D. T. Moore, J. A. Christians, T. Chakrabarti and J. M. Luther, *Science*, 2016, **354**, 92–95.
18 M. A. Boles, D. Ling, T. Hyeon and D. V. Talapin, *Nat. Mater.*, 2016, **15**, 141–153.
19 Y. Sun, Y. Chen, L. Tian, Y. Yu, X. Kong, J. Zhao and H. Zhang, *Nanotechnology*, 2007, **18**, 275609.
20 K. Nose, Y. Soma, T. Omata and S. Otsuka-Yao-Matsuo, *Chem. Mater.*, 2009, **21**, 2607–2613.
21 J. De Roo, M. Ibáñez, P. Geiregat, G. Nedelcu, W. Walravens, J. Maes, J. C. Martins, I. Van Driessche, M. V. Kovalenko and Z. Hens, *ACS Nano*, 2016, **10**, 2071–2081.
22 A. Pan, B. He, X. Fan, Z. Liu, J. J. Urban, A. P. Alivisatos, L. He and Y. Liu, *ACS Nano*, 2016, **10**, 7943–7954.
23 A. Monshi, *World J. Nano Sci. Eng.*, 2012, **2**, 154–160.
24 D. Cholico-Gonzalez, M. Avila-Rodriguez, G. Cote and A. Chagnes, *J. Mol. Liq.*, 2013, **187**, 165–170.
25 M. Kuno, J. K. Lee, B. O. Dabbousi, F. V. Mikulec and M. G. Bawendi, *J. Chem. Phys.*, 1997, **106**, 9869–9882.
26 J. S. Owen, J. Park, P.-E. Trudeau and A. P. Alivisatos, *J. Am. Chem. Soc.*, 2008, **130**, 12279–12281.
27 J. A. Walmsley, *J. Phys. Chem.*, 1984, **88**, 1226–1231.

Published on 23 November 2016. Downloaded on 11/02/2018 23:19:14.